Structures Research Report
FDOT Contract # BE932

Embry-Riddle Aeronautical University
Civil Engineering

ERAU

EMBRY-RIDDLE AERONAUTICAL UNIVERSITY

Final Report December 2023

Inspection of Flexible Filler Tendons

Principle Investigator:

Jeff Brown, Ph.D.

Co-Principle Investigator:

Dan Su, Ph.D., P.E.

Graduate Research Assistants:

Carley Gonzalez

Denis McDonald

Undergraduate Research Assistants:

Adam Dumas

Lucas Acosta

Nolan Metz

Raissa Bianco

Performing Organization:

Embry-Riddle Aeronautical University

600 S. Clyde Morris Boulevard
Daytona Beach, FL, United States 32114

Sponsor Organization:

Florida Department of Transportation

605 Suwannee Street
Tallahassee, FL, United States 32399-0450

Contract #:

FDOT No. BE932

Disclaimer

The opinions, findings and conclusions expressed within this report “Inspection of Flexible Filler Tendons” are those of the authors and are not necessarily those of the State of Florida Department of Transportation.

SI (Modern Metric) Conversion Factors

SYMBOL	WHEN YOU KNOW	MULTIPLY BY	TO FIND		SYMBOL
	LENGTH				
in	inches	25.4	millimeters		mm
ft	feet	0.305	meters		m
yd	yards	0.914	meters		m
mi	miles	1.61	kilometers		km
mil	1/1000th of an inch	0.025	millimeters		mm
	AREA				
in^2	square inches	645.2	square millimeters		mm^2
ft^2	square feet	0.093	square meters		m^2
yd^2	square yards	0.836	square meters		m^2
ac	acres	0.405	hectares		ha
mi^2	square miles	2.59	square kilometers		km^2
	VOLUME				
fl oz	fluid ounces	29.57	milliliters		mL
gal	gallons	3.785	liters		L
ft^3	cubic feet	0.028	cubic meters		m^3
yd^3	cubic yards	0.765	cubic meters		m^3
	NOTE: volumes greater than 1000 L shall be shown in m^3				
	MASS				
oz	ounces	28.35	grams		g
lb	pounds	0.454	kilograms		kg
T	short tons (2000 lb)	0.907	metric ton		Mg (or "t")
	TEMPERATURE (exact degrees)				
°F	Fahrenheit		Celsius		°C
	ILLUMINATION				
fc	foot-candles	10.76	lux		lx
fl	foot-lamberts	3.426	candela/m^2		cd/m^2
	FORCE and PRESSURE or STRESS				
kip	1000 pound force	4.45	kilonewtons		kN
lbf	pound force	4.45	newtons		N
lbf/in^2	pound force per square inch	6.89	kilopascals		kPa
ksi	kip per square inch	6.89	megapascals		MPa
ksf	kip per square foot	47.88	kilopascals		kPa
Msi	million pounds per square inch	6.89	gigapascals		GPa

Approximate Conversions **TO** SI Units

*Approximate Conversions **TO** USC Units*

SYMBOL	WHEN YOU KNOW	MULTIPLY BY	TO FIND	SYMBOL
LENGTH				
mm	millimeters	0.039	inches	in
m	meters	3.28	feet	ft
m	meters	1.09	yards	yd
km	kilometers	0.621	miles	mi
AREA				
mm^2	square millimeters	0.0016	square inches	in^2
m^2	square meters	10.764	square feet	ft^2
m^2	square meters	1.195	square yards	yd^2
ha	hectares	2.47	acres	ac
km^2	square kilometers	0.386	square miles	mi^2
VOLUME				
mL	milliliters	0.034	fluid ounces	fl oz
L	liters	0.264	gallons	gal
m^3	cubic meters	35.314	cubic feet	ft^3
m^3	cubic meters	1.307	cubic yards	yd^3
MASS				
g	grams	0.035	ounces	oz
kg	kilograms	2.202	pounds	Ib
Mg (or "t")	megagrams (or "metric	1.103	short tons (2000 Ib)	T
TEMPERATURE (exact degrees)				
°C	Celsius	1.8C+32	Fahrenheit	°F
ILLUMINATION				
lx	lux	0.0929	foot-candles	fc
cd/m^2	candela/m^2	0.2919	foot-lamberts	fl
FORCE and PRESSURE or STRESS				
kN	kilonewtons	0.225	1000 pound force	kip
N	newtons	0.225	pound force	Ibf
kPa	kilopascals	0.145	pound force per square inch	Ibf/in^2

Technical Report Documentation Page

1. Report No.	**2. Government Accession No.**		**3. Recipient Catalog No.**
4 Title and Subtitle Inspection of Flexible Filler Tendons			**5 Report Date** December 2023 **6 Performing Organization Code**
7. Author(s) Jeff R. Brown, Dan Su, Denis McDonald, Carley Gonzalez, Nolan Metz, and Raissa Bianco			**8 Performing Organization Report No.**
9 Performing Organization Name and Address Embry-Riddle Aeronautical University 600 S. Clyde Morris Blvd. Daytona Beach, FL 32114			**10 Work Unit No. (TRAIS)** **11 Contract or Grant No.** BE932
12 Sponsoring Agency Name and Address Florida Department of Transportation Research Center, MS 30 605 Suwannee St Tallahassee, FL 32399-0450			**13 Type of Report and Period Covered** Final Report February 2020-December 2023 **14 Sponsoring Agency Code**
15 Supplementary Notes			

16 Abstract

This research focused on developing an inspection protocol for post-tensioning (PT) ducts employing flexible filler materials for corrosion protection in bridge applications. Historically, cementitious grouts (CG) have been used to provide corrosion protection and bonding in PT systems. In contrast, flexible filler systems use wax or grease to maintain a physical barrier for corrosion protection but result in unbonded tendons. An initial literature survey focused on bonded systems with CG for corrosion protection, which led to the identification of three NDE methods that show promise for flexible-filler systems: ultrasound coda-wave interferometry, thermoelasticity, and radiography for anchorage cap imaging. Key priorities for the experimental work, which were identified in consultation with FDOT project managers, include NDE methods for identifying micro-cracking and assessing stress levels in concrete and non-invasive NDE methods for identifying corrosion in tendons and anchorages.

Proof-of-concept testing for thermoelasticity and ultrasound interferometry was conducted in ERAU laboratory facilities using small-scale specimens. Thermoelasticity was not effective for assessing the stress level in concrete and was removed from consideration. Preliminary investigations into ultrasound interferometry did demonstrate a capability for evaluating the change in stress level and presence of non-visible cracking. Proof-of-concept testing for radiography was completed using external contractors in October 2021 using large-scale specimens from other testing programs at the FDOT Structures Lab in Tallahassee. This testing yielded positive results for identifying wedge-grip dislocations at anchorages and tendon location in ducts. Large-scale testing was completed at the FDOT Structures Lab in Tallahassee during Summer 2023. Ultrasound interferometry was evaluated during post-tensioning and 4-point bending. Ultrasound interferometry was capable of identifying cracking during 4-point bending well before barely-visible cracking was observed.

17 Key Words Flexible filler, Post-tensioned bridge inspection, Ultrasound interferometry, Radiography		**18 Distribution Statement** No restrictions. This document is available to the public through the National Technical Information Service, Springfield, Virginia 22161	
19 Security Classification (of this report) Unclassified	**20 Security Classification (of this page)** Unclassified	**21 No. of pages** 210	**22 Price**

Acknowledgments

The authors of this publication would like to thank the Florida Department of Transportation (FDOT) for providing the necessary funding that has made this research possible and for providing the necessary facilities required for testing. Our project manager, Felix Padilla, provided essential guidance throughout the entire project. Furthermore, the authors would like to extend gratitude to the Marcus H. Ansley Structures Research Center personnel who played a vital role in this project by providing professional and technical insight as well as assistance with fabrication and testing. Special thanks to Felix Padilla, Christina Freeman, Yukai Yang, Stephen Eudy, Justin Robertson, Michael Waters, Paul Tighe, Ben Allen, and Miguel Ramirez. The advisory committee for this project included Dr. H.R. Hamilton, III, Dr. Daewon Kim, and Dr. Fady Barsoum. Their contributions are gratefully acknowledged. Dr. Jessica McKee provided invaluable assistance with editing and compiling the final document. Also, a special thanks to Bill Russo, Mike Potash, and Lucas Quilez from Embry-Riddle Aeronautical University for their contributions throughout the course of the research. Lastly, thank you to Steve Davis from CPS Pipe and Sika Corporation for donating their skills and materials to further help this research project.

Executive Summary

This research focused on developing an inspection protocol for post-tensioning (PT) ducts employing flexible filler materials for corrosion protection in bridge applications. Historically, cementitious grouts (CG) have been used to provide corrosion protection and tendon bonding in PT systems. Flexible-filler systems use wax or grease to maintain a physical barrier for corrosion protection but result in unbonded tendons. Maintaining prestress force in the structure is crucial to prevent visible cracking or load-induced micro-cracking. Severe corrosion may result in tendon rupture, which, for flexible-filler systems, may or may not be visible at the anchorage. The current inspection protocol for PT segmental bridges begins with a visual and mechanical sounding inspection. If defects are evident, invasive methods may be employed to access grout and strands. External contractors may be required for non-destructive evaluation (NDE) if needed. Subsequent invasive inspections may lead to repair actions, such as strand or tendon replacement.

An initial literature survey focused on bonded systems with CG for corrosion protection. A general overview of NDE methods and specific sensor systems that have been developed for CG systems is provided. This literature survey led to the identification of three NDE methods that showed promise for flexible-filler systems: ultrasound coda-wave interferometry, thermoelasticity, and radiography for anchorage cap imaging. Key priorities for the experimental work, which were identified in consultation with FDOT project managers, include NDE methods for identifying micro-cracking and assessing stress levels in concrete and non-invasive NDE methods for identifying corrosion in tendons and anchorages.

Proof-of-concept testing for thermoelasticity and ultrasound interferometry was conducted in ERAU laboratory facilities using small-scale specimens. Thermoelasticity was not effective for assessing the stress level in concrete and was removed from consideration. Preliminary investigations into ultrasound interferometry did demonstrate a capability for evaluating the change in stress level and presence of non-visible cracking. This method was identified as the primary focus for the large-scale testing.

Proof-of-concept testing for radiography was completed using external contractors in October 2021 using large-scale specimens from other testing programs at the FDOT Structures Lab in Tallahassee. This testing yielded positive results for identifying wedge-grip dislocations at anchorages and tendon location in ducts. Low-power medical-grade equipment was suitable for inspecting anchorages with Type 5 protection details and external ducts. For internal ducts with up to 12 inches of concrete, high-power industrial-grade equipment was required.

Large-scale testing was completed at the FDOT Structures Lab in Tallahassee during Summer 2023. The three post-tensioned specimens were 20 ft x 3 ft x 1 ft-10 in and included one continuous beam with a draped tendon, one match-cast beam with a straight tendon that simulated a closure pour, and one match-cast beam with a straight tendon that simulated match-cast construction with epoxy bonding. Ultrasound interferometry was evaluated during post-tensioning and 4-point bending. The beam with a simulated closure pour experienced shrinkage prior to post-tensioning and provided an imperfect surface at the midspan joint. The ultrasound interferometry was highly effective at identifying this imperfection during post-tensioning and 4-point bending. Ultrasound interferometry was capable of identifying cracking during 4-point bending well before barely-visible cracking was observed.

Table of Contents

Table of Figures

List of Tables

1 Introduction

The objective of this research is to develop an inspection protocol for post-tensioning (PT) ducts that rely on flexible filler materials for corrosion protection. Historically, PT systems in bridge applications have relied on cementitious grouts (CG). Traditional grouts provide corrosion protection in much the same way that concrete protects mild reinforcement and prestressing steel in conventional concrete structures. For the case of internal ducts, CGs also provide bond between the grouted tendon and the surrounding concrete. The wax or grease used in flexible filler systems provides corrosion protection by maintaining a physical barrier between the PT strands and corrosion-inducing elements (e.g., water). Unlike CG systems, flexible fillers always result in an unbonded tendon.

1.1 Current Guidelines/Applications of Flexible Fillers

Following a series of notable deficiencies related to corrosion protection in CG systems, FDOT adopted a formal policy requiring the use of flexible fillers in the 2016 Structural Design Guidelines.[1] This policy was originally directed towards the following PT applications:[2]

- External tendons
- Tendons with vertical deviation greater than 20”
- Continuity tendons in segmental box girders
- Tendons in I-beams and U-girders
- Strand tendons with vertical or predominantly vertical geometry
- Horizontal strand tendons in hammerhead, straddle, and C-piers.

The 2021 FDOT Structural Design Guidelines[3] (SDG) affirms the requirement for designing PT bridges with unbonded tendons using flexible fillers. Rather than provide a list of PT elements that should be designed as unbonded, this version of the SDG identifies the following elements as exceptions that are required to be designed as bonded using cementitious grouts:

- Top slab cantilever longitudinal tendons in segmental box girders
- Top slab transverse tendons in segmental box girders
- Tendons that are draped 2'-0" or less in post-tensioned slab-type superstructures.

Commentary in the 2021 SDG indicates that the motivation for continuing to use grouted tendons in these situations is the proximity of vehicles to the ducts and a desire to avoid cavities filled with flexible materials close to the roadway surface. The option for bonded tendons is also permitted for straight U-beam and other girder tendons not providing continuity. Bar tendons are also permitted to be designed as bonded with cementitious grouts.

1.1 Advantages of Flexible Fillers

The primary advantage provided by flexible fillers was that individual strands can be inspected and/or replaced during the service life of the bridge. Flexible fillers have an extensive track record in the nuclear industry for containment structures. In-service inspection of these systems involves routine pull-off tests to measure the post-tensioning force provided by a tendon; individual strand removal and inspection for damage; and chemical analysis of the flexible filler materials to ensure that the prestressing strands are not exposed to substances that might induce corrosion.

Another advantage provided by flexible fillers is the relative uniformity of the installed product compared to traditional CGs. One major factor contributing to corrosion in CG systems is bleed-water segregation. This can occur near the anchorages or at other locations in draped tendons. Direct exposure of PT strands to bleed water has resulted in multiple tendon failures. Other issues related to the grouting process, including chloride contamination in the grout material, improper mixing, and improper pumping, have also contributed to tendon failures over the years. Flexible fillers do not undergo any chemical property changes during injection. The material is simply pre-heated to a specified temperature to reduce the viscosity and then injected into the duct. As the flexible filler cools, it will regain its viscosity and provide a physical barrier to protect the PT strands.

1.2 Areas of Concern for Flexible Fillers

While the flexible filler material itself is not expected to contribute to corrosion of the PT strands, any errors in the injection process might lead to voids in a duct. Previous FDOT-sponsored research by Hamilton et al.[4] investigated the injection process through full-scale mock-ups. Voids did develop occasionally in the mock-up ducts (Figure 1), but it is important to note that the presence of a void in a flexible filler system is not necessarily going to cause corrosion the same way that a pocket of segregated bleed water might in a traditional CG system.

Other potential sources of corrosion in flexible filler systems include certain species of bacteria and fungi. The organic materials that are present in the flexible fillers can serve as a food source for these microorganisms. After consumption by microorganisms, the remaining material may be degraded and will no longer be capable of providing protection against moisture intrusion. Depending on the species of bacteria or fungi, the metabolic byproducts may also be acidic, which can lead to corrosion of the steel.[5] Research at Florida Atlantic University by Castaneda[6] involved exposing strand and wire specimens with flexible-filler coatings that had been inoculated with different fungi species. The fungi were able to break down the wax filler and lead to microbiologically induced corrosion (MIC). Castaneda's work sites several examples of MIC in structural engineering applications, but it is unclear how widespread the concern for this issue is in the post-tensioning industry. These effects can be mitigated by including an antimicrobial agent in the filler material. It is also suspected that the elevated injection temperatures may serve to pasteurize the filler and deactivate any microbes that may be present. In any case, the long-term degradation of flexible fillers remains an open question.[7]

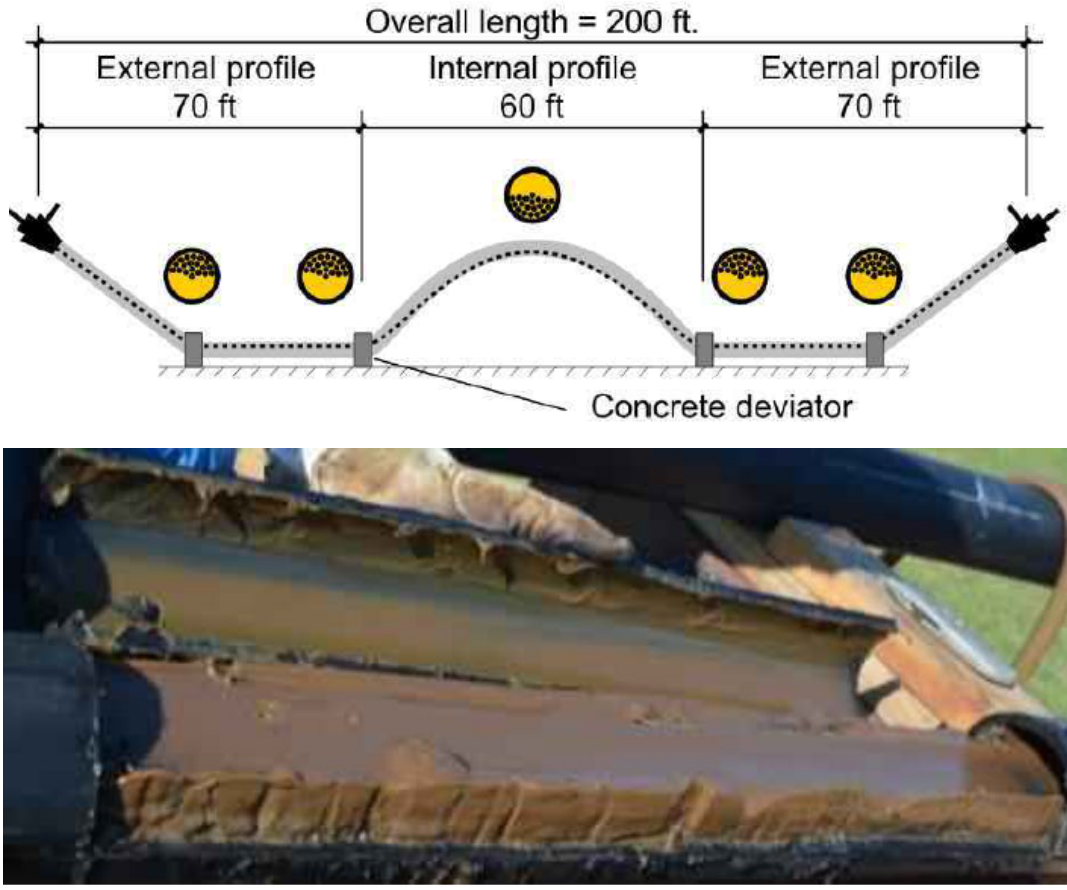

Figure 1. Void in duct during mock-up injection (Hamilton et al.).[4] Note that strands are still covered with filler material and the void itself is isolated in the overall system.

1.3 In-Service Inspection

In-service inspection of PT bridge elements is a topic of intense research. Because of the heavy reliance on CGs in the U.S. prior to the adoption of flexible fillers by FDOT in 2016, much of this work has focused on determining the following in CG systems:

- Whether or not corrosion has occurred in steel strands (i.e., identifying section loss in the steel)
- Whether or not the grout in the duct is sound and capable of providing corrosion protection for the steel (i.e., identifying voids, areas of bleed water segregation, or improperly cured grout)

One major area of concern for PT systems that rely on flexible fillers is that if corrosion is occurring in the strands, it may not result in the same visual indicators that occur in CG systems. In plain reinforced concrete, corrosion of the reinforcing steel results in corrosion byproducts that occupy a larger volume than the original steel. This leads to concrete cracking that can ultimately extend to the surface of the element. A similar phenomenon can occur in PT systems with cementitious grout. Corrosion in the prestressing strands can lead to cracking in the grout and splitting in the PT duct (Figure 2). In the case

of flexible fillers, the wax or grease will simply deform to accommodate any changes in volume generated by the corrosion byproducts.

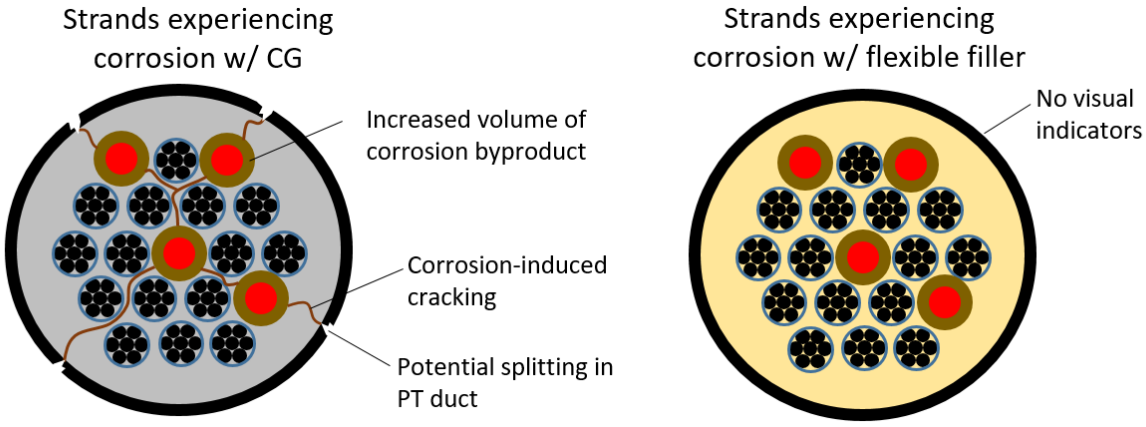

Figure 2. Comparison of visual indicators for cementitious grout and flexible fillers

Another potential challenge related to visual indicators for internal tendons is the unbonded behavior for PT systems that utilize flexible fillers. Internal tendons in traditional CG systems will exhibit bonded behavior. If localized corrosion occurs, the effective prestressing force will only be lost in the immediate vicinity of the corrosion damage. This phenomenon was recently observed on the Roosevelt Bridge in Stuart, Florida (Figure 3). The suspected cause of this corrosion damage was a poorly constructed closure pour that allowed chlorides to reach the metal PT duct. After the metal PT duct corroded, the chlorides further penetrated the cementitious grout and initiated corrosion in the tendon. The section loss in the tendons was localized to the closure pour, and, because the duct was grouted, the prestressing force was only lost at this specific section. Had this been a case of localized corrosion damage in an unbonded tendon, the effects of the prestress loss would have been distributed along the entire length of the structure between the anchorage points of the damaged tendons. It is unlikely that a corrosion protection system relying on flexible fillers would fail simultaneously for multiple tendons at the same location on a bridge. But the distinction between bonded and unbonded behavior is critical for in-service inspections.

Figure 3. Localized corrosion damage for internal tendon on Roosevelt Bridge in Stuart, Fl. (A) Concrete spalling and exposed tendons[8] and (B) location on bridge[9]

This research will provide an overview of previous efforts to inspect PT elements that rely on CGs. Some of this work may translate directly to flexible fillers, but we will also investigate alternative approaches that may be better suited for flexible fillers.

1.4 Current Inspection Protocols for CG Systems

For PT segmental bridges, FDOT currently relies on annual inspections to ensure that any active corrosion or cases of deficient grout can be identified and corrected before the overall serviceability of the bridge is jeopardized. These annual inspections begin with visual and mechanical sounding methods. If a deficiency is suspected, the inspection team may decide to call in external consultants to perform NDE work. Two NDE methods that are commonly used to inspect external tendons are ultrasonic pulse velocity (UPV) and electrical impedance (EI). Both methods are aimed at assessing the quality of the grout within the duct and identifying any voids or areas of bleed-water segregation. For the case of internal ducts, the impact echo (IE) method can be used to identify deeper voids or corrosion-induced splitting within the concrete.

The research team for the current project recently observed these NDE methods during follow-up inspections on two PT segmental bridges in the Daytona Beach area. During the annual inspection of the Broadway Bridge, several areas of concern were identified through visual inspection and mechanical sounding. One area involved rust stains on an external tendon (Figure 4) and another area involved suspected voids in an external tendon that was identified through mechanical sounding.

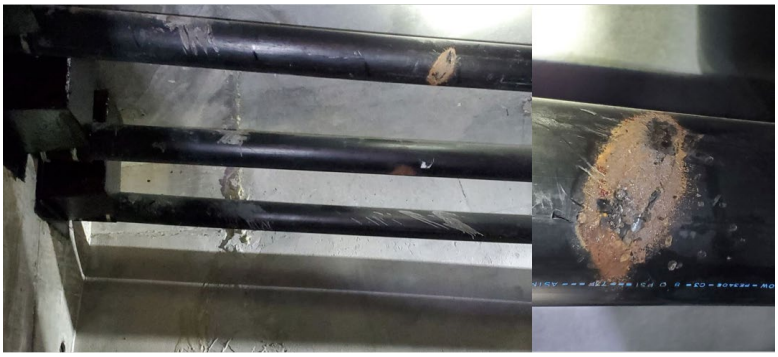

Figure 4. Visible rust stains on external tendon. Broadway Bridge, Daytona Beach

External tendons were evaluated in two locations using UPV and EI. The UPV testing involves an ultrasonic transmitter and receiver that are positioned on opposite sides of the external tendon. Multiple scans are recorded at different circumferential angles at 1-foot intervals along the length of the tendon in the area of concern (Figure 5). The resulting data requires interpretation by an experienced operator to identify abnormalities.

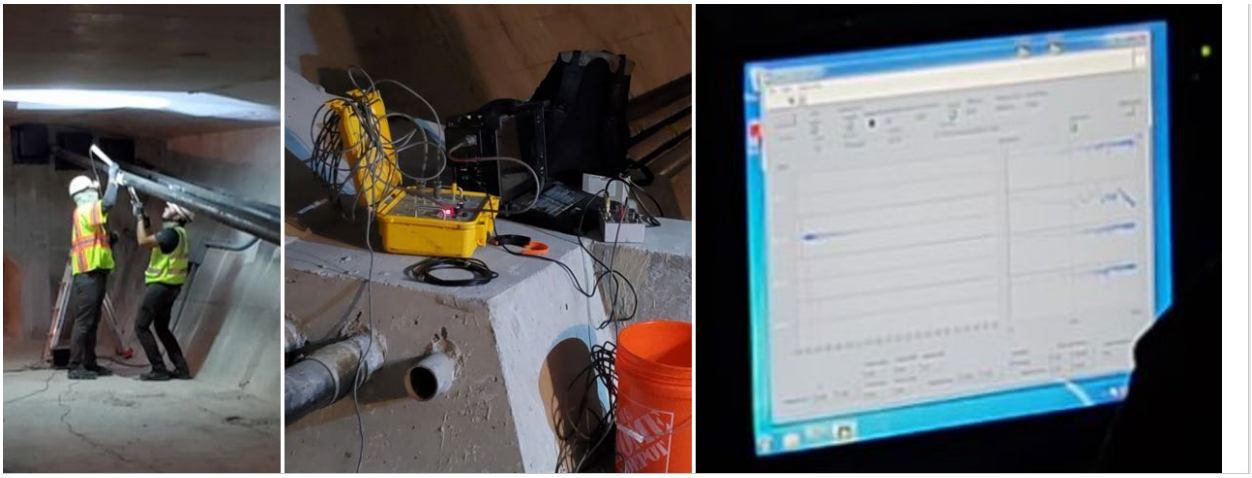

Figure 5. Ultrasonic pulse velocity testing on external tendon. Broadway Bridge, Daytona Beach

The electrical impedance testing was performed by a research group from USF. The device used for this inspection has been developed over the course of multiple FDOT-sponsored research projects.[10,11] The sensor device is clamped onto the external tendon and one operator rotates the device around the circumference (Figure 6). The process is repeated at 1-foot intervals over the area of concern. Another operator runs the data acquisition system, which consists of a small laptop. The output for this device is a cross-section of the tendon at each location a circumferential scan is performed. The tendon appears as a green area. Areas of concern within the duct (e.g., air voids, water voids, and defective grout) appear as different colors.

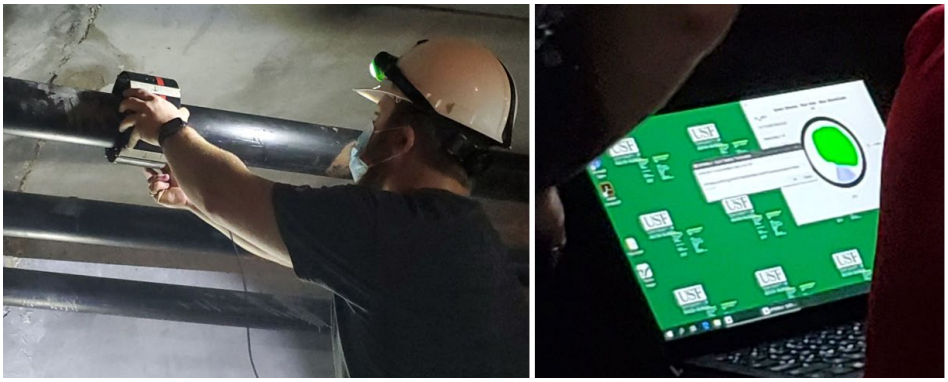

Figure 6. Electrical impedance inspection. Broadway Bridge, Daytona Beach

Several areas of concern were also identified during the annual inspection on the nearby Seabreeze Bridge. Mechanical sounding indicated potential problems in several anchorage blisters. Impact echo was used to evaluate the corresponding closure pours. The device used for the impact echo testing was a proprietary tool developed by the company performing the inspection (Vector Corrosion Services). A custom impactor was used to propel a stainless-steel BB into the concrete surface. An array of ultrasound transducers is positioned adjacent to the point of impact to record the ultrasonic waves as they travel through the structure. The data acquisition equipment is similar to the UPV, and the results also need to be interpreted by a highly skilled operator. The impactor device requires a pressurized nitrogen source to ensure that the impact energy remains consistent.

Figure 7. Impact echo testing across closure pour. Seabreeze Bridge, Daytona Beach

Once the NDE work is completed, the company performing the inspections will make recommendations regarding the need for additional invasive inspections. For external tendons, this will involve removing a section of the duct to gain direct access to the grouted tendon. The research team for this project did not observe any invasive inspections in December 2020, but there was evidence of previous invasive inspections of external ducts (Figure 8). Once a portion of the duct has been removed, it is possible to identify grout defects or corrosion damage. A borescope can also be used to visually inspect and evaluate any voids that extend beyond the area of the duct that was removed.

Accessing anchorages requires additional invasive procedures. The concrete pourback can be broken off to expose the anchorage cap and vent port. The grout in the vent tube can be drilled out to provide access for a borescope inspection of the strands and grout on the back side of the anchorage plate. For internal tendons, a coring operation is required to access the duct in question. Once the duct is exposed, further invasive inspection can continue to provide access for a borescope or to conduct chemical analysis on the tendon grout.

Figure 8. External ducts that were previously targeted for invasive inspection (Broadway Bridge) and concrete pourback for anchorage protection (Seabreeze Bridge).

In summary, the current protocol for inspecting PT segmental bridges always begins with a visual inspection and mechanical sounding (i.e., hammer tap). If the initial inspection reveals an obvious flaw or defect, the inspectors may proceed directly to invasive methods that will provide direct access to the grout and strands. For cases that are questionable, the inspectors may decide to call in an external contractor to perform NDE work. The results of the NDE inspection will determine if additional invasive methods are warranted. If the invasive inspection indicates significant damage to the tendon, the defect is further characterized, and provisions are made for a repair action. This may involve grout removal and replacement using a vacuum re-grouting procedure.[12] The general protocol is represented graphically in Figure 9.

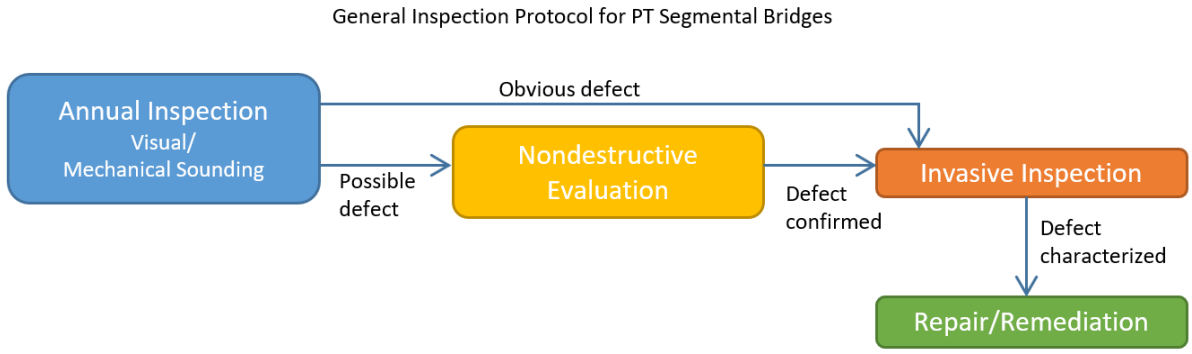

Figure 9. General inspection protocol for PT segmental bridges

1.5 General Framework for Inspections of Flexible-Filler Systems

1.5.1 Initial Considerations

There are five basic strategies for assessing the integrity of a post-tensioned structural element that relies on flexible fillers for corrosion protection:

1. Identify cracking in the concrete that develops due to a loss in prestress force.
2. Direct inspection of prestressing strands to determine if corrosion has occurred.
3. Direct measurement of the prestressing force
4. Inspection of anchorage assemblies for signs of prestress loss
5. Chemical analysis of the flexible filler to determine if corrosion-inducing chemicals are present (e.g., moisture, chlorides, etc.)

The following considerations are critical for developing an in-service inspection protocol for flexible fillers:

1. Visual indicators typically encountered in CG systems (e.g., split ducts, rust staining, cracks in anchorage blisters) may not/will not occur for flexible fillers.
2. Mechanical sounding methods may indicate voids in external ducts, but the presence of a void in a flexible filler system is not as concerning as it would be for CGs.
3. Mechanical sounding of anchorage blisters may not indicate the presence of corrosion near the anchorage. Internal splitting is not likely to occur due to the expansion of corrosion byproducts.

4. Existing NDE methods used for assessing external and internal ducts (e.g., ultrasonic pulse velocity, impact echo, and electrical impedance) require validation for flexible-filler systems.
5. Invasive inspections will require a modified approach. Cutting into external ducts is relatively straightforward and should not pose any major concerns. Removing anchorage caps is also easier if flexible fillers are used.

We began the development of a modified framework for flexible fillers by considering the overall prestress force maintained in a tendon throughout its service-life. Four distinct possibilities were considered as an initial starting point:

1. **Minor Losses** (Creep and Shrinkage): Under ideal conditions with no corrosion activity, a tendon will still experience some minor losses in prestress force due to creep and shrinkage of the concrete. These effects are considered in the design of the system, so creep and shrinkage should not result in excessive tensile strains or cracking in the concrete.

2. **Minor Losses** (Mild Corrosion): If some corrosion occurs in the tendon throughout its service-life, the overall prestress force provided may be reduced to the point that non-visible/micro-cracking occurs in the concrete. This would likely occur in the tension zone (bottom) near the closure pours at the middle of a span. Depending on the time at which this level of cracking is reached and the overall aggressiveness of the bridge environment, this may or may not present a concern for the overall serviceability of the structure. For this damage state, corrosion is assumed to occur over a long period of time with effects that are limited to individual wires within strands.

3. **Major Losses** (Severe Corrosion – Steady): If the rate of corrosion is severe enough, it can lead to visible cracking that would represent a major serviceability concern. For this damage state, corrosion in the tendon is assumed to occur over a relatively long period of time and may affect entire strands within the tendon.

4. **Major Losses** (Severe Corrosion – Rapid): This level of damage represents a case in which the entire tendon succumbs to corrosion in a short period of time.

This framework is illustrated graphically in Figure 10. If the prestress force is maintained throughout the service-life of the structure, concrete should remain in compression and no visible cracking or load-induced micro-cracking should occur. Some loss in prestress force due to mild corrosion may lead to load-induced micro-cracking that would not be visible during a routine biennial inspection.

Severe corrosion may ultimately lead to a tendon rupture event. Depending on the rate of the rupture event, this level of damage may or may not be visible at the anchorage. It was demonstrated by Hamilton et al. [4] that cutting through strand wires in a stressed tendon will result in visible dislocations at wedge grips for the damaged strand (Figure 11). If the anchorage cap was not removed (or if the anchorage was not evaluated using an appropriate NDE method), the dislocations would not be detected.

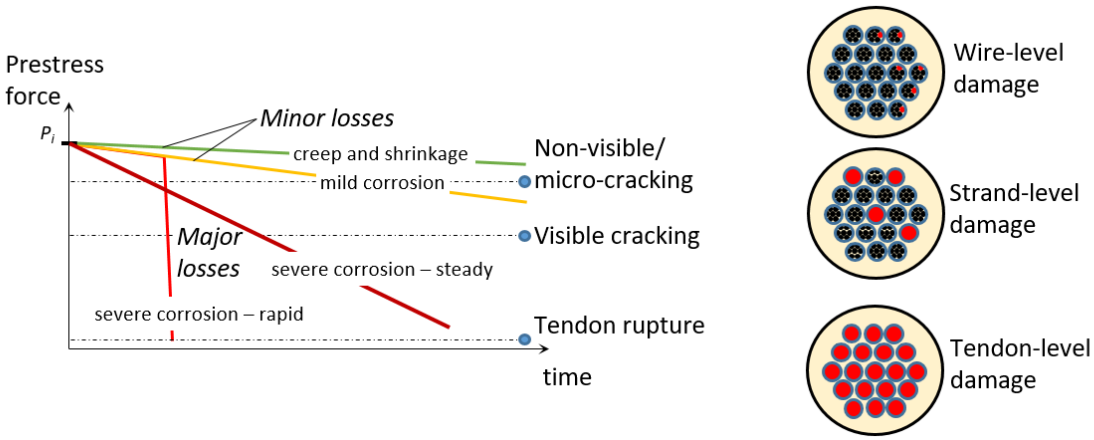

Figure 10. Prestress losses over the service-life of a tendon

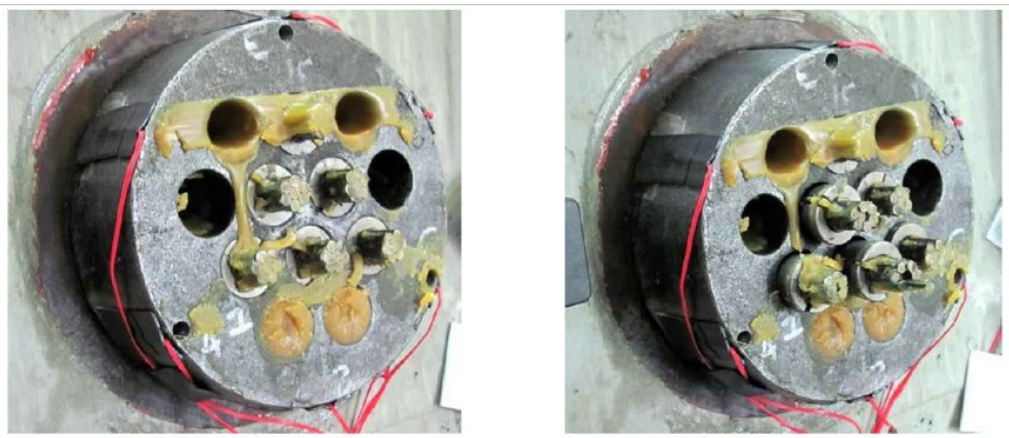

Figure 11. PT anchorage before and after intentional wire cutting (from Figure 7-5 on page 47 of Final Report for BDV31-977-15 by Hamilton et al.)[4]

If an entire strand or an entire tendon were to fail suddenly, the resulting damage to the anchorage may be noticeable during a visual inspection. Previous work by the US Army Corps of Engineers (USACE)[13] provides an interesting illustration of the severe damage that can occur in the vicinity of an anchorage when a post-tensioned element fails. The specific structures of interest in the USACE are dam spillway Tainter gates that rely on post-tensioned rods to secure the trunnion assembly to the concrete spillway pier. Tainter gates are widely used to control spillway flows through dams around the world. After approximately 50 years of service, the post-tensioned rods began failing at 10 dams across the United States. The anchorages for these rods are protected by a steel cover box. When the rods fail, they travel at a very high velocity until they encounter the steel cover boxes. The picture in Figure 12 shows dents in the cover box from rod strikes as well as rods that have completely penetrated the steel plate after ejecting from the anchorage.

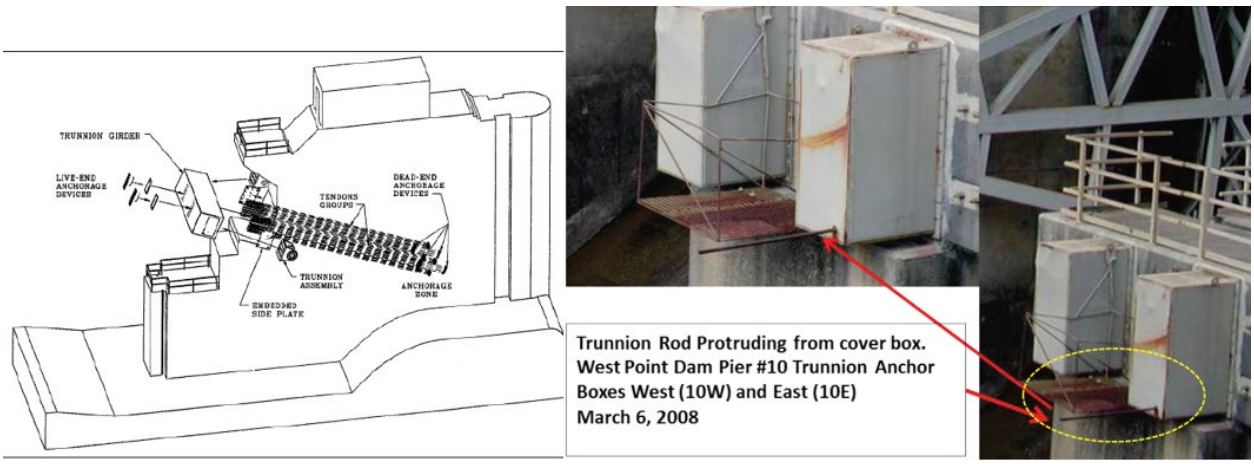

Figure 12. Corrosion failure of post-tensioned trunnion anchoring rods in Tainter gates.[13]

This example raises a very important question for the current study: Will strand-level or tendon-level corrosion-induced failures result in visible damage to the anchor caps? Details for the two most used anchorage protection systems on the Wekiva Bridge (Type 1 and Type 5) are provided in Figure 13. Type-1 systems include an epoxy grout pour-back that may serve to contain an ejecting strand. Type-5 systems only rely on an elastomeric coating over the permanent anchorage caps. Depending on the velocity of the strand as it leaves the anchorage, impact with the anchorage cap may lead to cracking or complete penetration by the strand/tendon.

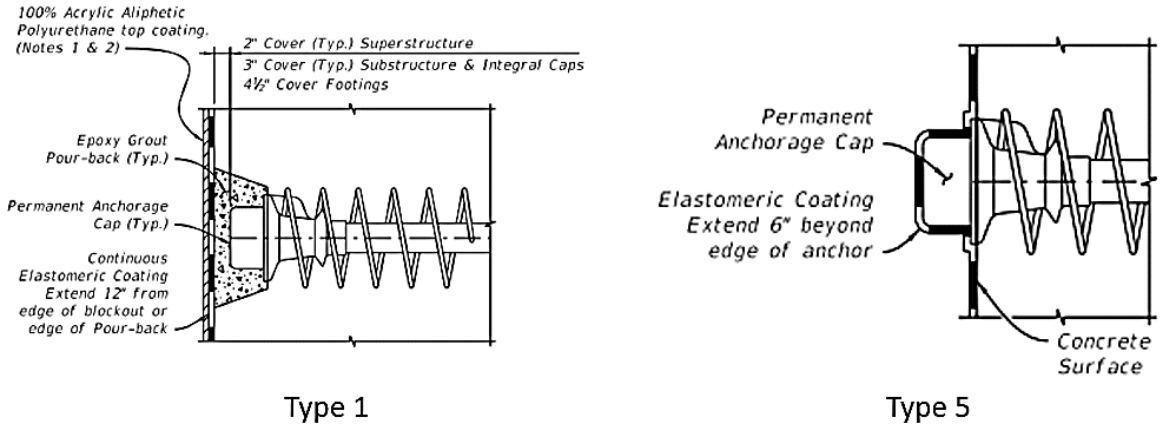

Figure 13 Standard details for post-tensioning anchorage protection[14] *(Type 1 and Type 5).*

1.5.2 Proposed Inspection Protocol

An initial proposal for a modified inspection protocol for flexible-filler PT systems is provided in Figure 14. The protocol relies on a biennial inspection that is similar to the current practice for CG systems. During this biennial inspection, FDOT inspectors will search for signs of cracking in the primary structural elements and visible damage at the anchorages.

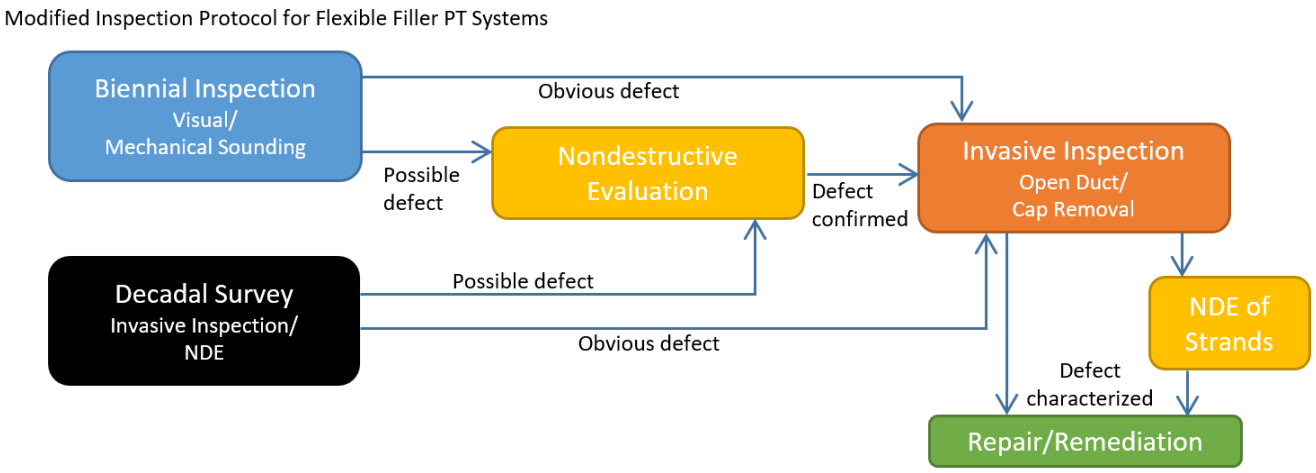

Figure 14. Proposed inspection protocol for flexible filler PT systems

In the case of an obvious defect or signs of severe distress during the biennial inspection, the inspection team will proceed to an invasive inspection. Key elements of the invasive inspection include the following:

- Anchorage cap removal and visual inspection of the wedge plate and exposed strand ends
- Removing a portion of the HDPE duct in an external tend to achieve direct access to the flexible filler and prestressing strand

If the biennial visual/mechanical sounding inspection indicates the possibility of damage within the PT system, an external contractor can be brought in to perform additional non-invasive NDE work. Examples of this might include magnetic flux leakage (MFL) inspection of external tendons to identify corrosion damage or ultrasound/ impact-echo inspections around the closure pours in segmental bridges to identify the early signs of prestress loss. Radiographic methods might also be employed to evaluate the condition of the anchorage and to ensure that the wedge grips and prestressing strands remain properly seated in the wedge plate. The results of this non-invasive NDE inspection will establish whether additional invasive inspections are required.

To account for the possibility of mild or severe corrosion damage that may occur over an extended period of time, it may be prudent to perform a more intense inspection of the flexible-filler system over a ten-year cycle. This decadal survey could involve non-invasive NDE inspections and invasive inspections for external ducts and anchorages. These inspections would be limited to a randomly selected sample of the overall system. Specific NDE methods might include MFL inspection on a sample of external ducts, ultrasound/impact-echo inspection around closure pours, and radiographic inspection of the anchorages.

To determine if the flexible filler is still capable of providing corrosion protection, several locations on a structure can be targeted for an invasive inspection during the decadal survey. This might include removing a random sample of anchorage caps and drilling into external tendons at multiple locations. Samples of the flexible filler can be extracted and subjected to a chemical analysis. Once the anchorage

caps have been removed, filler material can be sampled, and a visual inspection can be performed for the wedge plate and exposed prestressing strands.

Once the anchorage cap has been removed, there are additional options for NDE work related to the prestressing strands. Guided-wave ultrasonic testing (GWUT) can be performed to determine if the strands are damaged somewhere along their length. Variations of this method can also be used to evaluate the stress level in the strands to ensure that they are still providing the required prestressing force.

2 Previous Research

The literature survey has uncovered a large volume of work related to the inspection of PT systems. Most of the work has been focused on defect detection in bonded systems that rely on cementitious grout for corrosion protection. To make this review manageable, the research team divided the survey into four distinct categories:

- Comprehensive studies that compare different NDE methods for a range of defect types
- Development and evaluation of a specific sensor system
- General overview and applications of different NDE methods
- New methods that show promise for the inspection of flexible-filler systems.

2.1 Comprehensive Studies

Three comprehensive studies were identified through this literature review:

1. Hurlebaus et al. [15] completed an NCHRP-funded study at Texas A&M.
2. Azizinamini [16] has completed several FDOT projects related to tendon inspection at FIU.
3. The U.S. Army Corps of Engineers has completed multiple studies related to corrosion in PT systems for hydraulic structures.

2.1.1 Hurlebaus Study at Texas A&M

This NCHRP-funded project is by far the most comprehensive study identified by the research team. This work included the development of a mock-up bridge girder (Figure 15) with an array of internal and external tendons (Figure 16). The tendons were seeded with fabricated defects at multiple locations, and an array of NDE methods were deployed to inspect the tendons. An overall assessment of each method's functionality was provided.

The NDE methods evaluated in the study are summarized in Table 1. Additional description on the mechanism and specific applications for each method is provided in Section 2.3. The defects considered in the study were divided into two categories: strand defects and grout defects. Strand defects included corrosion, section loss, and breakage. The grout defects that were investigated included voids, water infiltration, and tendon deterioration at the anchorages. Another critical distinction was made between internal ducts and external ducts.

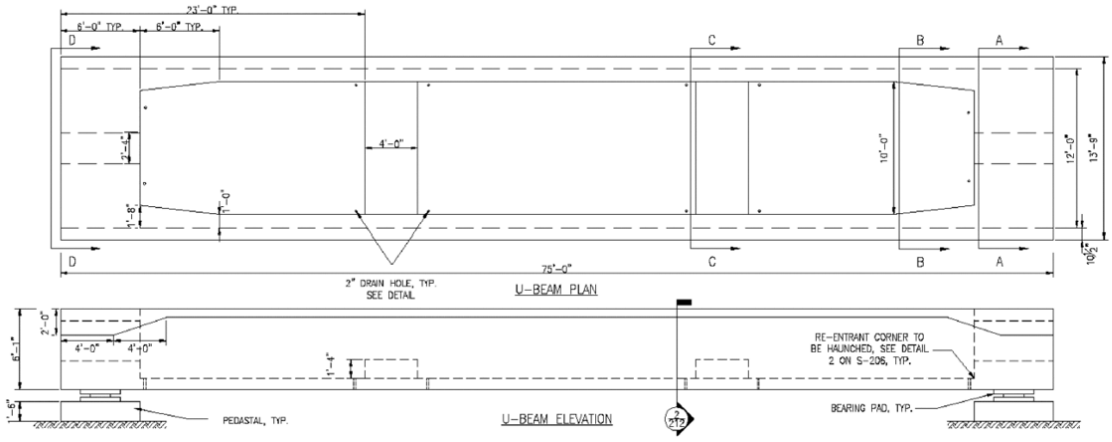

Figure 15. Plan and elevation of mock-up bridge girder for NCHRP study by Hurlebaus et al. [15]

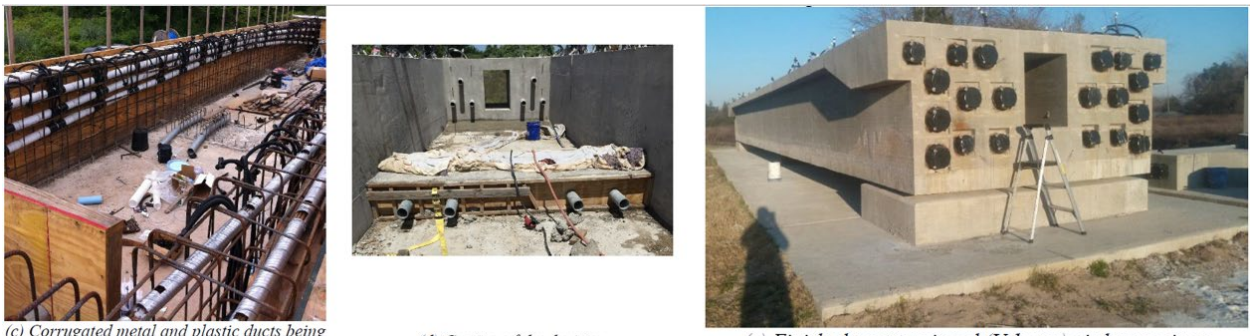

(c) Corrugated metal and plastic ducts being installed within the girder wall

(d) Casting of the deviator

(e) Finished post-tensioned (U-beam) girder specimen

Figure 16. Duct placement, concrete casting, and finished girder for NCHRP study by Hurlebaus et al. [15]

Table 1. Summary of NDE methods evaluated by Hurlebaus et al.[15]

Category	Methods
Electromagnetic	• Ground penetrating radar (GPR) • Infrared thermography (IRT) • Electrical capacitance tomography (ECT)
Magnetic	• Magnetic Flux Leakage (MFL) • Magnetic Main Flux Method: Permanent Magnet (MMF-P) • Magnetic Main Flux Method: Solenoid (MMF-S)
Mechanical Wave & Vibration	• Impact Echo (IE) • Ultrasonic Tomography (UST) • Ultrasonic Echo (USE) • Sonic/Ultrasonic Pulse Velocity (SPV-UPV) • Low Frequency Ultrasound (LFUT) • Sounding
Visual	• Visual Testing (VT) • Borescope (Bor)
Electrochemical	• Electrochemical Impedance Spectroscopy (EIS)

The general applicability and effectiveness of each NDE method for internal ducts are summarized in Table 2. A red color indicates that the method was not capable of identifying the specific defect type. A yellow color indicates that the method was moderately successful at identifying the presence of a defect but could not be used to characterize its severity. A green color indicates that the method is capable of both identifying and characterizing the severity of the defect. For internal ducts with cementitious grout, these results indicate significant challenges for almost all the NDE methods. Only the impact echo, ultrasonic echo, and borescope methods could identify grout defects for internal ducts. None of the methods could reliably identify strand defects.

Results were more encouraging for the external ducts . Magnetic methods were shown to be very accurate for characterizing strand defects. Equipment requirements for the magnetic methods are not trivial (Figure 17). The company that performed the magnetic flux leakage surveys in the Hurlebaus study, NDT Technologies, Inc., specializes in the inspection of large wire ropes commonly used in the offshore and marine industries.[17] Grout defects could also be characterized with infrared thermography, impact echo, and electrical capacitance tomography.

Two key findings from the Hurlebaus study are worth exploring in more detail:

- “None of the NDE technologies that were investigated is capable of detecting strand defects (corrosion/section loss/breakage) within the ducts buried in concrete, such as the webs, flanges, [and] deviators…”

- “None of the NDE technologies that were investigated is capable of identifying grout defects (compromised grout/void/water infiltration) with high accuracy for the ducts buried in the concrete, such as the webs, flanges, deviators and anchorage regions of the post tensioning system.”

Table 2 NDE methods and their effectiveness for internal ducts

NDE Method	Internal Ducts – Strand Defects			Internal Ducts – Grout Defects		
	Corrosion	Section loss	Breakage	Voids	Water	Anchorage
GPR						
IRT						
ECT						
MFL						
MMF-P						
MMF-S						
IE						
UST						
USE						
UPV						
LFUT						
Sounding						
VT						
Bor						
EIS						

For the case of internal ducts, there does not appear to be an existing NDE method that can reliably detect anomalies in either the prestressing strands or cementitious grouts. At this point, it isn’t clear how substituting flexible filler for cementitious grouts would improve the situation for detecting strand defects. The implications of this conclusion, at least for internal PT ducts, is that more invasive inspection methods that involve removal of the anchorage cap may be required. NDE methods for imaging through the anchorage end caps is also under consideration.

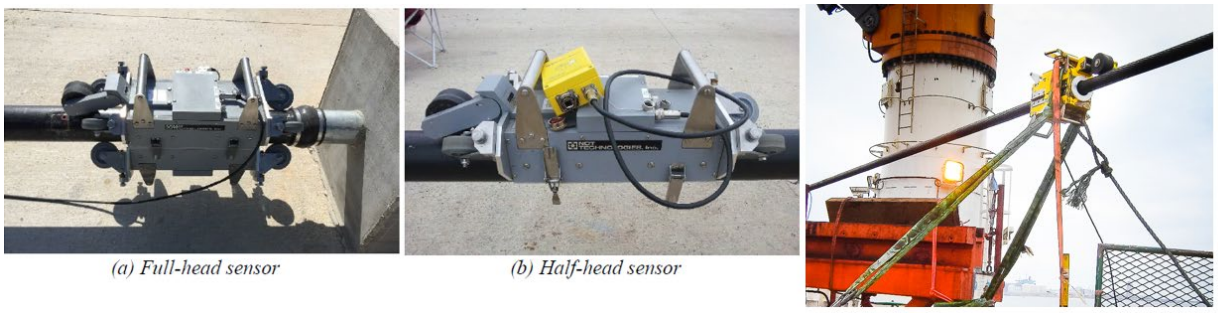

(a) Full-head sensor (b) Half-head sensor

Figure 17. NDE equipment for magnetic flux leakage inspection of external tendons in Hurlebaus et al. [15] study and inspection of large wire rope in the marine/offshore industry.[18]

The work by Hurlebaus also included a survey of DOTs from around the United States to better understand which NDE practices were in use at the time of the study. The general conclusion was that no DOT had developed a reliable inspection protocol for PT systems using NDE methods. The researchers also reported how several DOTs had previously deployed NDE methods for PT-system inspections but subsequently concluded that it wasn't worth the effort. Highlights from this survey are provided in Table 3.

Table 3 Summary of DOT experiences with NDE methods

NDE method no longer used	**Reason given for why they stopped using the method**
Magnetic flux leakage	Too expensive, assembly time for stay cables and external tendons too laborious and time-consuming
Ground penetrating radar	Only reliable for tendon location when used with other methods
Impact echo	Did not present the quality of inspection desired
Ultrasonics in general	Did not present the quality of inspection desired or were not fully aware of how to apply in field
Impedance measurements	Quit using in favor of MFL, but due to MFL's significant cost, reconsidering its use

Table 4 NDE methods and their effectiveness for external ducts

NDE Method	External Ducts – Strand Defects			External Ducts – Grout Defects		
	Corrosion	Section loss	Breakage	Voids	Water	@Anchorage
GPR						
IRT						
ECT						
MFL						
MMF-P						
MMF-S						
IE						
UST						
USE						
UPV						
LFUT						
Sounding						
VT						
Bor						
EIS						

2.1.2 FDOT-funded Research by Azizinamini

Dr. Azizinamini from Florida International University has performed numerous studies[19, 20, 21] related to the evaluation of PT systems. This comprehensive work has included laboratory and field investigations involving magnetic, electromagnetic, and mechanical vibration methods. The overall conclusions regarding the applicability of different NDE methods is summarized in Table 5. One relevant finding for the current study relates to magnetic flux leakage inspections for internal tendons. Azizinamini concluded that the presence of mild reinforcing steel surrounding the internal ducts can make the detection of strand defects difficult. It was shown that if the location of mild reinforcement was predetermined, their effects on the MFL signals could be subtracted to gain a clearer picture of any damage in the strands.

Another interesting observation from this work relates to the MFL device that was developed for experimental testing in the lab (Figure 18). This setup was developed for internal tendons and the overall complexity was minimal compared to the device used for external tendons in the Hurlebaus study (Figure 17). The device developed by Azizinamini was based on finite element analysis of the magnetic fields involved. This suggests that there may be opportunities to develop an MFL sensor that is better suited for external PT duct applications that would be easier to mobilize and deploy for routine inspections (a significant shortcoming of the method reported by Hurlebaus). Additional research to refine the sensor to include electromagnetic capabilities was recommended as future work in Azizinamini's latest study from 2017.[21]

Electrical inductance methods were also investigated. Again, a relatively simple device was developed using coils of wire and in inductance meter. The device could detect simulated section loss in a multi-strand tendon as long as no mild reinforcement was present (Figure 19). Results from an internal duct from a decommissioned bridge segment that included mild reinforcement were not as encouraging. Nonetheless, these results do suggest that a simple sensor could be developed for the inspection of external ducts with flexible filler.

Figure 18. Experimental testbed and sensor for MFL inspections by Azizinamini[21]

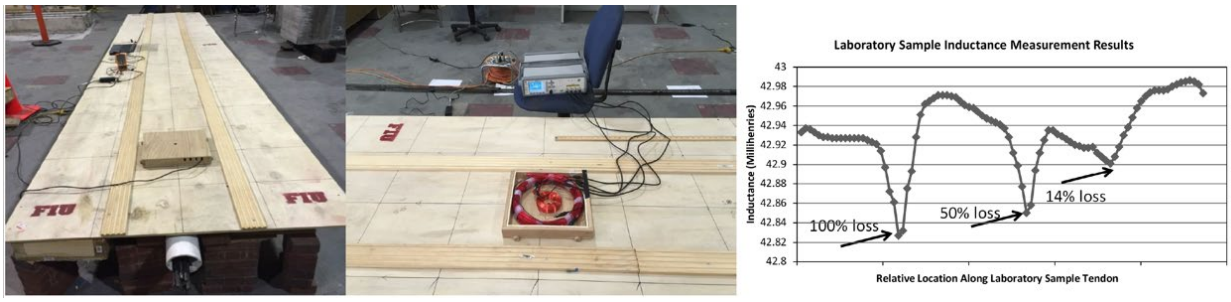

Figure 19. Experimental testbed, sensor, and results for inductance inspections by Azizinamini[21]

Table 5 General applicability of NDE methods for PT ducts with cementitious grouts from Azizinamini[20]

NDE Method		Inspection goal for grouted tendon			
		Strand/ cable breaks or section loss	Improper grout conditions/ voids	Active corrosion in tendons	Duct position and/or condition
Visual	Direct inspection				X
	Borescope		X	X	
Magnetic	Magnetic flux leakage	X		X	
Mechanical wave	Acoustic sounding		X		
	Acoustic emission	X		X	X
	Impact echo		X		
	Impulse response		X		
	Ultrasonic imaging		X		X
	Ultrasonic guided wave	X	X		
	Global vibration response				
Electro-Magnetic	Infrared thermography		X		X
	Impulse radar		X		X
Electro-chemical	Half-cell potential			X	
	Linear polarization resistance			X	
	Electro-impedance spectroscopy			X	
	Electrochemical noise			X	
Penetrating radiation	Radiography		X		X
	X-ray diffraction	X			
Other	Direct force measurement	X			

2.1.3 U.S. Army Corps of Engineers Research on Corrosion in PT Systems

Post tensioning is commonly used in a wide array of hydraulic structures that are managed by the USACE. Examples include locks, dams, and dam spillways. These applications are unique from a post-tensioning perspective because the dead ends of the tendons tend to be buried deep within the

structure or anchored into surrounding rock. The dead-end anchorages consist of a bonded length to secure the tendon, but then the stressing length is typically protected with a flexible filler. This allows for subsequent lift-off testing. These applications also differ from typical bridge applications because there is no access to the tendons along their length since the PT ducts are typically embedded within massive concrete structures.

An example of seven-wire multi-strand post tensioning is provided in Figure 20. This system was installed at the John Day Lock and Dam on the Columbia River in Washington state to remediate shifting in the lock walls. Cracking was also discovered at the base of lock walls near the mudline. The initial repairs were made in 1981. Inspections that occurred in 2003 indicated severe corrosion at multiple anchorages. Water was observed spewing from anchorages when the lock was full.

An example of solid-rod post tensioning for anchoring Tainter gates at the West Point Dam in Georgia is provided in Figure 21. This example was discussed previously in Section 1.5.1. The dead end of the rods sits within an anchorage that is cast deep into the pier wall. The stressed length of the rod is protected with a flexible filler and the live-end anchorage is protected by a steel cover. Stress corrosion cracking ultimately led to broken rods ejecting from the ducts and penetrating the steel covers.

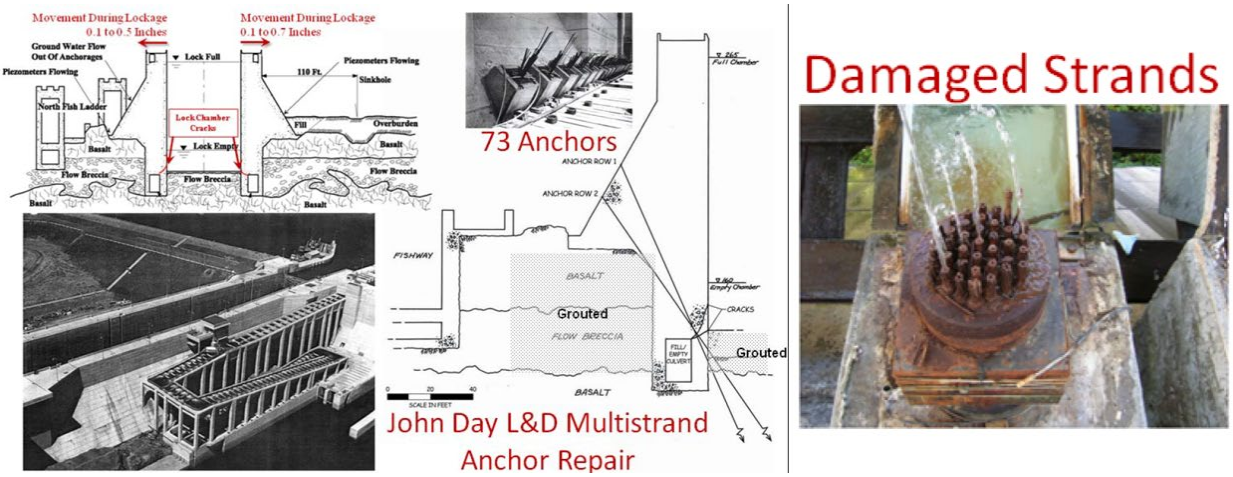

Figure 20. Seven-wire multi-strand tendon corrosion at John Day Lock and Dam[22]

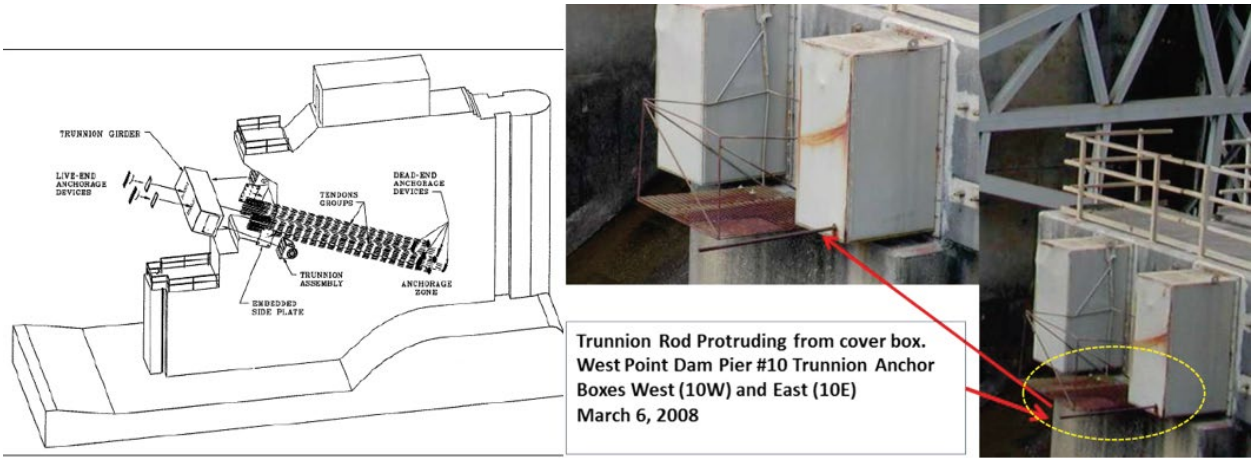

Figure 21. Corrosion failure of post-tensioned trunnion anchoring rods in Tainter gates[13]

The USACE evaluation program for both the multi-strand and solid-rod PT tendons was based on a two-pronged approach: lift-off testing and NDE. Since access was limited to the live-end anchorages, the major research effort focused on evaluating ultrasonic methods. For the multi-strand systems, the primary focus was identifying broken wires along the length of the strand. For the solid-rod system, it was important to identify the presence of stress corrosion cracking. This was considered a critical step to perform before any lift-off testing. If a lift-off test was performed on a rod with stress corrosion cracks, the rod may fracture suddenly and pose a serious safety concern for the inspection team.

After multiple iterations of laboratory and experimental testing, results reported in a 2019 technical note [13] on the solid-rod inspections appear to be the most promising. The system relies on guided wave ultrasonic testing (GWUT) and the basic apparatus is shown in Figure 22. Mounting the transducer to the end of the rod required an intermediate step of casting a small billet of metal alloy on the end of the rod. This resulted in a smooth end-surface at the transducer interface. Under normal circumstances, the required level of surface prep could be achieved with grinding and polishing, but the history of sudden catastrophic failures of the rods led to a prohibition on inducing vibrations into the rods.

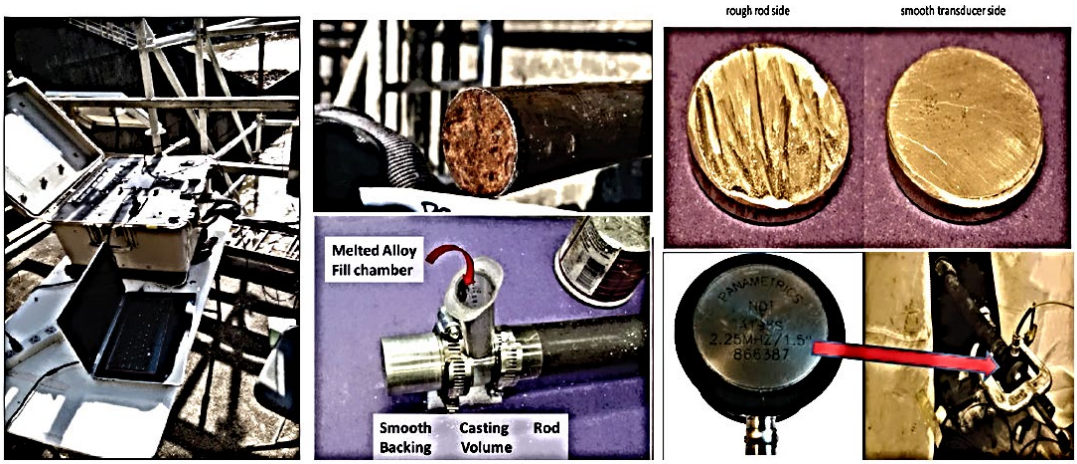

Figure 22. Data acquisition and transducer setup for GWUT of post-tensioned trunnion rods.[13]

Typical results for a sound rod and a rod with a suspected stress corrosion crack are provided in Figure 23. The scales on these figures are different, so it isn't clear how easy it is to identify the highlighted "concerns" from the raw data.

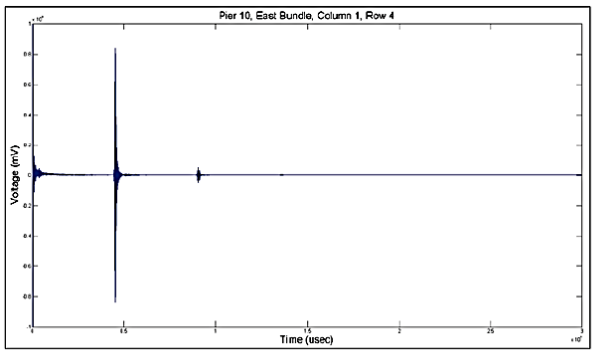

Figure 10. Typical acoustical guided waves response from rods.

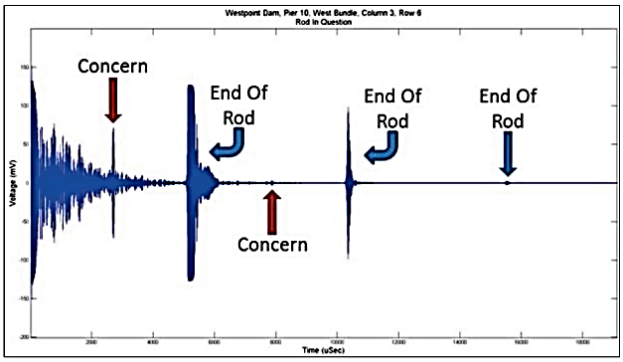

Figure 11. Pier 10, west bundle, column 3, row 6 display, showing areas for concern.

Figure 23. GWUT results from field survey of trunnion rods at West Point Dam, Georgia.[13]

USACE researchers did begin a study related to assessing corrosion damage in seven-wire-strand PT systems.[23] As of 2016, reported results were limited to laboratory-scale specimens with simulated wire cuts.[24] This work was focused on ultrasonic methods applied to the live-end anchorage. Another significant USACE research related to seven-wire-strand systems was focused on estimating the remaining tensile capacity of a strand after corrosion occurs.[25] Evaluation of these systems in the field appears to have been limited to lift-off testing. The report for this study does provide sophisticated modelling related to corrosion rates and the remaining tensile capacity in a strand, but it is unclear how these results might translate to the current study. In the USACE study, researchers artificially corroded seven-wire strands to varying degrees and then performed tensile testing to determine the residual tensile capacity of the corroded strand. This is a different mechanism, however, than what would happen in a PT structural application. If a prestressed strand experiences corrosion in an unbonded system, localized stress concentrations can lead to a rupture event in an individual wire. The question of how much corrosion can occur in a prestressed strand before a wire ruptures remains unanswered. The nature of the rupture and the resulting visual indicators in an unbonded system is also unclear.

2.2 Sensor Development

This literature survey also uncovered multiple efforts involving sensor development related to the inspection of PT systems and traditional prestressed concrete:

1. University of South Florida – Tendon imaging device for evaluating grout conditions
2. University of Florida – Detection of active corrosion using impedance-based measurements
3. University of Florida – Strain measurements at anchor head for wire-break detection
4. University of Virginia – MFL device for corrosion detection in traditional prestressed box girders

The purpose of this section is to summarize the operational features of each device and describe how they function. The overall efficacy of each device is also summarized.

2.2.1 Tendon Imaging Device for Evaluating Grout

Researchers at the University of South Florida have been involved in a multi-year effort to develop an impedance-based device for evaluating grout conditions in external ducts.[10] An example application of the latest generation of this device is provided in Section 1.4 and illustrated in Figure 6. This device combines both magnetic sensors and impedance measurements. The magnetic sensors are used to determine the position/location of the strands within the duct while the impedance measurements are used to assess the quality of the cementitious grout. The general process is illustrated in Figure 24.

As was previously mentioned, this device may not have direct application to flexible fillers. It may be possible to recalibrate the sensor to detect voids in PT ducts. The electrical impedance of degraded grout that is no longer capable of providing corrosion resistance may also be different enough from sound grout to result in a detectable difference.

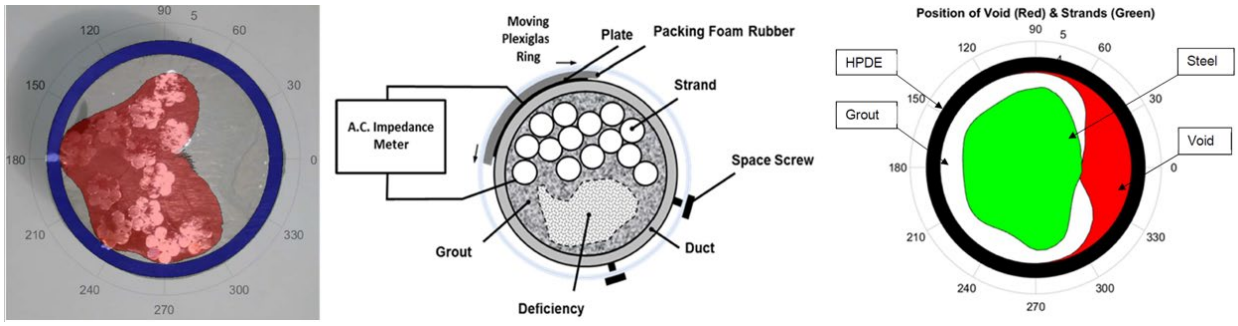

Figure 24. Impedance-based tendon imaging unit developed at USF[10]

Figure 25. Layout of electronics for tendon imaging unit[10]

On a conceptual level, this device has numerous advantages. It is easy to operate for external ducts and it provides a clear image for the operator to interpret in near real time. Such a device, if properly calibrated and validated for external ducts with flexible fillers, would allow an FDOT inspection team to rapidly assess suspect areas and proceed immediately to an invasive inspection if the results indicate it is necessary. Additional information on results from this research and how the impedance measurements compare with radiography methods is provided in Section 2.3.15. One additional important note: the original device described in the FDOT report [10] indicates that an electrical connection with the tendon steel is required. The latest generation device that we observed during the

inspection of the Broadway Bridge in Daytona Beach did not require any invasive operations or a direct electrical connection with the tendon steel.

2.2.2 Active Corrosion Detection with Indirect Electrochemical Impedance Spectroscopy

This study, led by Dr. Mark Orazem and Dr. David Bloomquist at the University of Florida,[26] relies on electrochemical impedance spectroscopy (EIS) to detect the presence of ferrous-oxide films on corroded prestressing strands. Experimental results obtained during a laboratory study on corroded tendons from the Ringling Causeway are highlighted in Figure 26. This method does require establishing direct electrical contact with the grout, so multiple holes must be drilled along the length of the duct for each desired inspection location around the circumference. Results from the experimental work indicated that corrosion could be detected only if it was occurring close to the surface of the duct and directly adjacent to the electrodes (see Location 4 in Figure 26). Additional discussion on the physics behind the method and deployment results for this device on the Texas A&M mock-up bridge girder is provided in Section 2.3.15.

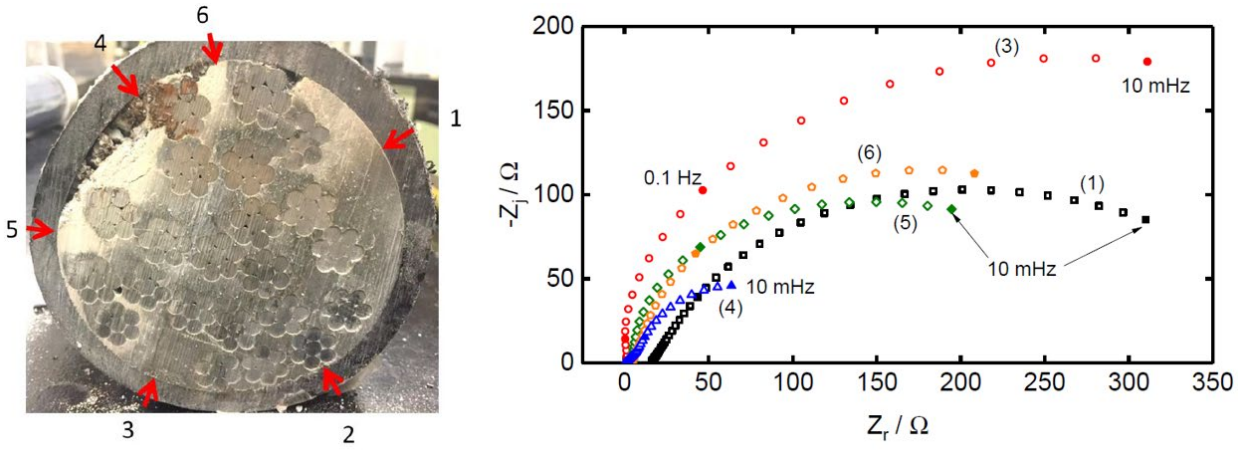

Figure 26. Electrochemical impedance spectroscopy results from corroded tendon. [26] Numbers in parentheses on chart correspond to circumferential locations on the tendon.

It isn't clear how this method could translate directly to flexible fillers. Establishing an electrical connection with individual strands through access holes in a duct may not be practical. Establishing these connections at multiple locations along the length of a tendon would also be a cumbersome operation. Work in this area aimed at developing non-contact methods for detecting corrosion in reinforced concrete is ongoing,[27] but adapting this method for the inspection of flexible-fillers PT systems would require an intensive research effort.

2.2.3 Wire-Break Detection Using Strain Monitoring at Anchorages

A major component of the multi-part study led by Hamilton and Rice at the University of Florida[4] involved developing a monitoring framework for wire break detection in flexible-filler PT systems. The system is based on strain gauges that are applied around the circumference of an anchorage wedge plate. This effectively converts an instrumented wedge plate into a load cell. If wires break due to corrosion damage, the strain in the plate will change and the resulting signal can initiate a physical

inspection of the anchorage in question. Results from a simulated wire-break study are provided in Figure 27. For wire breaks that occur in perimeter strands, the impact on strain is significant (~25-50 microstrain per wire). As the location of the damaged strand shifts towards the center, however, the impact on strain around the circumference of the wedge plate is diminished.

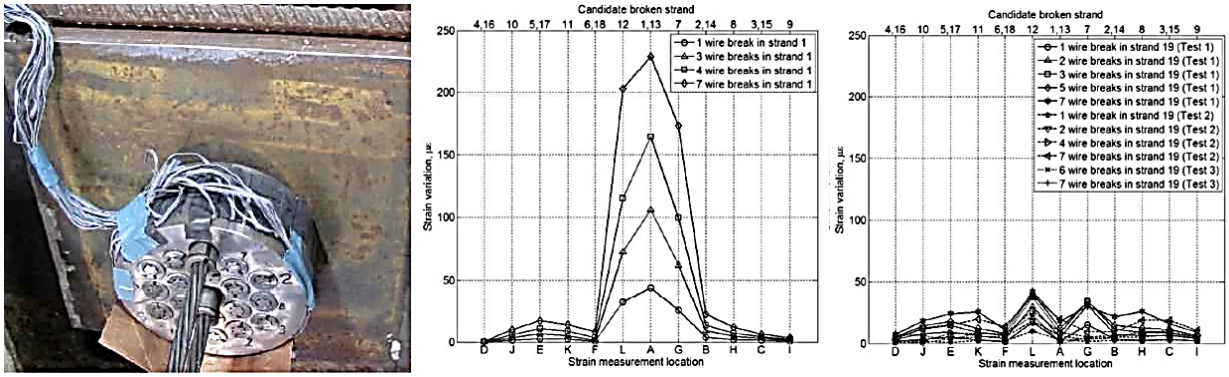

Figure 27. Instrumented wedge plate and resulting strain variations due to wire cuts. Middle graph is for cuts to top strand. Graph on the right is for cuts to center strand.

This approach is characterized in the study as part of a "tendon monitoring" framework. Full instrumentation of a wedge plate with strain gauges and the subsequent monitoring of the strains is a very involved process. The gauges could be installed before or after the tendon is tensioned, but an initial strain reading would be required in order to establish a baseline for comparison. How this system would integrate with the required anchorage cap isn't immediately clear, and significant modifications may be required to extract the wire pigtail from the cap. The data acquisition and monitoring system required for this system is also complex and may require significant maintenance and attention throughout the service life of the bridge.

One major effect of simulated wire breakage that was demonstrated in this study is the dislocation of the wedge grips and individual wires within a strand. This effect was illustrated in Figure 11. After individual wires are cut with a grinding blade, the energy released is sufficient to dislocate the wedge grips and induce relative displacements between the individual wires in a seven-wire strand. One question that remains unanswered is whether similar dislocations would be observed from corrosion-induced fractures. Depending on the nature of the corrosion damage, the fracture event might initiate a more catastrophic failure in which the entire strand ruptures. This could lead to a more severe dislocation that could potentially damage the anchorage caps. On the other hand, a slow and uniform loss of cross-section due to corrosion may result in wire breaks that don't disrupt the wedge grips at all.

2.2.4 Corrosion Detection in Prestressed Concrete Box Girders Using MFL

Researchers from the University of Virginia have developed a magnetic flux leakage (MFL) device intended to identify corrosion damage in traditional prestressed/pre-tensioned concrete box girders.[28] The researchers first conducted a finite element study to optimize the design of the MFL system. The resulting device is a manually operated surface scanner that is passed along the outer surface of the

concrete Figure 28. The device operates using a color-coded LED system where green lights indicate sound prestressing strands and yellow lights indicate potential areas of concern.

Figure 28. MFL device for corrosion detection in traditional prestressed (pre-tensioned) concrete box girders[28]

Conceptually, this type of device would be ideal for inspections by FDOT personnel. It is also very similar to the MFL device developed by Azizinamini[16] in his earlier studies. Ideally, a similar device capable of accessing internal tendons could be developed. There are, however, several anticipated challenges. First, the individual strands that this device is required to access will have the first layer centered three inches from the concrete surface. Internal ducts consist of a bundle of strands (as many as 22 seven-wire strands in the Wekiva Bridge) with centers positioned between 4.5-in and 12-in of concrete cover. This suggests that the modified device would need to be considerably larger. The presence of transverse mild steel will also interfere with the MFL signals generated within the tendon.

Additional information on MFL is provided in Section 2.3.4.

2.3 Overview of NDE methods

The goal of this section is to provide a brief overview of the NDE methods that have been previously investigated for CG systems. Some of these methods have been discussed previously, but the following discussion includes the basic physical principles behind the method. Additional commentary has been added regarding each method's applicability to flexible fillers where appropriate. Information about commercially available equipment that was used to validate each method is also provided.

2.3.1 Ground Penetrating Radar (GPR)

Ground Penetrating Radar (GPR) consists of emitting electromagnetic pulses from an antenna and analyzing the reflected pulses to determine anomalies in the bridges (Hurlebaus et al. [15]). This method can detect the location of internal ducts along with grouts defects in PT girders. In the study "Condition Assessment of Bridge Post-Tensioning and Stay Cable Systems Using NDE Methods" GPR was performed on internal ducts, external ducts, anchorages and two deviators in the PT girder specimen. To perform this study, they utilized the StructuresScan Mini HR GPR unit with a 2.6 GHz antenna which has a scan

depth up to 16”. This set up can be seen below (Figure 29). Due to the size of the PT girder specimen, it was divided up into several sections to allow for full coverage. To scan the external duct, wooden supports were added along the side to account for the circular shape to ensure the results were accurate (which can also be seen below).

Figure 29. StructureScan Mini HR GPR unit inspecting concrete and the external tendons (Hurlebaus et al. [15])

In this study, GPR was able to accurately show the profile of the metal ducts due to the strong reflections they produce, but the scans were not able to detect any strand or grout defects within the ducts. GPR produced more promising results while scanning the external tendons and was able to detect voids along with some water infiltration. When used upon the deviator region, the metal ducts were detected but none of the defects in the ducts were.

Some major findings of this method concluded that it is not effective for identifying grout or strand defects in internal metal or HDPE ducts. However, it was effective in identifying the location of these ducts, which is useful information for performing other methods such as impact-echo and ultrasonic tomography. This method is more advanced than some of the other methods and can be performed quickly. GPR is effective in detecting compromised grout in both external and internal HDPE ducts along with detecting voids in nonmetallic ducts. However, GPR is unable to detect corrosion or cable breaks along with water infiltration.

Another study with similar findings is “improved Inspection Techniques for Steel Prestressing/Post-tensioning Strand.” In this study Dr. Azizinamini states that steel ducts completely reflect the radar signals due to their conductivity, thus blocking the ability to detect tendon breaks or grout defects inside the duct.

2.3.2 Electrical Capacitance Tomography (ECT)

ECT has been primarily used and tested in the oil industry, which uses these sensors to analyze the flow of crude oil through pipelines, mainly identifying air pockets or voids in the flow. This method works by measuring the capacitance of the object below the sensor head. The sensor head consists of multiple electrode sensors which, through iterative scans, make a composite image showing the zones of

different capacitance (Hurlebaus et al. 2016). Below is a set of images of an ECT analysis from the study performed by Hurlebaus, which utilized varying premade samples of PT duct faults.

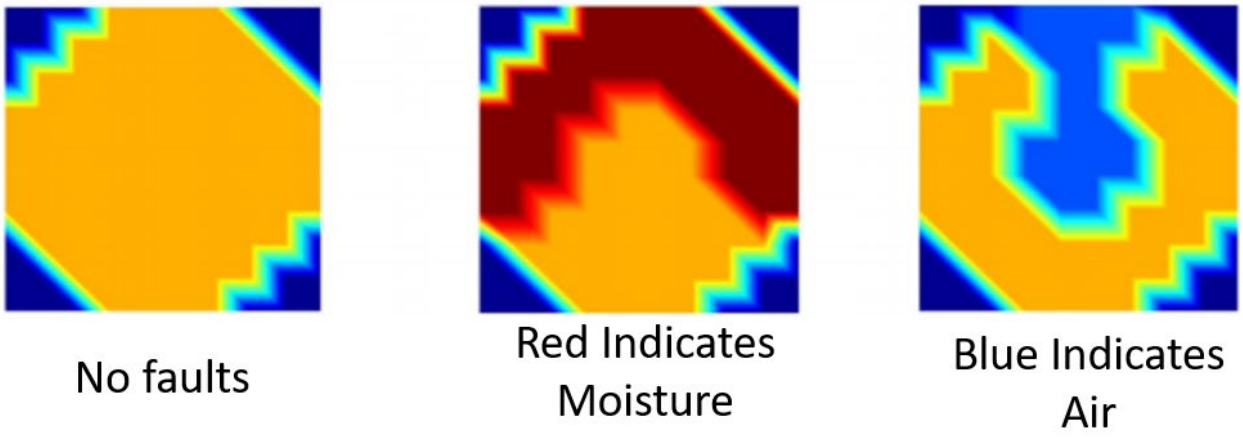

Figure 30. Examples of the composite images gathered by the ECT device in Hurlebaus's study reflecting the various types of flaw able to be detected (Hurlebaus et al. [15])

As evidenced by the Hurlebaus study, ECT is a promising method to identify grout defects in external nonmetallic ducts. Most interesting is the low cost of this method and its ability to easily differentiate between air voids and moisture pockets. With that said, though promising, the study found ECT to be inaccurate with the current technology available.

2.3.3 Magnetic flux leakage (MFL)

These methods are effective in identifying cross-sectional losses within the reinforcement tendons caused by corrosion. Magnetic flux leakage (MFL) relies on the interaction between ferrous materials and magnetic fields. MFL applies this interaction to find stresses in ferrous materials, such as steel, which can be caused by either cross sectional loss in reinforcement strands or oxidation of strands. To do this, the MFL method relies on magnetically saturating the strands. When areas with section loss or corrosion have become saturated the magnetic flux is forced to flow through the air as it becomes the least resistant path (Azizinamini 2012). The process described is shown below (Figure 31). This leakage can be quantified by measuring the vertical component of the magnetic field flowing through the air with a Hall Effect sensor. These methods for inspection have been used repetitively in many industrial fields such as nuclear power generation, cable stay bridges, and segmental box beam bridges, PT bridges with cementitious grout, along with natural gas and oil pipelines. With successful implementation of non-destructive inspection in these fields, it is expected that application of these methods to PT bridges with flexible fillers will be a fruitful endeavor.

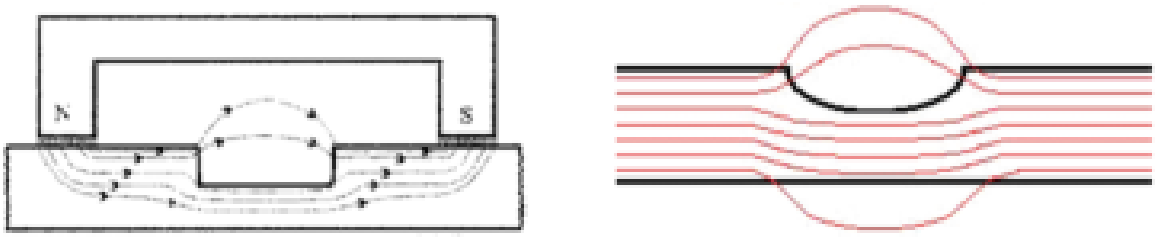

Figure 31. MFL magnetic field lines shown when encountering a flaw in a ferrous material, the magnetic field lines "jump" out of the normal alignment when encountering these flaws. (Azizinamini [19])

A study performed by Hurlebaus utilizing this method implemented a commercial device by NDT Technologies Inc. to test the feasibility of this approach on external PT ducts. Using prepared samples for multiple types of tendons and duct defects, the device is moved along the duct and data from this device is then sent to a portable unit for data analysis Figure 32 Shows the sensor head used for testing along with the unit used for analysis.

Figure 32. Shows the sensor head used for testing along with the unit used for analysis (Hurlebaus et al. [15])

The results of this MFL test were extremely promising for both metal and HDPE ducts (Figure 33). The metric used for analysis in this case was loss of metallic area (LMA). The results for the successful identification of the premade faults can be seen in the table below. These results indicate a strong success rate of identifying metallic faults in PT ducts.

	HDPE DUCTS			METAL DUCTS		
Condition	Total no. inspected	Positively identified # and (%)	Not positively identified # and (%)	Total no. inspected	Positively identified # and (%)	Not positively identified # and (%)
Corrosion	5	3 (60)	2 (40)	1	1 (100)	0 (0)
Section loss	30	13 (43)	17 (57)	0	-	-
Breakage	26	17 (65)	9 (35)	1	1 (100)	0 (0)
Compromised grout	24	0 (0)	24 (100)	1	0 (0)	1 (100)
Voids	27	0 (0)	27 (100)	1	0 (0)	1 (100)
Water infiltration	11	0 (0)	11 (100)	1	0 (0)	1 (100)
Good tendon	55	48 (87)	7 (13)*	3	1 (33)	2 (67)

* False positive

Figure 33. Results for MFL testing in the Hurlebaus study (Hurlebaus et al [15])

2.3.4 Infrared Thermography (IRT)

IRT utilizes an infrared camera to detect voids of the filler material within a PT duct. The camera's image of the duct shows differences in the heat map, where lower temperatures indicate a void in the duct. This works upon the principle that air will not conduct heat through the pipe wall as well as a filler material would. This method can utilize the latent heat within the structure or for a larger differential between the void and non-void regions an external heat sources can be applied. This is quickly becoming a popular method of NDT as it is relatively cheap and does not require extensive knowledge to identify voids within the ducts (Azizinamini[21]). That said, this method does not indicate if there is damage to the tendon within the duct nor does it indicate the severity of the damage. This method can be effectively used as a simple first pass inspection method that will require more advanced NDE techniques to pinpoint the issues in the areas flagged by IRT. Azizinamini concluded that IRT is most effective when utilizing an external heat source as it will allow for great consistency between different portions of the bridge. Another conclusion was that IRT is, generally, only useful when examining external PT ducts.

2.3.5 Magnetic Main Flux Method: Permanent Magnet (MMF-P)

Active methods for MFL inspection involve using a mobile device consisting of two permanent or electromagnetic devices along with hall-effect sensors to find areas of corrosion or cross section loss in steel tendons. As this device is moved along the length of the tendon, it saturates the steel between the two magnets, which induces a magnetic field within the tendon. If the tendon being inspected has regions of corrosion or section loss, the device will identify magnetic field leakages from the tendon as it moves atop them. Such a device was designed and prototyped for the Virginia Transportation Research Council (VTRC) for use on prestressed concrete box bridges (Figure 34) which can be seen below.

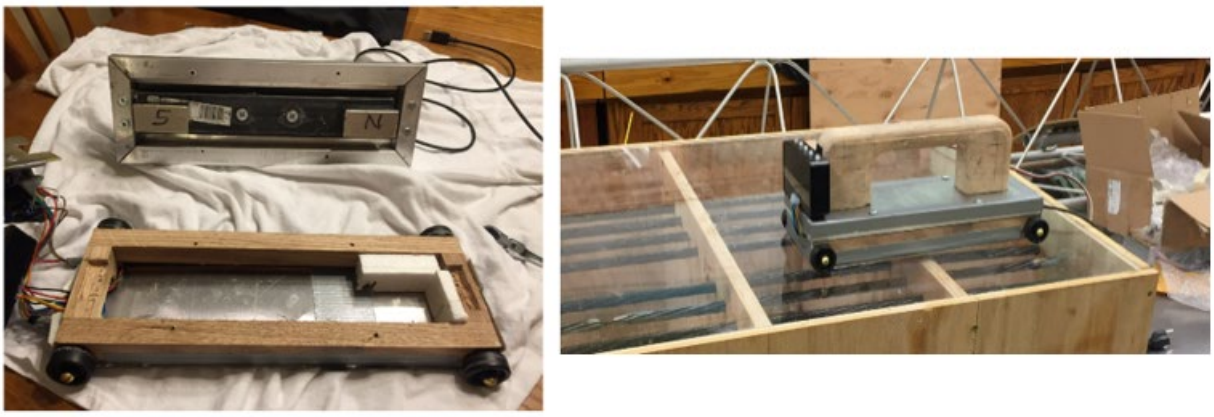

Figure 34. Example of a permanent magnet MFL device used to find defects in reinforcing steel (Chase and Balakumaran[28]).

Active MFL methods show promise in situations where large sections of corrosion or section loss may be present in a tendon. This is because active methods have an inability to detect small defects, though, they are portable, cheap, and are easily used by inspection crews. These small devices are to be run along the surface of the PT duct and can detect tendon loss at an approximate resolution of 0.1 inches with 2 inches of cementitious cover (Chase and Balakumaran[28]). In this study, section loss was detected by comparing the flux densities in the x and y planes as read by the Hall Effect sensors. As the variation between the two density plots increases, it can be inferred that the section loss is also increasing at a relative rate. This can be seen from laboratory results from the same study where their data correlates with the prepared tendon samples.

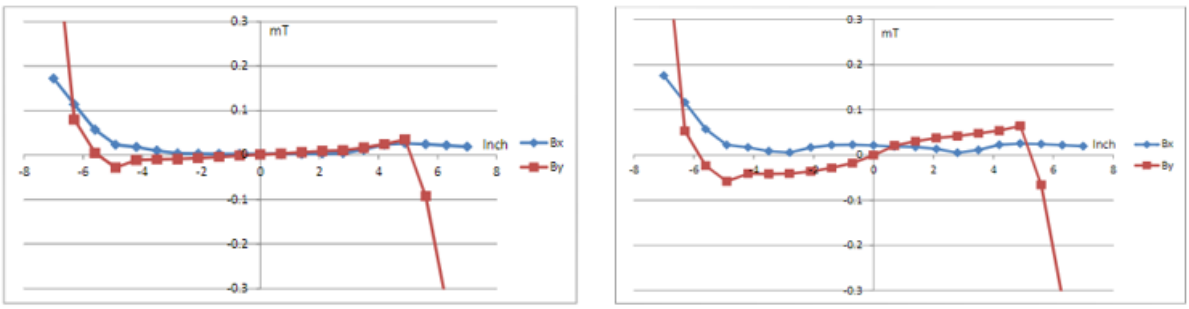

Figure 35. Graphs of the flux density read by the hall effect sensor on the VTRC MFL sensor. A clear difference in x and y densities can be seen on the broken strand (Chase and Balakumaran[28]).

A similar unit as the one produced for the VTRC was used in a study by the University of Toledo to inspect in operation prestressed box bridges. Using their sensor, the UT was able to find a linear relationship between the magnetic flux readings from their Hall Effect sensor and the level of deterioration of the steel strands in question (Fernandes et al. [29]). These findings were then confirmed

on other operating bridges in Ohio. Using these findings, it is possible to accurately find and diagnose sections of steel strands with deterioration.

Though success has been had with inspecting strands with minimal to no other mild reinforcing steel, it is not a practical inspection case when it comes to internal PT ducts. A study performed by Nanjing University of Aeronautics and Astronautics has found a solution of minimizing the effects of interfering ferrous materials during an MFL inspection. This solution is a method of signal processing; in this case it utilizes the moving average method. This method "operates by averaging a number of points from the input signal to produce each point in the output signal" (Xu et al.[30]). In simpler terms, this method averages the data points collected from a high sample rate sensor to remove MFL variations caused from mild reinforcing steel that may get in the way of internal PT ducts. The differences between the original and filtered results where the peaks in the filtered results correlate to the areas of section loss in the strand being measured can be easily seen in Figure 36.

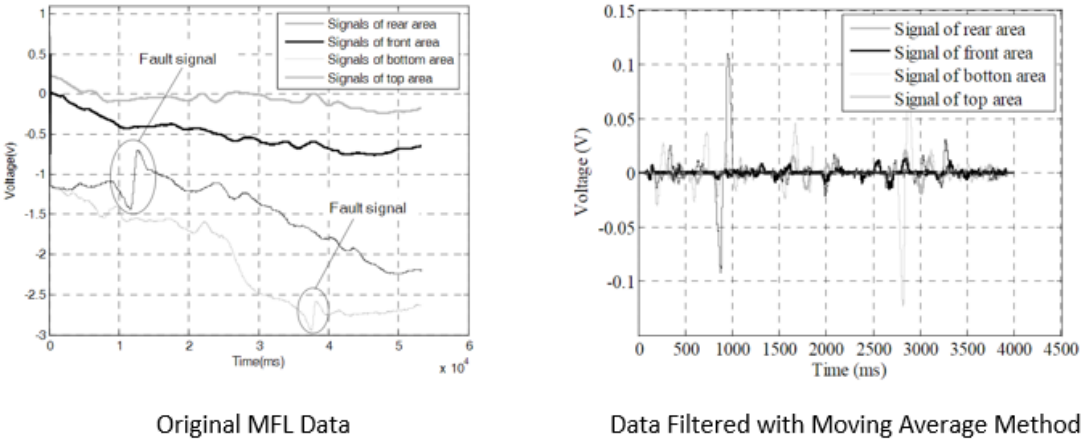

Original MFL Data

Data Filtered with Moving Average Method

Figure 36. Graphs using data from field trials showing how the moving average filtering method can reduce noise (Xu et al. [30])

2.3.6 Magnetic Main Flux Method: Solenoid (MMF-S)

This process utilizes a coil of wire set around the tendon in question, and then the tendon is magnetized by an external source to gather readings on the condition of the tendon. The coil of wire can be run along the length of the duct if there is no obstruction. This method can be used to find defects in the tendon such as corrosion or section loss. The main advantage of this method is the accuracy with which the coil device can locate the point of interest. The setup for this method developed, prototyped, and tested by Hurlebaus can be seen in Figure 37.

Coil System around the PT duct

Data Collection System

Figure 37. Solenoid type MFL Inspection System and the accompanying Data Collection System for the Analysis of PT Ducts (Hurlebaus et al. [15])

The testing performed by Hurlebaus on the solenoid method proved the feasibility of this MFL method on the inspection of external PT ducts. This study was performed on a multitude of prepared specimens with varying degrees of section loss, breakage, or voids in the tendon or PT duct. This inspection method can detect defects in the tendon at a minimum of 0.2% cross sectional loss (Hurlebaus et al. [15]). This testing also proved their hypothesis that this device was not able to detect voids of the grout material. It should be noted that using metal ducts significantly hindered this method. Overall, this method was very effective in identifying tendons that had no damage and was often able to detect areas of loss in the tendon. These results, and the percentage of effectiveness, can be seen in Figure 38.

	HDPE DUCTS			METAL DUCTS		
Condition	**Total no. inspected**	**Positively identified # and (%)**	**Not positively identified # and (%)**	**Total no. inspected**	**Positively identified # and (%)**	**Not positively identified # and (%)**
Corrosion	4	3 (75)	1 (25)	1	1 (100)	0 (0)
Section loss	20	10 (50)	10 (50)	0	-	-
Breakage	14	8 (57)	6 (43)	1	0 (0)	1 (100)
Compromised grout	9	0 (0)	9 (100)	1	0 (0)	1 (100)
Voids	14	0 (0)	14 (100)	1	0 (0)	1 (100)
Water infiltration	1	0 (0)	1 (100)	1	0 (0)	1 (100)
Good tendon	16	15 (94)	1 (6)*	3	3 (100)	0 (0)

Figure 38. Results of the Solenoid testing by Hurlebaus for varying deficiencies in the tendon, duct, and filler (Hurlebaus et al. [15])

This data indicates a strong performance for solenoid type MFL NDE in terms of identifying section loss, corrosion, and breakage of tendons within HDPE ducts. It is also able to identify tendons which are in good condition. The main drawback from this method is the amount of time need for the wrapping of the cable around the duct and the complete access need to perform the testing.

2.3.7 Impact Echo (IE)

Another common NDE method utilized by bridge inspectors is Impact Echo (IE). This method involves hitting the concrete surface with a small impactor/impulse hammer and analyzing the reflected wave energy with a displacement or accelerometer receiver mounted on the surface near the impact joint (Hurlebaus et al. [15]). This method can detect voids in metal and HDPE internal ducts. The impact device can measure the wave energy which is depicted in Figure 39. A fully grouted duct will emit a current passing straight through the duct, while a voided duct will behave differently and veer off.

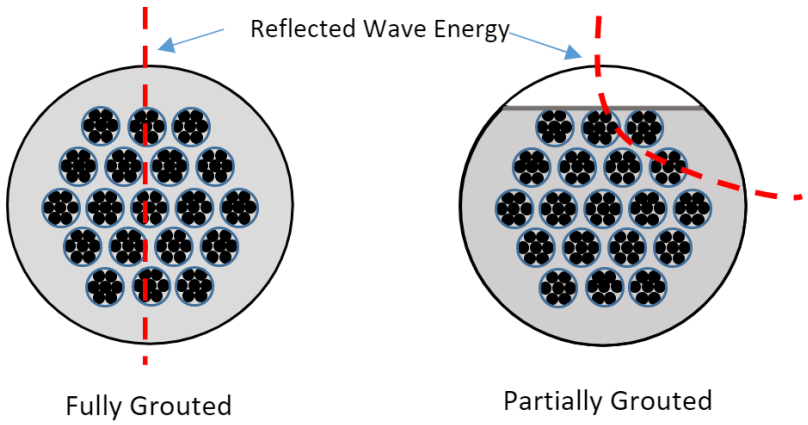

Figure 39. Illustration of wave energy from impact echo device passing through fully and partially grouted ducts.

The IE method was utilized on an internal and external PT girder systems using an Impact Echo Scanner test head and a PC data acquisition platform (Figure 40). Once GPR was performed to determine the location of the ducts, an impact echo test was performed at 6-inch intervals as determined by the inspector. In this study, the IE testing was effective in determining voids in the external and internal ducts up to 3.3 ft deep but not in the anchorages due to the minimum cover depth of 5 ft. Limitations of this method include accurately detecting voids in smaller diameter internal ducts with a large cover and identifying the presence of water or soft grout. This method is also more effective in metal ducts rather than HDPE ducts.

Figure 40. IE scanner test head, the PC data acquisition platform, and the IE device in use on an external duct (Hurlebaus et al. [15])

Another study with similar findings is "Durability of Precast Segmental Bridges." According to this study, IE is the most effective method for determining grout conditions in internal metal ducts, which coincides with the previously mentioned study. This study also emphasized the need for a skilled operator to analyze the results as a limitation to the method.

This study noted the first large scale use of IE occurring in 1997 on a 14-span precast segmental bridge, which consisted of internal metal-grouted ducts. IE was able to accurately detect voids throughout the ducts and findings were confirmed using a borescope. The ducts had severe grout loss along with no grout in some places. Due to the use of IE, the inspectors were able to accurately determine grout loss and if repairs were required.

2.3.8 Ultrasonic Tomography (UST)

Ultrasonic Tomography (UST) consists of reflecting ultrasonic waves at a material and measuring the change in acoustic impedance to identify grout defects in internal ducts. In the study "Condition Assessment of bridge post-tensioning and stay cable systems using NDE methods" UST was tested upon a 75-ft-long PT bridge girder along the anchorages and deviators. The device used for this specific test was the A1040 MIRA (Figure 41), which has many applications such as the identification of voids, rebar, cracks and substance filled cavities.

Figure 41. A1040 MIRA device and results from the deviator blocks (left is defect key, and right is the UST scan) (Hurlebaus et al. [15])

Due to the size of the specimen, data was collected in sections and later combined to be analyzed. As a nonhomogeneous material, concrete requires sample velocities and then an averaging of the results for each section. This method was unable to identify grout defects in the internal ducts, with difficulties inspecting metal ducts. UST was able to identify the location of the internal ducts and proved to be more effective when used upon HDPE ducts. UST was also unable to locate defects in the anchorage zones of the PT system.

2.3.9 Ultrasonic Echo (USE)

This method relies on the principle of exciting structural elements with ultrasonic waves and then reading the rebounded waves to gather data about the structure. In terms of PT ducts, this can be theoretically used to identify voids, compromised filler, and section loss of the tendon. This method requires extensive knowledge of the environment in which the device is being deployed along with a specific use plan for that setting, which would require a large amount of training (Hurlebaus et al. [15]). This is one of the methods that could be used on internal PT ducts, which could prove to be useful if some issues were solved with USE. The Hurlebaus study utilized this method on a variety of different duct and tendon defects the USE method could only identify a limited number of defects (Figure 42).

	PLASTIC DUCTS			METAL DUCTS		
Condition	Total no. inspected	Positively identified # and (%)	Not positively identified # and (%)	Total no. inspected	Positively identified # and (%)	Not positively identified # and (%)
Corrosion	2	0 (0)	2 (100)	5	0 (0)	5 (100)
Section loss	16	0 (0)	16 (100)	16	0 (0)	16 (100)
Breakage	12	0 (0)	12 (100)	12	0 (0)	12 (100)
Compromised grout	12	4 (33)	8 (67)	12	2 (17)	10 (83)
Voids	9	2 (22)	7 (78)	6	3 (50)	3 (50)
Water infiltration	5	3 (60)	2 (40)	7	5 (71)	2 (29)
Good grout	26	0 (0)	26 (100)	38	6 (16)	32 (84)

Figure 42. Ultrasonic echo testing on prepared internal PT ducts with cementitious grouts; this method had limited success (Hurlebaus et al.[15]).

As stated in the study, "USE testing suggest that this method is not capable of identifying grout defects in internal tendons for both plastic and metal ducts."

2.3.10 Sonic/Ultrasonic Pulse Velocity (SPV-UPV)

The pulse velocity method relies on sending either sonic or ultrasonic waves through the material and comparing the calculated time of travel against the recorded time of travel for the waves through the material (Hurlebaus et al. [15]). This data can then be used to interpret what time of material defects occurred for the travel time of the wave to change. This method was tested by Hurlebaus on internal ducts of both HDPE and metal construction. This testing consisted of using SPV and UPV sensors set up on opposing ends of the concrete surrounding the ducts (Figure 43). The wave was then sent and received by the sensors. Though SPV and UPV methods are proven, no conclusive data was able to be gathered due to the small nature of the defects looked at for comparison to the distance which the wave travels. Therefore, it is somewhat inconclusive with respect to the usability of the method, at least in the use case of the study in question.

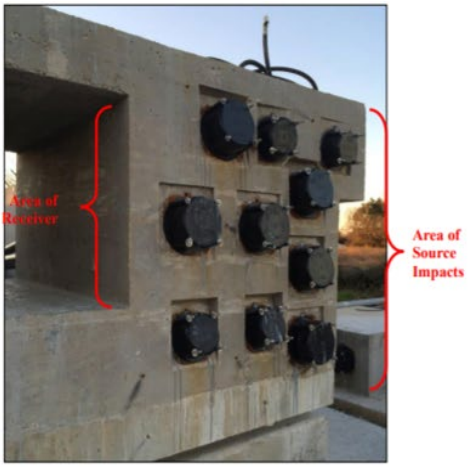

Figure 43. Testing area for UPV and SPV testing performed by Hurlebaus (Hurlebaus et al. [15]).

2.3.11 Low Frequency Ultrasound Testing (LFUT)

Low frequency Ultrasound Testing (LFUT) is used to assess grout conditions of external tendons. The LFUT system generates low frequency ultrasonic waves, which propagate across the cross section of the duct. This method is performed to determine grout conditions of the tendons and determine if the grout is solid, compromised, or voided. The low frequency ultrasound pulse transmitter and receiver used in this study are provided in Figure 44.

Figure 44. Pulse transmitter and receiver, prototype scanning head with encoder and data acquisition system

The measurements were taken every 12-18 inches along the length of the external ducts. LFUT proved successful in detecting grout defects in the external HDPE ducts and was unsuccessful when applied to internal or external metal ducts. This method is also capable of identifying water infiltration and air voids but with low accuracy. Additionally, the system detected grout defects in areas with good grout conditions thus proving to be inaccurate. This method is also limited due to not having the ability to determine the severity of these grout defects.

2.3.12 Sounding

Mechanical sounding is used in tangent with visual inspections. If an abnormality is visually apparent to the inspector, they will then conduct this method. Sounding is only effective for external tendons and consists of the inspector tapping along various points on the duct and listening for sound differences. An experienced inspector is trained to hear the dull/hollow sound that indicates the presence of voids. One downfall of this method is that it is not always accurate and is a loose indication of voids within the tendons. If an inspector suspects voids from performing this method, the inspector will then be prompted to perform a more in-depth inspection. This method is also unable to detect soft grout or smaller voids/defects.

The sounding experiment performed by Hurlebaus et al. [15] utilized the testing of six external post-tensioned ducts along with the end caps and anchorages. The spacing between the caps was determined to be 2” which is at the discretion of the inspector. This method was found to be consistent for different trials and inspectors when conducted on HDPE ducts but not metal ducts. As previously

mentioned, this method is only effective for detecting voids in the grout, the testing only further proved this limitation. This method was also ineffective in determining Any kind of defects in the anchorages but reliable for identifying grout condition in the end caps.

2.3.13 Visual Testing (VT)

Visual testing is effective in detecting grout defects, corrosion or any kind of deterioration that could negatively affect the structure. Visual testing is effective for internal and external tendons, but internal tendons pose more difficulties of accessibility to the tendon thus making it less common. In terms of external ducts, visual testing is one of the more common methods utilized to detect abnormalities. Visual testing consists of opening the duct or end cap in areas that are a cause for concern and looking inside to determine the state of the strands.

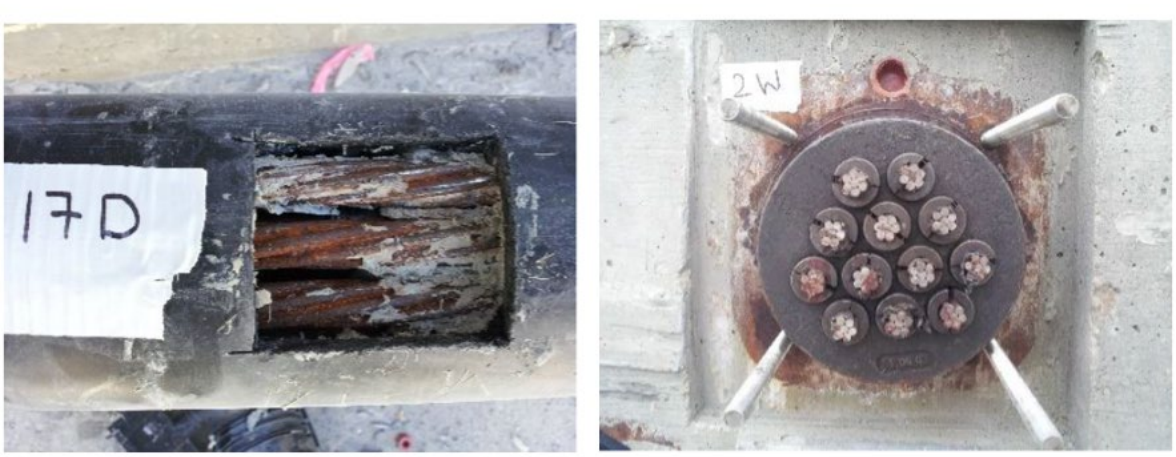

Figure 45. Visual testing of an external tendon (A) and end cap (B) in PT Girder Specimen (Hurlebaus et al.[15])

In this study, the end cap inspections were performed by removing the cap and carefully inspecting the grouting conditions while the duct inspections required creating a small opening and repairing it after. A downfall of this method is that it is more invasive than the other methods and more time consuming. It is not feasible to perform this method on many ducts/caps throughout the bridge, and it cannot identify the specific location of a defect until the later stages of deterioration where there are clearer visual indicators on the outside of the duct. As previously mentioned, this method works in tangent to mechanical sounding which is how the location of this testing was decided. This is not effective in detecting early stages of grout/stand deterioration, however.

2.3.14 Borescope (Bor)

Another tool that is utilized by bridge inspectors is the Borescope. This method is more invasive than some of the other NDE techniques, so it is sometimes referred to as a semi-destructive method because it requires creating an access port for the borescope to enter through (Figure 46). This method is effective for determining voids and corrosion in both internal and external systems. This method is deployed once sounding or visual testing is completed and detects degradation of the grout or strands.

This method allows the inspector to see the corrosion or voids within the duct by running the borescope inside the system.

Figure 46. Borescope access port and equipment used (Hurlebaus et al.[15])

In the Hurlebaus study, four external ducts were investigated along with the anchorages. In this inspection, the borescope was able to show voids, water infiltration defects and corrosion of the strands (Figure 47). This method is a more accurate representation of what is occurring within the ducts, which allows the inspectors to really see what is happening and decide on how and where and if repairs are necessary to keep the structural integrity of the bridge. Some limitations of this method include the inability to identify the amount of voided area between congested strands. The borescope also requires a void to enter the duct/anchorages, and the sight is limited to where the main voids are located.

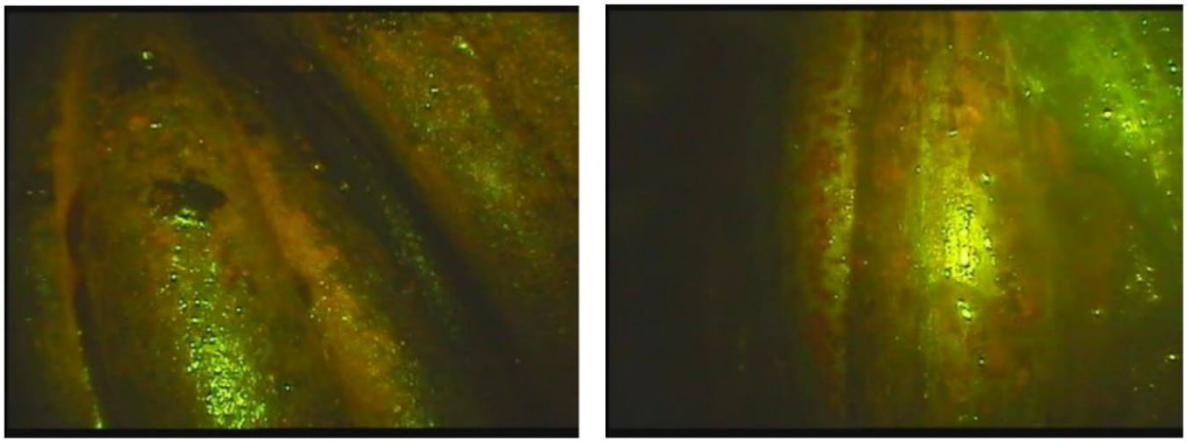

Figure 47. Images provided by the borescope inspection inside the external tendons depicting corrosion of the strands (Hurlebaus et al.[15])

2.3.15 Electrochemical Impedance Spectroscopy

Electrochemical impedance spectroscopy (EIS) relies on passing a low-amplitude voltage through the steel in varying frequencies. By measuring the signal amplitude and phase shift, the impedance of the filler can be determined. In the Hurlebaus study, four holes were drilled into the HDPE pipe of the prepared external tendons for electrodes to be placed. These holes would later be filled with an HDPE welding substance. The electrodes were powered by a portable power source and the electrodes are fed to a potentiostat. The readings from the potentiostat are then processed using a notebook computer to discover flaws in the tendon Figure 48.

Laptop and Potentiostat Potentiostat and Electrodes

Figure 48. EIS device with electrodes into the HDPE pipe and the potentiostat into the computing device (Hurlebaus et al.[15]).

This method was successful in positively identifying the broken and corroded strands within the prepared tendon (Figure 49). While relatively cost effective, this method is somewhat invasive as it requires drilling into the HDPE duct. Also, this method is limited to external PT ducts.

Condition	Total no. inspected	Positively identified # (%)	Not positively identified # (%)
Corrosion	2	1 (50)	1 (50)
Section loss	1	1 (100)	0 (0)
Breakage	0	-	-
Compromised grout	0	-	-
Void	0	-	-
Water	0	-	-
Good Tendon	4	3 (75)	1 (25)

Figure 49. EIS results from the Hurlebaus study, which indicates a relatively high success rate in identifying corrosion or breakages (Hurlebaus et al.[15]).

2.3.16 Radiography Methods

Mullins and Pearson [31] conducted one of the first x-ray examinations of concrete. Over the years, numerous studies have been performed on gamma-rays imaging for void and corrosion assessment. Whiffin [32] discussed using gamma-rays to extract steel reinforcement location in concrete slab. The British Standards Institute [33] published the recommendations for radiography of concrete. The methods have been developed using radiation produced by radioisotopes, X-ray generators, and nuclear reactors to bombard fresh or hardened concrete or grout samples. According to its density, thickness, and type and size of defects, the object attenuates radiation differently. Hence, an intensity distribution of radiation can be captured and used to make it visible by computed tomography. Both gamma-rays and X-rays are forms of electromagnetic radiation distinguished by the nature of the source (Bray and Stanley [34]). Gamma radiation is generated by the radioactive decay of unstable isotopes. Common radiographic isotopic sources are ^{60}Co, ^{137}Cs, ^{192} Ir, and ^{170}Tm. Because some of the radiation will pass through the sample while some of the beam will be absorbed or scattered out of the beam, penetration with attenuation can be used to characterize the interaction of gamma-ray with concrete or grout with the exponential relationship (Equation 1) (Mitchell) [35]:

$$I_g = I_o e^{(-\mu_g \rho_g x)} \qquad \text{Equ. (1)}$$

where I_g is the final intensity of the beam, I_o is the initial or reference intensity of the beam, μ_g is the mass attenuation coefficient of the grout, ρ_g is the density of the grout, and x is the length of the beam path through the grout.

Using scattering data from radiographic scans, computed tomography (CT) creates a cross-sectional image or picture of a slice of an object. One of the first experimental studies on using gamma-ray tomography to detect defects of protecting grout layers surrounding steel strands was done by Bligh et al. [36] Aimed at identifying voids and other defects in the grout layer of bridge cable stays, various NDE methods were applied including ultrasonics, film radiography, computed tomography (CT), and neutron radiography. They have demonstrated the feasibility of using CT for inspection of grout layer. Voids as small as 0.04 in. (1 mm) in diameter were identified in both the annular region of grout and inside the steel strand bundle. In this study, a 4.5-in. O.D., 19-strand cable-stay specimen was analyzed by International Digital Modeling (IDM) corporation using an in-house integrated real-time inspection (IRIS) system with ^{8}C and ^{60}Co isotope as radiation source. A total of 39 cross-sectional slices were taken through the 12-in sample. Both ultra-high resolution (UHR) and very-high resolution (VHR) were used to produce cross-sectional images. Figure 50 shows a UHR scan image below end cap. All the manufactured defects were easily found in both scan modes with size ranging from 0.03 in. to 0.375 in. The authors also mentioned the IRIS system is capable of low-resolution scanning with resolution of 0.12 in., which should be sufficient for grout inspection. Based on the experimental data, the authors concluded that radiographic techniques appear to be the only feasible choice for inspecting the anchorage region where anchorage details and fire and crash protection measures significantly complicate the geometry.

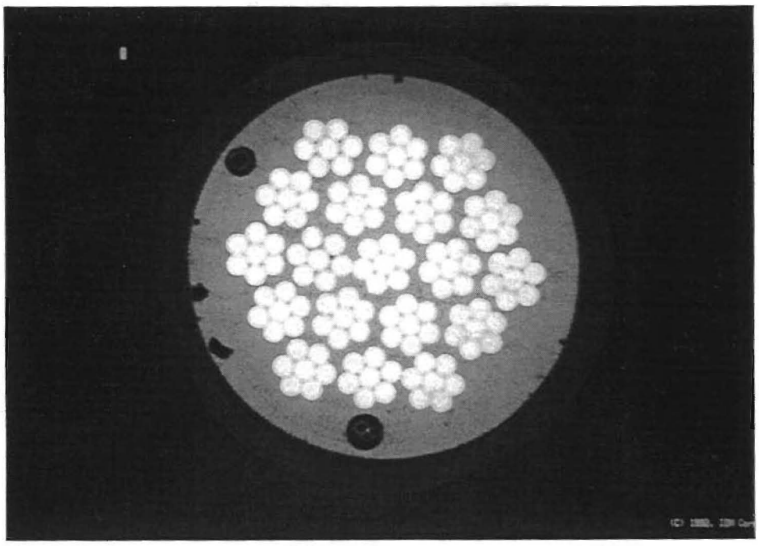

Figure 50. UHR scan of 4.5-in. cable below end cap (Bligh et al.[36])

Headed by ACI member, Mario Mariscotti, THASA has developed the reinforced concrete tomography (RCT) method to determine positions and diameters of reinforcing bars (Frigerio et al.[37] Mariscotti and Husni[38] and Pimentel et al.[39]). The details of their method and application were well documented in a paper by Mariscotti et al.[40] They chose ^{192}Ir as the radiation source because ^{192}Ir is the least energetic and thus requires the least amount of shielding material to make portable application possible. Figure 51 shows a conceptual drawing of a conventional ^{192}Ir source assembly.

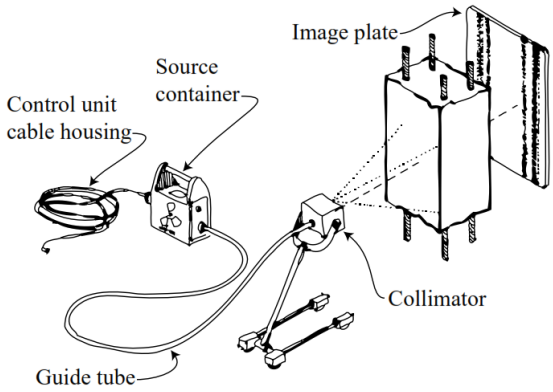

Figure 51. Schematic representation of a conventional ^{192}Ir source assembly (Mariscotti et al.[40])

The RCT method has been used to inspect a post-tensioned girder at the Zárate Bridge in Argentina. A total of six grouted ducts were inspected for voids in the grout using gamma rays from a 93 Ci ^{192}Ir source[40]. The voids in the grouting and corrosion of tendons were measured using the RCT method.

Azizinamini and Gull [41] reviewed various nondestructive evaluation techniques for post-tensioned and stay cable structures, including radiography methods. The inherent characteristics of this method is summarized in Table 6 . They have concluded that radiography in its current state is very expensive and

cannot be recommended for all inspection cases, but it is likely to be improved in the future and become a good candidate for infrastructure inspection.

Table 6. Summary of inherent characteristics and application of radiography (Azizinamini and Gull[41])

Advantages	Disadvantages	Best application case	What improvement can be made	Application with regard to duct type
• Can identify wire breaks and grout voiding. • Graphical output is easy to interpret • May be applicable to anchorage region.	• Significant safety and cost concerns. • Test geometry and access may be limited. • Radiograph gives no depth of field information	• Very broad application	• Can be improved by presenting data in 3-D visual format instead of a single radiograph	• Applicable to both internal and external ducts

Hurlebaus et al.[15], also concluded that gamma-ray radiography is highly versatile and is applicable for strand factures, breakage, section loss, and voids. It is also mentioned that gamma-ray radiography is a very expensive, time-consuming, and potentially hazardous technique. Table 7 provides a summary of application of gamma-ray radiography. It was revealed that gamma-ray radiography is an excellent method for detecting strand location in congested areas such as at anchorage.

Table 7. Gamma-ray radiography for condition assessment of PT and stay cable tendons (Hurlebaus et al. [15])

Advantages	Disadvantages	Best Application	Gaps
Breakage: Field tests show some capability in detecting strand fractures in internal tendons. *Voids*: Field tests reveal capability to detect voids in internal PT tendons (inside 12 in. girders). *Location*: Excellent at determining lateral location and diameter of internal ducts, reinforcement, and strands.	*General*: Time-consuming, costly, potential health hazards, and bulky (may be difficult to apply in congested areas). Cannot determine depth of defects and requires two-sided access. *Breakage*: Fractures, breakage, and section loss can go unnoticed, particularly in metal ducts. *Location*: Cannot determine depth.	*General*: Specific evaluation after damaged area has been localized and other methods exhausted. *Tendon deterioration at anchorage*: If accessible, excellent at detecting strand location in congested areas. *Location*: Very effective for determining lateral location and diameter of internal ducts, reinforcement, and strands.	*General*: Need lower cost, portability, 3D imaging. *Corrosion*: Need to field test corrosion detection capability and determine sensitivity. Some researchers have not had success with corrosion detection. *Breakage*: Limitations of detecting strand fractures/breakage unknown. *Water infiltration*: Potential application for water detection. Limitations unknown. *Tendon deterioration at anchorage*: Limitations of detecting tendon condition at anchorage unknown.

2.3.17 Electrical Impedance Measurements

For post-tensioned concrete bridges, the corrosion of tendons is associated with inadequacy or deficiencies of grouting. Freij et al. [10] developed a rapid imaging method to assess grout deficiencies of external tendons. The method uses electrical impedance measurements using a traveling sensor placed on the outer surface of the tendon duct. However, the presence and position of the post-tensioning strands within the tendon cross-section is needed to accurately detect grout deficiencies such as voids (Figure 52). Once the strand has been located, grout anomaly detection is performed using the impedance sensor (Figure 53). In this scheme, the AC impedance, Z, between an external conductor plate and a conductor is connected to the strand bundle. The strand bundle can be assumed to be electrically continuous and behaves, approximately, as a conductor bounded by the strand-bundle envelope since the strand bundle is electrically interconnected at the anchor points. By rotating the plate around the duct perimeter and measuring Z as a function of rotation angle, an angular impedance profile can be obtained. Eventually, these two components, magnetic imaging and impedance sensor, were integrated into a tendon imaging unit (TIU) (Figure 54). The TIU-I consists of a single capacitive high-frequency impedance module and two magnetic strand position detection modules. Using TIU-I, cross-section images of the tendons at chosen locations along the tendon, length can be captured one at a time (Figure 55). Furthermore, an advanced version of the TIU, TIU-II was also developed.

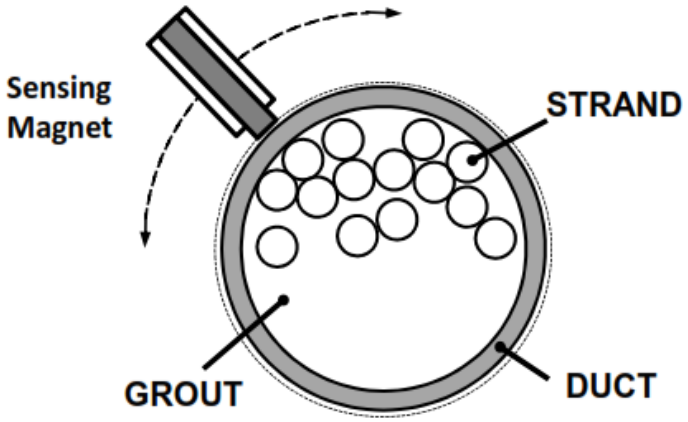

Figure 52. Strand arrangement and basic implementation for determining strand position (Sagüés [42])

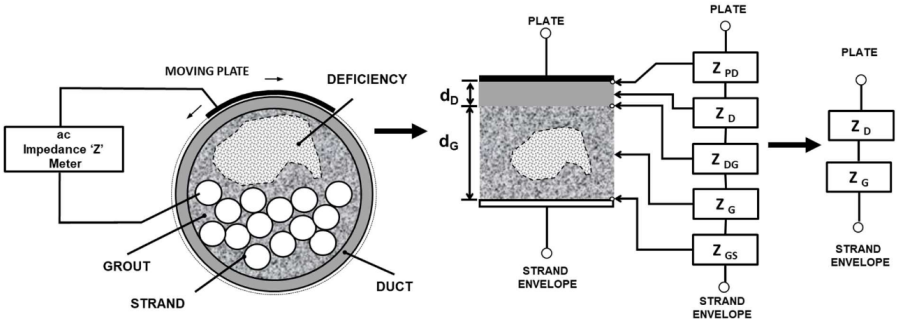

Figure 53. Left: Electromagnetic coupling test method arrangement. The moving metal plate is shaped to fit the external duct surface. Center: Simplified composite dielectric/conductive configuration. Right: Further simplification (Freij et al. [10])

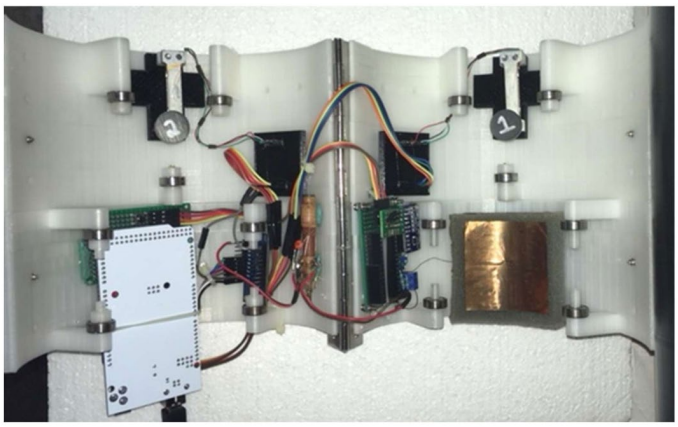

Figure 54. TIU-I with the clamshell opened to show internal components. Patent pending. (Freij et al. [10])

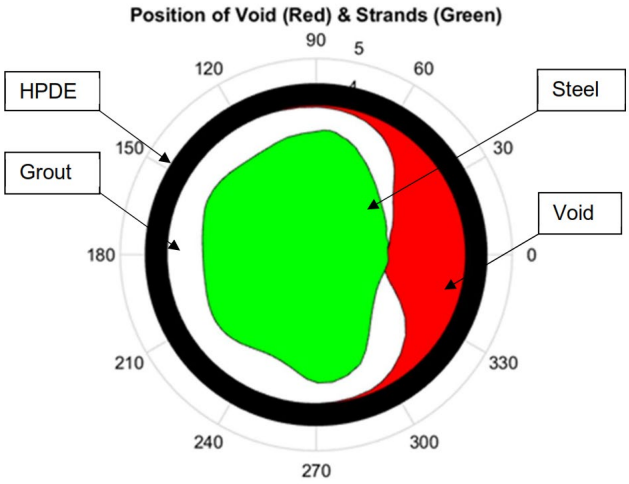

Figure 55. Image generated from TIU-I (Freij et al. [10])

In addition, the images from TIU-II were compared with the results from Gamma Ray Tomography (GMT) imaging for validation purposes. Four different tendon samples were used for this comparison referred to as duct A-D. The tendons have a 4.5-in external diameter and 19 ½-inch 7 wire strands embedded in grout. The duct wall was 7 mm. As shown in Figure 56, the samples are about 22.5 in. long, with various steel strand and grout configurations.

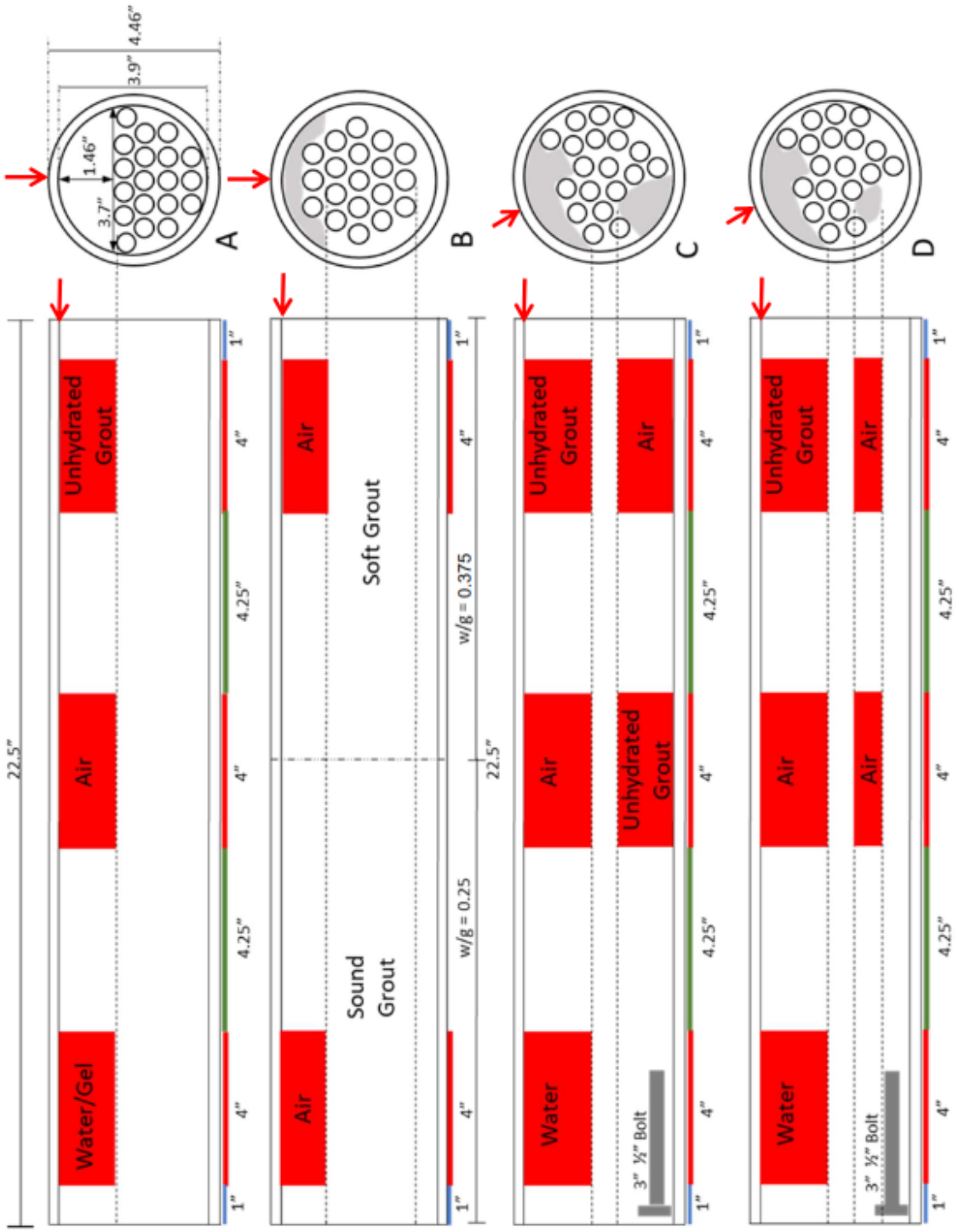

Figure 56. Approximate Configuration for Ducts A-D (Freij et al. [10])

Figure 57 shows the comparison between TIU-II (center) and GRT (right, conducted by THASA). Overall, TIU could detect the presence of unhydrated grout fill with a much lower cost and simplicity compared to GRT. However, GRT is capable of single-strand resolution which TIU is not capable of.

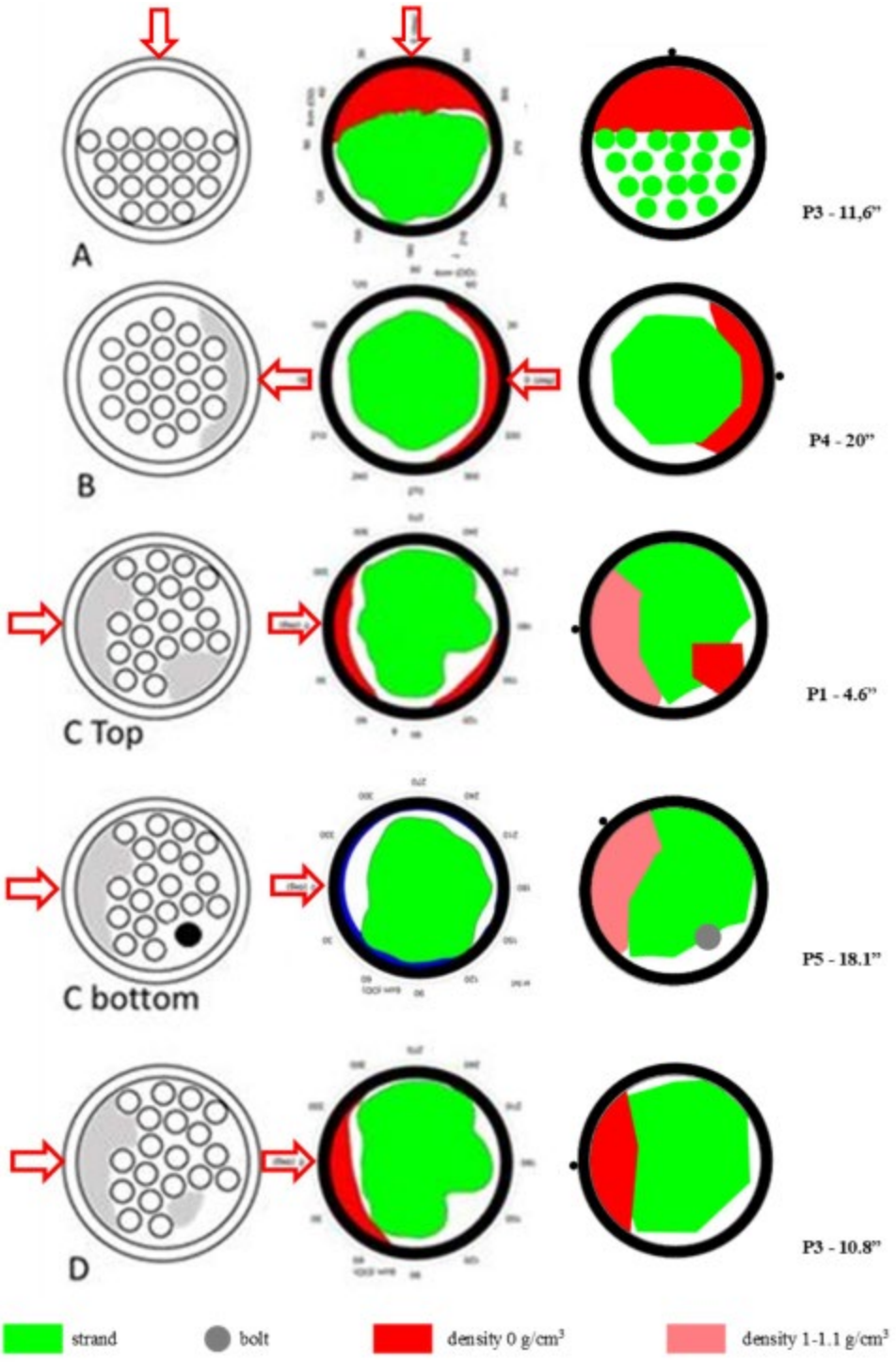

Figure 57. Comparison of selected cross-sections per design (left) obtained with the Laboratory Prototype (center) and GRT (right) (Freij et al. [10])

2.4 Visual Indicators

This section provides an overview on visual inspections for post-tensioned bridges that rely on flexible fillers for corrosion protection of tendons. Visual inspections are an important element of the bridge

inspection process, and unbonded tendons represent unique challenges compared to bonded tendons that utilize cementitious grout (CG). First, when corrosion occurs in CG systems, the expansive nature of the corrosion byproducts typically manifests as cracking in the adjacent concrete and/or splitting of the duct in the direct vicinity of the damage. For systems relying on flexible fillers, the expansion of the corrosion byproducts alone will not provide any signs of underlying damage.

Research on visual indicators for other types of structures with unbonded PT systems suggests that strand or tendon rupture in flexible filler systems typically results in an ejection event or an eruption event. An ejection event occurs when the energy released during rupture imparts significant velocity to the strand such that it dislodges from the grips at the end and, ultimately, protrudes from the anchorage. An eruption event occurs when the ruptured strand interacts with a draping profile to cause a portion of the cover concrete adjacent to the strand to "erupt" from the surface. This event would typically be associated with rapid corrosion that results in the rupture of an entire strand. If a single wire were to fail in a seven-wire strand, it may not release enough energy to cause an ejection through the HDPE cap or an eruption in the cover concrete.

2.4.1 Early Experience with Unbonded PT systems

A workshop held in November 2001 in Ghent, Belgium[43], highlighted the experiences of the global engineering community regarding the durability of post-tensioning tendons.A contribution to this volume by Harder and Webster [44] provides an excellent summary of failures associated with unbonded post-tensioning systems in Canada. The paper cites two examples of ruptured tendons in parking structures in the 1970s and four examples of ruptured tendons in office buildings between 1984 and 1991. In five of the six examples cited, the authors rely on the phrase "a tendon erupted" to describe how the damage was initially recognized. They describe scenarios in which the strands ejected from the anchors or erupted in "loops" projecting from the soffit or top side of structural slabs. One critical observation recorded in the paper was that strands with at least ¾-in of concrete cover did not typically result in the loop-type failure through the slab at the high and low points of the draping profile.

A subsequent report by Fallis et al. [45] provides representative images for the failure modes described in the Harder paper (Figure 58). A 2017 paper by Naso also describes tendon eruption from slab soffits in a parking garage in Chicago.[46] In this case, an erupted tendon led to spalling concrete that damaged a car window. The detailed inspection by structural engineers revealed several other smaller eruption zones in slab soffits that had gone undetected for an unknown period of time. More recent work by Bonger et al. [47] describes an extensive effort (experimental and analytical) to understand the ejection mechanism for vertically oriented post-tensioned bars in bridge piers. Their major relevant conclusion was that 0.6-in of concrete cover was not sufficient to prevent concrete spalling and protrusion of bars after rupture.

Figure 58. Erupted or ejected tendons from anchorage and slab soffit (Fallis et al. [45])

2.4.2 Office-Building Roof in Southeast Michigan

A four-story office building in Southeast Michigan, that was built in 1984, experienced strand failure in an unbonded post-tension system (Shear et al.[48]). In May 2006, occupants of the building reported hearing what sounded like a gunshot when strands ruptured. On-site building maintenance engineers later discovered two strands that were protruding from the roof slab. An initial inspection of the bottom side of the concrete slab, along the column line where the tendon failure occurred, did not reveal any signs of concrete cracking. The top side of the slab was not accessible due to a roof membrane system.

During the detailed inspection of the roof system after the failure, inspectors discovered an additional tendon that had broken and erupted through the bottom of the slab. Later, in June 2007, another tendon failure occurred that caused a large piece of concrete on the soffit of the slab to break off, which fell through the ceiling tiles and onto the floor below. In July 2007, another tendon failed, this time dislodging a small piece of concrete. By this time, safety netting had been erected, and it was able to catch the falling debris before it disrupted the building's occupants.

The most important question facing the building owner and the structural engineering firm hired to assess the problem was trying to understand the extent to which other tendons might be damaged. Concrete removal at six locations exposed 48 tendons with each tendon containing three strands. Of the 48 tendons exposed, 38 had a portion of the duct/sheathing removed to expose the steel strands. Forty percent of the exposed strands had water inside of the duct/sheathing. Twenty percent of the tendons with water were determined to be unstressed. Findings are summarized in Figure 59.

Water intrusion and subsequent corrosion damage in roof-slab post-tensioning system.

Relevant indicators:

- Ejected strands from edge of slab
- Gunshot-like noise at strand rupture
- Spalled concrete adjacent to tendon with ruptured strand
- Grease appeared to be emulsified
- Screwdriver insertion revealed unstressed strand

Figure 59. Exposed tendon after strand rupture in office-building roof (Shear et al. [48])

2.4.3 Bridge Structures

A recent FHWA-funded study by Lee [49] provides an overview of all major durability incidents connected to post-tensioned bridges in the U.S. through the time of publication. While flexible fillers are discussed as a strategy for mitigating the well-documented shortcomings of CG systems, the report did not identify any failures or durability concerns connected to any in-service bridges that used flexible fillers. During the performance period of the current study, a recently constructed bridge in Florida experienced rupture and subsequent ejection of a post-tensioning strand. The cause of the corrosion was water intrusion into the duct prior to tendon installation, tendon stressing, and injection of the flexible filler. When the strand ruptured, it ejected out through the cap a distance of several inches on one end. On the other end, the central wire of the 7-wire strand made a small puncture in the end cap and barely broke the surface. After cap removal, the wedge grips of the ejected strand were discovered to be entirely dislodged from the wedge plate.

Figure 60. Ejected strand on recently constructed bridge

2.5 Promising Methods

This literature survey also included an investigation into other NDE methods that have not yet been fully evaluated under field conditions related to the inspection of flexible-filler PT systems. Three distinct categories were identified for further exploration:

1. Coda-wave interferometry
2. Thermoelasticity
3. Radiography for imaging anchorage caps

2.5.1 Coda-wave Interferometry

Coda-wave interferometry (CWI) is an adaptation of the traditional ultrasonic pulse echo method (UPE). In UPE, the frequency of the ultrasonic waves is typically limited to about 50 kHz (Planes and Larose[50]).

This frequency limit avoids signal scattering due to the non-homogeneous nature of concrete. As a quick point of comparison, the ultrasound frequencies used in the USACE study investigating steel trunnion rods were between 1 and 3 MHz. If higher frequencies (e.g., > 100 kHz) are used in ultrasound inspections on concrete structures, the waves will reflect on small particles that make up the concrete and overwhelm the resulting signals with backscatter and noise (Figure 61).

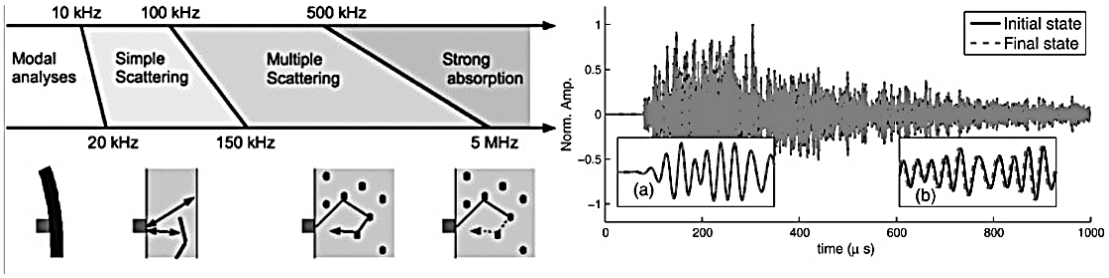

Figure 61. Scattering of ultrasonic waves in concrete for different frequencies and the resulting coda waves (Planes and Larose[50]).

Coda-wave interferometry seeks to take advantage of this backscattering through the careful analysis of the tail end ("coda") of the ultrasound signal that arrives at the receiver after a high-frequency input. The utility of CWI was first applied in the field of seismology as far back as the 1960s (Aki [51]) Researchers discovered that the behavior (especially velocity) of coda waves changes because of changes in the earth's crust.

Initial research into backscattered coda waves in concrete was performed in the early 2000's by Anuganda et al.[52] This early work led to subsequent research that involved the analysis of coda waves to monitor so-called "weak changes" in concrete. The basic concept is that the effects of small changes in the mechanical behavior of concrete (e.g., temperature effects, acoustoelastic effects, and micro-cracking) will accumulate in the coda waves because they propagate through the concrete on an elongated path compared to the initial ultrasound input. Even though the coda response appears random, it is repeatable when the ultrasound transmitter and receiver remain at the same location. Subsequent changes in the mechanical state of the concrete will result in a temporal shift of the coda wave that can be measured using interferometry techniques.

The following subsections discuss previous work related to CWI in concrete that may be useful for the inspection of flexible-filler PT systems. What is important to note in this discussion is that the CWI method is intended to assess the concrete that should be maintained in a constant state of compression by the PT system. This is a fundamental shift from the previous methods that are aimed at identifying if and where corrosion of the prestressing strands might or might have occurred.

2.5.1.1 Detection of Micro-Cracking in Concrete Using Coda Waves

Recent work by Popovics et al.[53,54] has explored the application of the diffusion behavior of coda waves to detect microcracking in concrete. This process may be useful in the current study on flexible fillers if a reliable methodology can be developed for assessing the concrete quality in closure pours for post-tensioned structures throughout their service life.

The first relevant study by Popovics[54] work involved experimental work on concrete samples with simulated micro-cracking. Micro-cracking was simulated with polypropylene fibers and results for two different damage levels (0.3% and 0.6% fibers by volume) were compared to an undamaged specimen. An ultrasound transmitter and receiver were attached to the surface of the concrete sample (Figure 62). The transmitter delivered 1 micro-second square-wave pulses at a frequency of 100 Hz. For each transducer location, the process was repeated 500-kHz times and the resulting coda waves were averaged together to obtain a single data series in the time domain.

Data processing involves taking the single data series in the time domain and dividing it into different frequency ranges with a width of 100 kHz and centered at 50 kHz increments over a range from 200 kHz to 450 kHz using a FFT and cosine-shaped filter. The resulting signals from the frequency domain are brought back into the time domain using an inverse FFT for additional processing.

After the inverse FFT data are squared to obtain the ultrasonic energy density as a function of time for each frequency range, a curve-fitting process is applied to the result for each frequency range. The resulting curve fits are then averaged together from 20 different spatial locations to obtain a single characteristic curve in logarithmic form (Figure 63). The characteristics of this curve are then related to the damage level in the concrete. Specifically, the diffusivity coefficient is related to the time at which the peak energy density is achieved, and the dissipation is related to the slope of the energy density vs. time plot after the peak level is achieved.

Results for the change in diffusivity as a function of damage level are provided in Figure 63B. Diffusivity was shown to decrease by an average of 19% and 25% for the mildly damaged (.3% fibers) and moderately damaged (.6% fibers) specimens, respectively. Results for the change in dissipation as a function of damage level are provided in Figure 63. Dissipation was shown to increase by an average of 18% and 32% for the mildly damaged and moderately damaged specimens, respectively.

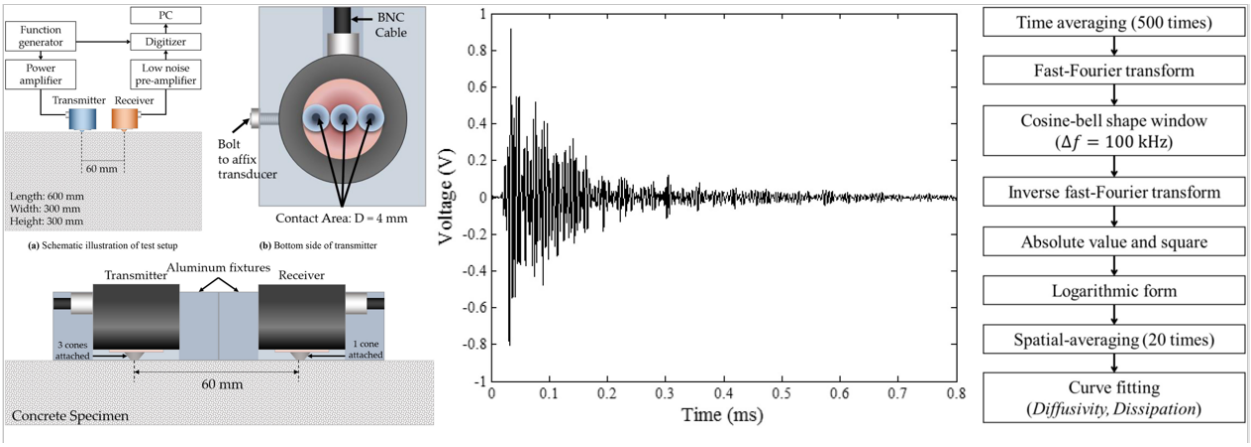

Figure 62. Test setup, time-averaged data after 500-kHz repetitions at one location, and data-processing algorithm used by Popovics et al.[54] to detect simulated micro-cracking in concrete.

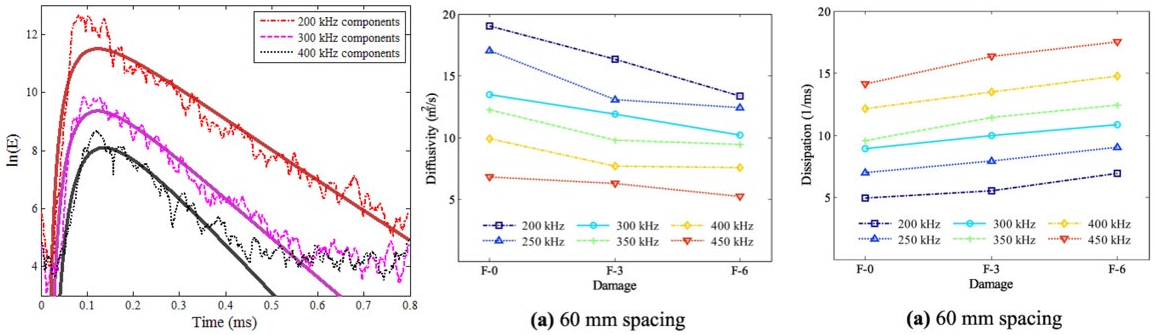

(A) (B) (C)

Figure 63. Results from coda wave analysis[54]. (A) Logarithmic curve-fits for energy density vs. time for moderately damaged concrete (.3% fibers) at 90 mm transducer spacing, (B) resulting plots for the change in diffusivity, and (C) change in dissipation as a function of damage. (Popovics et al.[54])

The second example of work by Popovics and Song[53] that we focused on attempts to identify distributed micro-cracking in non-homogenous materials by extracting non-propagating oscillatory fields from coda wave signals. The mathematical framework behind this method is complex, and we are still working through the details. Data collection involves acquiring ultrasound signals from multiple locations on the surface at fixed increments of distance away from a fixed transmitter location. The ultrasound frequency used in this study was 50 kHz, so the resulting signals at the receiver are expected to contain the following components:

- Forward-propagating waves corresponding to the driving frequency
- Backscattered waves due to interactions with constituent materials
- Non-propagating oscillatory waves due to interactions with micro-cracks
- Locally scattered waves due to cracks that extend to the surface

Results from a computer simulation are highlighted in Figure 64. The x-axis in the graphs is the normalized position of the receiver from the transmitter. The y-axis represents time, and the color represents the intensity of the ultrasonic wave on the surface. The region containing the distributed micro-cracks lies between 6 and 8.4 on the x-axis. When the receiver is located at a normalized distance less than 6 from the transmitter, the signal only contains the forward propagating and backscattered components. When the receiver is within the region containing micro-cracks, the signal contains components that oscillate due to the backscattered signals bouncing off the micro-cracks. But these oscillations do not propagate spatially beyond the micro-cracked zone (hence the name “non-propagating oscillatory waves”). As the level of simulated damage increases, the influence of the non-propagating oscillatory waves also increases. For the case where a simulated crack extends to the surface of the concrete, the receiver would measure locally scattered waves in the vicinity of the crack. Once the receiver is positioned beyond the crack, the forward-propagating component disappears. An overview of the geometry for the simulation model used to generate these results is provided in Figure 65.

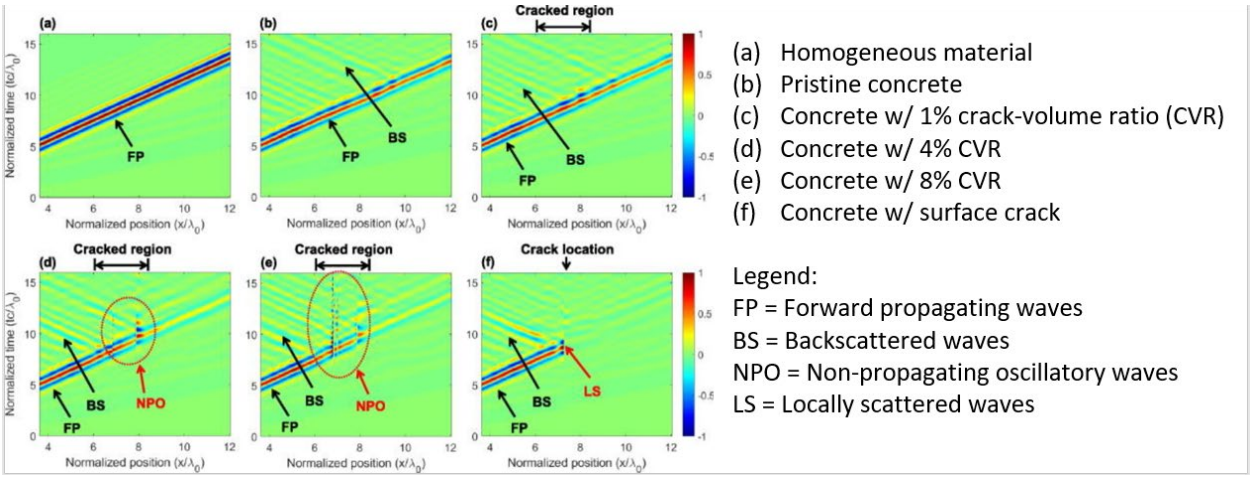

Figure 64. Micro-crack detection by identifying non-propagating oscillatory fields (computer simulation results)(Popovics et al. [53])

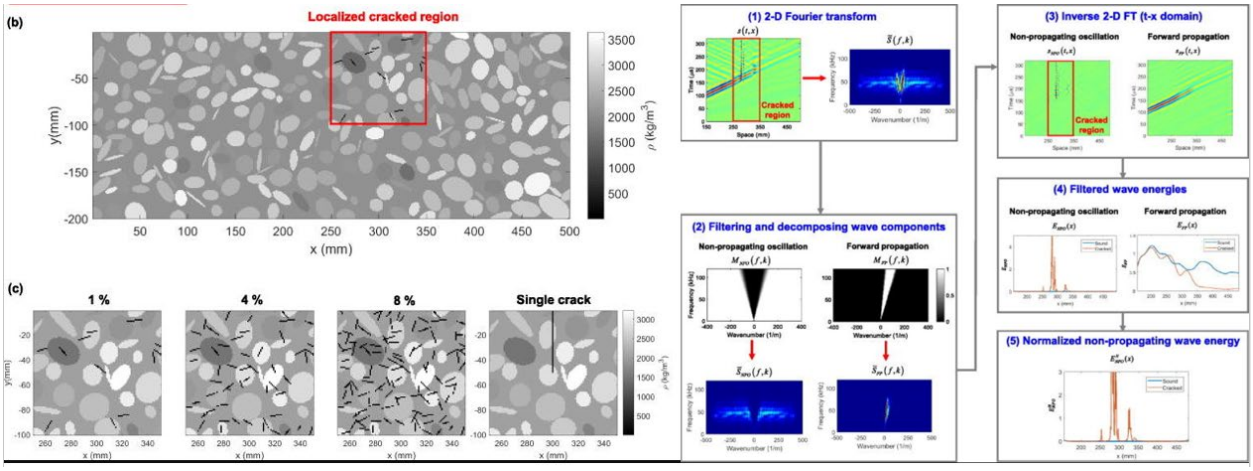

Figure 65. Computer simulation model and data processing algorithm (Popovics et al. [53])

The experimental results provided by Popovics and Song for the same concrete damage levels assessed in the previous study (no damage, 0.3% fillers, and 0.6% fillers) are promising. Samples for this experimental work consisted of concrete blocks with uniformly distributed polypropylene fibers (Figure 66). Since the defects were not confined to a predetermined zone, the ultrasound receiver picked up the components of FP, BS, and NPO waves from all sensor locations. The 2-D Fourier transform results clearly distinguish between the pristine, mildly damaged, and moderately damaged specimens.

Regarding the current study, both of the methods described by Popovics and his colleagues might be useful in determining whether or not critical areas on a post-tensioned structure are experiencing micro-cracking due to a loss in post-tensioning force. Furthermore, the natural diurnal temperature variations that a concrete structure experiences may also affect the backscattered coda waves differently for damaged and undamaged concrete. If this type of data could be collected for a closure-pour region on a post-tensioned element, it may be possible to verify that the PT system is still performing as desired.

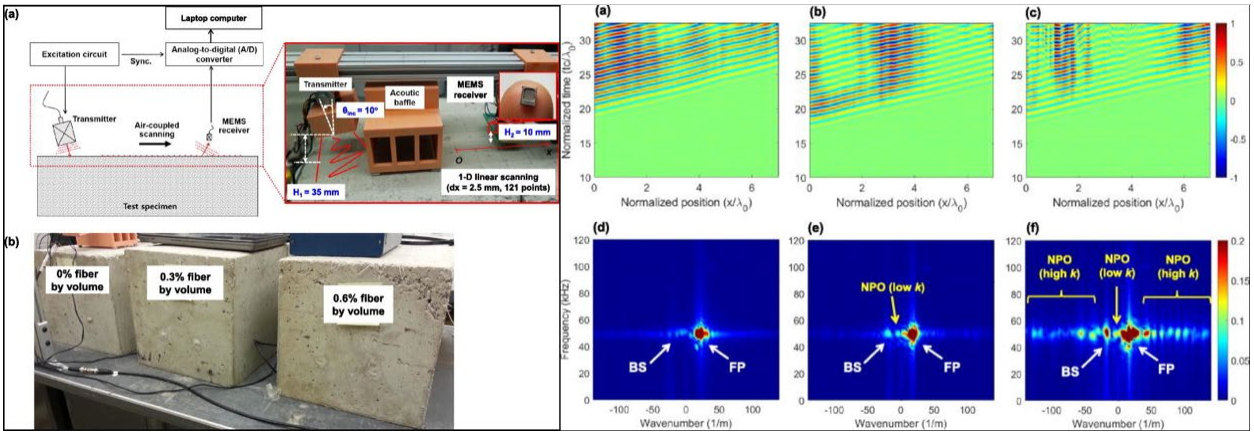

Figure 66. Experimental setup and results for micro-crack detection using coda waves (Popovics et al.[53])

2.5.1.2 Concrete Stress Level Assessment Using Coda-Wave Interferometry

Multiple researchers have relied on coda waves to assess the stress level experienced by concrete. The basic concept behind the method is to determine if the velocity of the ultrasound waves will change as a function of the stress level in the concrete. Higher stress results in a higher ultrasound velocity. The change in velocity is difficult to detect using basic ultrasound at 50 kHz. The changes are so subtle that they cannot be extracted from these low-frequency waves. Coda waves, however, contain higher frequency components that must travel a much longer distance through the concrete because they are scattered by particles in the material. When interferometry techniques are applied to coda waves obtained at the same location but for different stress conditions in the concrete, the resulting change in velocity can be captured. In their review paper on the method from 2013, Planès and Larose[50] reported that stress changes as small as 50 kPa (7.25 psi) could be observed through interferometric analysis of coda waves.

A recent Nebraska DOT study by Zhang et al.[55] demonstrated this method by monitoring stress transfer during strand cutting for AASHTO girders in the prestressing yard. Preliminary experimental results for concrete cylinders and a 6-in x 12-in x 20-in concrete beam are provided in Figure 67 and Figure 68, respectively. In both cases, the change in coda-wave velocity, expressed as a percentage of the initial velocity, exhibits a strong linear relationship with the applied compressive stress.

To validate the method under field conditions, the researchers bonded ultrasonic transmitters and receivers on the bottom flange at the midspan of a prestressed concrete girder. Coda wave measurements were made while the prestressing strands were being cut. Again, a very clear relationship was established between the resulting compressive stress in the concrete and change in velocity of the coda waves (Figure 69).

A major challenge posed by this method is that all the stress measurements are based on some initial state of stress. A single coda-wave signal cannot establish a state of stress on a concrete structure. There may still be some utility to the method, however. If stress changes due to diurnal temperature fluctuations can be monitored at critical locations on a structure using coda waves, it may be possible to differentiate between areas on the structure that are maintaining their desired level of prestress

compared to those that aren't. An additional advantage of this method is that stress level changes due to temperature fluctuations cannot be directly measured through strain gauges or other deformation measurement devices.

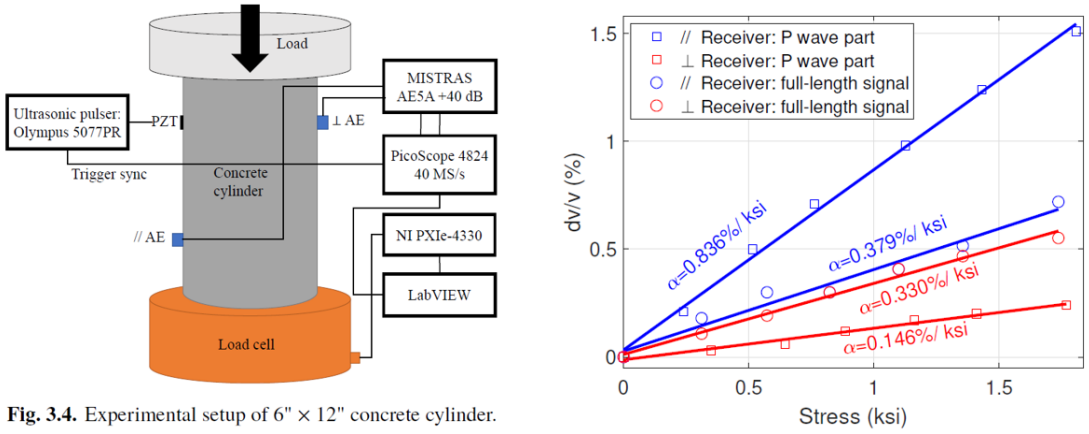

Figure 67. Experimental setup and results for coda-wave interferometry applied to compression test for concrete cylinder (Zhang et al. [55])

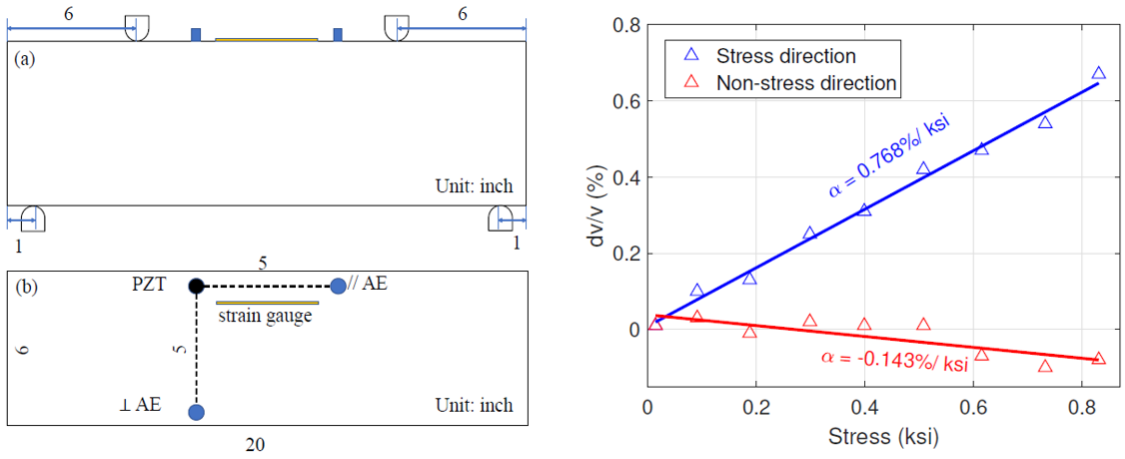

Figure 68. Experimental setup and results for coda-wave interferometry applied to flexural test for concrete beam (Zhang et al. [55])

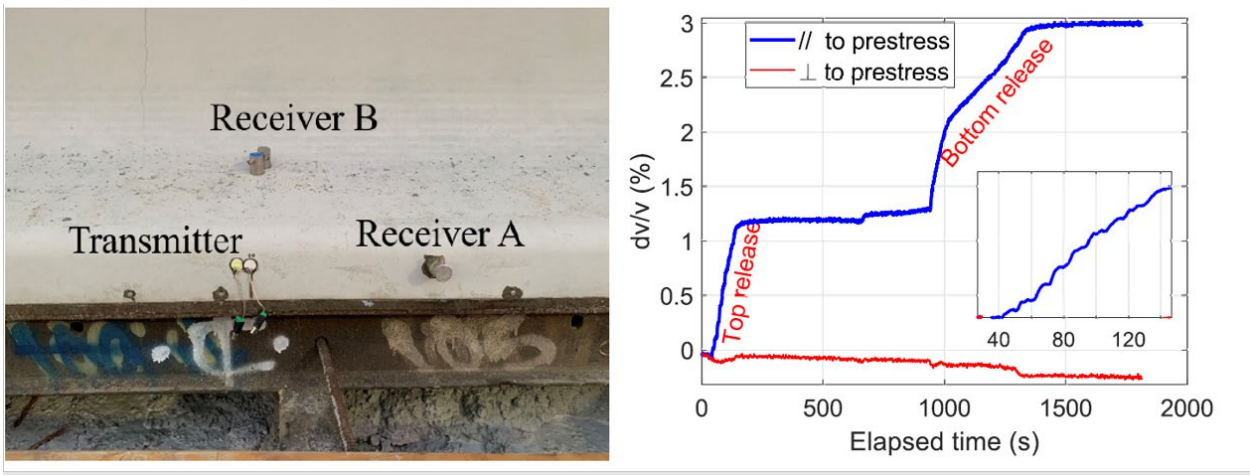

Figure 69. Ultrasound transmitter and receiver layout and coda-wave interferometry results for full-scale prestressed AASHTO girder at stress transfer (Zhang et al. [55])

2.5.2 Thermoelasticity

The most common understanding of thermoelasticity in structural engineering applications relates to the tendency of an object to expand or contract due to a change in temperature. Research for this project has led to another related phenomenon that may be useful for assessing the stress level in concrete. Thermoelasticity also includes a relationship/dependency between thermal conductivity and the stress experienced by a material.

The concept is best illustrated through an example from the mining industry. Demirci et al. [56] reported results from a study aimed at characterizing the variation of thermal conductivity in rock structures as a function of the triaxial state of stress. Apparently, the design of HVAC systems for mining operations is highly dependent on the thermal properties of the rock formations through which mine shafts are excavated.

The study involved direct measurements of thermal conductivity for rock specimens as they were subjected to varying degrees of triaxial stress. The test setup and sample results for conglomerate rock are provided in Figure 70. For the zero-confinement condition ($\sigma 3 = 0$), the thermal conductivity increases from approximately 5 W/m-^{o}C to approximately 8.25 W/m-^{o}C (a 65% increase) when 10 MPa (1450 psi) of compressive stress is applied in the axial direction.

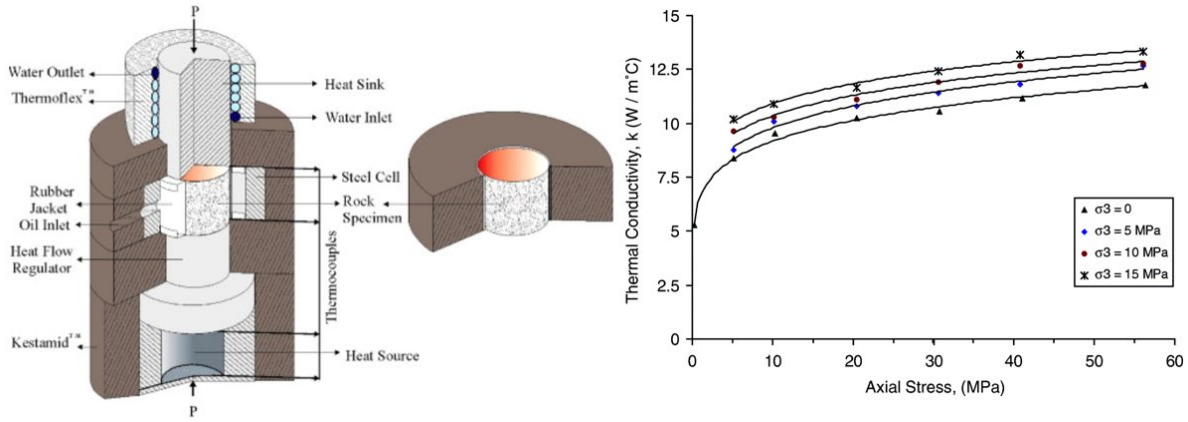

Figure 70. Test setup and experimental typical results for thermal conductivity variations in rock specimens due to axial stress (Demirci et al. [56])

Assuming that concrete exhibits similar variations in thermal conductivity due to applied loading, it may be possible to take advantage of this phenomenon and evaluate the stress level at critical locations in a post-tensioned structural element. Other research also suggests that the thermal conductivity of concrete may change as a result of mechanically induced damage.[57] One advantage of this approach over the coda-wave method is that thermal conductivity values can be measured and estimated in absolute terms for a given stress state. This method may be especially useful in the vicinity of anchorage blisters to determine if a specific tendon has lost a significant level of post-tension force. Diurnal temperature effects on the overall stress level in a post-tensioned element might also be assessed at critical locations by making direct measurements of thermal conductivity. The magnitude of these diurnal changes can be compared to expected values for the specific location. These results can provide an indication of whether an appropriate level of post-tensioning is being maintained in the structure.

2.5.3 Radiography Methods for Imaging Anchorage Caps

A complete review of radiographic methods applied to civil infrastructure was provided in Section 2.3.16. The basic narrative attached to radiographic NDE methods seems to be built around three basic shortcomings: (1) too expensive, (2) difficult to deploy, and (3) poses a potential health risk for the operator. Part of the challenge posed by civil infrastructure applications is the relatively high amounts of x-ray energy that is required to penetrate concrete and steel at typical thicknesses. This can be conceptualized by considering the half-value layer (HVL) thicknesses for some common materials (Table 8). The HVL thickness represents the thickness of a material needed to reduce the intensity of transmitted radiation by 50%. Lead, which is commonly used in x-ray shielding applications, has a very low HVL (0.06 mm at 50 keV). On the other end of the spectrum, muscle requires 18 mm of thickness at 50 keV to reduce the amount of energy by 50%.

Table 8 Half-value layer (HVL) thicknesses for materials of interest

X-ray energy (keV)	HVL thickness				
	Lead (mm)	Iron (mm)	Concrete (mm)	Bone (mm)	Muscle (mm)
50	.06	.45	4.3	4	18
100	.27	2.3	15.1	12	30
150	.30	4.5	22.3	23	45

Common medical imaging devices that rely on x-rays would be challenged to deliver enough energy to penetrate civil infrastructure components. Most of the imaging systems for infrastructure inspections rely on gamma ray sources. These sources generate beams of energy at higher energy levels, which can penetrate concrete and steel more easily than x-rays, for the same level of power input.

In the current study, we are trying to detect strand and wedge grip dislocations at PT anchorages. For Type 5 anchorage protection systems, the x-ray source only needs to be strong enough to produce a beam capable of penetrating the permanent nylon anchorage cap and the flexible filler contained within the anchorage. The strand tails will all protrude one inch from the wedge grips. Any wedge grip or strand dislocations will appear in the x-ray image if the x-ray generator and plate are oriented as shown in (Figure 71).

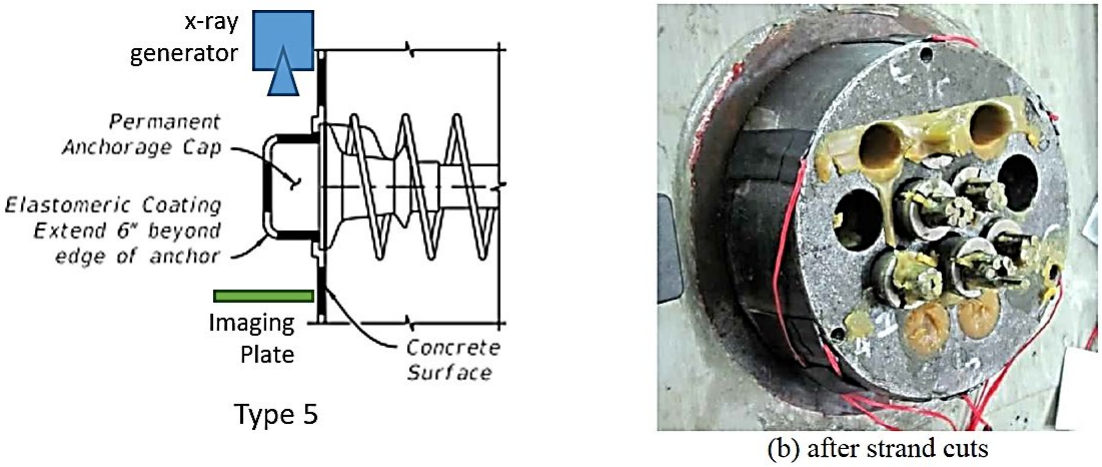

Figure 71. Possible inspection setup for x-ray imaging of PT anchorages with Type 5 protection systems. (Hamilton et al.[4])

Imaging for Type 1 anchorages that include an epoxy-grout pour back or internal PT ducts would require a significantly stronger radiation source, which reintroduces the limitations of excessive cost, difficulties with deployment, and operator safety. Imaging for Type 5 anchorages should be manageable with standard medical grade imagers. Recent advances in this technology have led to the development of multiple "off-the-shelf" portable x-ray imaging systems. Many devices are 100% battery powered and can generate 300 exposures on a single charge. These systems are commonly used in veterinary medicine applications (Figure 72) as well as forward military operations (Figure 73).

Figure 72. Portable X-ray generating unit for veterinary applications from OR Technology[58]

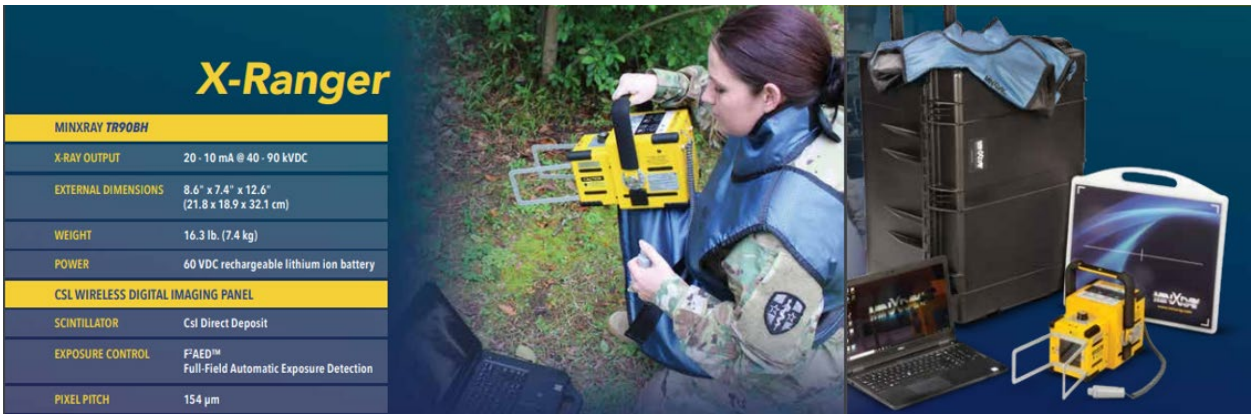

Figure 73. Portable X-ray generating unit and imaging plate for military applications from MinXray, Inc.[59]

3 Work Plan Development

The volume of literature and previous research devoted to the inspection of PT systems is extensive. The literature survey that was developed as part of Task 1 for the current study remains limited, and there are numerous examples of previous work related to each of the NDE methods that were described in Section 2.3. The comprehensive study completed by Hurlebaus et al. [15] could be repeated for mock-up specimens with fabricated defects that rely on flexible fillers for corrosion protection. Moving forward, though, the focus will be on efforts to enhance the general inspection framework that was first presented in Figure 14 and reprinted here for convenience.

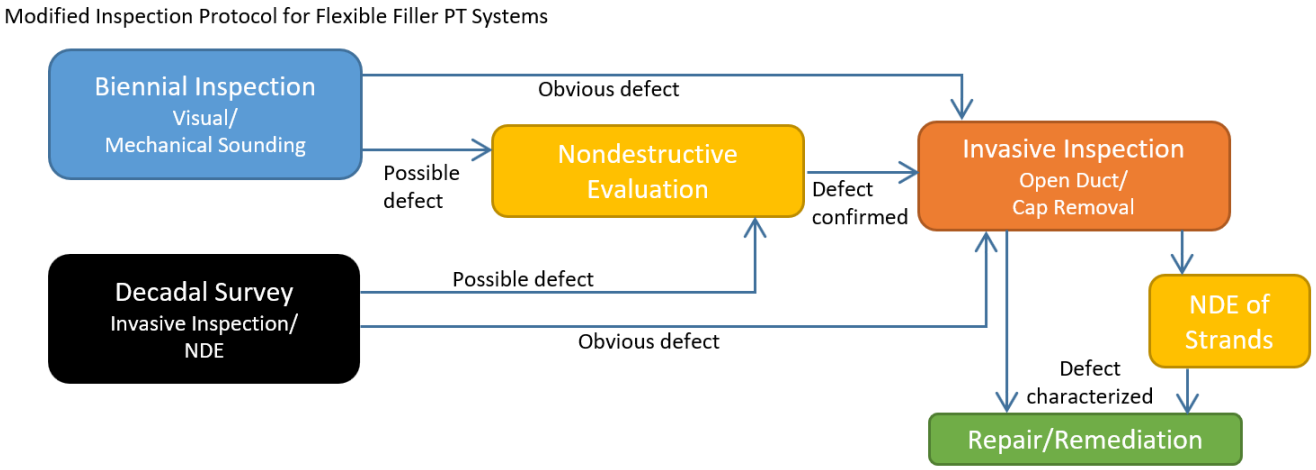

Figure 74. General inspection framework for PT systems relying on flexible filler.

3.1 Strategies and Knowledge Gaps

Developing this comprehensive inspection protocol for flexible-filler PT system will require a significant research effort before it can be effectively deployed. The following research questions are intended to serve as a starting point for addressing the existing knowledge gaps and laying a foundation for experimental work in the current study. These questions are organized around the five basic strategies that were described at the beginning of Section 1.5:

1. Identify cracking in the concrete that develops due to a loss in prestress force
2. Direct inspection of prestressing strands to determine if corrosion has occurred
3. Direct measurement of the prestressing force
4. Inspection of anchorage assemblies for signs of prestress loss
5. Chemical analysis of the flexible filler to determine if corrosion-inducing agents are present (e.g., moisture, chlorides, etc…)

3.1.1 Question-Set 1: Identify Cracking in the Concrete Structure

This group of questions is aimed at identifying a reliable process for evaluating the stress level in concrete at critical sections on a post-tensioned structure. The overall goal of prestressing concrete structures is to ensure that concrete remains in compression and does not experience cracking. One of

the fundamental indicators that a flexible-filler PT system has experienced damage will be the presence of cracks at critical locations on the structure.

Q1-1: What is the required loss in prestress force within the flexible-filler system before concrete cracking can be detected through a visual inspection? Where on the structure is this cracking likely to occur?

Possible solutions: Perform an analytical/modeling study using several existing structures with flexible fillers as case-studies.

Q1-2: What NDE methods can be used to identify micro-cracking in concrete at critical locations on the structure?

Q1-3: What NDE methods can be used to assess the stress level in concrete at critical locations on the structure?

Possible solutions (Q1-2 and Q1-3): Experimental investigation of coda-wave interferometry to assess the feasibility of evaluating microcracking and stress level at closure pours and other critical locations on post-tensioned structures.

Q1-4: How sensitive is the concrete stress level to diurnal temperature changes?

Possible solutions: Analytical/modeling study to better understand how concrete stress levels will respond to diurnal temperature changes. There is considerable literature related to thermal loading in PT segmental bridges. After the analytical/modeling study, these effects can be evaluated experimentally on existing structures.

3.1.2 Question-Set 2: Identify Corrosion Damage in Prestressing Strands

These questions are focused on the direct assessment of corrosion activity in the prestressing strands. Non-invasive NDE methods refer to inspection techniques that can be performed without damaging the HDPE duct or removing the anchorage cap. Invasive NDE methods require breaching the duct or removing the anchorage cap.

Q2-1: What **non-invasive** NDE methods are appropriate for identifying corrosion damage/section loss of strands in flexible-filler PT systems?

Possible solution: Further investigation of magnetic flux leakage for the inspection of external tendons. This may require the development of a new sensor that is optimized for external tendons. Direct assessment of corrosion on strands for internal tendons.

Q2-2: What **invasive** NDE methods are appropriate for identifying corrosion damage/section loss of strands in flexible-filler PT systems?

Possible solution: Invasive methods for direct identification of corrosion would either involve removing a portion of the duct and some of the surrounding filler material to perform a visual inspection of the exposed strands.

This level of access could also provide an opportunity for electrochemical impedance

spectroscopy if an electrical connection can be established at multiple points along the tendon

If the anchorage cap is removed, guided-wave ultrasonics can be used to identify possible corrosion damage along the strand. This is similar to the method deployed in the USACE study described in Section 2.1.3.

Finally, if the anchorage cap is removed, it may be possible to detect ongoing/active corrosion in a strand or tendon using acoustic emissions.

3.1.3 Question-Set 3: Assess the Stress Level in prestressing Strands

This set of questions addresses different methods for measuring the stress level in a prestressed tendon. A similar distinction is made between invasive and non-invasive methods.

Q3-1: What **non-invasive** NDE methods are appropriate for stress level of strands in a flexible-filler PT systems?

Possible solution: Magneto-electric methods can be used to determine the magnetic properties of prestressing strands. Making these measurements in-situ may be possible for external ducts. The magnetic properties of the steel will vary as a function of stress. We also need to develop a complete literature survey on this topic if there is sufficient interest.

Q3-2: What **invasive** NDE methods are appropriate for stress level of strands in a flexible-filler PT systems?

Possible solution: Assuming the cap is removed, guided wave ultrasonics and mechanical impedance methods could be used to evaluate the stress level in steel.

Q3-3: How sensitive is the stress level in a prestressing strand to diurnal temperature changes?

Possible solution: Similar to Q1-4, an analytical/modeling study could be executed to better understand how diurnal temperature changes affect the stress level in PT strands. These insights could be used to refine guided wave ultrasound and acoustic emissions testing to identify damage more accurately in a strand.

Q3-4: Is a lift-off test for an individual strand or an entire tendon practical?

Possible solution: If a lift-off test is possible, what are the conditions under which it would be considered necessary? Is it possible to replace an individual strand, or would an entire tendon need to be replaced?

3.1.4 Question-Set 4: Inspection of anchorage assemblies

Q4-1: What are the expected visual indicators at the anchorage cap for a corrosion-induced strand failure? How will these indicators vary depending on the anchorage protection detail (Type 1 vs. Type 5) that is used?

Possible solution: Experimental study on small- and full-scale specimens that evaluate the failure mechanism for corrosion-induced failures of strands and tendons under full prestress load. This work will verify if the strand and wedge grip dislocations observed in the study by Hamilton and Rice et al.[4] will be experienced during a corrosion-induced rupture event.

Q4-2: What **non-invasive** NDE methods are appropriate for assessing anchorage assemblies?

Possible solution: Experimental validation of x-ray imaging for Type 5 anchorages. This work could also include a study on possible strategies for Type 1 anchorages. The inspection of the Type 5 anchorages could be validated using commercially available medical imaging equipment. Type 1 anchorages will likely require involving consultants with more sophisticated gamma ray-based systems. Coda-wave interferometry and thermal conductivity assessment around the anchorage blisters may also be a viable method for validating that force transfer is still occurring at an anchorage. Small- and full-scale experimental testing can be completed to assess the feasibility of both methods. This is essentially the same as the possible solution to Q1-2 and Q1-3.

Q4-3: What **invasive** NDE methods are appropriate for assessing anchorage assemblies?

Possible solution: Assuming the anchorage cap is removed, what is the appropriate inspection protocol? This work would likely focus on determining what conditions encountered during a routine inspection would warrant the removal of an anchorage cap?

3.1.5 Question-Set 5: Chemical analysis of flexible fillers

These questions are aimed at assessing the ability of the flexible filler to continue providing corrosion protection based on the presence/absence of indicator contaminants.

Q5-1: What existing ASTM methods are appropriate for the chemical analysis of flexible fillers in typical civil infrastructure applications?

Q5-2: What is an appropriate sampling rate/frequency for a given structure?

Possible solution: Adapt existing protocols from the nuclear industry to establish a routine sampling program for flexible fillers.

3.2 Objectives for Experimental Work in Current Study

The literature survey completed for Task 1 indicated several NDE methods that may provide insight into the overall status of the PT system. These methods are grouped into three basic categories:

1. Ultrasound
2. Thermoelasticity
3. Radiography

There are several variations that may be applied within each method based on the overall goals of the inspection. Recall that we are proposing two basic levels of enhanced inspection that may include NDE activities:

1. **Preliminary** – intended for a six- or 10-year inspection cycle (or other appropriate time period) when no visual indicators are present. The goal of this inspection type is to ensure that the structure is behaving as expected and the PT system is maintaining sufficient compressive stress in concrete at critical sections. The scope of these inspections is broad and intended to cover span-level behavior.
2. **Advanced** – intended for situations where visual indicators or a preliminary NDE inspection indicate a problem with the PT system. The goal of this inspection type is to identify which tendon in a PT system may have suffered damage.

Figure 75 further illustrates this distinction in the context of the overall loss in prestress force. Four different "Loss Types" are used to describe different levels of prestress loss that may result from varying degrees of damage to PT tendons. In the first scenario, Loss-type 1 (LT-1), the structure experiences normal time-dependent losses in prestressing force due to creep and shrinkage of the concrete. These losses are accounted for in the design of the structure and, as a result, the entire cross-section should remain in compression ($f_c > 0$) under Service III and Service IV loading conditions. Loss-Type II describes a scenario in which the PT tendons experience mild corrosion at a relatively slow rate. This results in some tensile stresses in the concrete with no concrete cracking. In LT-3, the rate of corrosion is more severe than in LT-2, but it is assumed to occur at a uniform rate. The ultimate effects of LT-3 include visible indicators (e.g., concrete cracking), but there is an extended period in which the concrete is experiencing a state of tension before the actual cracking occurs. Finally, LT-4 describes a scenario in which the corrosion of PT strands is both rapid and severe. In this case, there is little or no time between the loss in prestress force and the onset of visible concrete cracking.

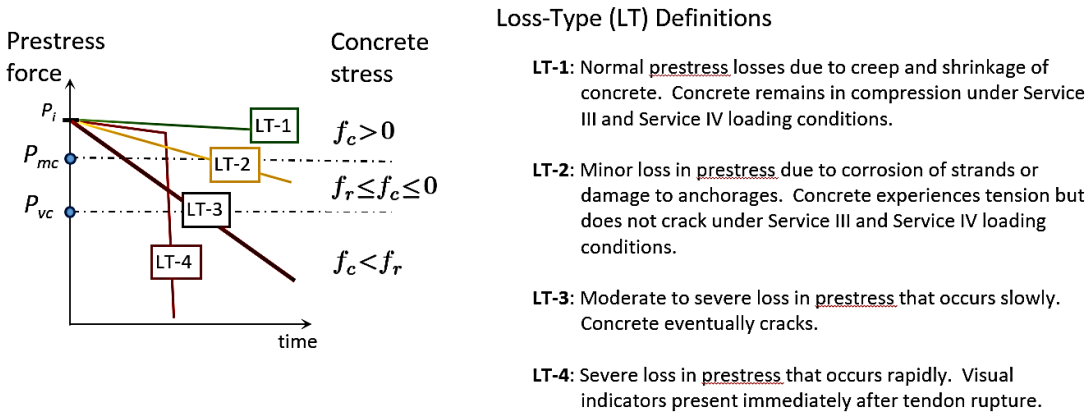

Figure 75. Different scenarios for loss in prestressing force

Ideally, the methods developed for the preliminary NDE inspections should be able to identify if a structure is experiencing LT-2 or early-stage LT-3 that results in tensile stresses in the concrete at critical sections but without any visual indicators. For late-stage LT-3 and LT-4, visual indicators will preclude the need for any of the preliminary NDE methods. Nonetheless, advanced NDE methods or invasive inspections are still required to identify which PT tendon and/or strands are experiencing the prestress loss.

After discussing the inspection strategies and knowledge gaps with FDOT Project Managers, the following items were identified as priorities for the current study:

Q1-2: What NDE methods can be used to identify micro-cracking in concrete at critical locations on the structure?

Q1-3: What NDE methods can be used to assess the stress level in concrete at critical locations on the structure?

Q2-1: What **non-invasive** NDE methods are appropriate for identifying corrosion damage/section loss of strands in flexible-filler PT systems?

Q4-2: What **non-invasive** NDE methods are appropriate for assessing anchorage assemblies?

The three NDE methods described in Section 2.4 (ultrasound interferometry, thermoelasticity, and radiography) were also identified as worthy of additional experimental exploration and validation. The general strategy was to complete small-scale proof-of-concept testing using ERAU laboratory facilities, which was followed by large-scale testing at the FDOT Structures Laboratory in Tallahassee, Florida. Proof-of-concept testing is described in Section 4 and large-scale testing is described in Section 5.

4 Proof-of-Concept Testing

4.1 Radiography

Radiographic testing was performed in October 2021 at the Florida Department of Transportation Marcus H. Ansley Structures Research Center in Tallahassee, Florida. The goal of this testing was to determine if radiography is an effective NDE method for internal ducts, external ducts, and anchorage regions.

4.1.1 Specimens

Testing was performed on a variety of specimens to replicate different portions of a post-tensioned structure that would be evaluated in the field.

Table 9 Specimen summary

Specimen 1	Small-scale mock-up tendon
Specimen 2	Large-scale external mock-up tendon
Specimen 3	Prestressed girder with internal duct (no tendon)
Specimen 4	Prestressed Girder with internal duct (with tendon)

The first specimen is a full-scale anchorage mockup made of a VSL ECI 6-19 anchorage system (Figure 3). This specimen consists of the trumpet, anchorage plate, wedge plate, and end cap. To represent a post-tensioned duct, the wedge plate was loaded with 16 strands that extended through the trumpet region. In the cap region, this mockup simulates a Type 5 anchorage protection detail, which is commonly used in PT bridges with FFs. This anchorage type allows for more accessibility to the cap compared to other anchorage protection details.

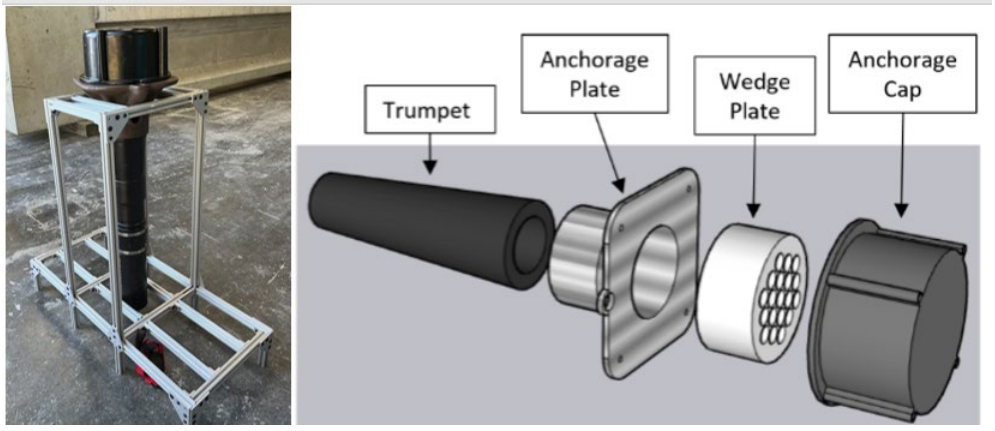

Figure 76. Anchorage assembly

By utilizing imaging techniques that penetrate the anchorage cap, inspectors can thoroughly examine the strand ends and the proper seating of the wedge grips without the need to remove the cap. This approach aligns with the preferences of the FDOT, as cap removal is a laborious and time-consuming task for inspectors. The anchorage cap serves as a strategic point for investigating potential loss of post-tensioning (PT) force. If the positions of the strands and grips are not as expected, it signals that more extensive inspections along the duct's length may be necessary to identify the root cause of the issue. Consequently, the research places significant importance on assessing the feasibility of detecting defects through radiographic images taken from beneath the caps.

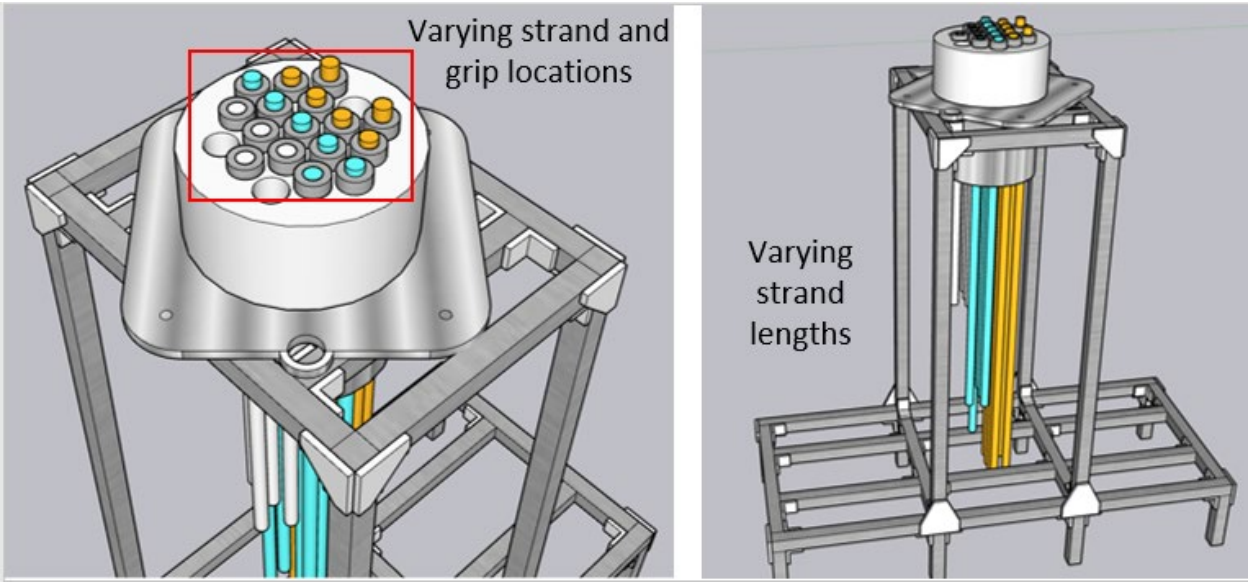

Figure 77. Anchorage mock-up showing varied strand and grip locations for testing

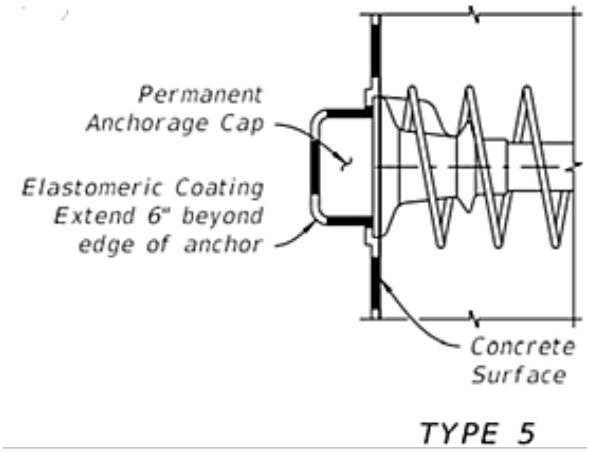

Figure 78. Type 5 anchorage (FDOT SDG)

The second specimen subjected to testing was an external tendon mockup filled with flexible fillers (FF). This mockup was fabricated at the FDOT structures laboratory and serves as a training tool for field personnel to learn the process of filling these ducts. Essentially, this specimen replicates a genuine duct and functions as a filled external duct specifically for testing purposes.

By conducting tests on a duct that was already filled, we can ascertain whether radiography proves effective in capturing images of the internal strands through the FF material. This experimentation provided valuable insights into the feasibility of using radiographic techniques for imaging through FF and visualizing the enclosed strands.

Specimens 3 and 4 both pertain to internal duct systems. Specimen 3 comprised an empty duct without any strands, while Specimen 4 contained strands within. These beams were repurposed from a previous study by Consolazio and Hamilton [60], as illustrated in Figure 6.

Inspecting internal ducts presents a significant challenge due to the presence of concrete cover. This presented a problem because radiographic equipment can only penetrate a specific amount of concrete depending on the energy level of the radiation source. As the ducts become more deeply embedded in the concrete, achieving clear imaging became progressively more difficult.

The cross-section of this specimen is depicted in Figure 6, revealing a 10-inch web that the imaging equipment must penetrate. Furthermore, to conduct these tests effectively, the imaging plate must be positioned on one side of the beam, while the radiographic source is located on the opposite side. When the beam is excessively thick or difficult to access, it compounds the obstacles encountered during testing.

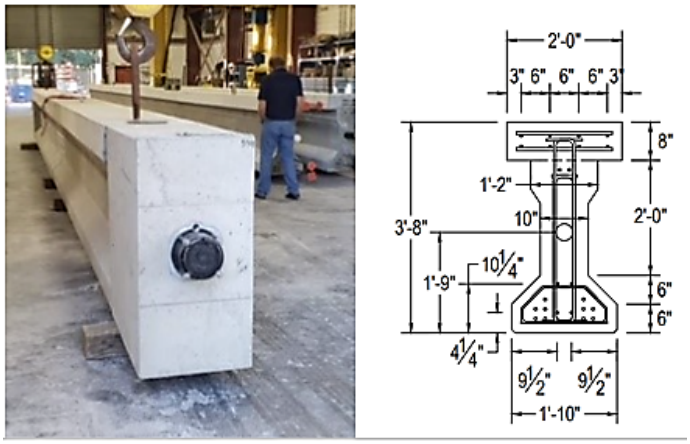

Figure 79. Internal Duct Large Scale Specimen (Consolazio and Hamilton[60])

Figure 80. Filled external tendon mock-up

4.1.2 Equipment

To identify the optimal radiographic setup, two different X-Ray systems were evaluated. The first setup featured the POSKOM PXM-20BT, a portable X-Ray machine commonly utilized by equine veterinarians for evaluating their patients. This device operates at low power levels (60-80 kV, 1.3-1.6mAs), is lightweight (approximately 20 pounds), user-friendly, and requires minimal setup. Its compatibility with standard 120-volt electrical outlets makes it versatile for use at various locations. Some models even offer battery-powered options, enhancing portability, especially in hard-to-reach sites. Importantly, this machine operates at low power, reducing the need for extensive Personal Protective Equipment (PPE) usage, which is critical for ensuring the safety of veterinarians and their animal patients.

Due to its simplicity, portability, and user-friendliness, this device appeared to be a viable option for regular bridge inspections. However, it does have a notable limitation: its limited power output, which restricts its ability to penetrate concrete for imaging purposes.

Figure 81. POSKOM PXM-20BT

The second setup involves the YXLON X-Ray machine, an industrial-grade device with higher power capabilities (250kV, 2.4mAs) that can penetrate through concrete layers of up to 12 inches. This machine is well-suited for assessing internal tendons but necessitates more extensive setup and safety precautions.

As an industrial-grade device, the YXLON offers greater power compared to the POSKOM PXM-20BT. However, it demands additional equipment and power resources for operation. The YXLON is notably larger and less portable than the POSKOM PXM-20BT, requiring more careful planning and logistical considerations for effective bridge inspections.

Furthermore, the YXLON's safety requirements dictate a larger safety radius of 30 feet between the machine and the operator to ensure a safe distance from the strong radiation source. In certain scenarios, closing the bridge to conduct inspections may become necessary, although this is not an ideal or always feasible solution.

Figure 82. YXLON

4.1.3 Data Collection

We obtained images from each of the previously mentioned specimens. The POSKOM PXM-20BT was used to capture images through the anchorage mockup (Specimen 1), the external duct specimen (Specimen 2), and multiple end caps. On the other hand, the YXLON machine was employed to capture images through the end caps and the internal duct specimens (Specimens 3 & 4). The outcomes of these tests are detailed in the following section.

4.1.3.1 POSKOM PXM-20BT

As previously mentioned, this is a low-power portable device. This device can be seen in use in Figure 83.

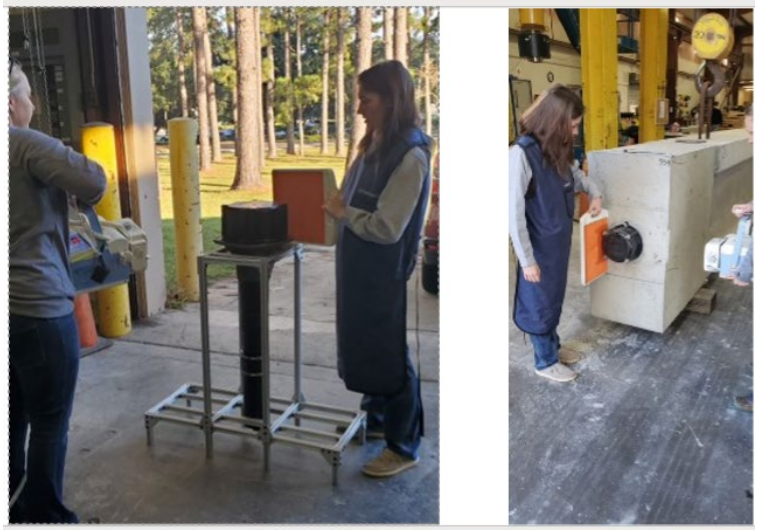

Figure 83. POSKOM PXM-20BT setup.

4.1.3.1.1 Anchorage Cap (Specimens 1,2, & 4)

The POSKOM PXM-20BT machine delivered promising results when employed for imaging through the anchorage cap region. The obtained images offer valuable insights, enabling inspectors to identify the positions of strands and grips, as well as detect any defects within the cap, such as voids or corrosion. This inspection method could serve as a rapid additional assessment to complement existing inspection procedures, ensuring the integrity of the cap region. The anchorage mockup (Specimen 1) incorporated strands of varying heights to simulate damage, and these variations are clearly depicted in the images, substantiating the effectiveness of this method for field applications.

When used on the cap of Specimen 2, the images provided a clear view of the filled cap, allowing inspectors to discern any voids or defects. Notably, the flexible filler material (FF) did not interfere with image quality, as it was easily penetrable. However, it's important to note that further research should be conducted on filled ducts to confirm the accuracy of this method, given that this project examined only one filled specimen. It's plausible that tendons filled with cementitious grout (CG) might pose greater challenges for imaging, potentially affecting the clarity of strand and wedge grip visibility.

Additionally, the machine's performance on the full-scale internal specimen cap was consistent with its previous successes. Once again, it effectively penetrated the cap, providing inspectors with a clear image of the cap's interior.

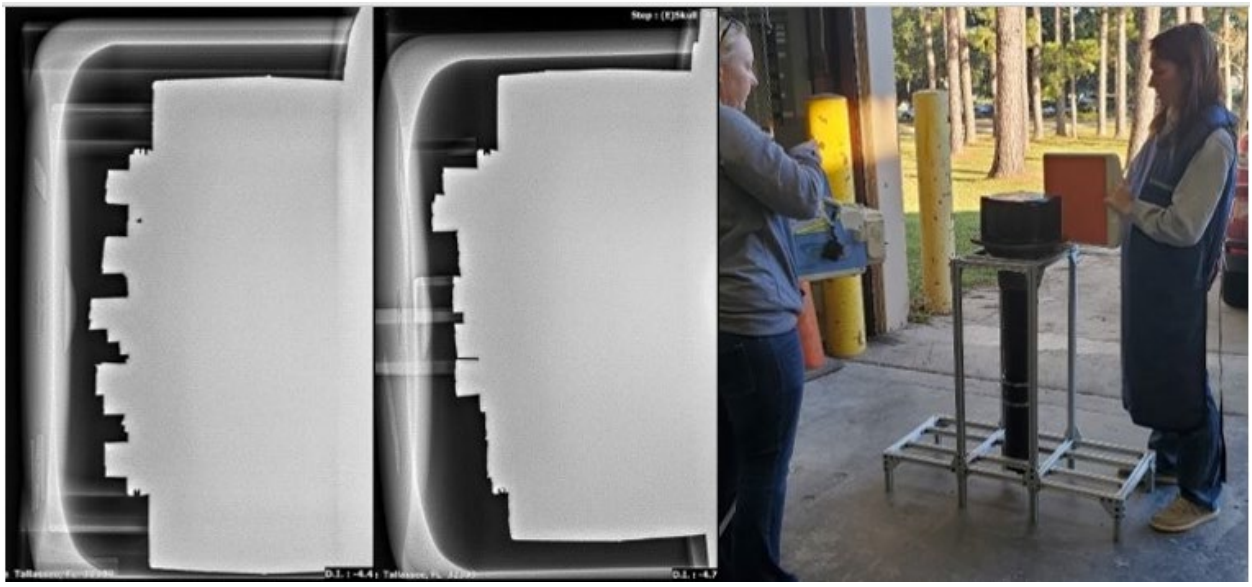

Figure 84. Specimen 1 anchorage cap results: images collected from POSKOM PXM-20BT from different angles.

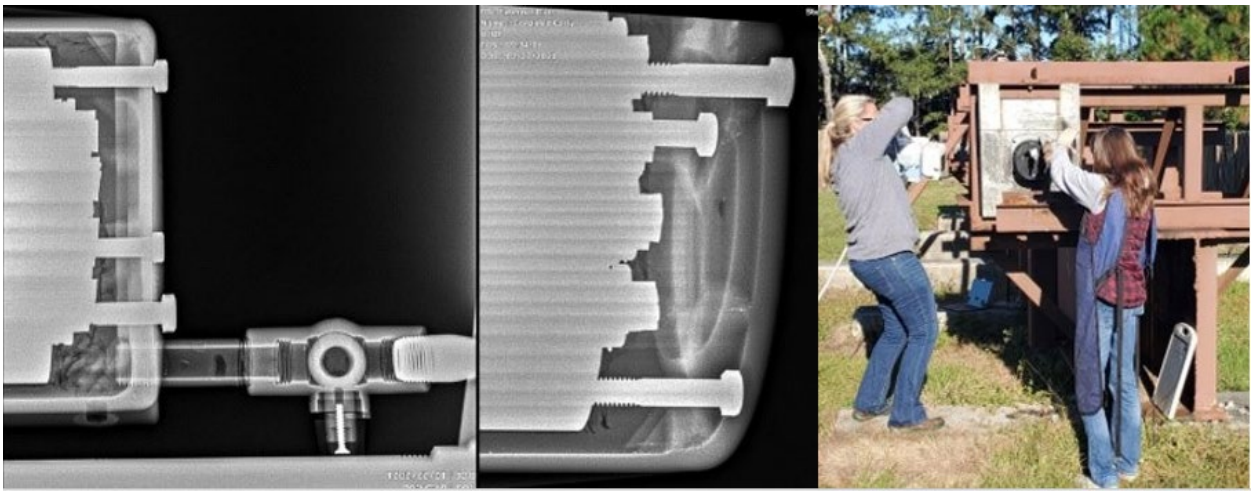

Figure 85. External duct mockup: filled anchorage cap results

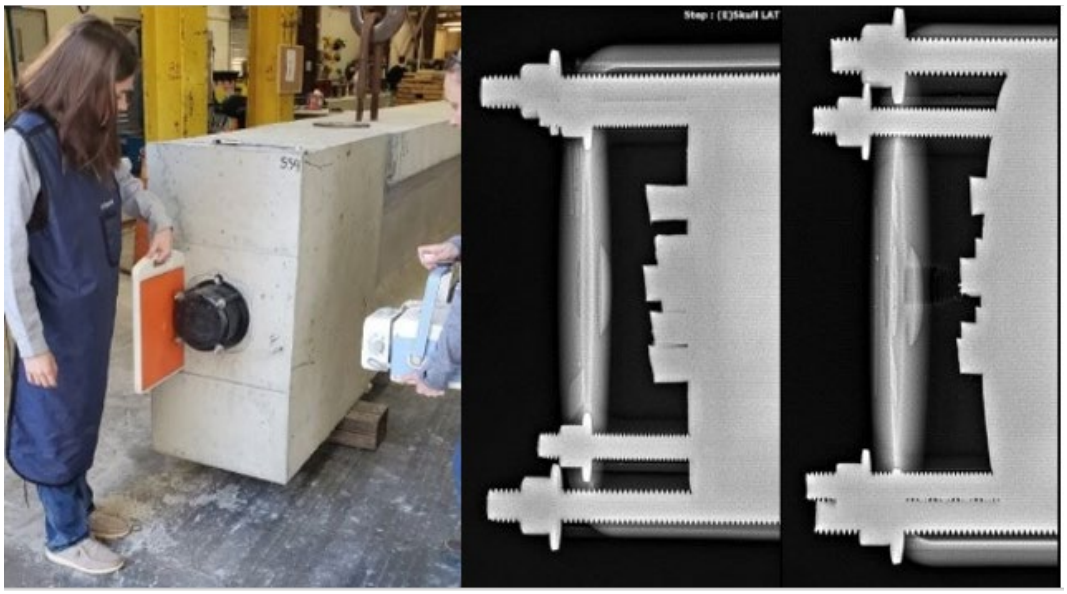

Figure 86. Internal specimen: anchorage cap results

4.1.3.1.2 Internal Duct Specimen (Specimens 3 & 4):

The POSKOM PXM-20BT setup proved inadequate for the inspection of internal ducts. This machine encountered significant challenges in imaging through 4 inches of concrete, rendering it unsuitable for imaging through full-scale beams. The image below illustrates the attempt to capture an image through concrete using this machine, revealing only a faint and barely discernible outline of the strands. Consequently, it is not advisable to employ this device for inspecting internal duct systems.

Figure 87. Anchorage mockup: duct results

4.1.3.1.3 External Specimen (Specimens 1 & 2)

The POSKOM PXM-20BT demonstrated its effectiveness without encountering any issues when imaging through the external duct system, producing encouraging results. In tests involving the filled external duct system, it even allowed the identification of small voids within the filler material, in addition to visualizing the cluster of strands. However, an important consideration arises when examining grouped strands within the tendon. It became evident that distinguishing each individual strand, or detecting potential corrosion within the strand bundle, can be challenging using this machine.

Figure 88. Specimen 2: filled duct results

The testing of the POSKOM PXM-20BT on the trumpet section of the anchorage mockup produced outcomes like those observed in the other external duct specimen images. These images provided a clear view of the strands, although discerning individual strands within the bundled duct region remained challenging. For this mockup, the strands were intentionally cut at various lengths and heights to examine whether the images could reveal these height differences. The resulting images displayed these variations, showcasing the machine's capability to capture differences in strand heights. It must be noted, however, that the orientation of the source and detector has significant impact on the resulting images.

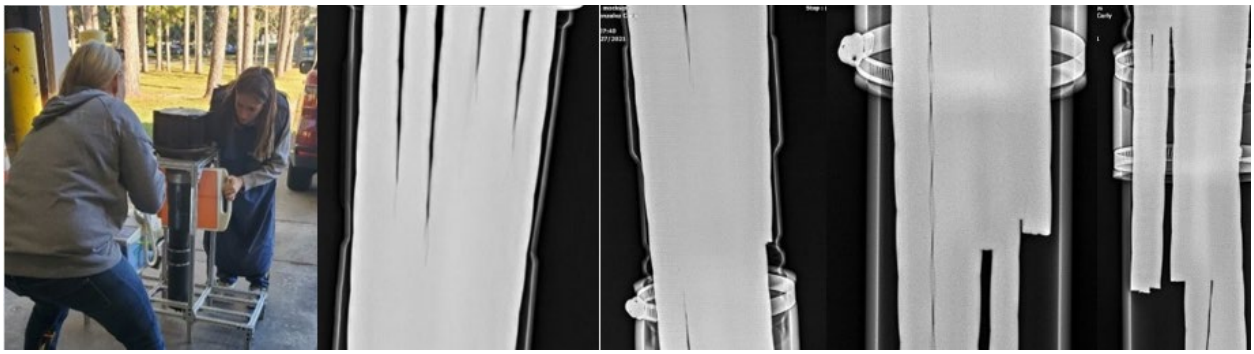

Figure 89. Anchorage mockup: trumpet results

4.1.3.2 YXLON

The setup of the YXLON machine for evaluating the internal-duct specimen is provided in Figure 90. The imaging plate is on the left and the radiation source is on the right.

Figure 90. YXLON X-Ray machine on internal duct specimen

4.1.3.2.1 Anchorage Cap (Specimen 4)

Due to the considerable power of the YXLON X-Ray machine, the images captured through the cap exhibited a slight overexposure, leading to the "grayed" appearance of the cap (Figure 91). To mitigate this issue in future testing, it may be worthwhile to explore reducing the exposure time. Fortunately, despite the overexposure, it remains possible to discern the outline of strand and grip locations in

these images. For inspection purposes, this level of visibility would suffice in assessing the cap and alerting the inspector to any potential faults within it.

Figure 91. YXLON machine on internal specimen anchorage cap

4.1.3.2.2 Internal Specimen

The YXLON X-Ray is capable of imaging through 12” of concrete. The first specimen that was examined contained an empty duct with no strands. Since the width of the web containing the duct was only 10” , it was easy to identify in the resulting image (Figure 92). The location of the mild reinforcement was also discernable from the images.

The second specimen contained a duct with six 0.6-in prestressing strands. The YXLON machine successfully captured images that revealed mild reinforcement in addition to the strands. In this case, the specimen featured a 12-strand wedge plate, filled to only half its capacity. Consequently, the strand bundle appeared less concentrated when compared to the external specimen. The advantage of having fewer strands in this configuration was that the YXLON machine could provide a highly detailed image, allowing for the visualization of the individual wires comprising the strands. This capability holds promise for detecting voids and potentially even corrosion within these strands during field inspections.

It's important to highlight the limitations of this technique when applied to internal specimens. Due to the orientation of the duct within the beam, it allows for imaging from only one angle, thus constraining the view to a specific perspective.

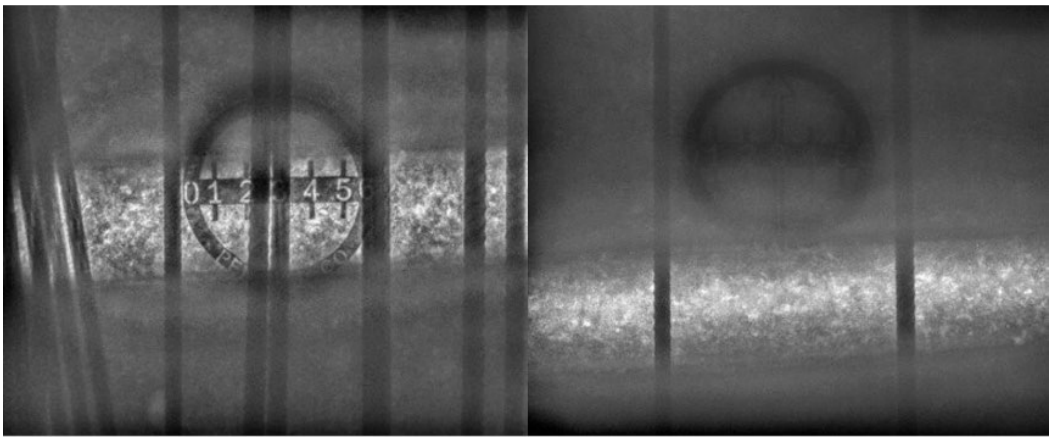

Figure 92. Internal duct specimen: duct without strands

Figure 93. Internal Duct Specimen: duct with strands 1ft away from end block (Left) and 5ft away from end block (Right)

4.1.4 Conclusion

At this stage, radiography stands out as a promising Non-Destructive Evaluation (NDE) method for assessing post-tensioned (PT) bridges employing flexible fillers (FF). This technique proves capable of detecting a range of issues, including voids, strand breakages, corrosion, and other defects that may be present within anchorage caps, internal ducts, and external ducts (Table 4). Integrating radiography testing into the existing biennial inspections would provide inspectors with a clear view of the internal components of these ducts and anchorage caps.

However, it's essential to acknowledge certain limitations when considering the implementation of this method. These limitations include the cost associated with acquiring the equipment, ensuring a sufficiently robust radiation source, and addressing operator training and safety.

The equipment itself carries a significant price tag, and when coupled with the need for highly skilled operators, the testing costs can escalate quickly, depending on the specific project. Operators must

undergo comprehensive training and collaborate closely with inspectors to ensure that the crucial points of interest within the bridge are thoroughly inspected.

Additionally, high-power equipment like the industrial YXLON machine necessitates strict safety protocols, including establishing a 30-foot radius around the imaged area that must be cordoned off. Given the potential harm posed by radiography, maintaining a safe distance from the radiation source is imperative. During these tests, there may be instances where it becomes necessary to temporarily close the bridge, although this is not the preferred course of action, as it can lead to delays and disrupt traffic flow.

In conclusion, radiography has demonstrated considerable promise as an NDE method, but its practical implementation in the field comes with certain challenges.

Table 10 Effectiveness of radiographic NDE

	Anchorage		**Internal Duct**				**External Duct**			
	Wedge grip seating	Strand-end location	*Tendon Location in Duct*	Broken Strand	Broken Wire	Void in Filler	Tendon Location in Duct	Broken Strand	Broken Wire	Void in Filler
POSKOM PXM-20BT										
YXLON										

Legend	
	Recommended
	Method works, but limitations based on geometry or accessibility
	Not Recommended
	Needs more research

4.2 Thermoelasticity

4.2.1 Introduction

Thermoelasticity encompasses the response of a material as it undergoes expansion and contraction due to temperature variations. Furthermore, it includes the correlation between changes in thermal conductivity and stress levels within the material. This concept opens the door to monitoring stress levels in concrete by analyzing surface temperatures as the material undergoes heating and cooling cycles. By evaluating the temperature fluctuations of concrete bridges during daily heating cycles , this approach holds the potential to assess stress levels and verify the continued effectiveness of post-tensioning systems.

The diurnal temperature effects on the overall stress level in the PT element may also be assessed at critical locations by making direct measurements of thermal conductivity. The diurnal changes can be compared to the expected value at the specific location, which will give an indication of whether an appropriate level of post tensioning is being maintained in the structure. If the thermal conductivity is found to be lower than usual, the inspector could then assume that loss of PT force is occurring due to the lower stress levels that the concrete is experiencing.

Although this method seemed promising when completing initial research on the subject, we were unable to validate the theory through direct measurements. The following section describes the analytical and experimental work that was conducted as part of Task 3.

4.2.2 Finite Element Analysis (FEA)

To evaluate the viability of utilizing principles of thermoelasticity to evaluate the stress level in concrete, we developed an ANSYS model to establish a baseline for our small-scale testing. This approach provides a straightforward means to examine how heat should propagate through the concrete while minimizing the influence of external variables that could potentially impact the results.

4.2.2.1 Model Geometry

The model consisted of a simple 12”x 3.5”x 4.75” concrete block, to simulate the specimens that would be tested on. The model can be seen in Figure 94 below. The circular ring on the bottom represents the heating lamp and where the heat will be applied in the model. The vertical line is where the temperature will be measured as the surface heats and cools.

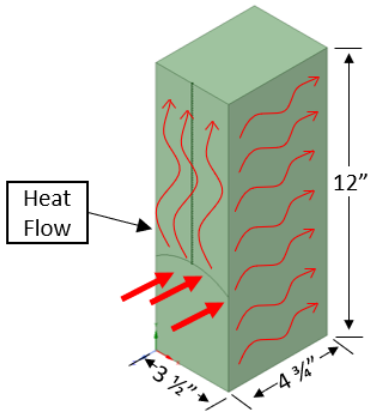

Figure 94. Model geometry

4.2.2.2 Material Properties

To create our ANSYS model, we employed material properties specific to concrete. In this model, we varied the thermal conductivity (k) within a range of 0.75 W/(m°C) to 2 W/(m°C). This variation allowed us to simulate both non-loaded specimens (with lower thermal conductivity) and loaded specimens (with higher thermal conductivity).

Thermal	
Isotropic Thermal Conductivity	2 W/m·°C
Specific Heat Constant Pressure	780 J/kg·°C

Figure 95. ANSYS concrete properties

4.2.2.3 Boundary Conditions

The initial temperature was set to 22°C, which corresponds to the typical ambient temperature of the concrete surface in the laboratory. The analysis consisted of two phases: a 5-minute heating period followed by a 10-minute cooling period, totaling 15 minutes (or 900 seconds). This duration aligns with the tests that will be conducted on the actual specimens in the laboratory.

To visualize the heat source application, we delineated the lamp's outline on the block, as depicted in Figure 96. The blue section represents the region where the heat was applied, while the yellow section corresponds to the area being measured. Additionally, we applied a convection boundary condition on the front face where the heat was expected to propagate through.

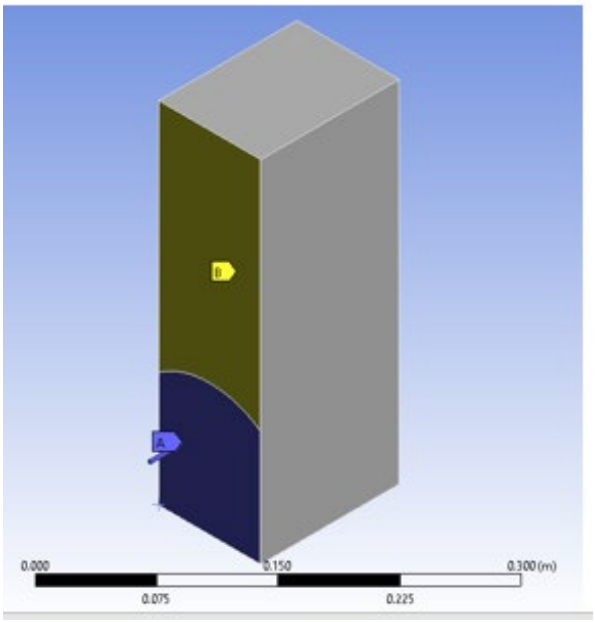

Figure 96. Model geometry & boundary conditions

4.2.2.4 Mesh Reinforcement Study

We conducted a mesh refinement study to determine the optimal mesh size for our analysis. We explored multiple mesh sizes, ranging from 0.003 meters to 0.02 meters. The goal was to identify the coarsest mesh size that could be employed without compromising the accuracy of the analysis.

After conducting numerous tests with various mesh sizes, we settled on a mesh size of 0.01 meters. This choice enabled us to complete the analyses within a reasonable timeframe while still yielding precise and reliable results.

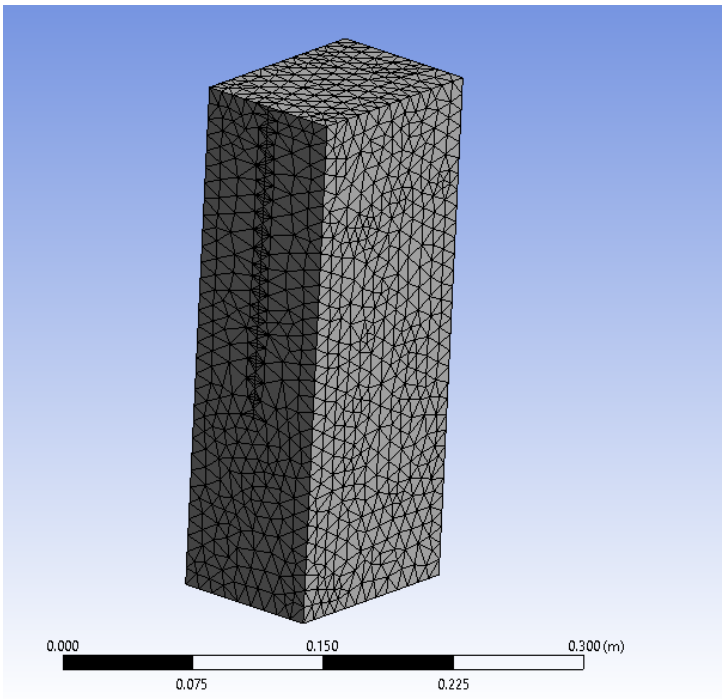

Figure 97.0.01-m Mesh Size

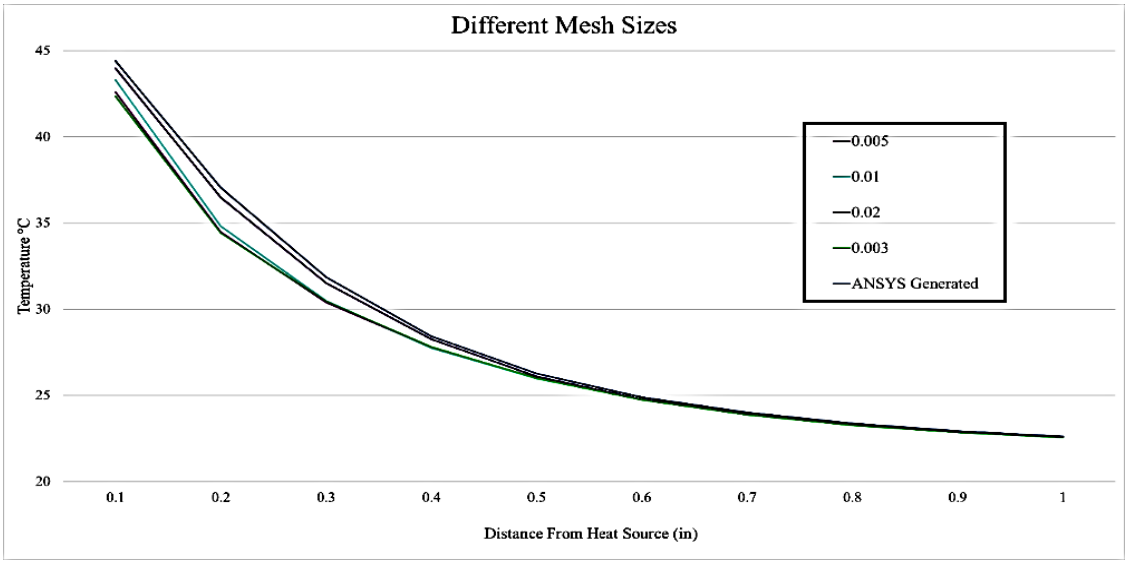

Figure 98. Mesh refinement study – temperature profile at end of heating

4.2.2.5 Results

The same test was conducted twice, varying the thermal conductivity values to 0.75 W/m°C and 2 W/m°C. This choice was made because concrete tends to exhibit higher thermal conductivity under increased stress. Therefore, the thermal conductivity of 0.75 W/m°C simulates conditions with no applied load, while 2 W/m°C simulates the expected conditions when a load is applied. A visual representation of how heat propagates through the concrete under varying thermal conductivity is provided in Figure 99.

The accompanying graph illustrates the temperature at T=5 minutes (at the start of the cooldown period) and compares the results for different thermal conductivity values. As evident in the graph, the initial temperature right next to the heat source consistently registers lower for the k=2 W/m°C test. This implies that loaded tests should exhibit a correlation with these results and experience lower temperatures when compared to the unloaded test. The higher thermal conductivity allows heat to propagate through the specimen more rapidly, resulting in a cooler specimen. Moreover, both tests indicate that the temperature reaches the initial value of 22°C at 2" inches away from the heat source.

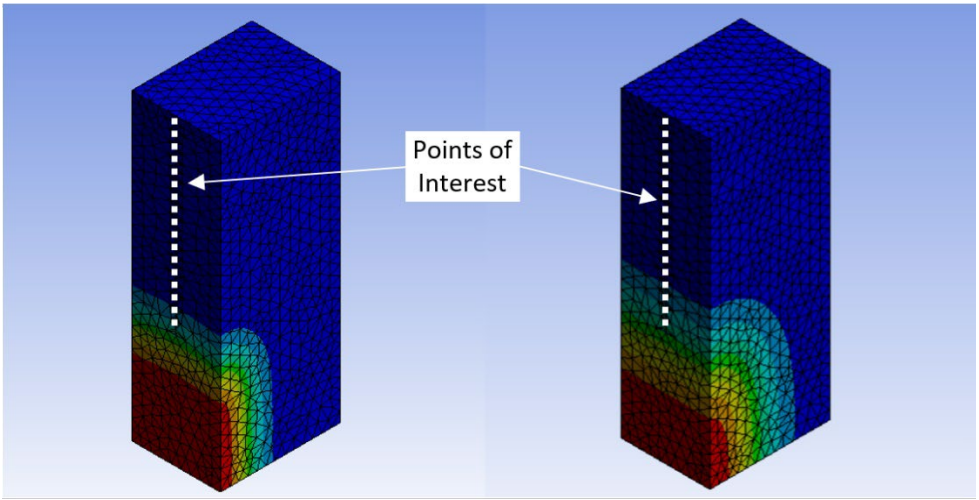

Figure 99. k=0.75 W/m °C (left), k=2 W/m °C (Right)

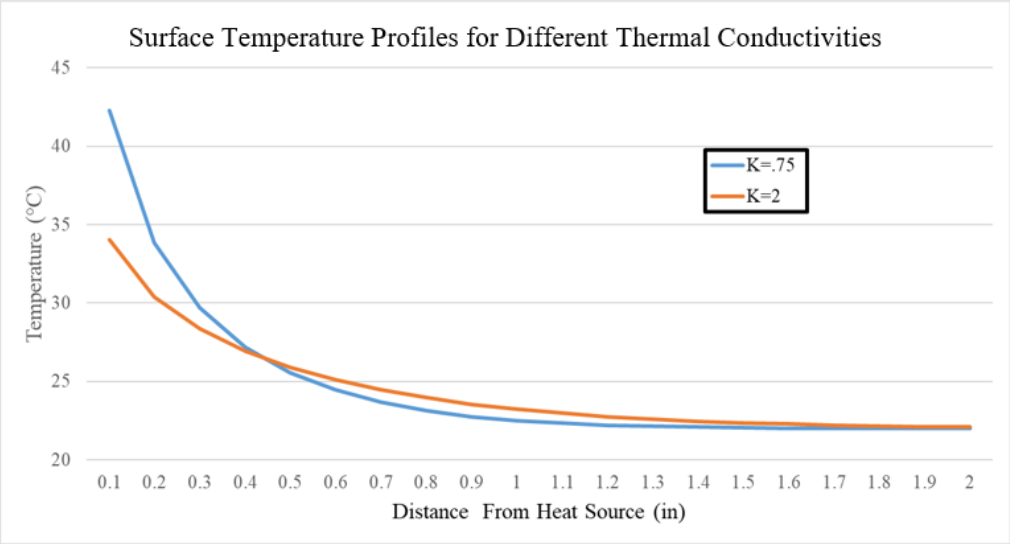

Figure 100. Surface temperature profiles for different thermal conductivities at T=5 min

4.2.3 Experimental Validation

The next phase of our study involved conducting tests on small concrete blocks within the laboratory to validate the findings obtained from the ANSYS model. Our objective was to ascertain if a discernible relationship could be established between thermal conductivity and stress levels in the concrete, as was initially hypothesized.

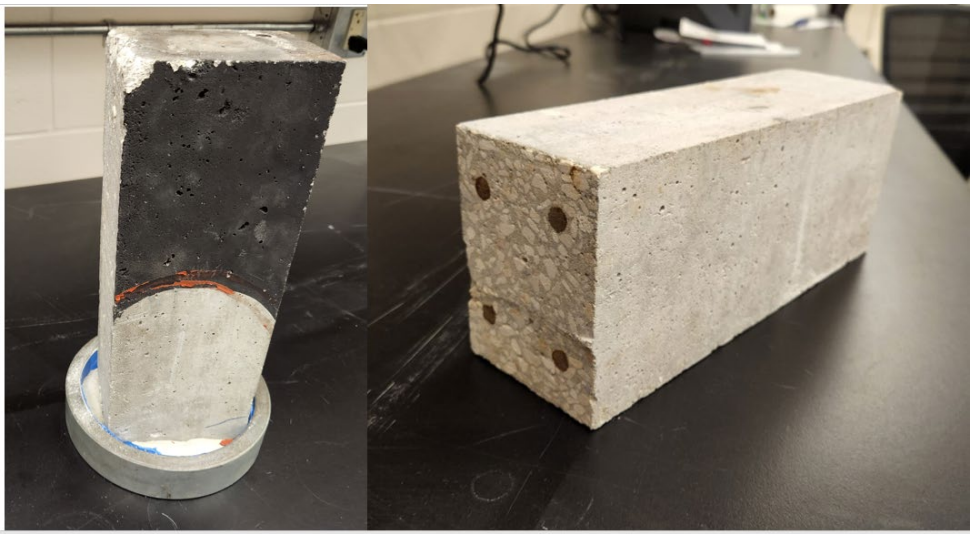

Figure 101. Block that was tested with identical block to show reinforcing

4.2.3.1 Block Geometry

The concrete block subjected to testing is depicted in Figure 102. This block was constructed using QUIKRETE 500-kHz0 concrete mix, which attains a compressive strength of 500-kHz0 psi after 28 days of curing. Additionally, the block incorporates four #3 bars of mild reinforcing steel, and 1/8-inch diameter stirrups spaced at intervals of 1-3/4 inches to simulate transverse reinforcement.

4.2.3.2 Experimental Setup

The testing apparatus utilized in this study includes the Tinius Olsen Super “L” Universal Testing Machine (Model 398 Display & CHM 496 Controller), which applied a consistent load of 15 kips to the specimen during the loaded tests. The heating source employed was a 250-watt heating lamp, while the camera used for capturing thermal images is the FLIR A600-Series Infrared Camera. You can observe the entire setup in Figure 30.

Initially, neoprene pads were positioned on both the top and bottom of the specimen within the testing machine. However, after several tests, it became apparent that these pads were contracting under the applied load, causing movement of the specimen during the loaded tests, and thereby altering the results. To rectify this issue, a rigid non-shrink grout was employed to securely affix the specimen to the base plate. This measure ensured that the specimen remained stationary when the load was applied, preventing any movement between tests.

Additionally, a frame constructed from 80/20 aluminum shapes was used to secure the camera and lamp onto the machine, preventing any unintended movement of these components during testing. To create an effective seal between the lamp and the concrete surface, a high-temperature rubber sealant was applied to shield the surface under study from the heat source.

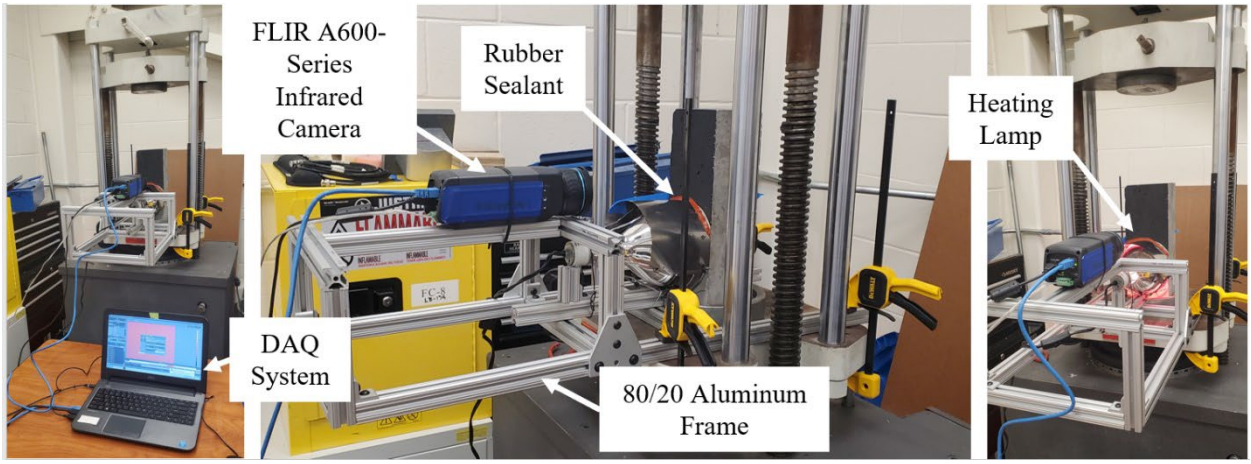

Figure 102. Testing setup

4.2.3.3 Testing Parameters

Like the ANSYS model, we executed a five-minute heating phase where the lamp was activated, followed by a 10-minute cooling period. Multiple runs were conducted to compare the outcomes between loaded and unloaded tests. To ensure the reliability of the data, each test was performed twice. Experiments 1 and 3 had no load applied, while Experiments 2 and 4 involved the application of

a constant 15 kips load during the 15-minute runs. These tests were all conducted on the same specimens, on the same day, with intervals between tests to permit the concrete to cool back down to ambient temperature. This approach helps maintain consistency in the testing conditions.

Table 11. Summary of load levels for thermoelasticity measurements

Exp. 1	No Load
Exp. 2	15 Kips Applied (Concrete Stress = 755 psi)
Exp. 3	No Load
Exp. 4	15 Kips Applied (Concrete Stress = 755 psi)

4.2.3.4 Results

As previously noted, these tests yielded inconsistent results, making it difficult to establish a conclusive correlation between the applied stress and the thermal conductivity of the concrete. Figure 103 presents the results for Experiments 1 and 2. The different lines represent the high and low temperatures during the 10-minute cooldown period. The pink and red lines correspond to T=5 minutes, while the blue and yellow lines represent T=15 minutes. Notably, both experiments exhibited very similar temperature profiles that did not appear to be affected by the load level.

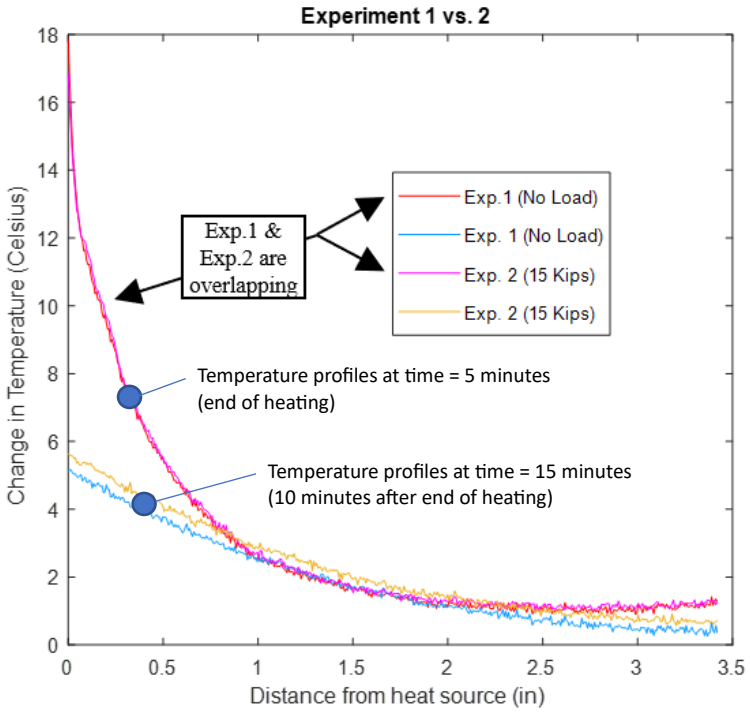

Figure 103. Experiment 1 and 2

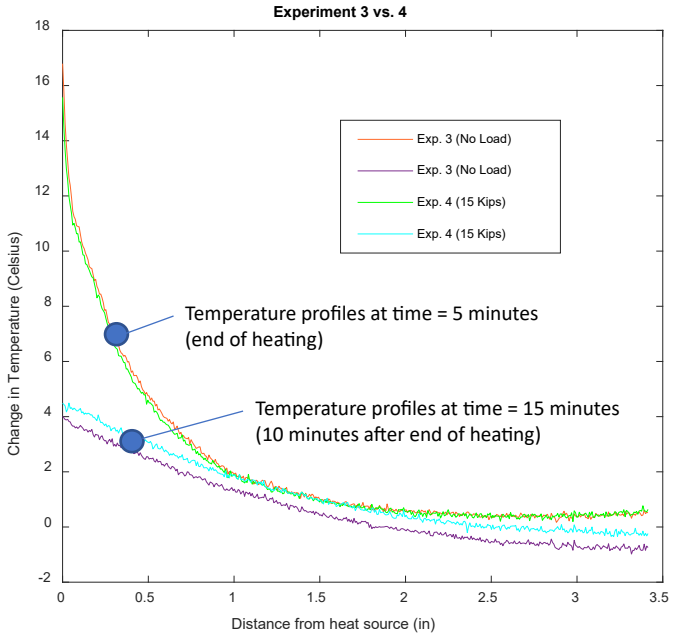

Figure 104. Experiment 3 and 4

4.3 Diffuse Ultrasound

4.3.1 Instrumentation for Ultrasound

The setups for both diffuse ultrasound and coda-wave interferometry testing share similarities in equipment used. This section will provide a detailed discussion of the equipment used for data collection, along with the respective equipment settings. Our testing involved multiple trials to explore various bonding methods for the transducers. Due to the porous nature of concrete, establishing a mechanical connection between the two sets of transducers posed challenges. These bonding issues are discussed in the transducer bonding section of this chapter.

The testing setups were primarily developed based on the testing plan outlined Ahn et al.[61]. However, modifications were introduced, including the incorporation of an extra set of transducers for coda-wave interferometry and adjustments to the amplification levels for both pre- and post-amplifications for both emitting and receiving transducers in each type of test. To provide a clearer overview, a flow chart and a detailed list of the equipment used are presented in Figure 105.

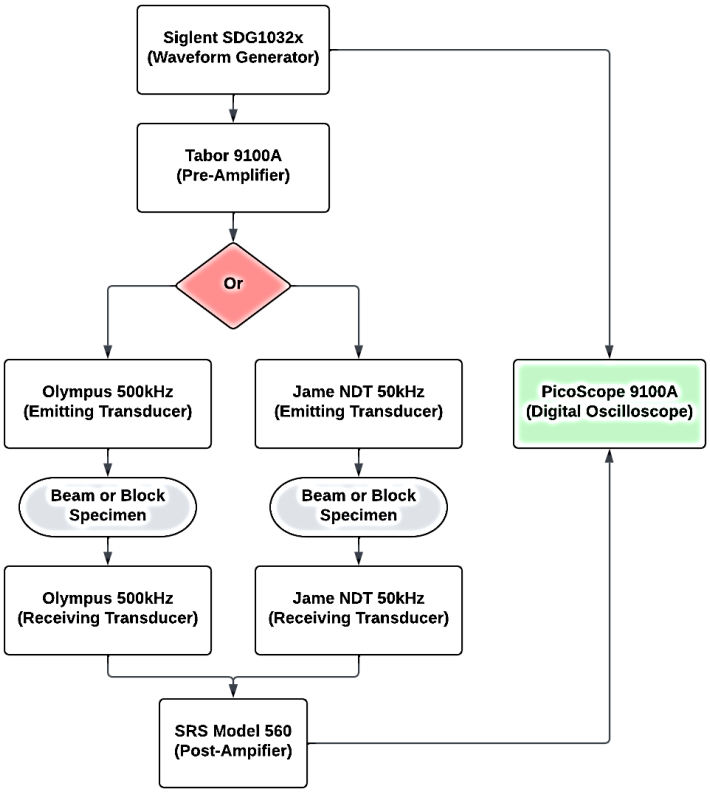

Figure 105. Experimental test equipment flowchart

4.3.1.1 Waveform Generator

The Siglent SDG1032x was chosen due to its output maximum of 20 volts peak to peak and the variety of waveforms preloaded on the device. For the two tests, diffuse ultrasound analysis and coda wave interferometry, a square pulse was utilized, which was repeated 50 times at a frequency of 50hz. The individual square pulses had a pulse width of 2.5 microseconds with an amplitude between 2 and 3.5 volts depending on the specimen. Another benefit of this device is its ability to output square waves in groups to assist with averaging over 50 test samples per data set.

4.3.1.2 Pre-Amplifier

We selected the Tabor Electronics 9100A as the pre-amplifier for these experiments. It amplifies the input square wave, boosting it up to 400 volts from peak to peak, depending on the input waveform's amplitude. The output from this device was fed directly into the excitation transducer. This amplifier was necessary because the two chosen transducers required high activation voltages. The Tabor Electronics 9100A takes the input square wave and elevates the peak voltage to an average of 150 volts, which is sufficient to activate both the 50 and 500-kHz transducers used for coda-wave interferometry and diffuse ultrasound. Importantly, it maintains the fidelity of the waveform generator's square pulse throughout the amplification process.

4.3.1.3 Transducers

1. Olympus 500-kHz: The Olympus 500-kHz transducer was chosen for its ability to generate the high-frequency signal necessary for interacting with the concrete aggregate, enabling the detection of microcracking within the concrete's microstructure.
2. James NDT 50-kHz: We selected the James NDT transducer for coda-wave interferometry testing because of its 50-kHz frequency and high-power output. These characteristics ensure consistent and reliable results when evaluating stress levels using the coda-wave method.

4.3.1.4 Post-Amplifier – Stanford Research Systems Model 560

The SRS Model 560 amplifier was used as the post-amplifier, allowing for the Pico scope to receive the signal from the receiving transducer. The device has a variable, low noise amplification, which ranges from 1 to 500-kHz0 times amplification, along with a high-pass filter, further reducing signal noise. Low signal noise is vital when using such high frequencies in a non-homogeneous material such as concrete. The variable amplification provided by the Model 560 allowed for the received signal to be fine-tuned for greater signal homogeneity between specimen types.

4.3.1.5 Digital Oscilloscope – PicoScope 4000A

The digital oscilloscope utilized for these experiments is the PicoScope 4000A, an 8-channel oscilloscope with a maximum acquisition rate of 80 mega-samples per second. The primary reason for selecting this device is its high capture rate, which is crucial given the frequency range of the transducers used (50 to 500-kHz). Additionally, this oscilloscope offers useful software features that facilitate the data collection during the loading and unloading of test specimens. Particularly relevant to the ultrasound experiments are the math channel and trigger features. The math channels provided by the PicoScope software enabled waveform averaging prior to saving each file, which significantly enhances efficiency. The trigger feature allowed us to capture the returned waveform by using the initial pulse from the waveform generator as an initial flag, which was routed into the oscilloscope, resulting in the capture of the received signal.

4.3.2 Transducer Bonding and Placement

A primary concern discovered during the early testing stages was the transducers' placement and how they should be bonded to the surface of the concrete specimens. In the Ahn study, the transducer could be placed anywhere between 90mm and 120mm (Ahn, Myoungsu, Popovics, & Weaver, 2019). However, the optimal transducer distance can vary from sample to sample and depends on the amount of energy supplied to the transducer. As for the bonding of the transducers to the concrete surface, there are many methodologies, ranging from traditional ultrasonic couplant to cyanoacrylate glue, as used by Ahn. Both variables must be kept constant and should be selected to maximize the energy transfer from the transducer through the medium and back to the transducer.

Testing to isolate and identify these variables was performed on a 2-inch-thick slab of unreinforced concrete with no loading applied and a reinforced beam segment that was subjected to direct compression loading. The method employed to grade the effectiveness of each bonding method and

placement distance was to maximize the received waveform amplitude, while maintaining signal fidelity, and minimizing the required amplification.

4.3.2.1 Transducer Bonding

The bonding of the transducers to the surface of the concrete specimens has two metrics for success: how well the method can mechanically couple the transducer to the specimen and how well the method can fill surface voids to prevent unwanted signal variations. The transducers need to be mechanically coupled with the specimen to allow for proper excitation of the specimen. This will minimize the need for post-amplification of the signal and provide higher fidelity. The bonding method must also be able to support the self-weight of the transducer while still providing electromechanical coupling.

The bonding methods outlined in this section can be separated into assisted and unassisted bonding methods. The assisted bonding mediums are non-hardening and therefore require the use of an external mounting mechanism to hold the transducer to the surface of the specimen. These coupling methods are ultrasonic gel couplant and petroleum jelly. The unassisted bonding methods are hardening and therefore do not require an external apparatus to affix the transducers to the specimen. These bonding methods are paraffin wax, thickened cyanoacrylate glue, and quick-set epoxy.

4.3.2.1.1 Ultrasonic Gel Couplant

Ultrasonic gel couplant is the most traditional method of coupling transducers to specimens, as it provides excellent void filling. However, it is primarily used in circumstances where the surface of the material being examined is smooth and non-porous. Throughout the testing of this coupling method, one problem remained constant. Concrete, a porous material, constantly leached the water content out of the gel couplant, reducing its effectiveness in transferring ultrasound into the concrete specimen. As the testing planned later in the experimental procedure called for long periods of continuous load testing, this factor alone eliminated this couplant type from consideration.

It should be noted that the gel couplant performed very well immediately after it was applied. The couplant also provided excellent signal fidelity and did not require post-amplification. The signal quality did vary depending on how firmly the transducer was pressed into the surface of the specimen with external pressure from the fixture shown in Figure 107.

Figure 106 shows how the amplitude and signal quality drastically decreases after the couplant is left to sit and then retested after 30 minutes. This test was performed with 500-kHz transducers placed two inches apart with a post-amplification of 100 times.

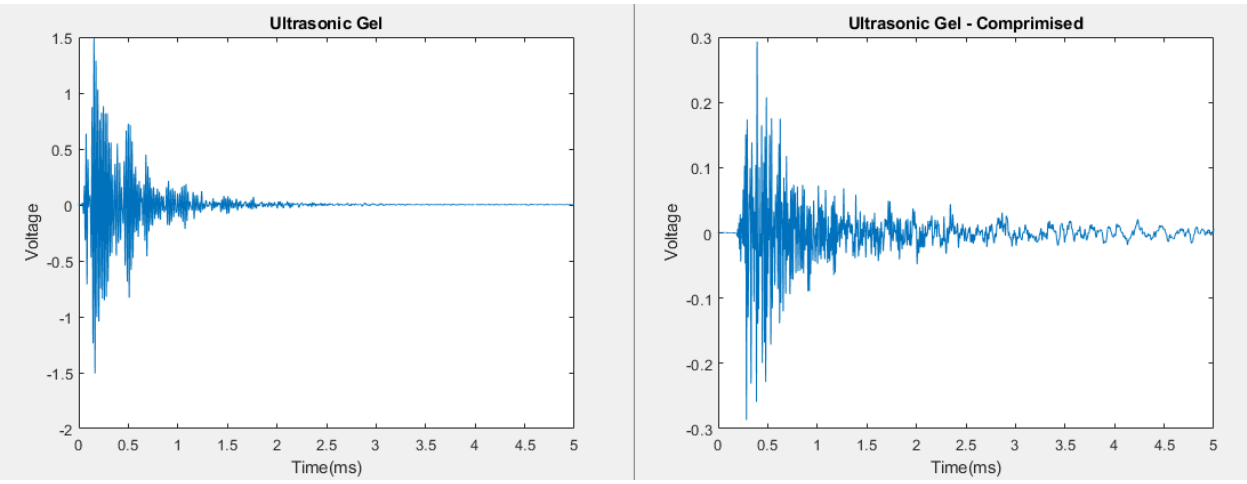

Figure 106. 500-kHz transducer test 30 minutes apart with ultrasonic gel couplant

The testing with this couplant led to the understanding that a non-water-based couplant would be necessary for ultrasound testing on concrete due to its porous and water leeching tendencies.

4.3.2.1.2 Petroleum Jelly

Figure 107. Test setup for compressive loading with fixture-assisted mounting for UT transducers.

Based on the understanding that a non-water-based couplant must be employed for ultrasound testing on concrete, the next step was an oil-based couplant. Petroleum jelly (PJ) was chosen for this application due to its ease of procurement, its inert characteristics, and its similar viscosity to the ultrasonic couplant. Since PJ is a non-hardening bonding solution, an external mount was required to

attach the transducers to the surface of the concrete samples. This apparatus was designed using 3-D solid-modeling software and fabricated using a 3-D printer (Figure 36).

Petroleum jelly has a much longer working time and is suitable for the long-term testing of the small-scale beam. As for effectiveness, in terms of surface void filling and signal quality, the petroleum jelly is on par with freshly applied ultrasonic gel couplant. Figure 37 shows the positive region of two received waveforms using 50-kHz transducers with 5x amplification, with the test spaced 24 hours apart. The orange line is the initial test, and the blue line is the second test.

The only drawback to testing with petroleum jelly couplant is the lack of self-adhesion to the surface of the specimen. Petroleum jelly requires significant prep work before the transducers can be placed on the surface of the concrete, and the feasibility of this method is entirely dependent on the time available and the willingness to affix the mount to the sample permanently.

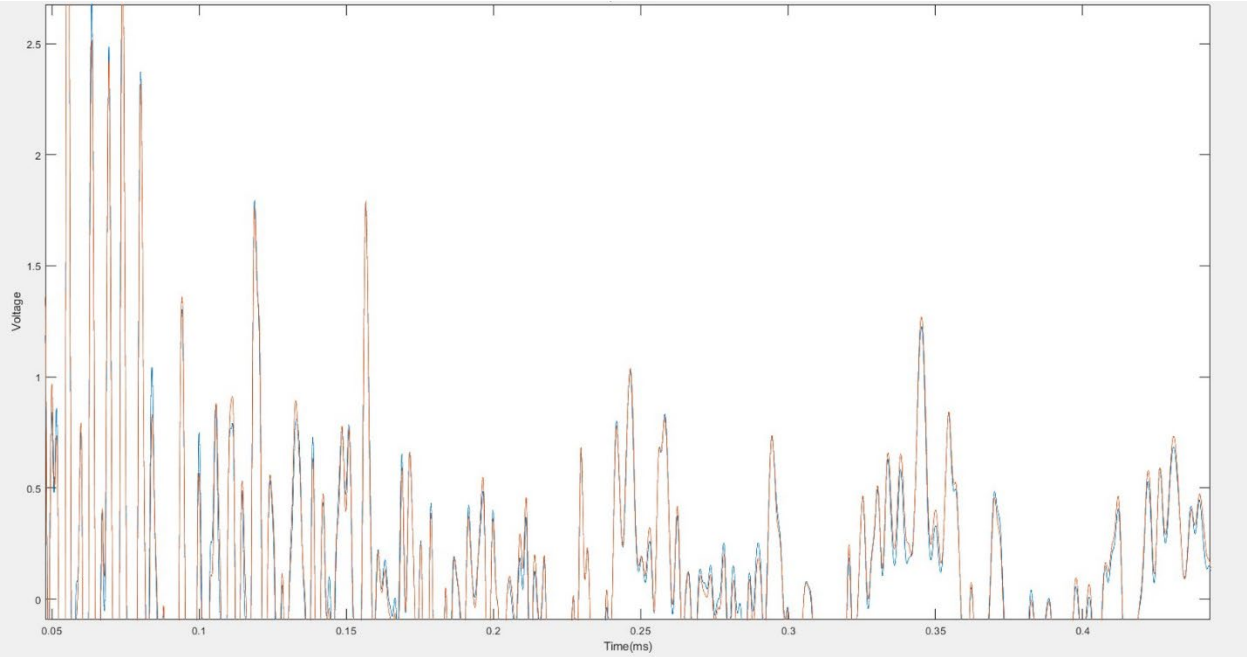

Figure 108. Waveform of 24-hour endurance test for petroleum jelly couplant

4.3.2.1.3 Paraffin Wax

In the bonding experiments, the next phase involved testing couplants that can harden, eliminating the need for external support to secure the transducers to the specimen. Paraffin wax was considered as it falls between non-hardening methods and more aggressive adhesives in terms of bonding strength. The advantage of using paraffin wax is that it can be softened by applying heat, making it relatively easy to remove the transducers after they are attached.

However, using paraffin wax on concrete presented some challenges. First, the wax needs to be heated to 140 degrees Fahrenheit, which is close to the upper limit of temperatures that can potentially damage concrete. Additionally, the rapid solidification of the wax upon contact with the concrete, due to the specimen's large thermal mass, resulted in a limited working time. Furthermore, the mechanical coupling and signal quality with this bonding method proved to be problematic. Paraffin wax was

difficult to work with and often resulted in significant air voids between the transducer and the specimen. Combined with lackluster results from testing, these issues led to the exclusion of this bonding method from further experimentation.

4.3.2.1.4 Thickened Cyanoacrylate Glue

A thickened cyanoacrylate glue was chosen as the next medium to evaluate in the unassisted bonding method category. Advantages of this medium include a 15-minute working time and an ability to be de-bonded using acetone. The concrete surface needed to be smoothed using sanding disks for proper adhesion with the thickened super glue. Without proper sanding, the pits in the concrete surface would not be filled by the couplant, and the waveform would not be effectively transmitted into the specimen.

A major limitation of cyanoacrylate was discovered during compressive load testing. The hardened couplant was too brittle to withstand the imposed deformations from the axial loading. In some cases, this resulted in incoherent signals once the couplant failed. In other cases, the transducers completely debonded from the concrete surface. After these deficiencies were realized, cyanoacrylate was removed from consideration.

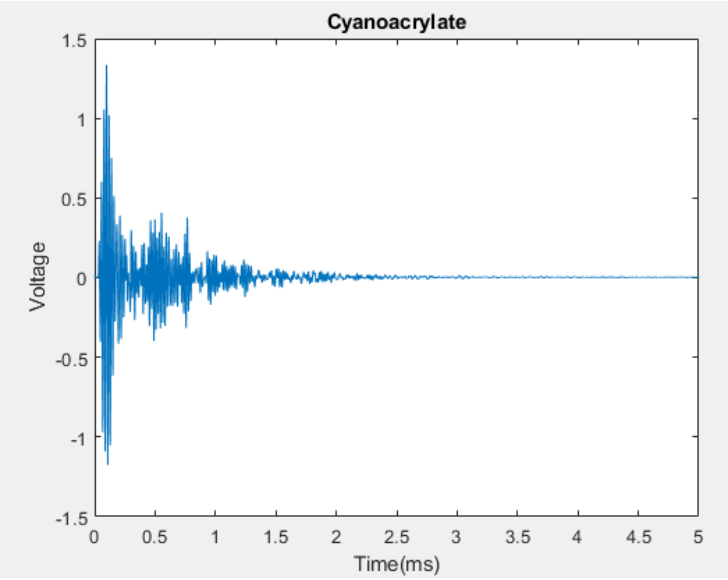

Figure 109. Waveform from cyanoacrylate test

4.3.2.1.5 Quick Set Epoxy

To address the challenges encountered with the thickened cyanoacrylate glue during bonding experiments, a standard quick-set epoxy was chosen as an alternative. Initially, epoxy was not the preferred option when considering the mechanical coupling of transducers to concrete because epoxy forms a permanent bond. A substantial force is required to break this bond and remove the transducers from the specimen's surface. In the bonding tests, a piece of wood and a mallet were used to shear the transducers off the sample's face when testing was completed.

However, the quick-set epoxy proved to be highly effective in securely holding the transducers to the concrete surface with no debonding issues. The signal fidelity during testing with epoxy was excellent, requiring minimal amplification for both the 50- and 500-kHz transducers. This bonding method consistently yielded results during load testing and did not deteriorate over time, unlike some other coupling methods. Therefore, this method was selected for testing the small-scale beam specimens.

4.3.2.2 Transducer Placement

Placement of the transducers has important effects on the resulting waveform received for processing. The further away the transducers are from each other, the less energy is directly received, but in trade, there is more scattering, resulting in more apparent feature characterization. The initial placement of the transducers came from the Ahn study, which described 90mm to 120mm between transducers (Ahn, Myoungsu, Popovics, & Weaver, 2019). However, some studies, such as the one by Deroo, recommend a planar distance of as little as 46mm between transducers (Deroo, Kim, Qu, Sabra, & Jacobs, 2010). The Zhang study proposed placing the transducers across from each other on the sample (Zhang, et al., 2012). The Larose study further endorsed the cross method where transducers were placed across from one another for CWI testing (Larose & Hall, 2009)

As for the diffuse ultrasound setup using the 500-kHz transducers, a cross method is being implemented due to the experimental success found in these preliminary experiments, along with the prior endorsement by both the Zhang and Larose studies.

For the coda-wave interferometry testing, a planar approach will be taken. Though the two studies by Ahn and Deroo use small distances between their transducers, the experiments on the small-scale specimens in this study will be spaced at 4 inches from the center. The larger spacing is because the transducers used in these experiments are higher energy and can be placed further from one another without a penalty to the received signals. The increased spacing promotes flexibility while testing small-scale beams, mainly allowing the placement of transducers on either side of the loading head in the 3-point loading test.

4.3.3 Data Processing

Two separate algorithms exist for processing the diffuse ultrasound and coda-wave interferometry. Both algorithms were implemented in MATLAB and function independently. The process and background for creating these algorithms are described in sections 2.3.3.1 and 2.3.3.2.

Each time the transducers are fired, 50 samples will be collected and averaged, resulting in a single waveform with decreased noise. The waveforms will be averaged before being passed into the algorithms for additional processing.

4.3.3.1 Diffuse Ultrasound

The goal of the data processing for the diffuse ultrasound method is to isolate the diffusivity and dissipation coefficients for each dataset. The coefficients from tests at differing points can provide insight into the state of microcracking in the samples. An increase in microcracking can indicate that the PT system is not maintaining the required level of compressive stress in the concrete.

4.3.3.1.1 First Iteration

The inspiration for the first method employed to find the coefficients of diffusion and dispersion came from the Ahn study. This processing technique is in the flowchart shown in 3, which consists of a time-frequency analysis of the data.

$$\log\langle E(x,y,z,t)\rangle = C_0 - \frac{3}{2}\log(Dt) - \frac{d^2}{4Dt} - \sigma t \tag{3}$$

The first step after averaging the data set is to perform a fast Fourier transform on the data. The Fourier transform changes the data from a time domain to a frequency domain. From here, the program will apply a Hanning window to the transformed data set to isolate three frequency windows, 200-300kHz, 300-400kHz, and 400-500-kHz. The program then uses an inverse Fourier transform on the windowed signals in the frequency domain to bring them back to a time domain. Then windowed signals back in the time domain are converted to their absolute value and squared; the absolute value and squaring results in a plot of the ultrasounds energy density with respect to time. The algorithm then takes the logarithmic form of the energy density dataset per windowed section. The logarithmic form of the energy density of each frequency window is then curve fit to the diffuse ultrasound equation in Equation 5. The curve fitting provides solutions for the coefficients of dissipation and diffusivity, allowing for the characterization of microcracking in the test sample.

The first iteration of the diffuse ultrasound processing algorithm provided inconsistent data when comparing the energy density of the frequency windows. Instead of the energy density of the windowed frequency ranges following a decreasing energy density trend as the frequency increased, the energy density stayed similar across all frequency windows. Figure 110 shows the overlap of the energy density per windowed section.

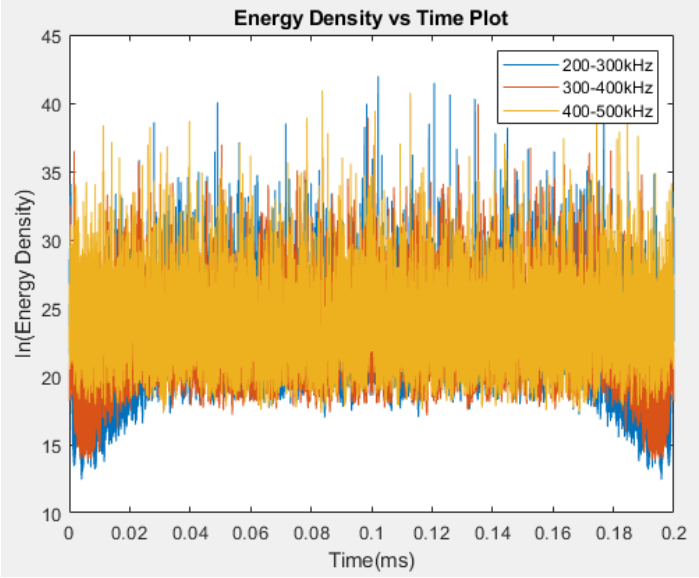

Figure 110. Diffuse ultrasound algorithm first iteration energy density vs. time

The most likely culprit of the non-distinct frequency bands is that the Fourier transform was being applied to the whole signal simultaneously. The second iteration of this program with a varied approach to using the Fourier transform was necessary.

4.3.3.1.2 Second Iteration

To calculate the coefficients of diffusivity and dissipation and to curve fit the equation, the algorithm divides the averaged signal received from testing into time intervals of 50 microseconds with 90% overlapping the previous interval. The program takes the integral of the time intervals over the frequency bandwidth of interest, in this case, 500-kHz. The energy density of each time interval is associated with the instant of time at the center of the interval. The algorithm then plots the values of energy density with respect to time. Curve fitting of the diffuse ultrasound equation to this plot will find the coefficient for both dissipation and diffusivity. The two coefficients will identify trends in microcracking of the specimens during testing.

This algorithm has proven to work effectively in finding both coefficients of interest. Therefore, the small-scale testing with direct compression and 3-point beam load testing will use this version.

4.3.3.2 Coda Wave Interferometry

The algorithm for identifying the time lag of concurrent datasets to perform CWI is a more straightforward process than that of diffuse ultrasound. The first iteration of this algorithm worked as planned and therefore did not need a revision.

The algorithm begins by processing a series of files related to one cyclical loading test conducted on small-scale specimens. These files are organized in chronological order, and the algorithm identifies a time interval that corresponds to the waveform area with the clearest delay between wave arrivals, linking it to its associated load.

Next, the program employs a cross-correlation function, like the one outlined in Equation 3, to correlate each incremental load increase and eventual decrease with the initial zero-load reading. The algorithm then calculates the percentage change in wave velocity, which serves as an indicator of concrete stress level. The resulting plot, showing the relative velocity change against the corresponding load values, reveals a trend of increasing time lag (lower velocity) when the sample is under tension and decreasing time lag (higher velocity) when the sample is under compression (Gondim and Haach [62]).

Initial testing of this algorithm has demonstrated linear relationships between tension-induced increases and time lag, as expected. Notable features, such as abrupt shifts in time lag when cracking or yielding occurs, also align with predictions. Given the success of this CWI algorithm in preliminary testing, it will be used in further experiments on small-scale specimens in this study.

4.3.3.3 Test Specimens

The experiments in this study began with the fabrication of three specimens designed for testing and verifying the diffuse ultrasound and coda-wave interferometry methods. These testing approaches will encompass direct compression testing, 3-point bending of a simply reinforced beam, and 3-point bending of a post-tensioned beam with plain reinforcing. The basic geometry for all small-scale beams is provided in Figure 111.

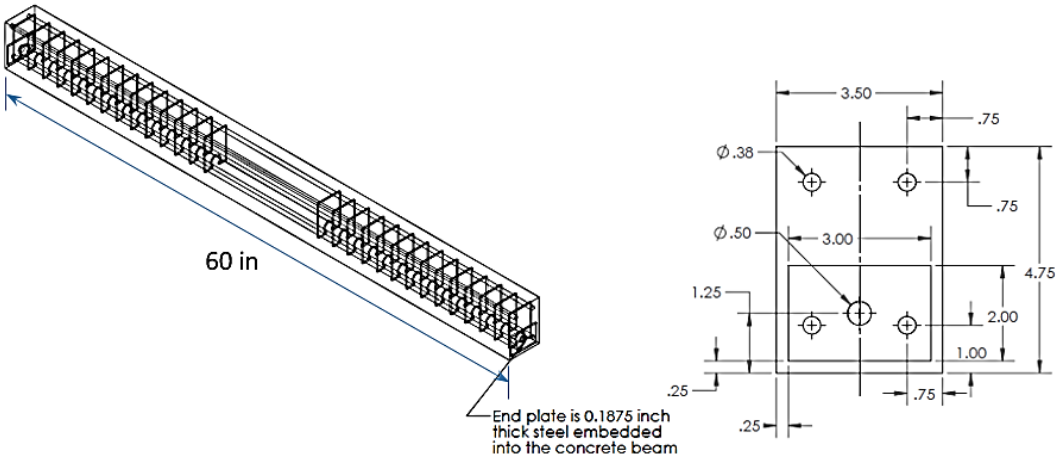

Figure 111. Geometry for small-scale beams

Direct-Compression Testing: This test will involve a 12-inch cut section from a 5-foot beam, identical to the one used in the subsequent 3-point load testing. A Tinus and Olsen universal testing machine will apply loading to the cut section, which is oriented vertically. The 50-kHz transducers will be affixed using the petroleum jelly bonding method, mounted externally in a planar configuration with a 4-inch separation, while the 500-kHz transducers will be positioned in a cross configuration across the center of the beam.

3-Point Bending (Normally Reinforced Beam): This test will be conducted on a 5-foot-long beam with a cross-section measuring 4.75x3.5 inches. The beam's reinforcement will consist of four #3 bars and shear reinforcement through 14 eight-inch stirrups spaced at 1.75-inch intervals on each side of the beam. The 50-kHz and 500-kHz transducers will be attached using epoxy bonding. The 50-kHz transducers will be centered on the beam with a 4-inch spacing, while the 500-kHz transducers will be arranged in a cross configuration at the beam's central point. The apparatus for this test will include a Tinus and Olsen universal testing machine and a 3-point load testing frame (Figure 112).

3-Point Bending (Post-Tensioned Beam): The post-tensioned 3-point load testing also utilized a 5-foot-long beam with a cross-section measuring 4.75 x 3.5 inches. The beam reinforcement included four #3 bars and shear reinforcement provided by 14 eight-inch stirrups spaced at 1.75-inch intervals on each side of the beam. Additionally, a 3/8 inch threaded rod was incorporated for post-tensioning. The post-tensioning force was applied by tightening two nuts on either end of the beam, and the load was measured using a load cell situated between the metal plate on the beam's end and the tensioning nut.

The tranducers were attached to the beam using two-part epoxy. The 50-kHz transducers were positioned at the beam's center with a 4-inch spacing, while the 500-kHz transducers were arranged in a cross configuration at the beam's central point.

Figure 112. 3-point load testing frame and the Tinius and Olsen universal testing machine.

4.3.4 Experimental Testing

The small-scale testing for all specimens was performed using a Tinius Olsen universal testing machine to apply load. The data were captured from the transducers using the PicoScope software packaged with the digital oscilloscope. Each small-scale specimen was broken into testing groups by specimen type and test type; these testing groups were further broken down into loading cycles. The naming convention for each test followed the format of (Testing Group).(Loading Cycle).

4.3.4.1 Beam-Blocks

Testing for the beam blocks involved data collection for the diffuse ultrasound and coda-wave interferometry methods. Both transducer sets were attached to the beam blocks using an external mounting bracket with petroleum jelly as the coupling medium. The 50-kHz transducers were affixed to the 4.75-inch-wide face of the blocks in a planar configuration at a distance of four inches. The 500-kHz transducers were placed across the thin distance of the block at the bottom of the beam.

The load testing procedure involved two loading cycles of interest, one with the 50 kHz transducers and one test with the 500-kHz transducers. These direct compression tests, performed in the Tinus and Olsen machine, applied force to the specimen in 1,500-kHz-pound increments; at each increment, a transducer pulse was fired, and a set of data was collected until a peak loading of 15,000 pounds was reached. At this point, the sample was unloaded at increments of 3,000 pounds; again, a transducer pulse was fired, and data were collected at each increment until 0 pounds of force was applied to the sample. This exact procedure was followed for each of the two tests, one 50-kHz test followed by a 500-kHz transducer test. These tests are labeled as 1.1 and 1.2; the first number relates to the testing group, and the second is the test's time-correlated place in the group. The specific settings used with the equipment are provided in Table 12, and an image of the testing setup is provided in Figure 113.

Figure 113. Testing setup for small-scale block testing

Table 12 Parameters for 50-kHz and 500- kHz testing on block specimens

Parameters	50 kHz Test (1.1)	500-kHz Test (1.2)
Unamplified Pulse Amplitude (V)	3	2.5
Pulse Width (µs)	2.5	1
Post-Amplification	1	100
Number of Pulses	50	50
Frequency of Pulses (Hz)	50	50
Sampling Rate (MS/s)	10	10

4.3.4.2 Beams

The scale-beam testing applied the same principles as block testing. The specimen is loaded and unloaded in increments with transducer pulses, and data is collected at each point. For the scale beams, the transducers, both 50 and 500-kHz, were epoxied directly to the face of the beam. The loading increments for each beam and loading cycle varied from test to test, though the parameters for the recording equipment stayed mostly steady across all trials. The testing was completed using the Tinus and Olsen machine and a 3-point load testing frame. The frame consisted of a steel beam with metal rollers on each end corresponding to the end of the small-scale concrete beams and a rounded loading head at the center point of the beam.

4.3.4.2.1 Simply Reinforced

Testing on the small-scale simply reinforced beam involved diffuse ultrasound and coda-wave interferometry methods with one diffuse ultrasound test and three coda-wave interferometry tests for a total of 4 tests. The 50-kHz transducers were centered on the bottom of the beam with 4-inches of center-to-center spacing. The 500-kHz transducers were placed at the bottom center of the beams' sidewall. As stated previously, all transducers were epoxied directly to the surface of the beam. The setting used on the data collection equipment for the load testing can be found in Table 2.

Table 13 Data collection parameters for simply-reinforced beam loading test.

Parameters	50 kHz Test (2.1)	500-kHz Test (2.2)	50-kHz Tests (2.3, 2.4)
Unamplified Pulse Amplitude (V)	3	2.5	3
Pulse Width (μs)	2.5	1	2.5
Post-Amplification	5	100	1
Number of Pulses	50	50	50
Frequency of Pulses (Hz)	50	50	50
Sampling Rate (MS/s)	10	10	10

Load test 2.1 involved 50-kHz transducers and a loading increment of 50 pounds until 350 pounds and unloading at 50-pound increments until 0 pounds; this loading cycle was performed twice. Load test 2.2, involving the 500-kHz transducers, followed the same loading cycle as test one. Load test 2.3 aimed to bring the beam to a state of cracking and followed a loading increment of 100 pounds until 400 pounds, then an increment of 50 pounds until 3,000 pounds; the unloading process involved 200-pound increments until the beam was completely unloaded. Load test 2.4 aimed to load the beam until yielding; therefore, the increment of loading was 100 pounds until 3,100 pounds, then 50 pounds until 3,350 pounds; the unloading of the beam followed in increments of 100 pounds until fully unloaded. For tests 3 and 4, displacement data for the loading cycles was also taken to correlate later to the coda-wave interferometry data.

4.3.4.2.2 Post Tensioned

Testing for the small-scale post-tensioned beam occurred in two portions, tensioning of the beam and 3-point load testing. For both test modes, the transducers, both 50 and 500-kHz, were coupled to the surface of the beam using epoxy. The placement of the transducer was identical to the plain reinforced beam and is as follows. The 50-kHz transducers were centered on the bottom of the beam at 4-inches from the center. The 500-kHz transducers were placed at the bottom center of the beams' sidewall. The 3-point testing was completed using the Tinus and Olsen machine and a 3-point load testing frame. The frame consisted of a steel beam with metal rollers on each end corresponding to the end of the small-scale concrete beams and a rounded loading head at the center point of the beam.

The post-tensioning for this small-scale beam was accomplished by tightening a threaded rod placed through the center of the beam. The tensioning cycle was measured using a force cell placed on the threaded rod (Figure 42), which was connected to a multimeter for tension readings.

Figure 114. Load cell used for post-tensioning measurements on small-scale beam

The loading cycle 3.1 tensioned the rod in increments of 1000 pounds from zero to 7000 pounds and then de-tensioned to 1000 pounds, then increased tensioning to 8000 pounds in 1000-pound increments. For each increment of the tensioning cycle, the 50-kHz transducers were used to collect data for coda-wave interferometry testing. The data collection equipment settings can be seen in Table 14.

Table 14 Parameters for data collection for small-scale tensioning tests.

Parameters	**50 kHz Tensioning Tests (3.1)**
Unamplified Pulse Amplitude (V)	2
Pulse Width (µs)	2.5
Post-Amplification	5
Number of Pulses	50
Frequency of Pulses (Hz)	50
Sampling Rate (MS/s)	10

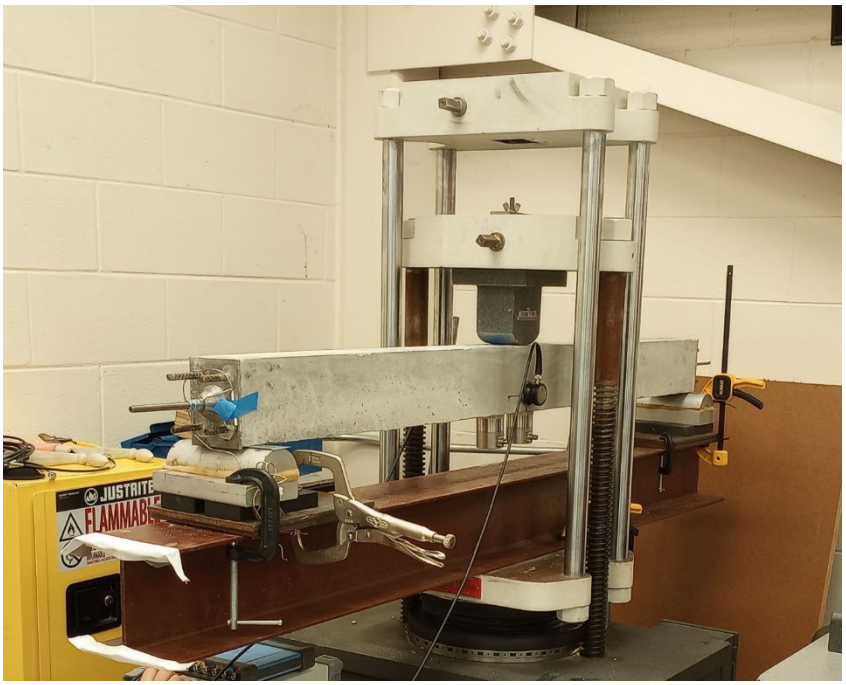

Figure 115. 3-point load testing setup for the PT-scale-beam

For the 3-point load testing of the PT-beam, a total of 5 trials were performed, 4 with the 50-kHz transducers and 1 with the 500-kHz transducers. The first test, 4.1, was conducted with the 50-kHz transducers; the loading was applied and then unapplied at increments of 50 pounds from 0 to a maximum of 350 back down to 0 pounds. The second test, 4.2, was conducted with the 500-kHz transducers; the loading was applied and then unapplied at increments of 50 pounds from 0 to a maximum of 350 back down to 0 pounds. The third test, 4.3, utilized the 50-kHz transducers; the loading increment for the test was 50 pounds from 0 to 350 back to 0 pounds. Test 4.4 used loading increments of 100 pounds up to a maximum of 1200 pounds, then increments of 200 pounds down to 0 pounds of force. At this point, one of the coils inside the main pre-amplifier burnt out, and a similar replacement was sourced to conduct the final two tests. The replacement pre-amplifier was calibrated to mimic the original device's amplification perfectly. The fifth test, 4.5, aimed to bring the beam to a state of cracking; therefore, the loading reached a maximum of 2,200 pounds at an increment of 100 pounds; the beam was then unloaded at an increment of 200 pounds until it was completely unloaded. For all tests on the PT-beam displacement, measurements were taken simultaneously with the test. Figure 115 provides an image of the beam setup, and Table 15 will give the parameters used in the data collection equipment for all tests.

Table 15 Data collection parameters for load testing the small-scale PT-Beam

Parameters	50 kHz Tests (4.1, 4.3, 4.4, 4.5)	500-kHz Test (4.2)
Unamplified Pulse Amplitude (V)	2.5	2.5
Pulse Width (μs)	2.5	2.5
Post-Amplification	5	20
Number of Pulses	50	50
Frequency of Pulses (Hz)	50	50
Sampling Rate (MS/s)	10	10

4.3.5 Results

4.3.5.1 Coda-Wave Interferometry

The outcomes being sought for Coda-wave interferometry for the NDE of PT flexible filler systems is an indirect evaluation of the health of the post-tensioning system. For CWI, this means having damage feature recognition from the stress level and, therefore, the phase shift of waves being passed through the specimen. These features can either be the identification of substantial cracking or yielding of the materials in the flexible filler system. The specimens used for these tests and testing procedures are outlined in detail in Section 2.3.4 of this document.

4.3.5.1.1 Block Testing

The beam block specimens' testing will show the general feasibility and efficacy of the CWI testing setup for identifying damage features relevant to flexible filler PT systems. The CWI algorithm would identify the features via the relative velocity change plots generated and would take the form of deviations in the slope or shape of the plots.

The importance of Test 1.1 is the movement of the relative velocity change in the negative direction during direct compression loading, the consistent slope change with progressive loading, and the clear differentiation between the starting and ending points of the loading cycle. The velocity variation is expected to move in the negative direction when in compression as the wave properties predict faster arrival times when a specimen is experiencing compression. This effect is clearly shown in the plot for Test 1.1 and, therefore, is the first step in validating the effectiveness of the testing setup. The plot's curved shape and the shifted endpoint compared to the initial test point show the expected effect of the concrete's memory of damage. The general trend of the increasing slope with respect to increasing stress further proves that the testing setup used for CWI in this study is operating correctly and therefore is applicable to further use on small-scale specimens.

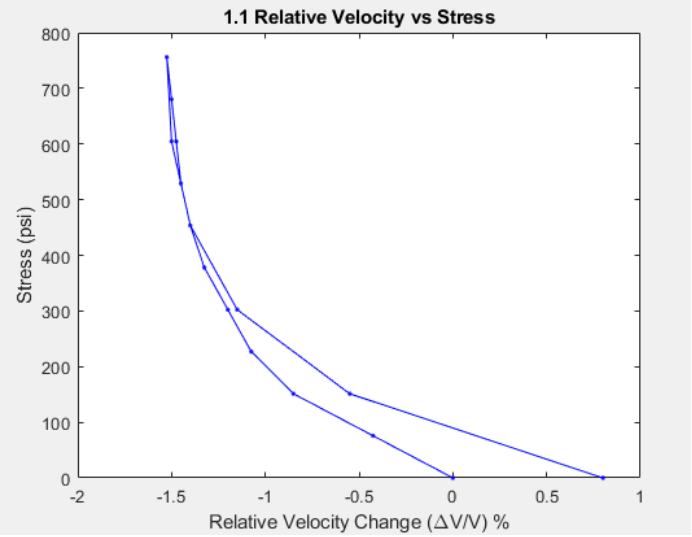

Figure 116. Small-scale beam-block, direct compression, coda-wave interferometry Test 1.1 – Graph of relative velocity vs. stress

4.3.5.1.2 Beam Testing

After validating the testing setup with the beam block testing, the next step is small-scale beam testing in both normally reinforced and PT beams. These beams will undergo 3-point load testing, described in Chapter 4. In these tests, the same damage features as the beam blocks are expected to appear in addition to possible cracking and yielding of the beams. These damaged features are expected to cause dramatic changes in the relative velocity change vs. load plots and, in a real-world application, point to the deterioration of the PT flexible filler system.

4.3.5.1.2.1 Normally Reinforced

Test 2.1

This test acted as the preliminary validation for the application of the transducers to the new specimen and the 3-point load test on the beams. This test consisted of a two-cycle loading, reaching approximately 350 psi each time. This loading was chosen due to its probability of not cracking the specimen in any way, allowing for direct comparison between the cycles. The plot shown in Figure 117 shows the relative velocity change vs. stress plots for both load cycles. As expected, the two plots mimic each other near-perfectly aside from the shifting caused due to concretes tendency to have a memory for loading and damage. The damage most likely to be causing the shift would be microcracking caused by the first load cycle.

It should be noted that as the stress increases, the relative velocity change moves in the positive direction. This shift indicates the area in which the transducers are placed in tension. This indication is correct as the transducers are placed on the bottom of the beam, which undergoes tension when in a 3-point load test. The repeat nature of the shifts in the expected direction proves both the CWI setup's efficacy on the beam specimens and foreshadows that if extensive damage such as cracking or yielding should occur, then there will be a significant observable change in the plots.

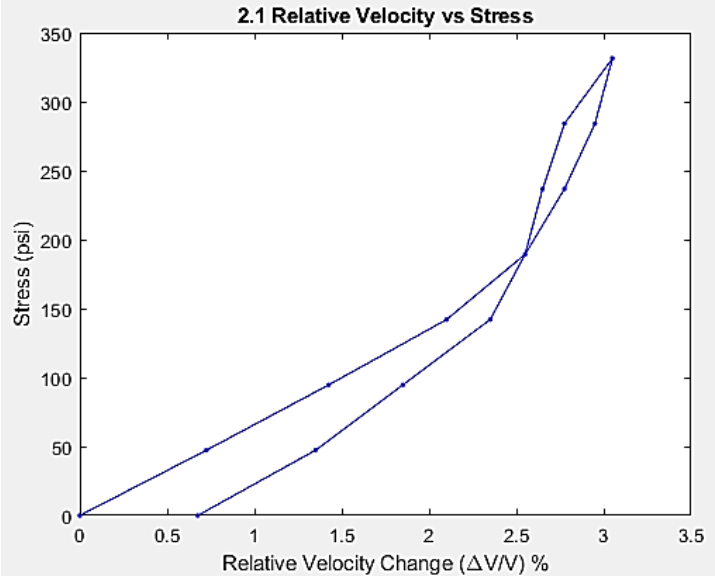

Figure 117. Small-scale normally reinforced beam, three-point load; Coda-wave interferometry Test 2.1

Test 2.3

The purpose of Test 2.3 was to bring the normally reinforced beam to the point of cracking, which would hopefully reflect on the relative velocity change plot. For this test, displacement data for the loading cycle was also collected and compared to the relative velocity change plot to coordinate signal features. As shown in Figure 118, as the stress applied to the beam approaches 2500-kHz psi, the displacement vs. stress graph data shows a slight shift reflected in the relative velocity change plot by a sizeable horizontal change between data collection points. This shift points to the onset of cracking in the specimen, which is confirmed by the effect on the displacement plot. As expected, when this cracking occurred, the time taken for the waveform to travel between transducers was slightly increased, resulting in a significant shift in the relative velocity.

Another relevant feature of this plot is the significant shift between start and end points, which confirms that CWI is sensitive to the effects of compression and tension over time and damage to the specimen.

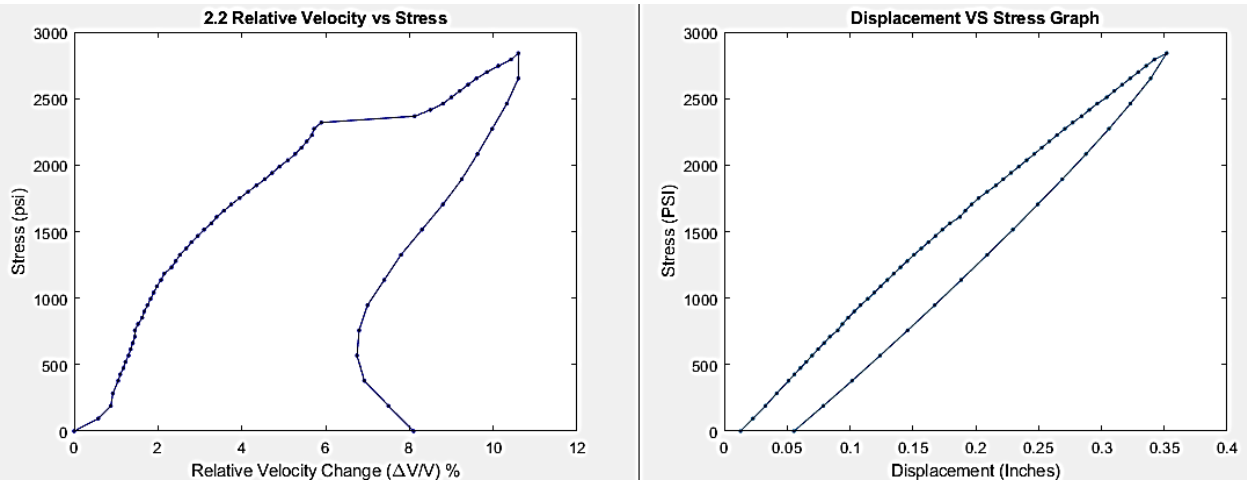

Figure 118. Small-scale normally reinforced beam, three-point load, Coda-wave interferometry Test 2.3- Graph of relative velocity change vs. Stress and displacement vs. stress

3. Test 2.4

After Test 2.3, the next logical step would be to observe beam yielding, which is the goal of Test 2.4. This test will hopefully show a drastic and varied response to the yielding of the beam when compared to the cracking that was previously observed. The results of Test 2.4 can be seen in Figure 119, which shows the expected harsh response to yield. As the stress approaches and exceeds 3000 psi, an evident change in the displacement plot is seen, which is a clear sign of yielding due to the drastic slope change. The change in the displacement plot is reflected even more drastically in the relative velocity change vs. stress plot; as 3000 psi of stress is reached, the relative velocity change becomes near horizontal over the remainder of the increasing load portion of the test. This signal feature should be easily identified in further tests and is varied enough from the feature caused by cracking.

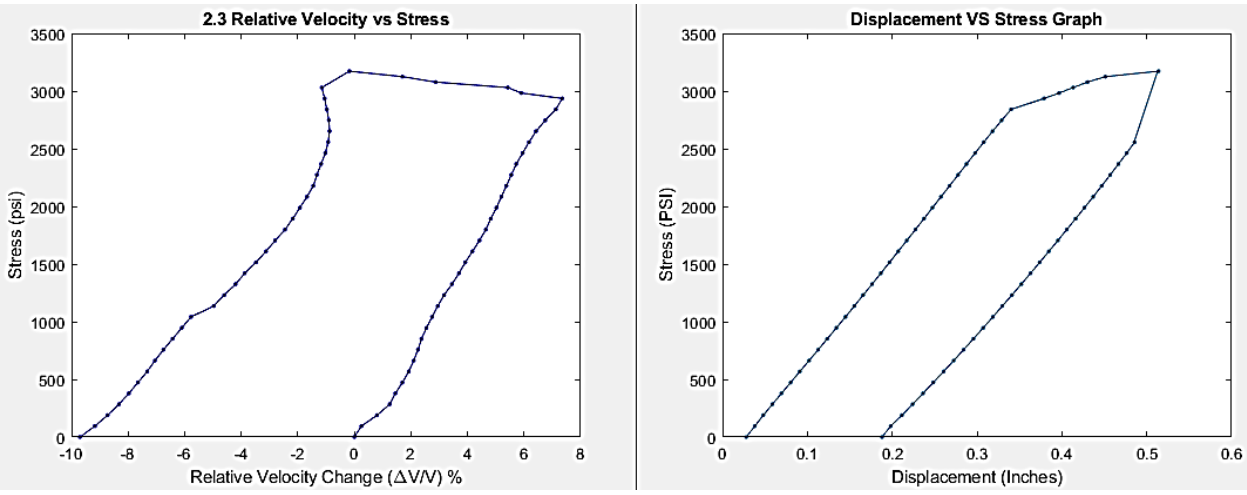

Figure 119. Small-scale normally reinforced beam, three-point load, Coda-wave interferometry Test 2.4 - Graph of relative velocity change vs. stress and displacement vs. stress

4.3.5.1.2.2 Post Tensioned

Test 3.1

The first test for the PT scale beam involved the tensioning process outlined in Section 2.3.4.1.2.2. This test was implemented to validate the sensitivity of CWI to the tensioning and de-tensioning of a simulated PT strand, which is a full-scale application that could be an indicator of PT failure. This observation was successful, as can be seen in Figure 48. The relative velocity change plot vs. the loading moved in the negative direction during tensioning and in the positive direction during de-tensioning, which was as expected. Also, the second tensioning brought the beam up to the final 400 psi of PT force, closely following the slope and shape of the first cycle up until the previous maximum. This provides a positive insight into the consistency and sensitivity of the CWI method to the application and removal of post-tensioning force.

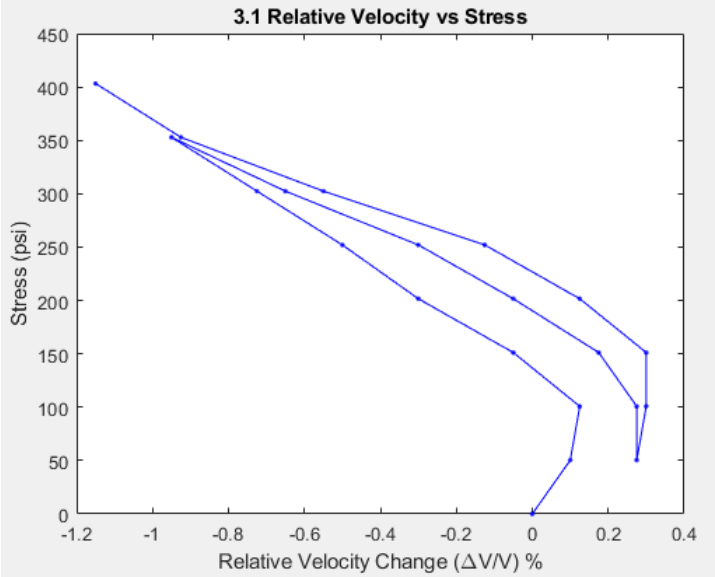

Figure 120. Small-scale PT beam, tensioning, Coda-wave interferometry Test 3.1 - Graph of relative velocity change vs. stress

Test 4.1

The first of the 2-point load tests on the PT small-scale specimen was test 4.1, which had the goal of matching the displacement vs. stress plot to the relative velocity change vs. stress graph for use as a control to compare against damage features caused by excessive loading. Both plots in Figure 49 follow the same trends as the normally reinforced beam, which underwent the loading process with one key distinction: the reduction in the shift between starting and ending points. This is expected as the post-tensioning present in this specimen serves to increase the elastic nature of the specimen. Furthermore, this test proves the proper attachment of the transducers to the beam and application of CWI to this specimen by the closely matched plots of the displacement vs. stress and relative velocity change vs. stress plots.

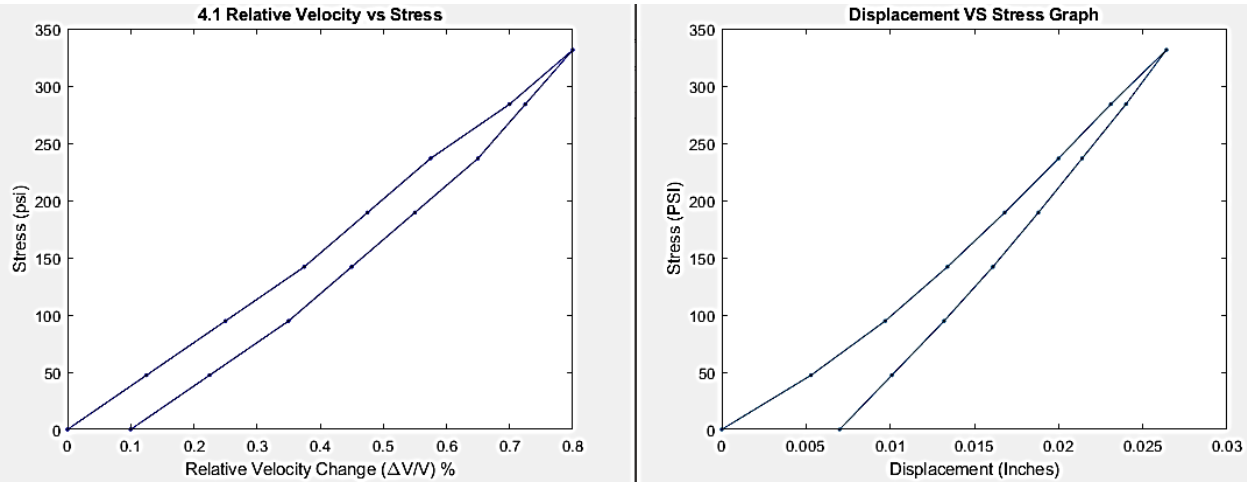

Figure 121. Small-scale PT beam, three-point load, Coda-wave interferometry Test 4.1 – Graph of relative velocity change vs. stress and displacement vs. stress

Test 4.3

This test is a direct recreation of test 4.1; no previous test exceeded the 350-psi maximum. The results shown in Figure 50 illustrate the same outcomes as Test 4.1 and validate the effectiveness and repeatability of CWI. As seen previously, the displacement vs. load and relative velocity change vs. stress plots follow the same slope and shape trends as expected from the previous testing. No evidence of additional damage to the concrete could be witnessed, which was expected because there was no extreme loading being applied before this test.

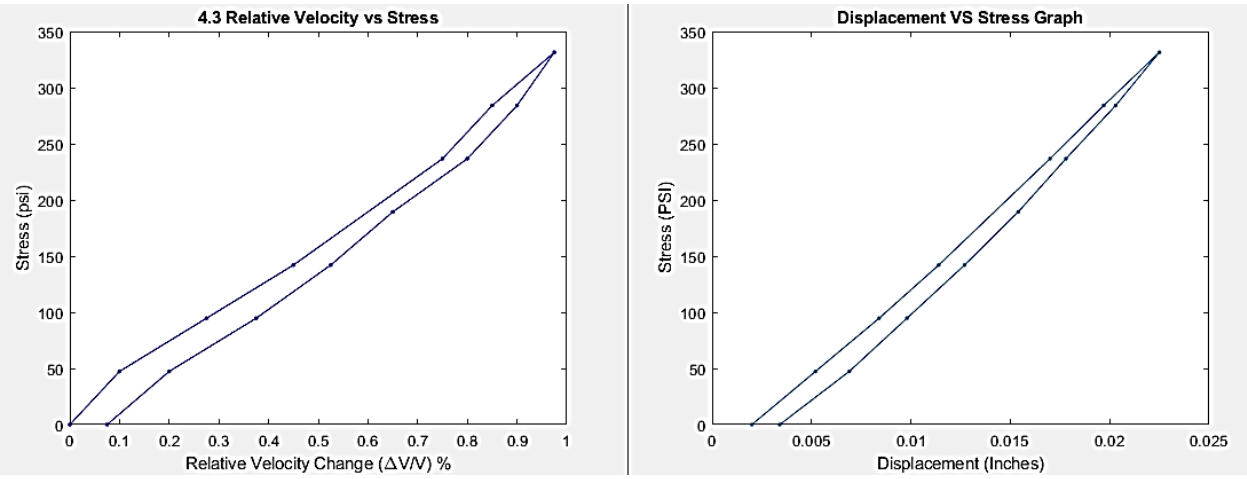

Figure 122. Small-scale PT beam, three-point load, Coda wave interferometry Test 4.3 – Graph of relative velocity change vs. stress and displacement vs. stress

Test 4.4

Following the normally reinforced scale specimen testing, this test will seek to increase loading to identify damage features in the plots. Figure 51 shows the displacement plots and relative velocity change vs. stress. Contrary to the normally reinforced beam, the two plots do not follow each other for

the entirety of the loading cycle; instead, as the loading approaches and exceeds 600 psi, the relative velocity change plot begins a vertical trend. This trend can be attributed to the post-tensioned reinforcement being mobilized, resulting in less and less tension in the bottom-most portion of the beam where the transducers are placed. Since the maximum stress of 1200 psi did not yet reach the calculated cracking point of this specimen, there is no damage feature found on the plots of either displacement or relative velocity change.

This test proves a distinction between the mobilization of PT reinforcement and actual damage features, which would display on the output relative velocity change plot as a nearly horizontal line. Another notable outcome is the small shift in the relative velocity change between starting and ending points which is consistent with what is expected of PT reinforced beams and specimens. As stated in the results of Test 4.1, the PT reinforcement provides more elasticity to the beam allowing for a closer return to the original state of the beam prior to loading when compared to a non-post-tensioned specimen.

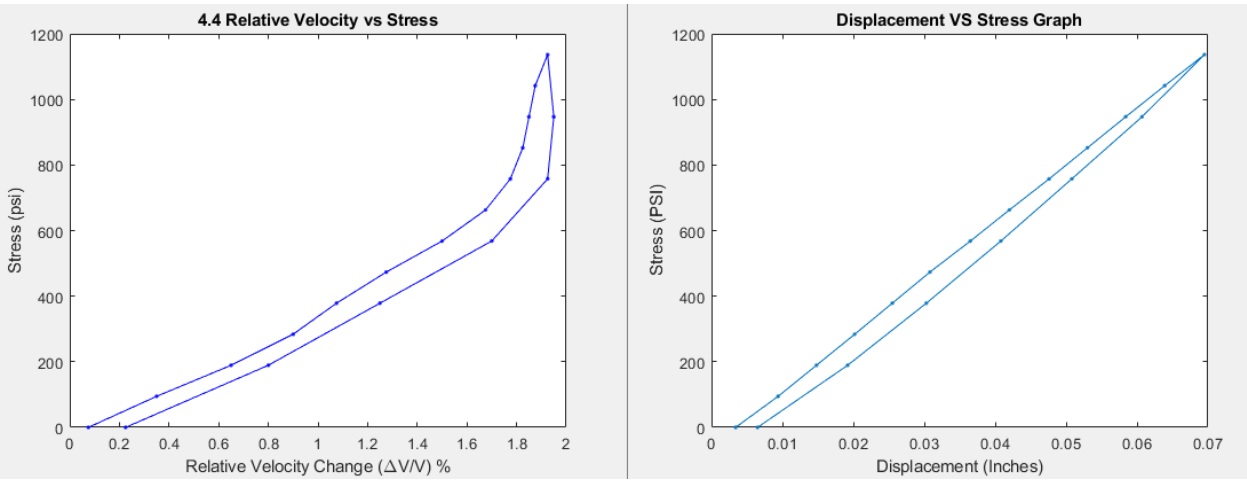

Figure 123. Small-scale PT beam, three-point load, Coda-wave interferometry Test 4.4 - Graph of relative velocity change vs. stress and displacement vs. stress.

Test 4.5

The final test on the small-scale PT specimen aimed to induce cracking within the specimen; yielding was not explored for this specimen due to the large load expected to be required to do so. Figure 52 shows the displacement and relative velocity change vs. stress plots. These plots both show damage indicators for cracking; the displacement plot shows a starting at 1500-kHz psi, indicating that cracking occurs in the beam. As experienced with the normally reinforced beam, the coinciding effect on the relative velocity change plot is significantly more prominent. As experienced in Test 4.4, there is a near-vertical slope of the line while the PT reinforcement is mobilized, and then, as the beam is cracked, there is a horizontal trend to the plot. This change in the slope proves the variation between the two effects and can be used effectively to identify the two features. Though not tested, it is expected that the yielding of the beam would provide a longer lasting and more prominent horizontal trend in the relative velocity change vs. load plot.

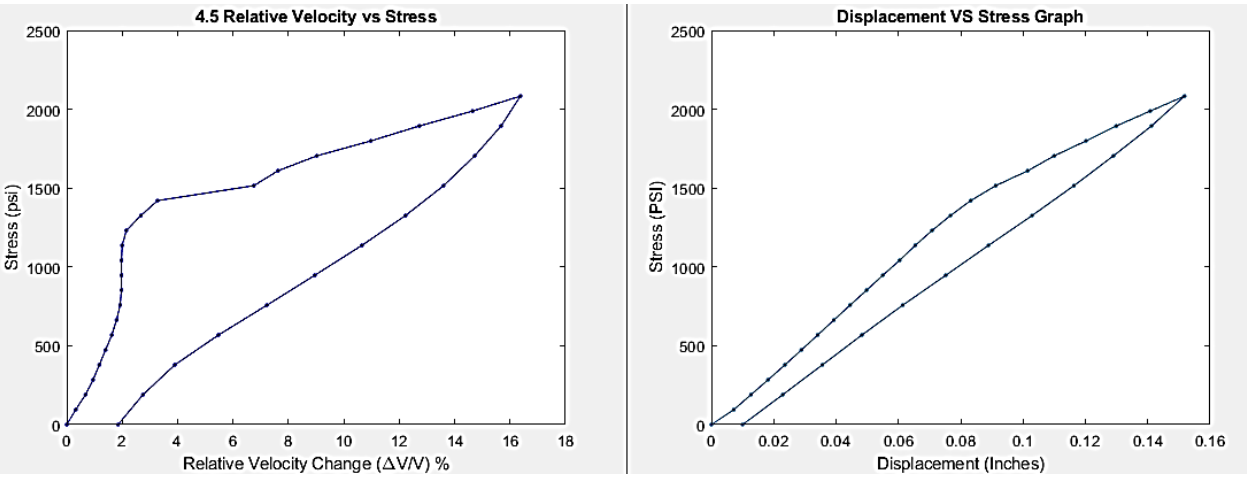

Figure 124. Small-scale PT beam, three-point load, Coda-wave interferometry Test 4.5 - Graph of relative velocity vs. stress and displacement vs. stress

4.3.5.2 Diffuse Ultrasound

The outcome sought for diffuse ultrasound evaluation for the NDE of PT flexible filler systems is an indirect evaluation of the health of the post-tensioning system. For DU, this means having damaged feature recognition from increases in microcracking. This feature can indicate increased loading on the structure in question or a decrease in the effectiveness of the post-tensioned reinforcement allowing for more tension in the concrete.

4.3.5.2.1 Block Testing

The beam block specimens' testing will show the general feasibility and efficacy of the DU testing setup for identifying damage features relevant to flexible filler PT systems. These features would be identified via the coefficient of diffusivity plots generated by the DU algorithm. They would take the form of decreases in the diffusivity of the material due to an increase in the size or quantity of microcracking.

The beam-block test serves the same purpose as it did with the CWI testing, to validate the effectiveness of this method and the equipment setup used to carry out testing. It was expected for an increase in microcracking to occur as the concrete was damaged from the direct compression testing. This trend can be clearly seen in Figure 53 via the diffusivity vs. stress plot. The diffusivity coefficient of a material is expected to decrease due to an increase in microcracking size and presence. Due to the presence of this effect, it can be assumed that the testing setup derived for DU testing was appropriate. It can also be seen that as the loading was reduced in the second half of the loading cycle, the coefficient of diffusivity increased again but did not return to its prior level before loading; both of these effects were expected as the microcracking in the specimen receded with the unloading of the beam-block.

A plot of the integration values of the intervals is shown In Figure 126 for this test's zero load initial point. This plot has the best fit line, which is used to find the diffusivity value for the specified load point. The value for diffusivity is the coefficient D in Equation 3. The value D affects the slope of the

decaying leg of the logarithmic function. As the value of diffusivity increases, the slope of the decaying leg of the logarithmic function increases. Therefore, as there is an increase in damage to the concrete, the general slope of the interval integration plot for a specific load point will also increase.

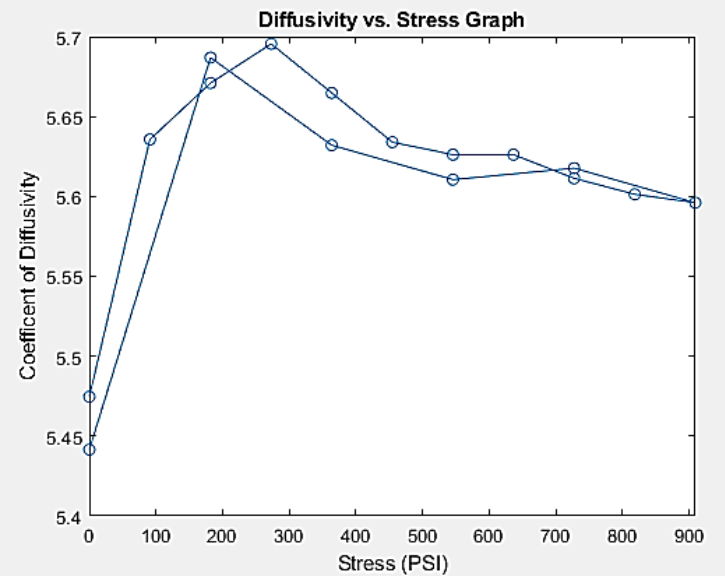

Figure 125. Small-scale beam-block, direct compression, diffuse ultrasound Test 1.3 - Graph of coefficient of diffusivity vs. stress

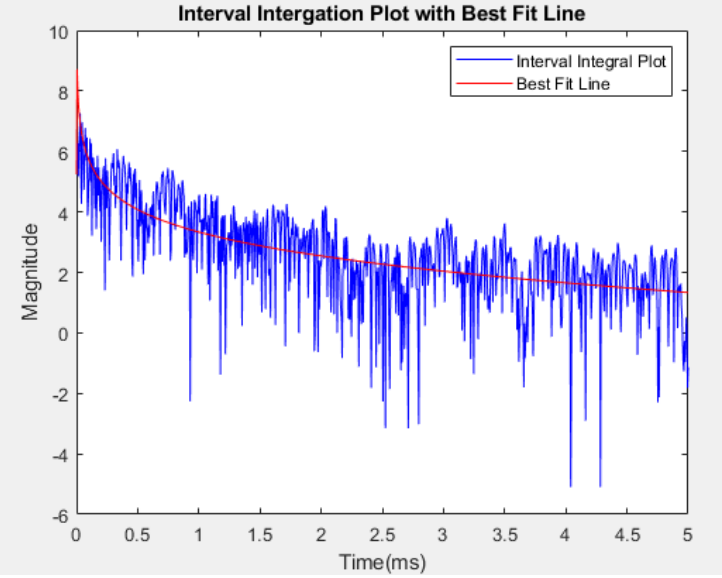

Figure 126. Interval integration plot with best fit curve for diffuse ultrasound spectroscopy

4.3.5.2.2 Beam Testing

After validating the testing setup with the beam-block testing, the next step was small-scale beam testing for both normally-reinforced and PT beams in three-point bending.

4.3.5.2.2.1 Normally Reinforced

Due to unknown circumstances in the testing process for the normally reinforced specimen, the data collected during the loading cycle could not provide any meaningful insight into the effectiveness of the DU method. The data points received followed no trends and seemed to randomly change slope and position without regard to the applied load. In future work, more testing on normally reinforced specimens would need to be done to identify the reasons behind the issues faced during these experiments. Due to time constraints, no further test could be completed after the defunct data for this specimen was discovered.

4.3.5.2.2.2 Post Tensioned

Testing on the post-tensioned beam proved to be more fortunate than the normally reinforced beam. Test 4.2 was a loading and unloading cycle up to approximately 350 psi, resulting in no cracking of the specimen. Figure 127 shows the expected decrease in the coefficient of diffusivity that was also seen in Test 1.3. The presence of this trend in correlation to the displacement vs. stress plot shows that the decrease in the diffusivity coefficient occurred solely from the variation in microcracking caused by the loading cycle. The endpoint's lower value of diffusivity than the starting point also proves the increase in microcracking in the structure from the load test.

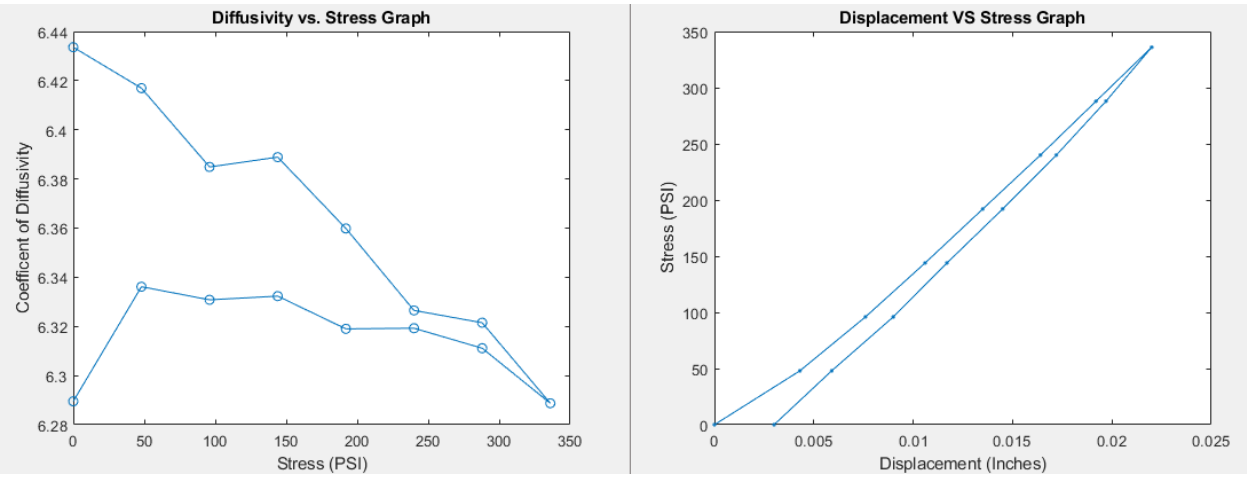

Figure 127. Small-scale PT beam, three-point load, diffuse ultrasound Test 4.2–- Graph of coefficient of diffusivity vs. stress and displacement vs. stress.

5 Large-Scale Testing

The initial testing plans primarily centered around post-tensioned beam samples containing bonded strands. Additionally, pre-tensioned concrete samples with post-tension ducts were planned for fabrication at a prestress yard. These samples would then be transported to the FDOT structures lab, where cast-in-place end blocks would be added to accommodate post-tensioning.

Regrettably, the budget al.located for producing these beams had been finalized in early 2020, predating the Covid-19 pandemic. By the time the FDOT Structures Lab approved the final designs for the beams in Spring 2022, the costs for materials and production had surged nearly threefold from the initial estimates. Consequently, a determination was reached to construct all samples as cast-in-place concrete with provisions for post-tensioning. This shift yielded substantial cost savings compared to the original strategy relying on the prestress yard. The plans for the original and redesigned samples can be found in the Appendix. The subsequent discussion will concentrate on the cast-in-place concrete samples that were constructed in the FDOT Structures Lab during Spring 2023.

5.1 Specimen Description

Three large-scale specimens were investigated in the current study:

- Beam A – Main element with draped tendon
- Beam B – Simulated closure pour
- Beam C – Simulated epoxy-bonded match-cast segmental construction

The overall geometry for each beam is provided in Figure 128, Figure 129, and Figure 130. All of the formwork used for the specimens was fabricated by the FDOT Structures Lab staff. The mild steel reinforcing bars were ordered from a steel fabricator and delivered pre-bent to the lab. A 3.5-inch HDPE post-tension duct was used for a 12-strand tendon with strand diameters of 0.6 in. The ECI 6-12 anchorage system[63] was provided by Structural Technologies VSL. Beam A and the first half of Beam B and Beam C were poured on May 22, 2023.

An FDOT Class IV concrete mix with a specified 28-day compressive strength of 5500 psi was used for all specimens. The match-cast pours for the second half of Beam B and Beam C were completed on June 7, 2023. The epoxy-bonding process for Beam C was completed on July 10, 2023, using Sikadur 31 SBA Normal Set[64] epoxy-paste adhesive. A bonding pressure of 40 psi was achieved using two ¾-inch ultra-high-strength threaded rods. One rod was passed through the main 3.5-inch post-tensioning duct while the second rod was passed through a provisional 2.5-inch duct located 12 inches from the top of the beam. The rods were stressed using Enerpac 603 hydraulic cylinders that were actuated with a hand pump. Once the target force of 16 kips was achieved in each rod, a coupling nut was used to tie off each rod and prevent any loss of force due to pressure loss in the cylinder. The epoxy was allowed to cure for 48 hours before the force in the threaded rods was removed.

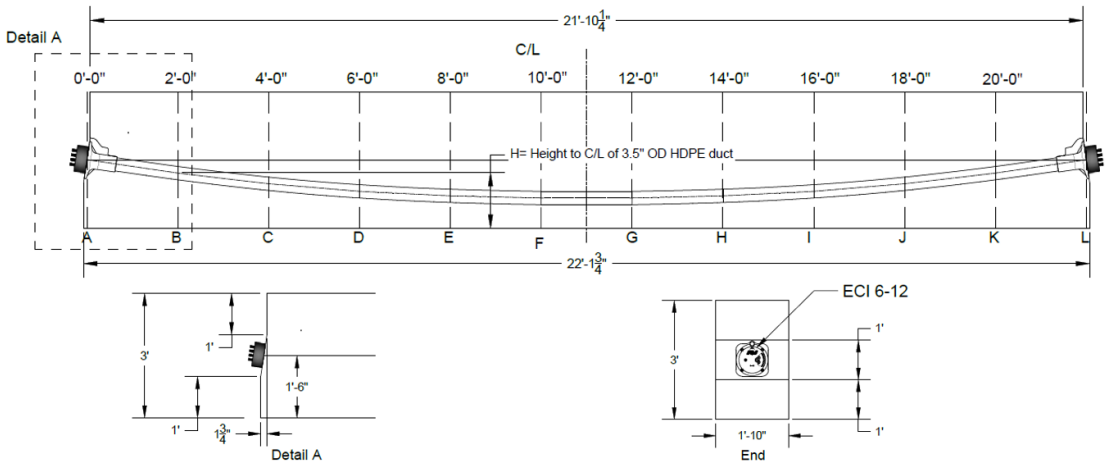

Figure 128. Beam A – Specimen geometry

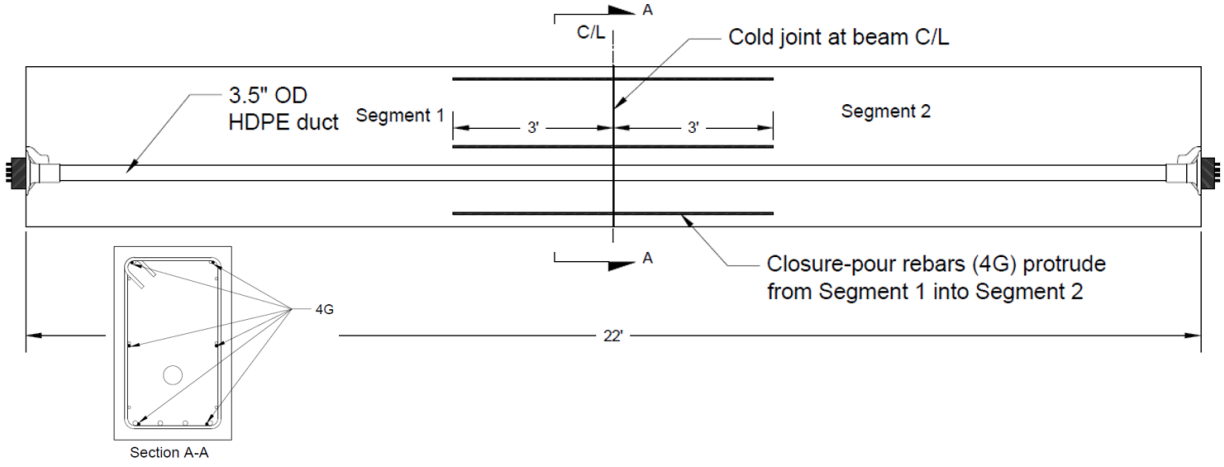

Figure 129. Beam B – Specimen geometry

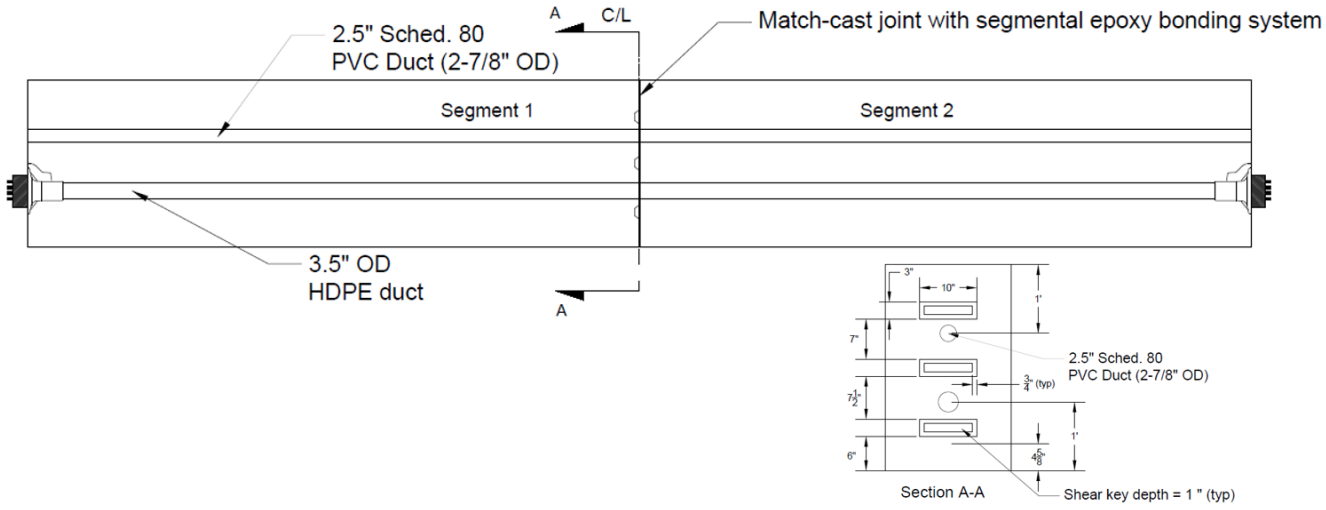

Figure 130. Beam C – Specimen geometry

5.2 Instrumentation

The instrumentation plan included the following measurement devices:

- Dual-bridge load cell for measuring load during flexural testing
- Laser displacement sensors for measuring displacement during flexural testing
- GEOKON 4200 vibrating wire strain gauges were embedded in concrete for strain measurements
- Fiber-optic sensors for monitoring strain and crack development on the surface of concrete
- 50 kHz ultrasound transducers for evaluating stress level and cracking in concrete

The general layout for all instrumentation is described in Figure 131 and Figure 132. Subsections describing the fiber-optic sensors, ultrasound transducers, and vibrating wire strain gauges are provided below.

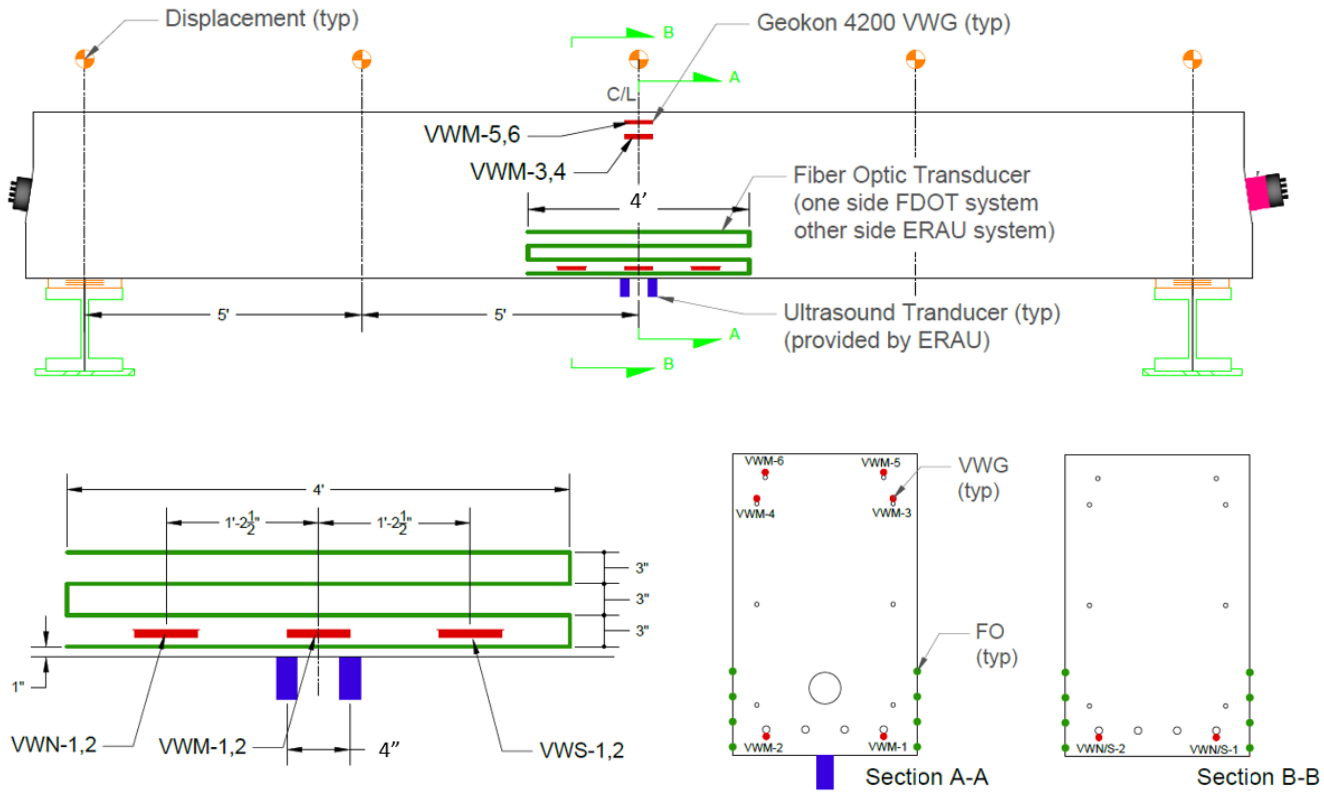

Figure 131. Instrumentation layout for Beam A

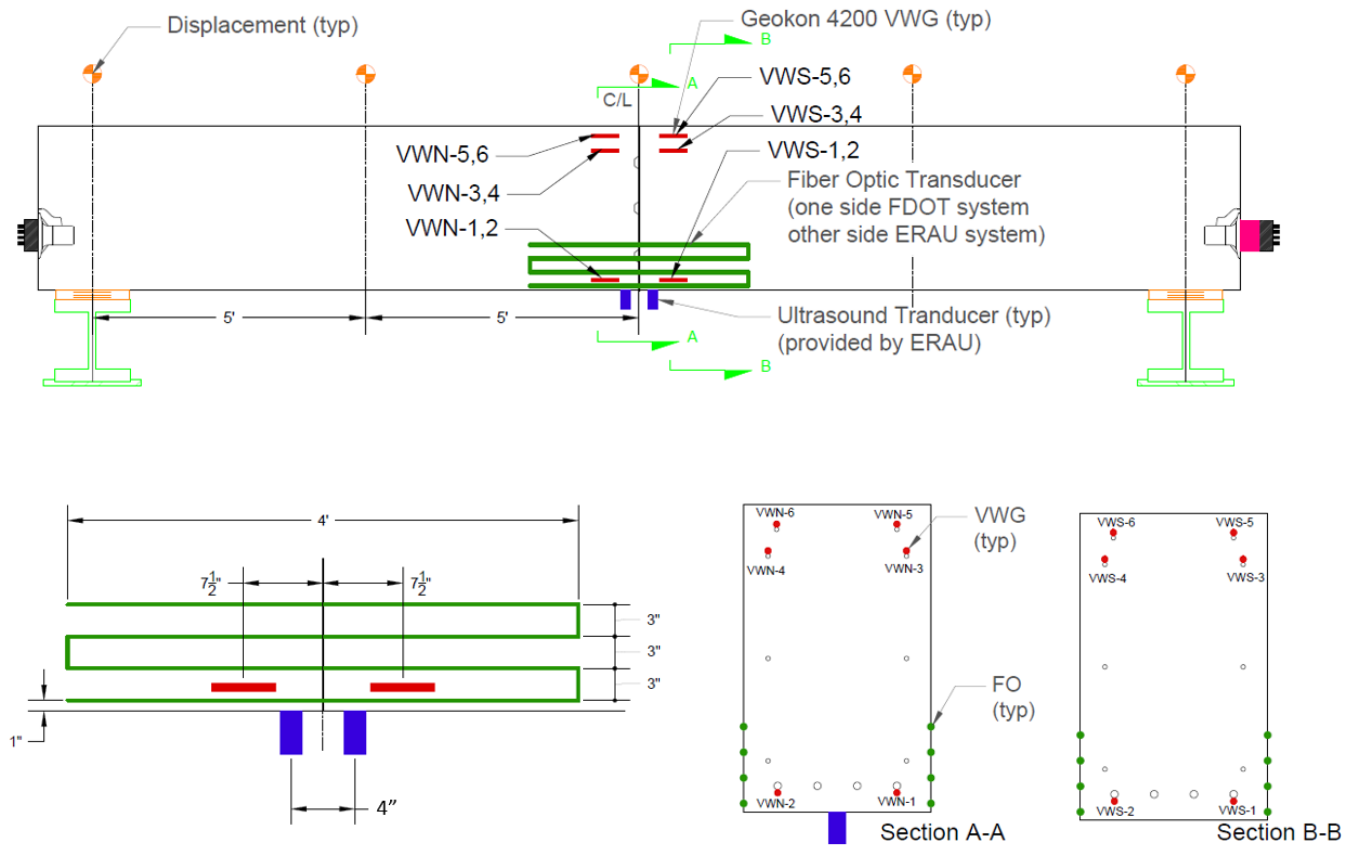

Figure 132. Instrumentation layout for Beam B and Beam C

5.2.1 Ultrasound Transducers and Instrumentation

The setup for generating and receiving ultrasound signals through the concrete beams was similar to the setup used for the small-scale testing (Figure 133). The high-voltage linear amplifier used in the small-scale testing was damaged and a Piezo EPA-104 linear amplifier was used in its place. One additional minor deviation from the small-scale testing was that Oatey Fix-It Stick two-part epoxy bonding putty was used mount the transducers. The two-part liquid epoxy used in the small-scale testing was not suitable for bonding the transducers on a vertical surface. The bonding putty did provide a solid connection that was able to support the transducers for extended periods of time (> 2 weeks before they were removed) and did not result in any noticeable attenuation of the ultrasound. Approximately 7 g of putty was required to bond each transducer.

The research team also developed a fixture for mounting the transducers. The purpose of the fixture was to hold the transducers firmly in place while the two-part epoxy cured (typically less than five minutes). The fixture was effective for both vertical and horizontal (overhead) surfaces (Figure 134). In certain cases where the mounting fixture could not be secured to the beam, the research team was able to place the 7-gram slug of mixed putty on the center of the transducer and press it firmly against the beam until a visible bead of putty was extruded around the circumference. Simple hand pressure

for five minutes was sufficient to establish a durable and non-attenuating bond on both vertical and overhead surfaces.

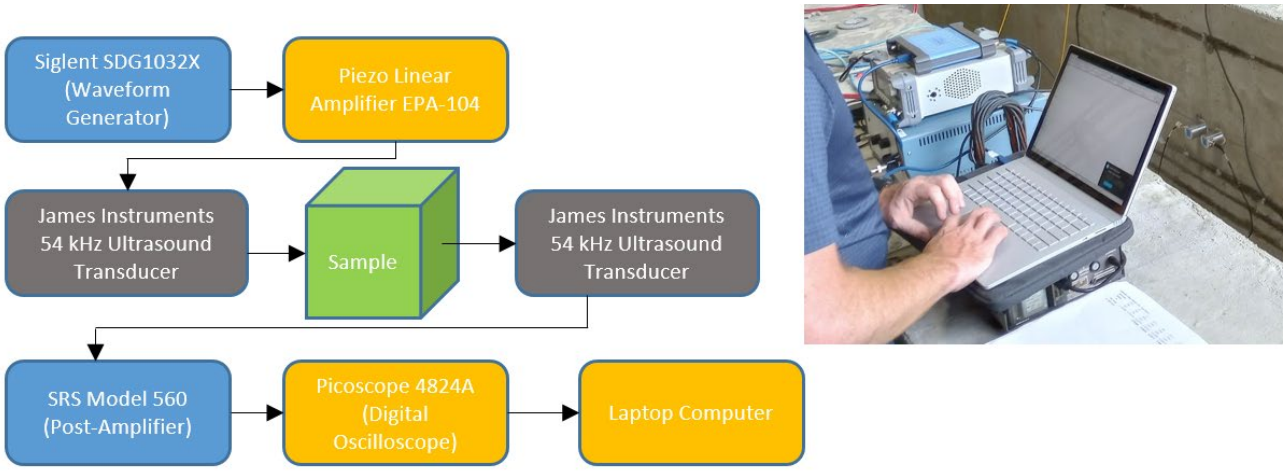

Figure 133. Instrumentation for ultrasound generation and data acquisition

Figure 134. Fixture for mounting transducers using two-part epoxy

5.2.2 Fiber Optic Sensors

5.2.2.1 Luna oDiSI – B

The Luna Innovations Optical Distributed Sensor Interrogator (oDiSI-B) employs swept-wavelength coherent interferometry, a precise light wavelength control technique, to achieve highly accurate temperature and strain measurements using optical fiber as the sensing element. One of oDiSI-''s standout features is its capability in providing distributed measurements across expansive areas while maintaining a remarkable spatial resolution. The system accommodates pre-made optical fibers ranging from 1 to 20 meters in length, enabling the measurement of strain or temperature at multiple specific points of interest along the optical fiber, with intervals as fine as 0.64mm. In our research, a gauge

length of 1.25mm was utilized. Additionally, the optical fibers supported by this system are distinguished by their small diameter, measuring less than 0.2mm. For our study, a diameter of 0.155 mm (about 0.01 in) was used. This slender profile facilitates the fiber placement in locations previously inaccessible to conventional sensors such as foil gauges and thermocouples.

5.2.2.2 Sensuron RTS125+

The Sensuron RTS125+ Fiber Optic Sensing unit is commonly used in Civil Engineering practices for precise structural health monitoring and design validation. This specific Sensuron unit comes equipped with the ability to simultaneously monitor 8 fibers with over 2000 equally spaced sensors per fiber. Each fiber's resolution ranges from 1.6mm – 6.3mm, has a gauge length that ranges from 1.6mm-25.4mm and has an acquisition rate of up to 100 Hz. The Sensuron system also allows the use of a fiber length up to 104 meters, but this is also customizable using a fusion splicer in case the fiber breaks during instillation. For the purposes of this research the fiber was used to monitor strain throughout the beam, but the fiber is also capable of monitoring temperatures ranging from -200℃ - +200℃. This specific Fiber Optic Sensor was used due to its versatility and it's rugged design.

5.2.3 Vibrating Wire Gauges

The GEOKON 4200 vibrating wire gauges (VWG) were mounted to the mild reinforcing steel as shown in Figure 135. Readings from the gauges were obtained using a standalone, battery-powered data acquisition (DAQ) system with outputs to the main PC-based DAQ.

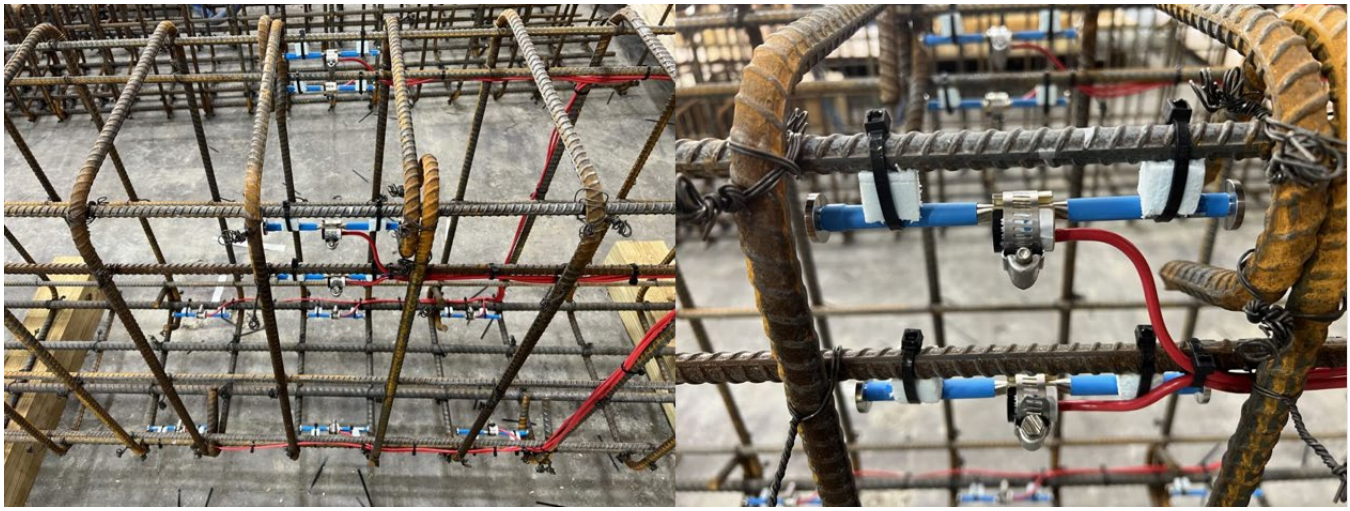

Figure 135. Installation of GEOKON 4200 vibrating wire strain gauges

5.3 Test Setup

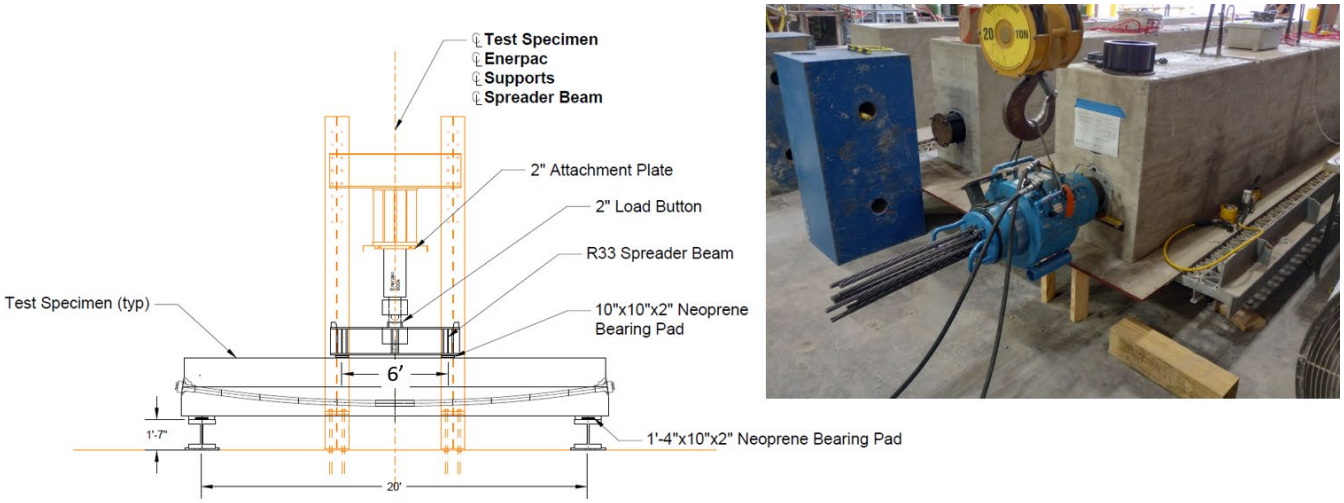

Figure 136. Test setup for post-tensioning and 4-point bending

5.4 Post-Tensioning Results

Post-tensioning was performed with a 300-ton hydraulic actuator and pump system that was provided by Structural Technologies VSL. Post-tensioning was completed for Beam A, Beam B, and Beam C on June 23, June 30, and July 14, respectively. The hydraulic actuator was manually controlled during the stressing operation based on the pressure on the service side of the pump. Target pressures and the corresponding post-tension force are provided in Table 16. Imperfections in the concrete around the cold joint in Beam B required several minor alterations in the location of the ultrasound transducers and the fiber-optic sensors. For Beam A and Beam C, the ultrasound transducers were located 16 in from the bottom of the beam or two inches below the neutral axis. The two ultrasound transducers for Beam B were located 14 in from the bottom or four inches below the neutral axis. The bottom run of the fiber-optic sensor was located one inch from the bottom for Beam A and Beam C and two inches from the bottom for Beam B (Figure 137). This resulted in minor variations for the anticipated stress levels at the sensor locations.

The maximum jacking force for the 12-strand tendon was 562 kips (80% of the ultimate strength of each strand, which is 270 ksi). In order to simulate a scenario in which a substantial amount of PT force was lost over time, the target post-tensioning force was 246 kip (35% of the ultimate tendon strength). This force generates a compressive stress of 621 psi at the bottom of the beam (495 psi if self-weight is included).

Figure 137. Fiber-optic sensor location and ultrasound transducer location for post-tensioning

Table 16. Jack pressure, PT force, and corresponding stresses in concrete at level of sensors

Jack pressure (psi)	**PT force (kip)**	**Approx. normal stress at ultrasound transducer (psi)**		**Approx. normal stress at bottom run of FOS (psi)**	
		Beams A & C	Beam B	Beams A & C	Beam B
0	0	0	0	0	0
500	35.5	-50	-55	-87	-85
704	50	-70	-77	-123	-119
1000	71	-100	-110	-174	-169
1500	107.5	-151	-167	-263	-256
2000	144	-202	-222	-353	-343
2500	181.5	-254	-280	-445	-432
3000	219	-307	-338	-537	-522
3351	246	-345	-380	-603	-587

5.4.1 Beam A

Coda-wave interferometry results for Beam A that were obtained during post-tensioning are summarized in Figure 138. The relative velocity change was determined for two 100-microsecond time time intervals beginning at 20 microseconds and 50 microseconds. Stress values were obtained at the level of the transducers 2 in below the neutral axis of the gross cross-section), which varied from 0 to -345 psi (345 psi in compression) as the applied post-tension force was increased from 0 to 246 kip. In general, the velocity of ultrasound is expected to increase as the level of compressive stress increases. There was a minor decrease in velocity through the initial 100 psi in compressive stress. We observed similar results in our small-scale testing, but don't have a conclusive explanation for why this occurs during the initial loading of concrete in compression. After the compressive stress exceeded 100 psi, the ultrasound velocity did increase to a maximum value of 0.58% and 0.15% for the 20- and 50-microsecond start times, respectively. The 10 corresponding waveforms for the 100-microsecond window are also provided in Figure 138. The overall variation between the waveforms is minor and the set of waveforms illustrates the overall repeatability of the coda waves in sound concrete subjected to stress variations.

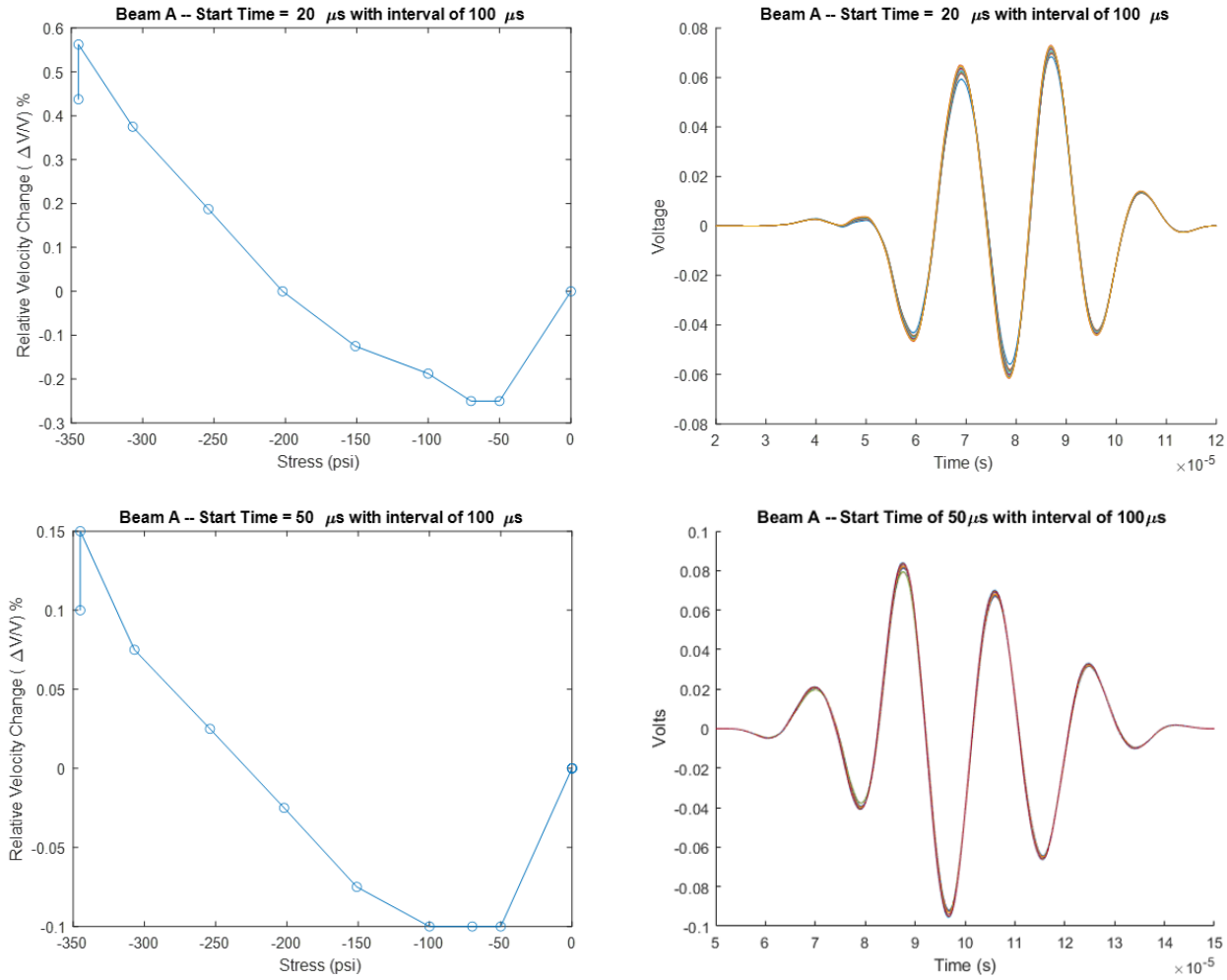

Figure 138. Coda-wave interferometry results for Beam A (post-tensioning)

Vibrating wire strain gauge data are summarized in Figure 139. The bottom gauges on the east side of the beam (VWG N/M/S-1) were all in agreement with a maximum compressive strain 113 microstrain. The three gauges on the bottom/west side (VWG N/M/S-2) displayed a slightly larger variation with the north and south gauges averaging 114 microstrain for a maximum compressive strain and the middle gauge only reaching a maximum value of 100 microstrain. Strain data recorded from the fiber optic systems are summarized in Figure 140. Each plot contains four data series that represents that average strain measured across the entire four-foot segment of the fiber-optic cable. Segment A was located 10 in from the bottom of the beam and Segment D was located 1 in from the bottom. Strain measurements from all three systems (VWG, FDOT FOS, and LUNA FOS) were in reasonable agreement. Furthermore, the theoretical maximum compressive strain at a distance of 1 in from the bottom of the beam was 112 microstrain. This value was computed using the gross section properties and a modulus of elasticity of 5.4E6 psi, which is consistent with the 9000 psi compressive strength obtained from 56-day compressive strength tests.

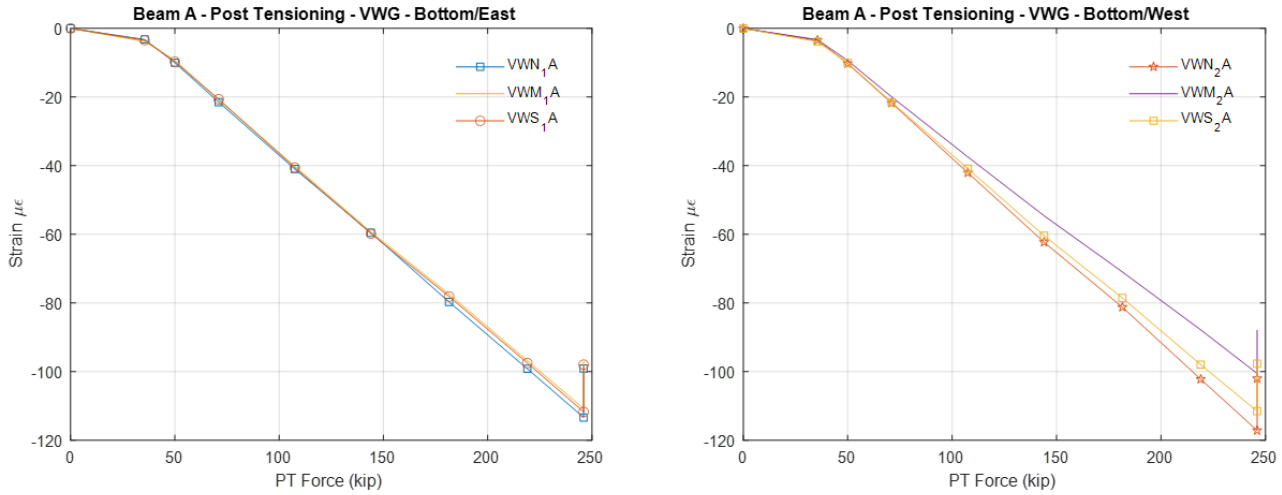

Figure 139. Beam A: VWG results

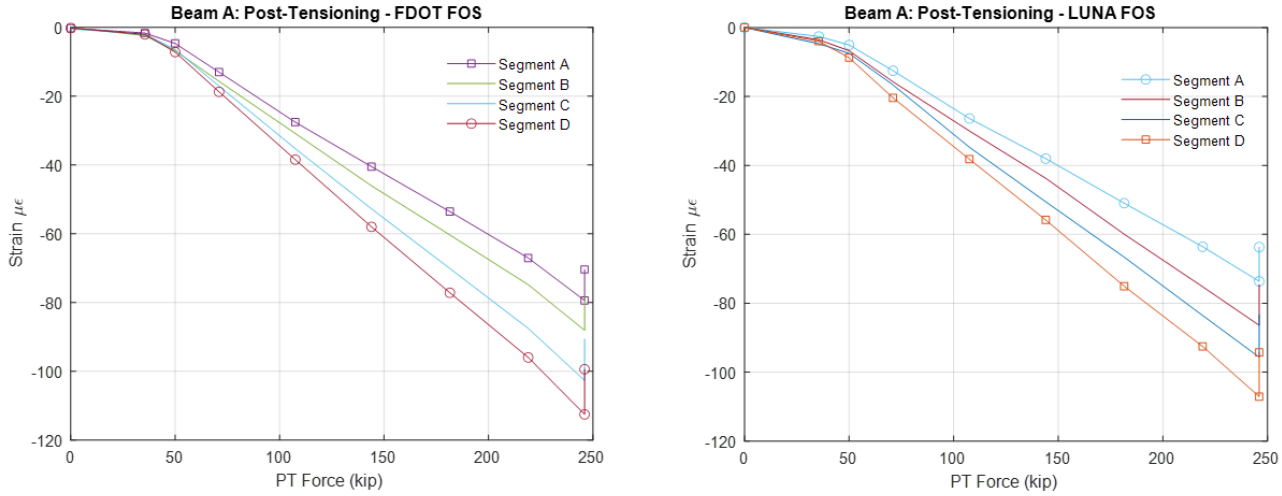

Figure 140. Beam A: FOS strain results

5.4.2 Beam B

A similar procedure for data acquisition during stressing was applied for Beam B. The FDOT FOS system was used on both sides of the beam due to challenges encountered with the installation of the LUNA FOS. The purpose of Beam B was to simulate a cast-in-place closure pour that might be encountered at the midspan of segmental box-girder bridge. Six bars protruded from the first half of Beam B. The second half was cast directly adjacent to the first half and the post-tensioning was used to generate compressive stress in the bottom of the beam.

Ultrasound results obtained during post-tensioning were considerably different from Beam A. First, the peak amplitude of the signal received through the cold joint of Beam B before post-tensioning was approximately 81% less than the peak amplitude of the signal for Beam A. In order to obtain a reasonable voltage level at the digital oscilloscope, the SRS post-amplifier was used to amplify the input signal by a factor of two. The resulting waveforms and corresponding relative change in velocity are provided in Figure 141. The magnitude of the velocity change as a function of stress level (PT force) was also significantly higher than what was observed for Beam A. The amplitude of the signal also increases by a factor of 2 as the compressive stress at the level of the transducers increases from 0 to 380 psi.

A likely explanation for the significant difference in ultrasound behavior between Beam A and Beam B is concrete shrinkage during curing of the simulated closure pour. This shrinkage resulted in a weak interface between the two halves of Beam B. As the compressive force from the post-tensioning was applied, the amplitude and the relative velocity of the ultrasound increased as the cold joint was subjected to the post-tension force.

Another major difference was observed for Beam B in the FOS data. Results for Segment D (bottom run) are summarized in Figure 142. The interface region at the beam's midspan experienced a large compressive strain after the first load step of 35.5 kip was applied. This localized spike in compressive strain continued to increase until the maximum post-tension force was applied. The maximum compressive strain value recorded for this peak was 1190 microstrain, or approximately 13 times the peak compressive strain measured with the VWG sensors.

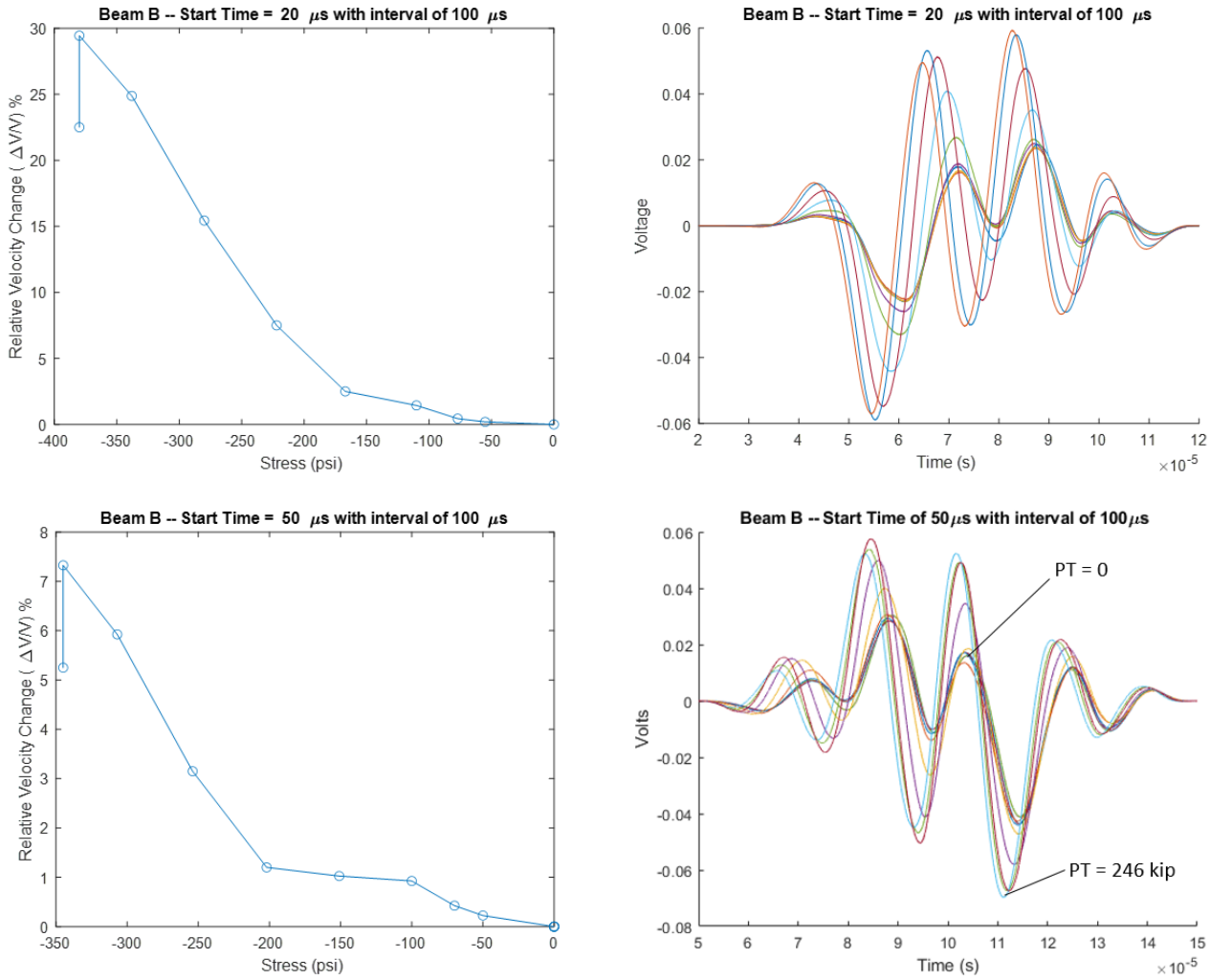

Figure 141. Coda-wave interferometry results for Beam B (post-tensioning)

The VWG data are summarized in Figure 143. The relatively flat slope for the initial load steps may have been the result of misreading the pressure gauge on the hydraulic actuator. The gauge was initially installed on the return side of the hydraulic pump, which resulted in uncertainty regarding the true pressure on the supply side before the error was discovered. The maximum compressive strain of 88 microstrain was less than the value of -112 microstrain that was obtained for Beam A at the same post-tension force. This may have been a result of the fact that Beam A was a draped tendon while Beam B (and Beam C) were straight tendons. The VWG results obtained for Beam C were similar to those obtained for Beam B.

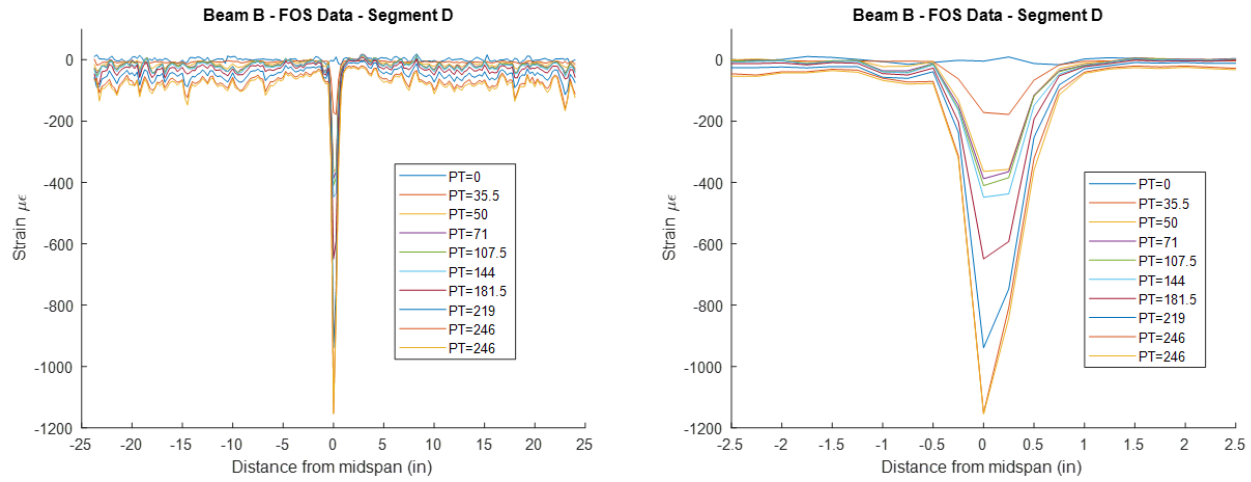

Figure 142. Beam B: FOS data for Segment D

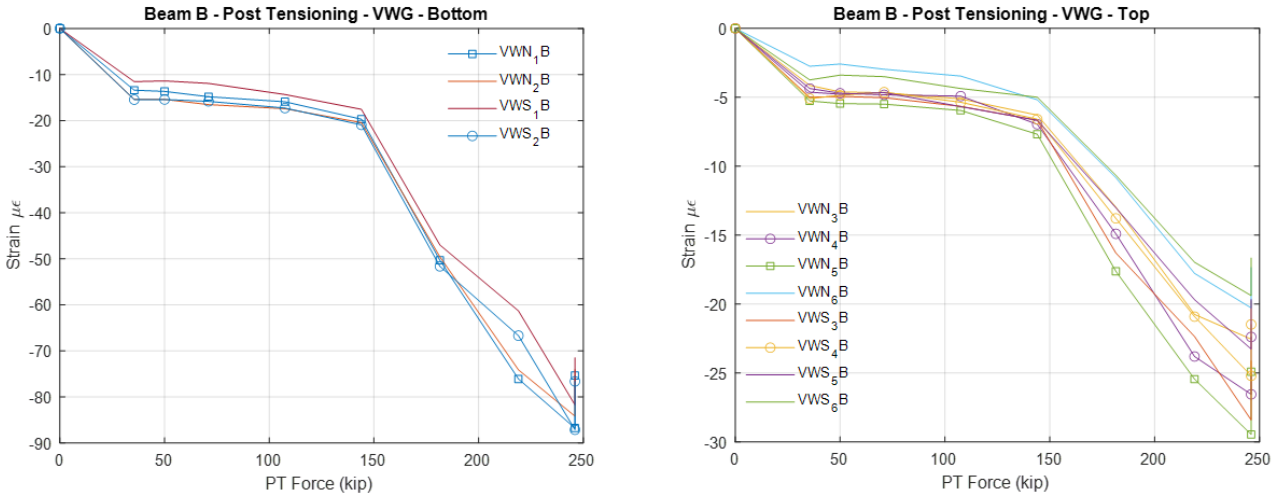

Figure 143. Beam B: VWG Results

5.4.3 Beam C

The ultrasound results obtained for Beam C (Figure 144) were very similar to the results obtained for Beam A. The maximum relative velocity change varied from 0.2% to 0.3% depending on the start time of the window. The ultrasound waveforms were also highly repeatable. Beam C differed from Beam B in that no reinforcing steel passed through the cold joint. Furthermore, any shrinkage that would have occurred in the second half of Beam C was not restrained. Once the two halves of Beam C were separated and then re-joined using epoxy paste, most of the effects of shrinkage would have been mitigated. There is, however, a weaker paste layer that would have formed on the exterior surface on both sides of the interface. This may explain the localized spike in compressive strain that developed during post-tensioning (Figure 145). The VWG results (Figure 146) were similar to Beam B with a maximum compressive strain of 90 microstrain at the maximum post-tension force.

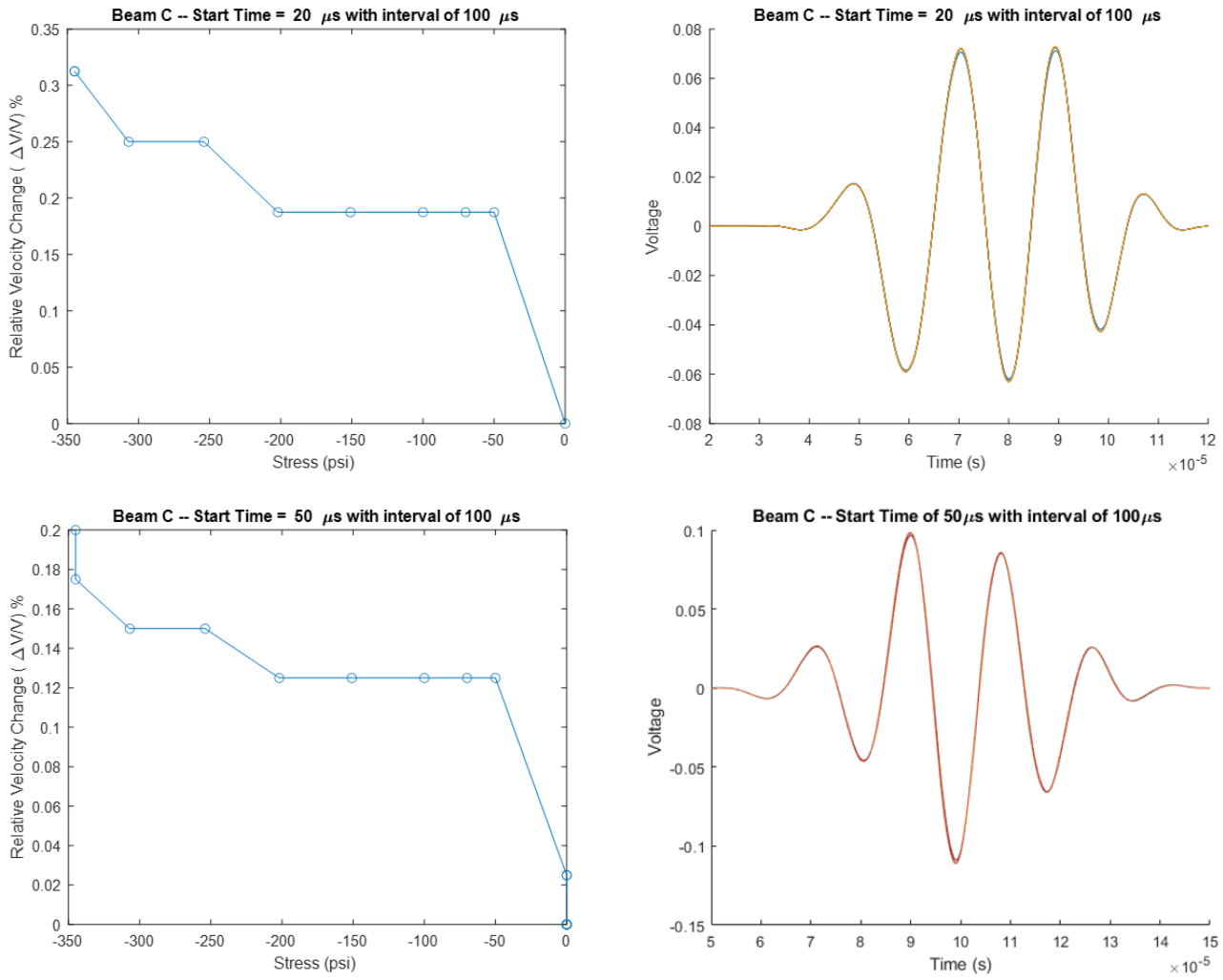

Figure 144. Coda-wave interferometry results for Beam C (post-tensioning)

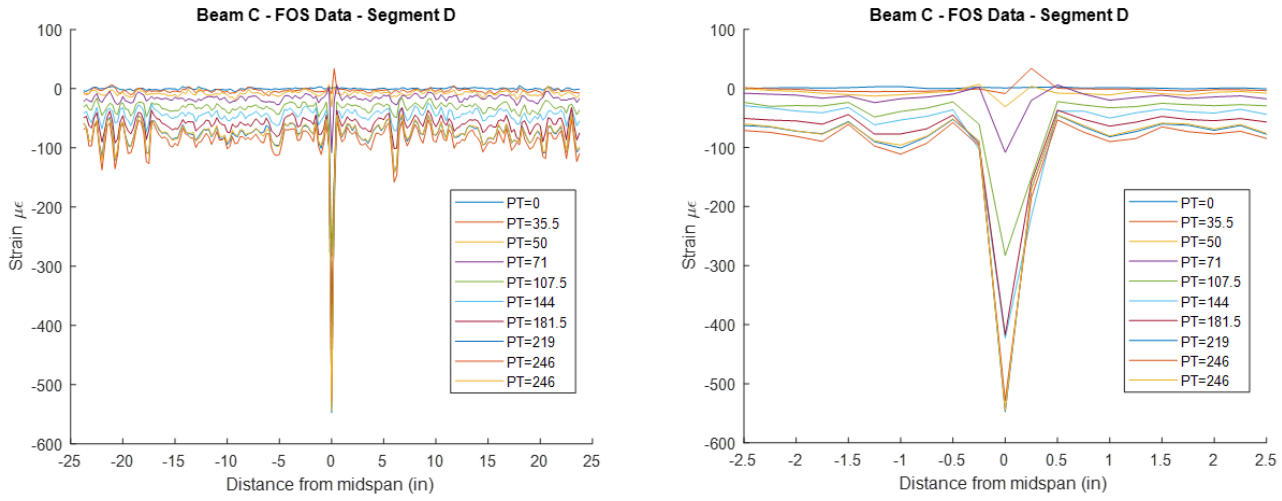

Figure 145. Beam C: FOS data for Segment D

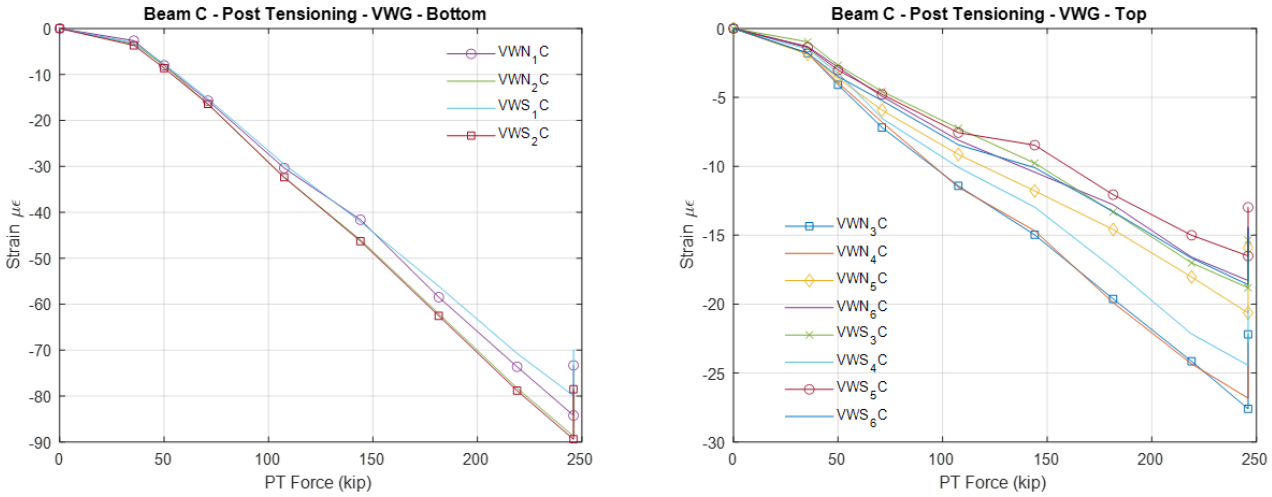

Figure 146. Beam C: VWG Results

5.4.4 Post-Tensioning Conclusions

The most significant observation made during the post-tensioning phase of the study relates to the coda-wave interferometry and FOS results for Beam B. The restrained shrinkage resulting from the simulated closure pour in Beam B led to a weakened concrete interface at the cold joint. When this weakened interface was subjected to minor compressive stress variations (0 to 346 psi), the response of the coda waves varied significantly with respect to amplitude and relative velocity. For Beam A and Beam C, which were not subject to the same degree of restrained shrinkage, the change in coda-wave response from 0 to 346 psi showed very little relative velocity change. The coda-wave plots in Figure 147 are practically indiscernible for Beams A and C at 0 kip and 246 kips of PT force. Beam B, however, experiences a 7.5% increase in relative velocity over the same stress range.

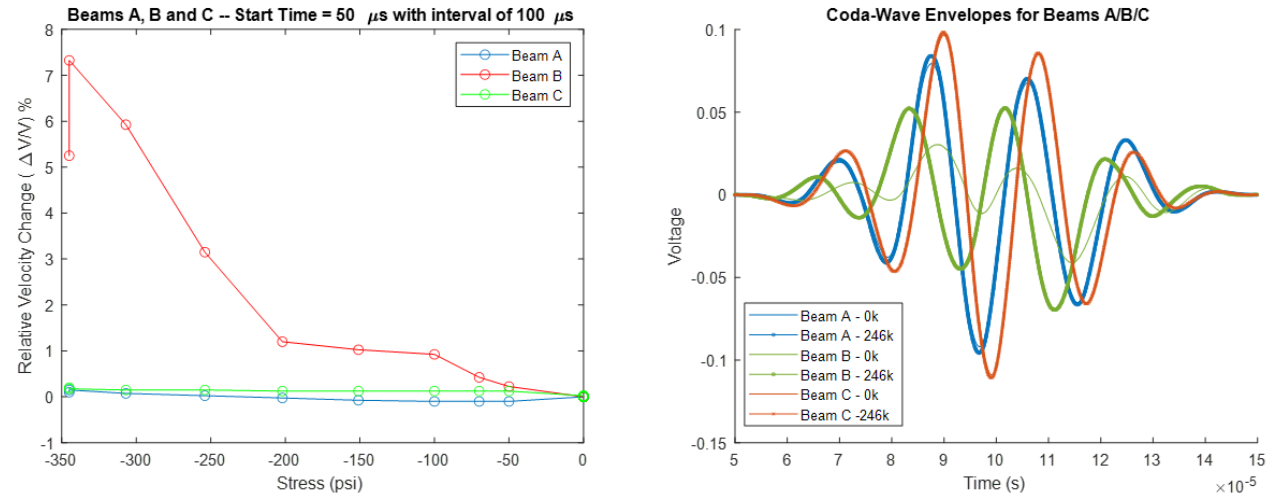

Figure 147. Coda-wave interferometry summary for Beams A/B/C

5.5 Flexural Testing Results

Flexural testing was completed in the FDOT Structures Lab on July 27-28, 2023. Data acquisition was similar to the post-tensioning process. One additional fiber-optic sensor was installed on the bottom tension face of Beam B and Beam C. This ensured that any excessive deformations or spikes that occurred in the side-mounted sensors during post-tensioning would not be a factor during the flexural testing. Another major change was that the ultrasound transducers were placed on the bottom of the tension face spaced at 4 in and centered on the midspan of the beam.

The four-point bending load and corresponding compressive stress on the beam's tension face at midspan are summarized in Table 17. The initial concrete compressive stress of -517 psi at Force = 0 includes the contribution of the post-tension force and the self-weight of the girder. At approximately 30 kips, the concrete stress on the bottom face was estimated to be 0. The anticipated cracking load for the girder was expected at 86 kips using a compressive strength of 5500 psi. The actual compressive strengths of the concrete varied from 7200 psi to 9200 psi.

Table 17. Four-point bending load and corresponding concrete stress on tension face of beam

Force (kip)	$\sigma_{concrete}$ (psi)
0	-517
10	-340
20	-163
30	13.25
40	190
50	367
60	543
70	720
80	897
90	1074*
100	1251*
110	1427*
120	1604*
130	1781*

*Stress value expected to exceed the modulus of rupture of concrete

The loading plan for each beam consisted of six steps: (1) Increase four-point bending load in 10-kip increments until barely-visible cracking was observed. (2) Reduce four-point bending load to 20 kips to reestablish compression on the bottom of the beam. (3) Increase load to 75% of the barely-visible cracking load (BVCL). (4) Continue increasing load in 5-kip increments to a point just beyond the BVCL. (5) Decrease load in 5-kip increments to 75% of BVCL. (6) Decrease load in 20-kip increments to 0. A three-minute pause was held after each load increment for Steps 1 and 2 where ultrasound data were

recorded at each the beginning and end of each hold. A one-minute pause was held at the end of the remaining load intervals and only one ultrasound waveform was captured. This resulted in 54 waveforms for Beam A, 43 waveforms for Beam B, and 53 waveforms for Beam C.

5.5.1 Beam A

Load vs. displacement data for Step 1 are provided in Figure 148. The first and only barely-visible crack was observed at a load of 120 kip. The first major indication of crack formation from the FOS was observed at a load of 100 kip (Figure 149). Since the constant-moment region spanned a total distance of six feet, the location of cracks was unpredictable. It appears that around the 120-kip load level a crack did open near the midspan of the beam that passed between the two ultrasound transducers.

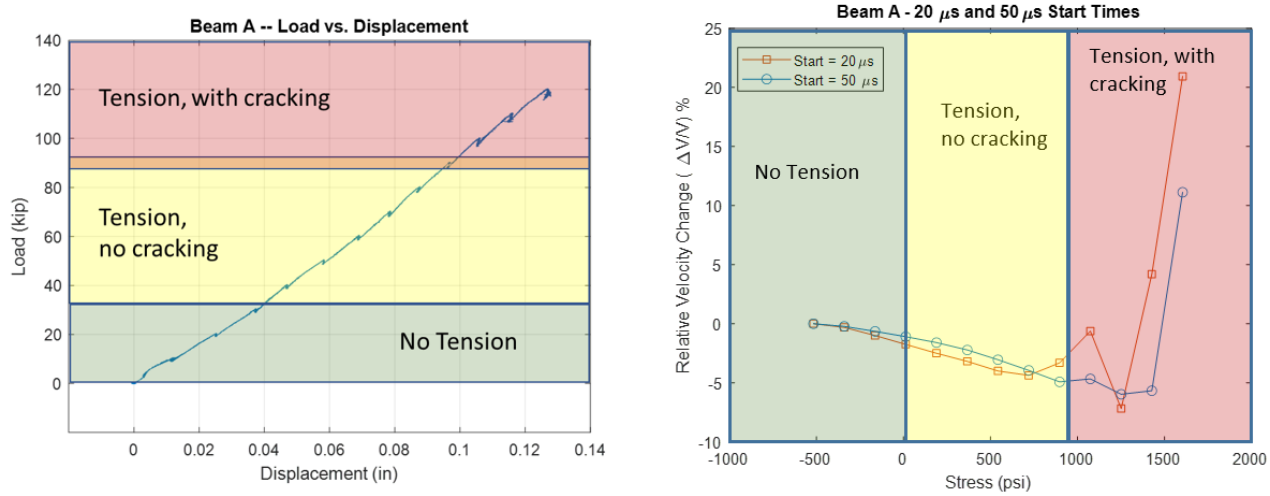

Figure 148. Load vs. deflection and CWI results for Beam A (Step 1: 0 to barely-visible cracking load)

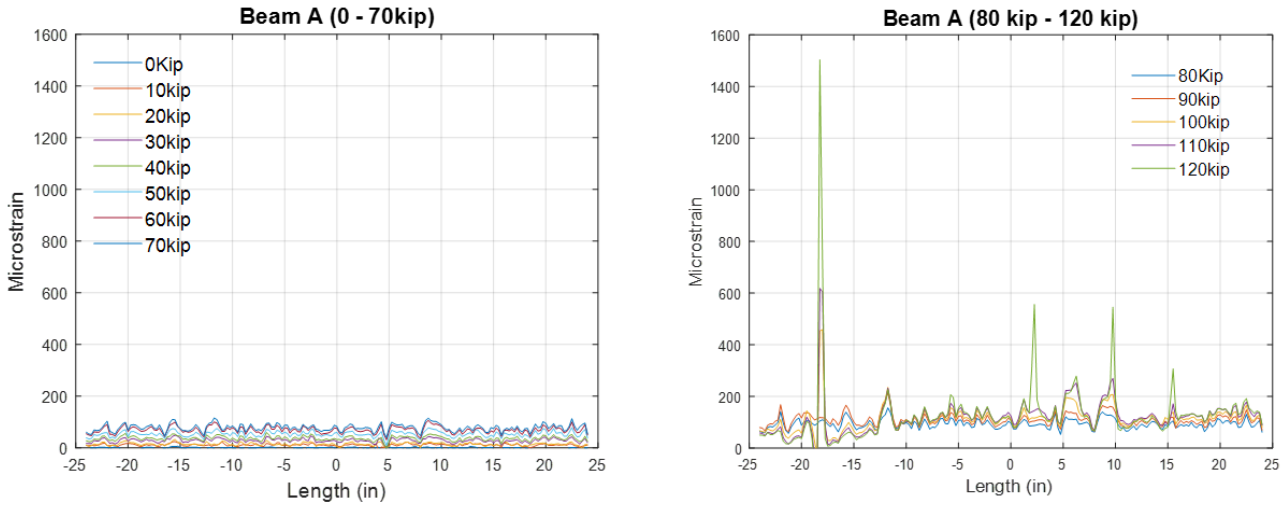

Figure 149. FOS data for Beam A (Segment D on FDOT system)

The relative velocity change (ΔV/V) measured through coda-wave interferometry for load values between 0 and 80 kip are summarized in Figure 150. The start time for these waveforms was 50

microseconds. The relationship between ΔV/V and stress on the bottom face of the beam is nonlinear but the overall coherence of the waveforms through this stress level is high. Overall, the velocity change from -517 psi through 897 psi was -5.4%, which is consistent with the expected behavior of a decrease in velocity as the stress increases from compression through tension.

When the load was increased from 80 kip to 120 kip, the overall coherence of the waveforms decreased dramatically (Figure 151). The relative velocity trend begins to follow a different path and ultimately culminates with a major jump from -5.5% to +11% when the load increases from 110 to 120 kip. The positive jump is not indicative of an increase in ultrasound velocity. The coherence of the waveforms begin to vary significantly from the P = 0 baseline around P = 110 kip and the phase shift is so dramatic that a large jump in the positive direction is produced by the interferometry algorithm. This is likely the result of an increase in path length that the ultrasound is required to travel due to the internal cracking that occured at these high load levels.

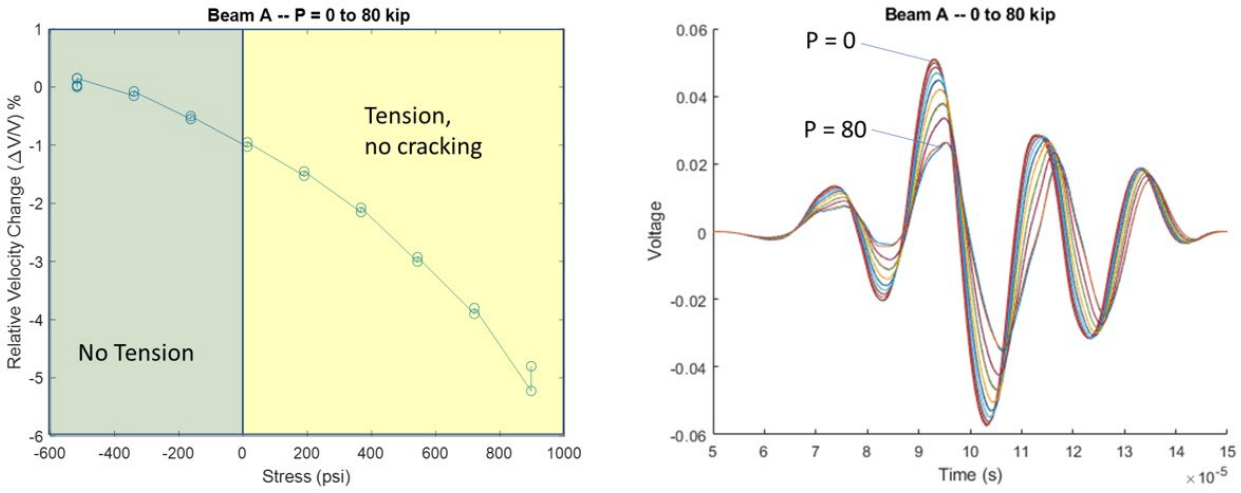

Figure 150. Coda-wave interferometry results for Beam A (four-point bending: 0 to 80 kip, start time = 50 microseconds)

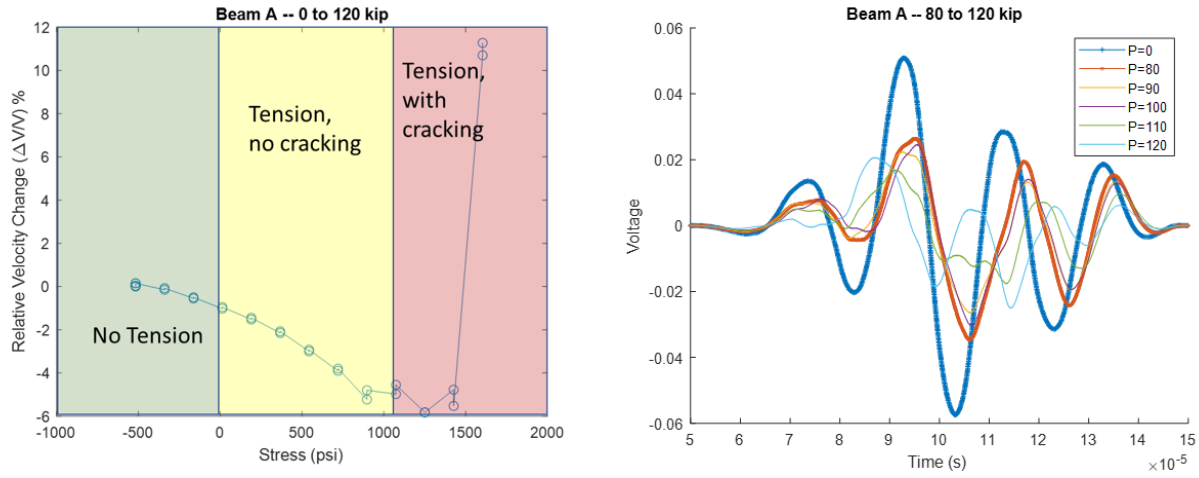

Figure 151. Coda-wave interferometry results for Beam A (four-point bending: 80 to 120 kip, start time = 50 microseconds)

Another important question is how the ultrasound waveform responds when the load is reduced and the post-tension force re-engages the bottom of the beam in compression. Based on the data recorded during the initial load step to 120 kips (Step 1), it appears that a crack formed outside of transducers between 90 kips and 100 kips. As the loading increased from there, a crack formed between the transducers. The relative velocity measurements for the remaining load steps are provided in Figure 152. Depending on the start time chosen for the interferometry (20 microseconds or 50 microseconds), slightly different behavior was observed during the unloading segments. The most important finding, however, is that once the crack opens, a large apparent increase in velocity occurs as a result of incoherent waveforms. Once the load is reduced and the crack closes, the waveforms assume a similar shape to the pre-cracked signal and then continue to exhibit an increase in velocity as the stress in the concrete moves from tension to compression.

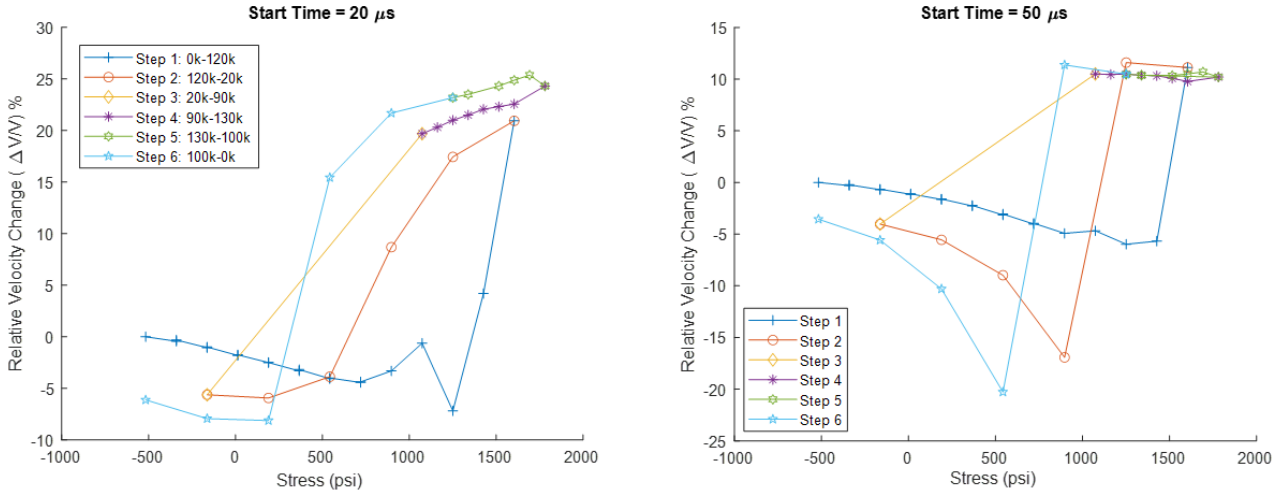

Figure 152. Coda-wave interferometry results for Beam A (all six load steps – start time = 20 and 50 microseconds)

5.5.2 Beam B

The initial load step for Beam B proceeded from 0 kip to 70 kip. During the load increment from 60 kip to 70 kip, a minor shift in the load vs. displacement curve was observed (Figure 153) and a decision was made to end Step 1. The FOS data indicated that a crack was forming at the cold-joint location by the end of the very first load increment of 10 kip (Figure 154). This was surprising since the bottom face of the beam should have experienced compressive stress due to post-tensioning for four-point bending load values between 0 kip and 30 kip. The initial load increment of 10 kips should have reduced the maximum compressive stress in the cold joint from -517 psi to -340 psi. Overall, it remains unclear how the weakened concrete interface at the cold joint influences the FOS strain response at the midspan of the beam. The response appears to be very sensitive to small changes in stress. It should also be noted that the FOS gauge was reading an increase in strain over the middle one inch of the beam. This may be an indication that the fiber-optic cable experienced localized debonding due to high strain in the vicinity of the crack at midspan.

Coda-wave interferometry results for Beam B varied significantly from Beam A. One critical observation was that the interferometry algorithm for determining the relative velocity change was extremely sensitive to the start time and the width of the window. Three plots of stress vs. relative velocity change are provided in Figure 153. The small-scale/proof-of-concept testing and large-scale post-tensioning tests had indicated that a start time of 50 microseconds and a window width of 100 microseconds was appropriate for capturing the change in relative velocity as a function of stress level. For Beam B, these parameters resulted in an initial increase in relative velocity for the first two load steps, which is not consistent with theory (an increase in stress – going from more to less compression – should result in a decrease in velocity. This unexpected trend was amplified when the start time was shifted to 20 microseconds while retaining the 100-microsecond time window. The relative velocity appeared to increase for the first two load steps and then began to decrease to a maximum value of -20% at P = 70 kip. The third data series provided highlights results for a start time of 20 microseconds and a time window of 50 microseconds. These parameters exhibit the expected behavior with a very significant decrease in relative velocity as the load increases from 0 kip to 70 kip.

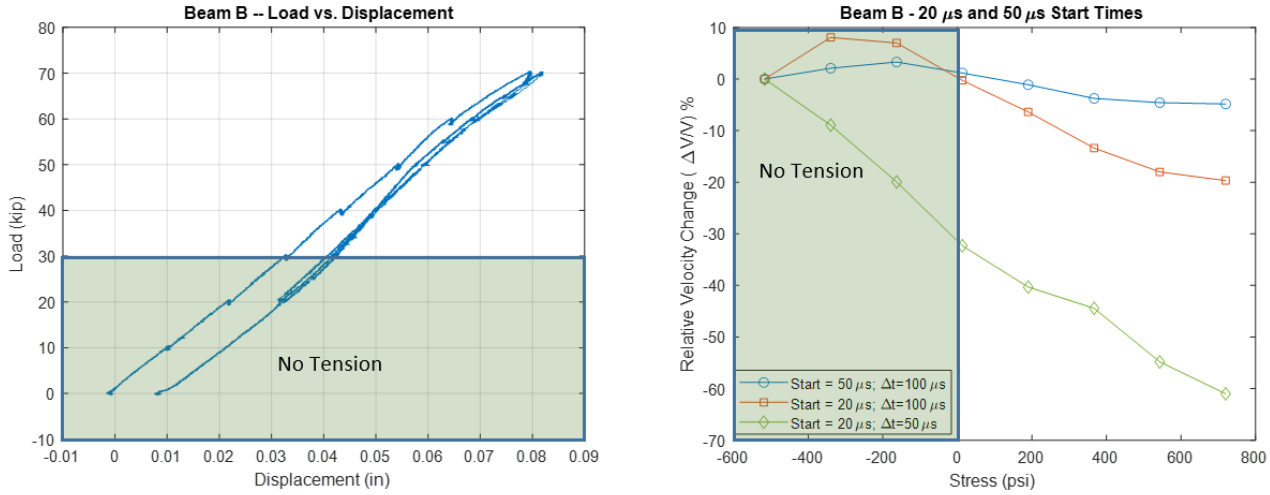

Figure 153. Load vs. deflection and CWI results for Beam B (Step 1: 0 to barely-visible cracking load)

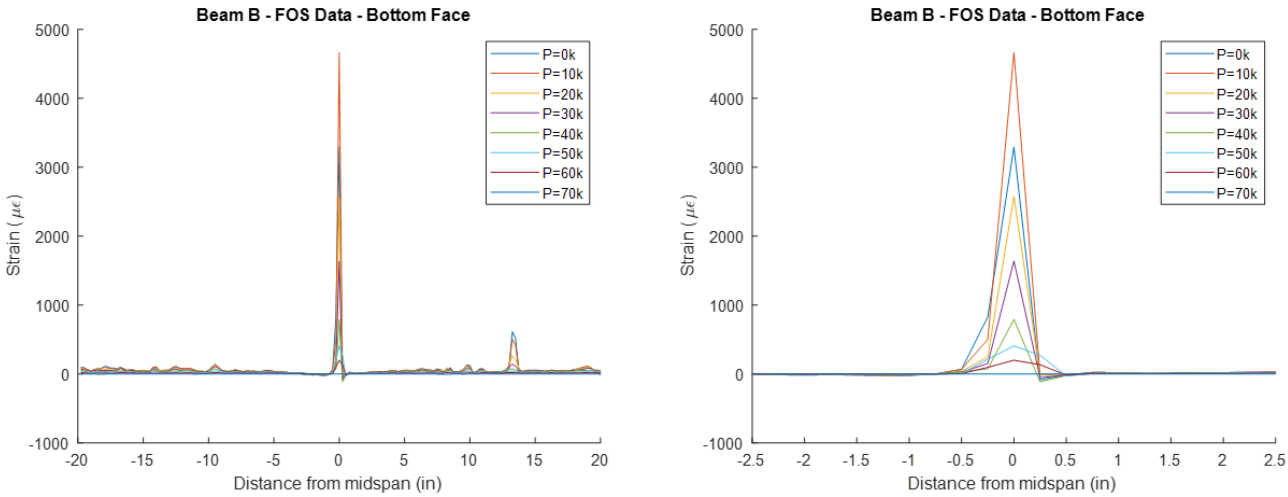

Figure 154. FOS data for Beam A (Bottom fiber on FDOT system)

A closer inspection of the waveforms obtained with a start time of 20 microseconds (t_o = 20) and a window of 50 microseconds (Δt = 50) illustrates how changing the window can lead to different interferometry results. The waveforms obtained for P=0k, P=10k, and P=20k begin to trend in the negative direction around t = 2.5 microseconds before reaching a local minima between 3 and 3.25 microseconds. These waveforms then experience local maxima around 4 microseconds. The remaining waveforms for P=40k to P=70k begin to trend positive around 3 microseconds and then experience local maxima around 3.75 microseconds(all at significantly lower amplitude than the lower-load-level waveforms). The P=30k waveform is positioned in between these two groups. The blue dots on the left graph in Figure 155 indicate the local peaks that are captured by the interferometry algorithm that results in the near-linear stress vs. relative velocity curve in Figure 153. While capturing these peaks does produce a stress vs. relative velocity curve that is consistent with theory (decreased velocity with increasing tensile stress), it does not account for the fundamental difference in the shape of the curve, which may be due to cracking.

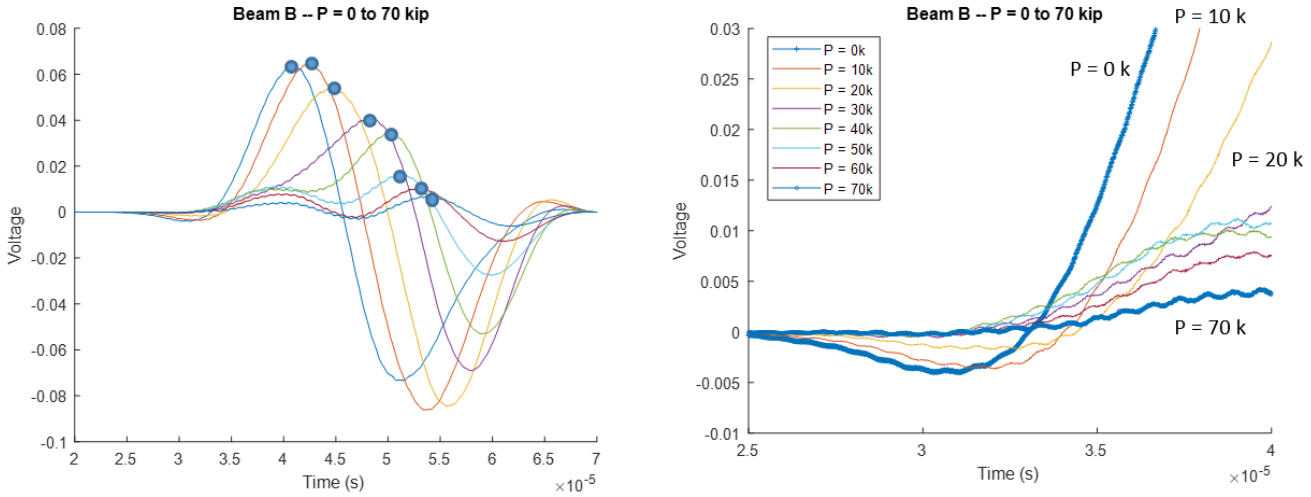

Figure 155. Ultrasound waveforms for Beam B (P=0k to P=70k; t_o = 20 and Δt = 50)

This phenomenon is illustrated again when the time window is decreased from 50 microseconds to 30 microseconds (Figure 156). The curves for P=0, P=10, and P=20 follow the expected trend, but the shortened window clips the upward trend for the P=30 curve, indicating an increase in relative velocity from P=20. For the remaining curves, the local maxima correspond to a completely different peak than the Δt = 50 version of the waveform, which results in a large jump in the apparent relative velocity. Again, this is not due to the change in stress alone, but rather a change in the overall pathway of the ultrasound due to cracking in the concrete.

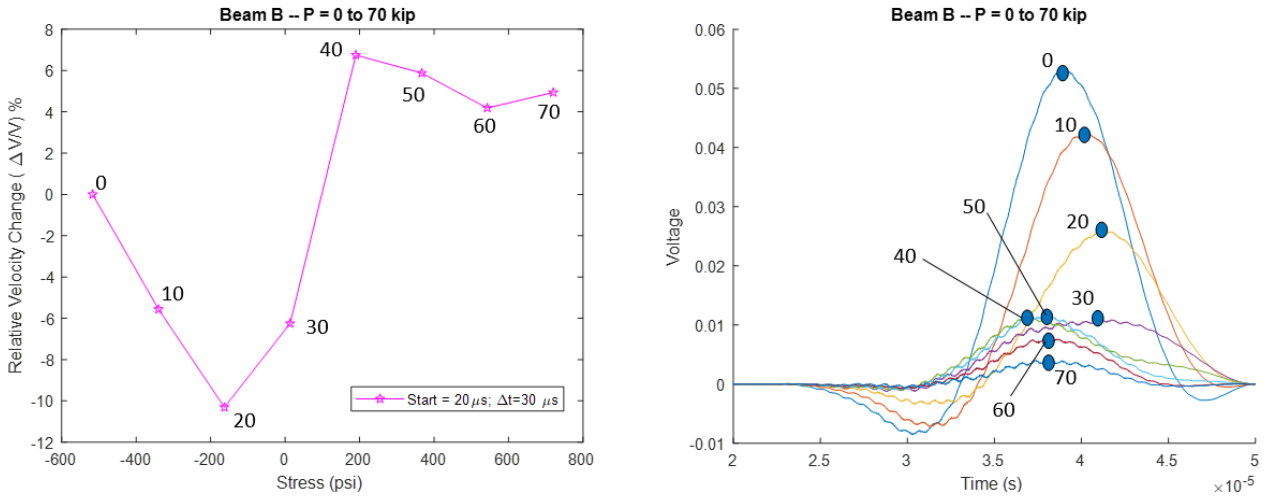

Figure 156. Interferometry results and ultrasound waveforms for Beam B (P=0k to P=70k; t_o = 20 and Δt = 30)

Interferometry results for the load reversals applied to Beam B are summarized in Figure 157. The start time for all three plots are held constant at 20 microseconds while the window length was evaluated at 30, 50, and 100 microseconds. For Δt = 50 and Δt = 100, the relative velocity change decreases with increased stress level and stress reversals show the response following on roughly the same trajectory. For stress levels greater than zero, the Δt = 50 curves for each step are roughly linear. The Δt = 30 curves display the large positive jump in Step 1 as the load increases from 10 kip to 30 kip. Once the load is reduced from the maximum at 70 kips and cycled back to 20 kips, the relative velocity tracks on a similar path. It is difficult to draw any clear conclusions from these curves other than they are highly variable depending on the start time and the window width. The fact that reinforcing bars are present between the two segments could be affecting the ultrasound results even at higher load levels where the concrete is assumed to have cracked.

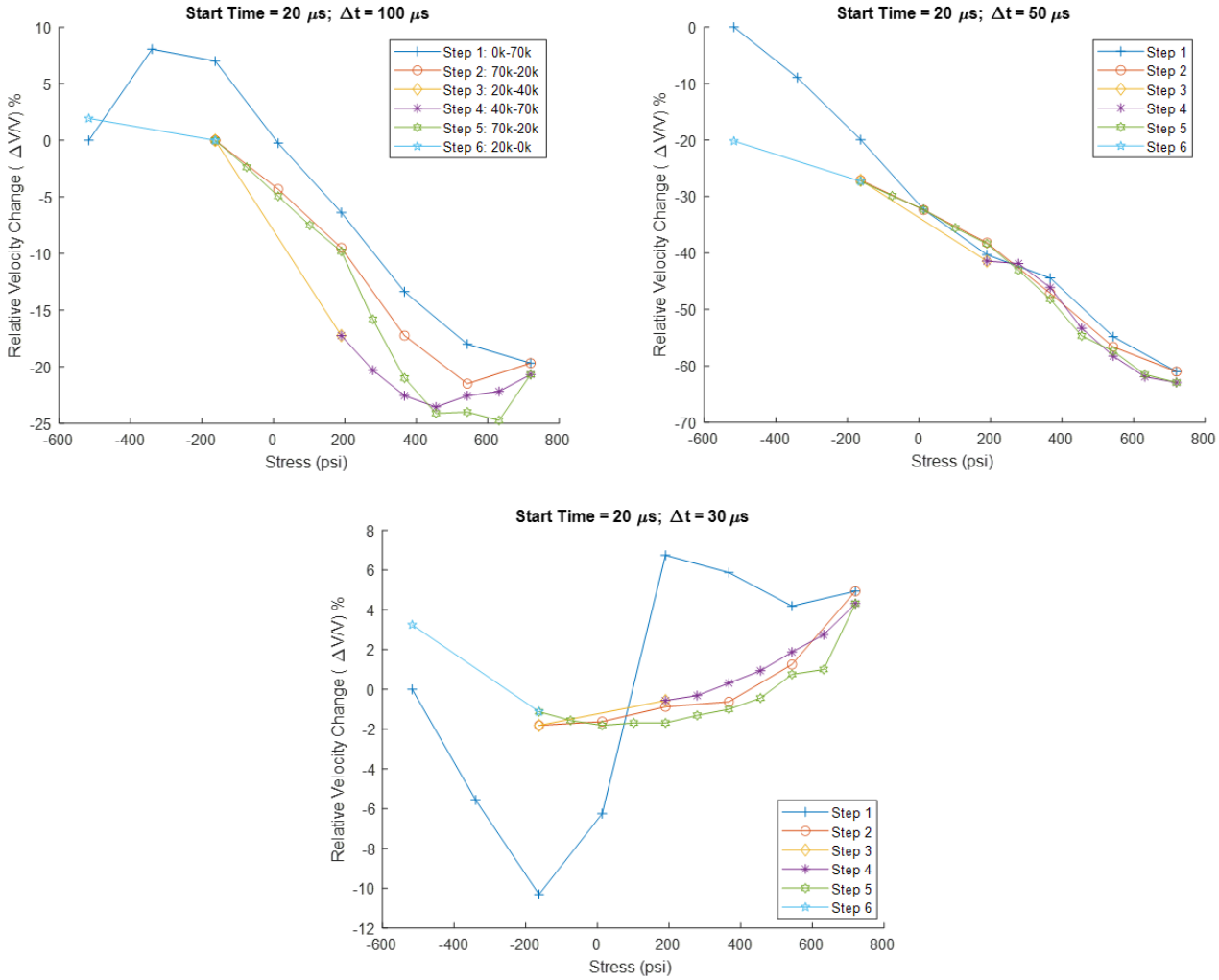

Figure 157. Coda-wave interferometry results for Beam B (all six load steps – to=20, Δt = 30, 50, 100)

5.5.3 Beam C

The initial load step for Beam C went from 0 kip to 81.2 kip (Figure 158). The loading was paused at 80 kip to obtain an ultrasound measurement. Soon after the load was increased for the next increment, a large displacement occurred with no corresponding increase in load. The actuator was stopped and a visual inspection revealed that a crack had formed at the interface between the two segments. Recall that there are no reinforcing bars between the segments. Examination of the ultrasound data indicated an abrupt shift in the relative velocity between P = 70 kip and P = 80 kip. This suggests that the crack likely formed at some point in this load increment but only became discernable in the load vs. deflection plot once the load exceeded 80 kips. Once again, the relative velocity change depended on the start time and the window width, but the response was stable and follows a similar trajectory to what was observed for Beam A (as opposed to Beam B, which had much higher variability and inconsistency regarding the direction of the curves).

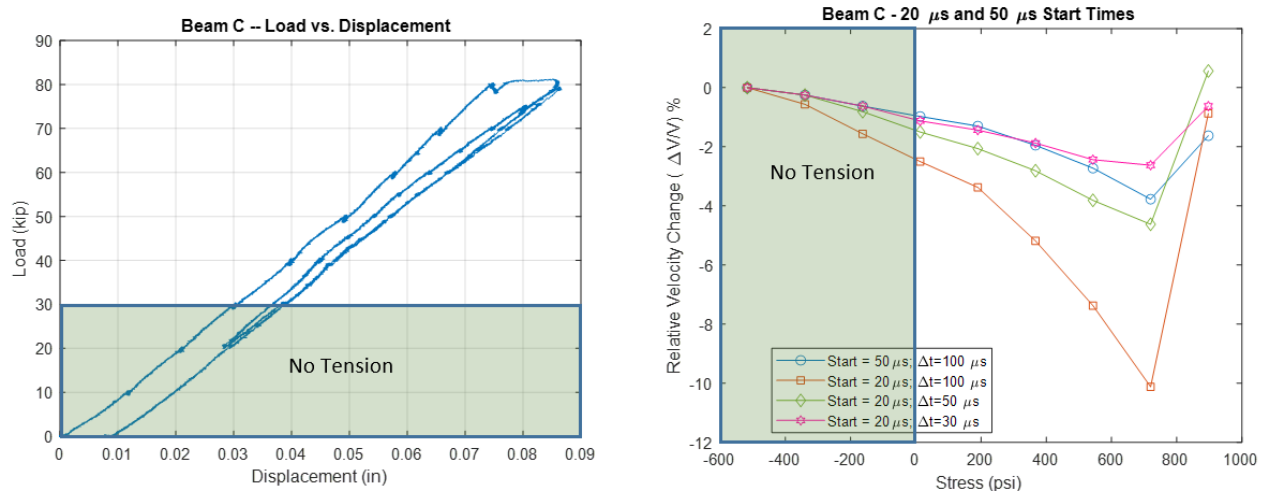

Figure 158. Load vs. deflection and CWI results for Beam C (Step 1: 0 to barely-visible cracking load)

Somewhat unexpectedly, the fiber-optic sensor bonded to the bottom of Beam C over the middle 40 in exhibited a similar response to the sensor bonded to Beam B. All indications from the ultrasound suggested that the epoxy-bonded interface did not crack until the load approached or exceeded 80 kips. Load levels as small as 10 kips resulted in a spike in strain at the interface between the segments (Figure 159). These spikes also occurred over a 1-inch gauge length, which could indicate debonding of the sensor due to localized cracking near the surface. It should be noted that spikes were also observed at the segment interface on Beam C during stressing, though not quite as severe as Beam B. This result does raise some interesting questions about strain measurements using FOS for segmental bridges. Our results indicate that these sensors are extremely sensitive to movement at segment interfaces – both epoxy-bonded and cast-in-place closure pours. Unfortunately, the surface strain data does not provide a clear understanding of what is happening through the entire segment interface.

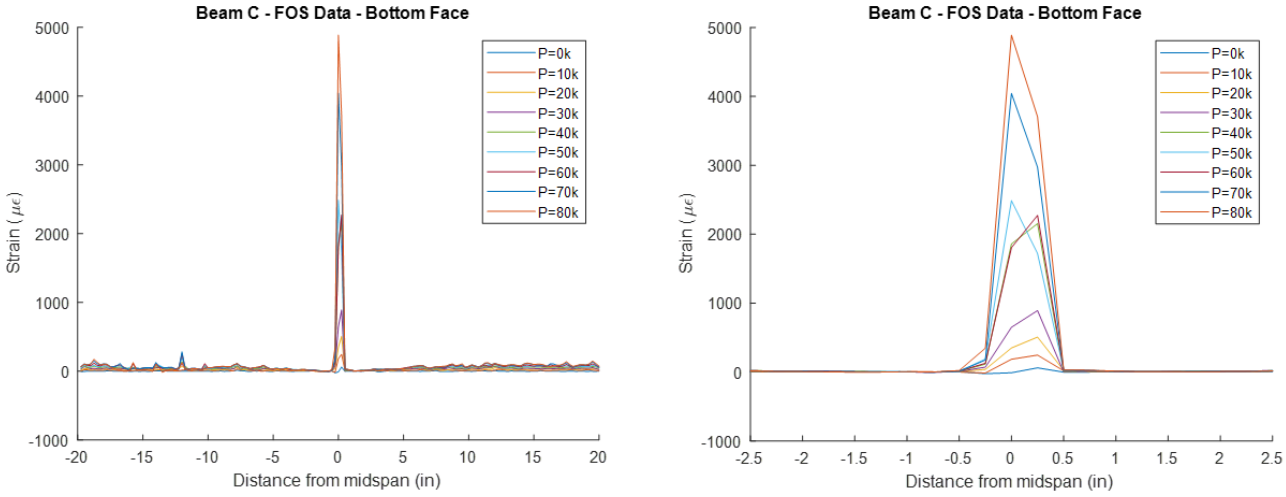

Figure 159. FOS data for Beam A (bottom fiber on FDOT system)

The coherence of the waveforms obtained during the first load step (P = 0 kip to P = 80 kip) support the conclusion that the interface region did not crack before a load level of 70 kip was obtained (Figure

160). For t_o = 50 and Δt = 100, the amplitude of the waveforms remains more consistent than what was observed for Beam A, while the decrease in relative velocity is only 3.8% (compared to -5.4% for Beam A, which had no cracking). A similar trend is observed t_o = 20 and Δt = 50 (Figure 161). One minor difference is that the amplitude of the waveform decreases dramatically at the P = 80 kip load level. This is consistent with the behavior observed in Beam B when cracking occurred near the 0-stress level.

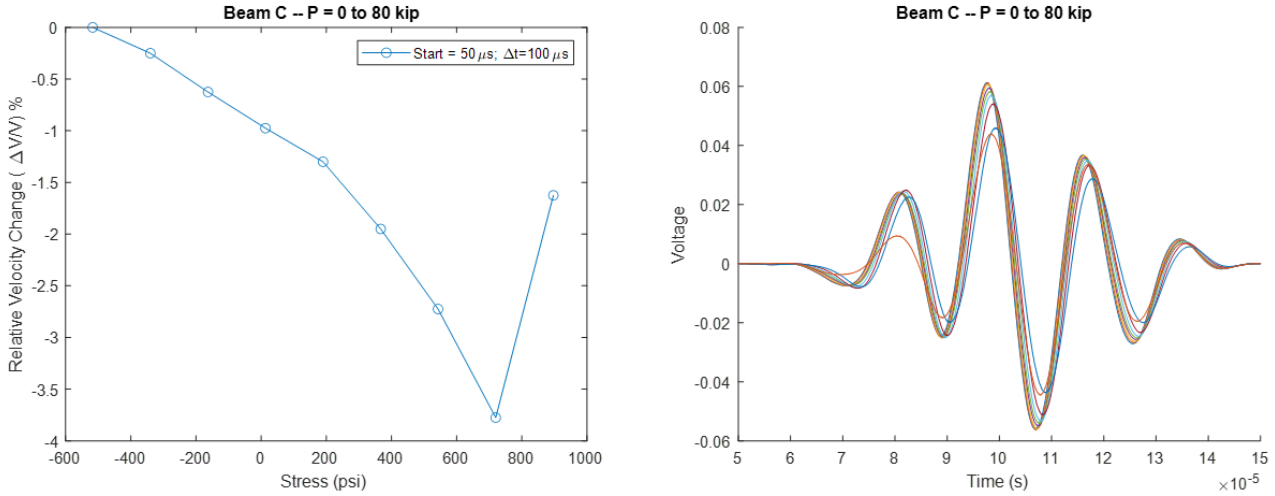

Figure 160. Ultrasound waveforms for Beam C (P=0k to P=80k; t_o = 50 and Δt = 100)

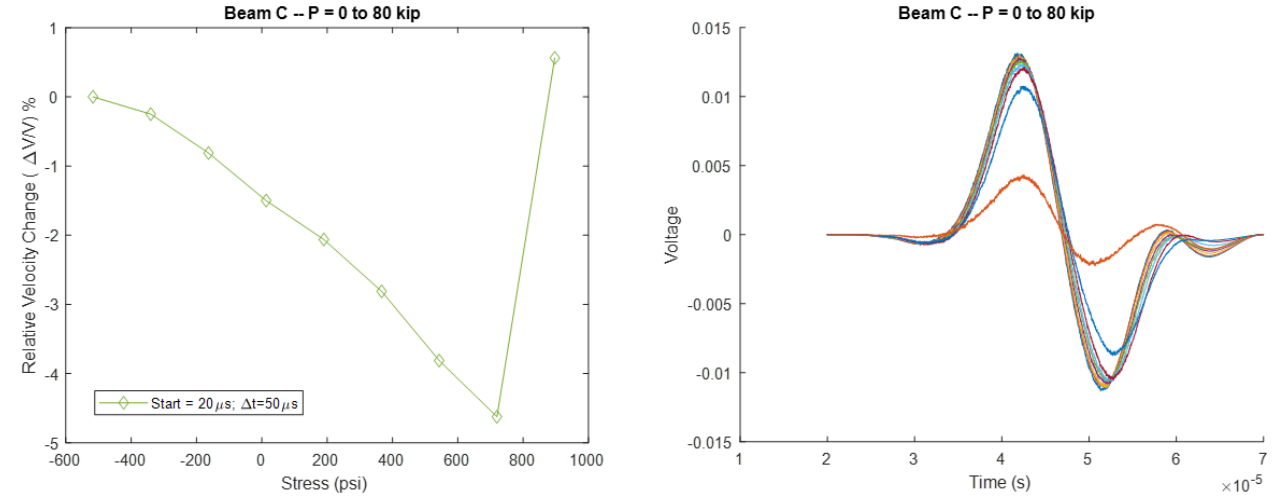

Figure 161. Ultrasound waveforms for Beam C (P=0k to P=80k; t_o = 20 and Δt = 50)

Interferometry results for the load reversals applied to Beam C are summarized in Figure 162. What is notable in these results, especially for Δt = 50, is the large shift in relative velocity that occurs when the section cracks on the increasing load step but then recovers to the path established during Step 1 when the load is removed and the post-tensioning reestablishes contact between the surfaces on the bottom half of the beam.

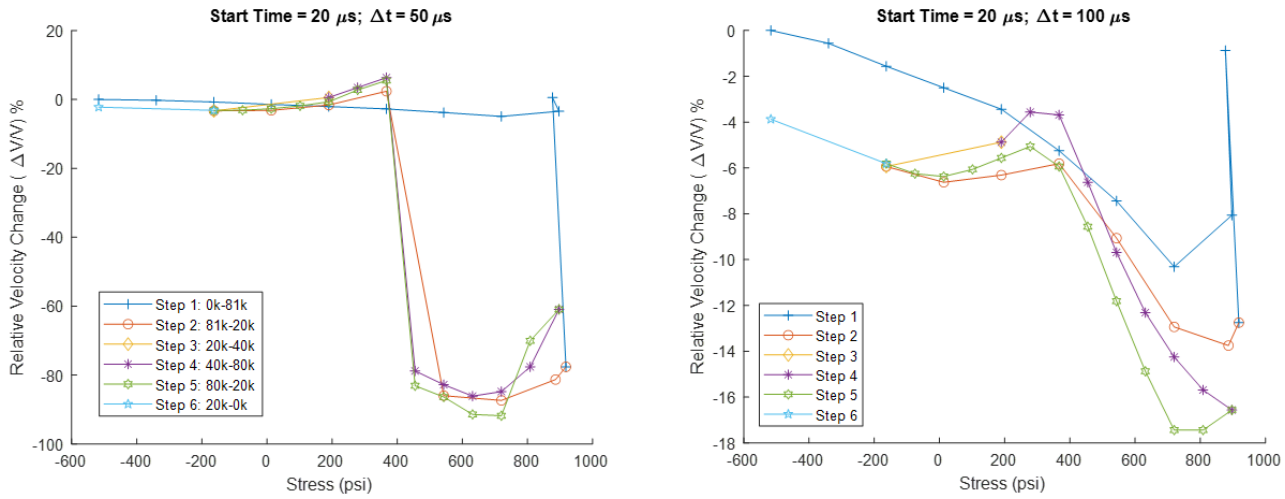

Figure 162. Coda-wave interferometry results for Beam C (all six load steps – to=20, Δt = 50 and 100)

6 Conclusions

6.1 Summary of Findings

The overall objective of this research was to investigate inspection methods for post-tensioned structural systems that rely on flexible fillers for corrosion protection. After an extensive literature that focused on traditionally grouted tendons, this work was divided into two broad categories: (1) direct inspection of the strands/tendon for signs of damage or loss of force; and (2) indirect inspection of the post-tensioned concrete for signs that it may be nearing serviceability limits. This was represented as the region between LT-2 and LT-3 in Figure 163.

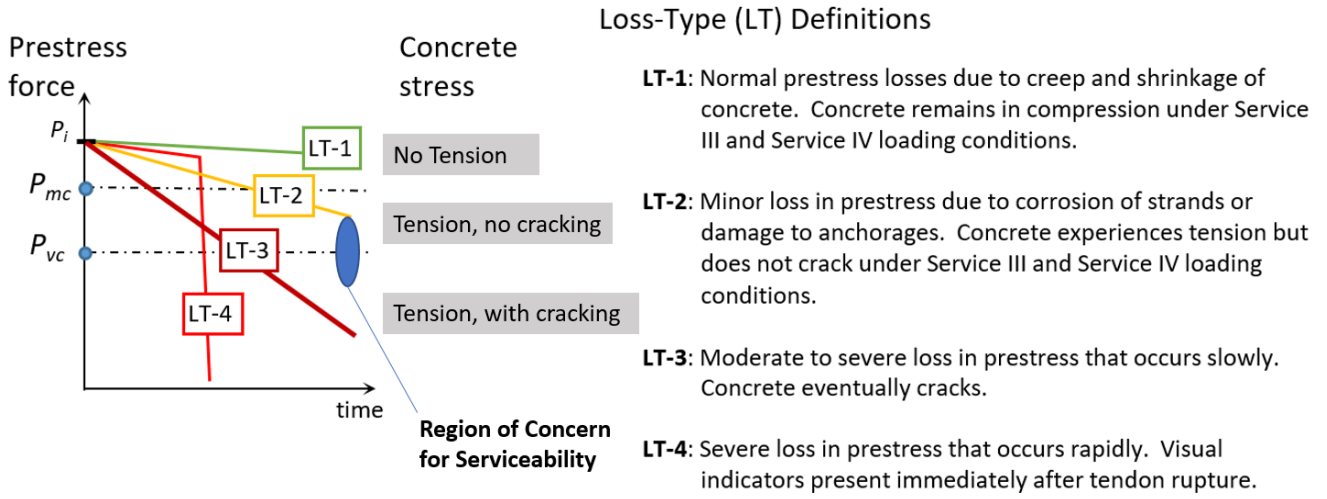

Figure 163. Varying degrees of pre-stress loss and corresponding impact on concrete stress level.

The radiography method does have potential for direct evaluation of tendons. Our findings are summarized in Figure 164. For Type 5 anchorage protection details, strand and wedge-grip dislocations beneath the HDPE cap may be identified without having to remove the cap and expose the flexible filler. Both types of radiography equipment (low-power medical-grade and high-power construction-grade) should be suitable for these inspections. For the case of internal ducts, only the high-powered equipment was shown to be feasible if the overall thickness of the concrete was less than 12 inches. Additional limitations will apply depending on the accessibility of the duct and the position of the damage within the tendon relative to the radiation source and the detector. For external ducts, both types of equipment can be used to verify the location of the tendon within the duct and, potentially, any strand or wire breakage. Detectability will depend on the location of the damage with respect to the radiation source and the detector.

	Anchorage (Type 5)		Internal Duct				External Duct			
	Wedge grip seating	Strand-end location	Tendon Location in Duct	Broken Strand	Broken Wire	Void in Filler	Tendon Location in Duct	Broken Strand	Broken Wire	Void in Filler
POSKOM PXM-20BT										
YXLON										

Legend	
	Recommended
	Detection possible, but access- and location-dependent
	Not Recommended
	Additional research needed

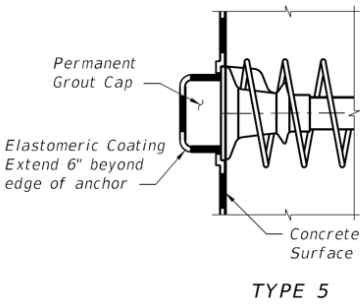

Figure 164. Summary of results: radiography

Two methods were evaluated for the indirect assessment of the stress level in concrete: (1) thermoelasticity and (2) diffuse ultrasound interferometry. The thermoelasticity method did not yield any viable inspection options based on the small-scale proof-of-concept testing that was completed in this study. The ultrasound interferometry, however, was able to provide a strong indication of the presence of cracking well before any visual indictors were present. This was demonstrated for Beam A where cracking occurred at a load level of 90 kips, but cracking wasn't visible until a load level of 120 kips. The level of cracking observed at 120 kips was barely visible to the point where detection under field conditions would have been highly unlikely. One potential shortcoming, however, was that the crack needed to pass between the ultrasound transducers in order to generate the detectable signal. This may pose challenges for non-segmental construction.

The most useful finding from the large-scale experimental testing is summarized in Figure 165. These results include ultrasound interferometry data for Beam A, Beam B, and Beam C, all plotted on the same vertical scale for relative velocity change. The results were obtained through a stress range of -540 psi through 800 psi, which effectively covers the "region of concern for serviceability" in Figure 163. Beam A and Beam C, which are not believed to have experienced cracking through this stress range, show a 5% to 10% variation in relative velocity response across the entire stress range. Furthermore, the relative-velocity response maintains similar shape characteristics across the range of start times and window widths that were investigated. Beam B, on the other hand, experienced a high degree of variability in the relative velocity response (as high as 60%), and the overall shape of the response was highly dependent on the start time and window width. Prior to testing, we did not anticipate that the simulated closure pour would experience shrinkage and provide a damaged interface prior to post-tensioning. It was also unclear the extent to which this may also be occurring in in-service closure pours.

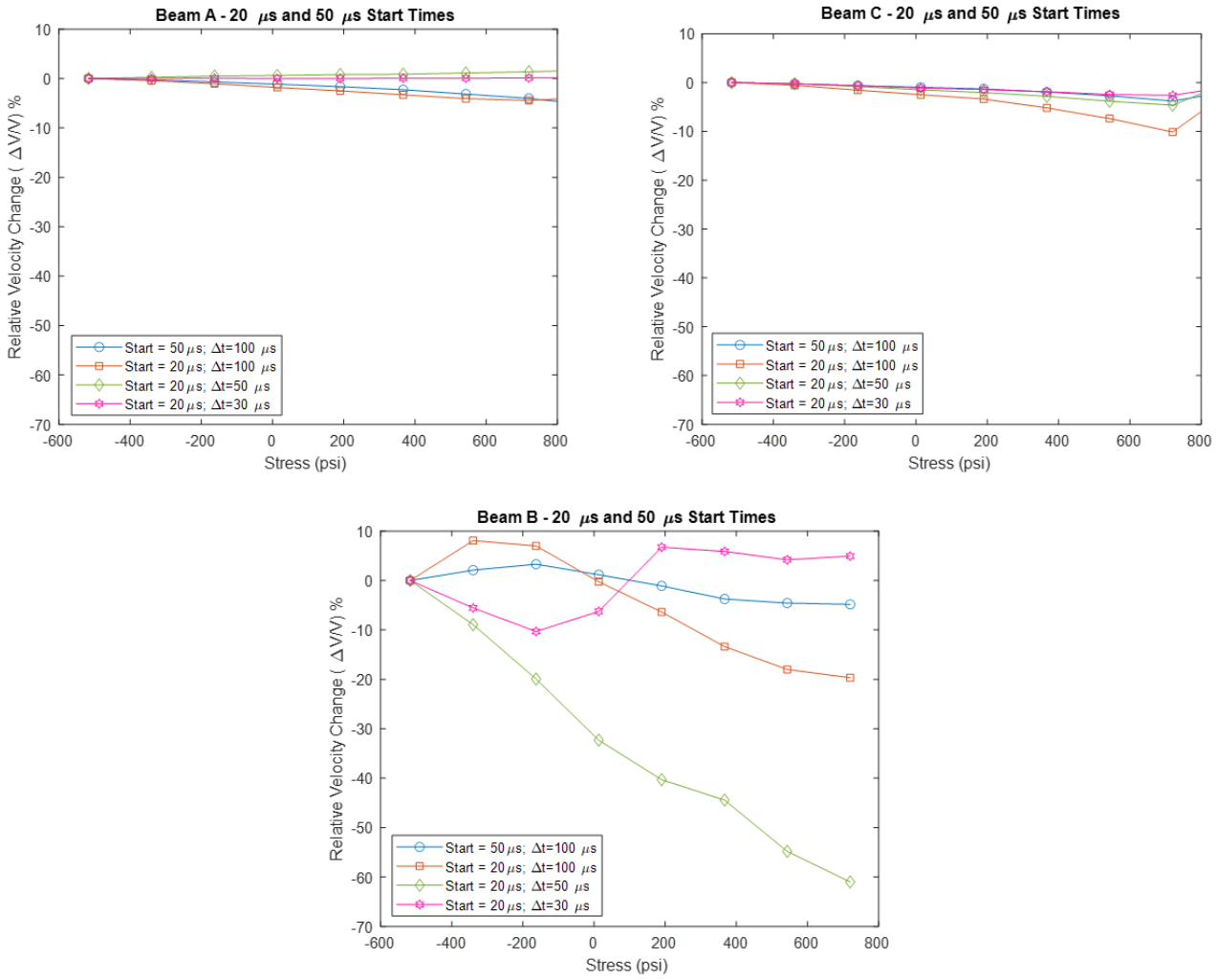

Figure 165. Summary of ultrasound interferometry results for Beams A, B, and C.

6.2 Recommendations for Future Research

While ultrasound interferometry generated promising results for evaluating the cracked state of a post-tensioned concrete structure, there are several items that will require additional research before this method can be successfully deployed for an in-service bridge. Most notably, the current study relied on laboratory-controlled four-point bending to initiate cracking in the large-scale specimens. It might be possible to apply loads with this level of control during an in-service load test for a bridge, but that poses numerous logistical challenges. An alternative approach would be to rely on diurnal temperature effects to initiate a measurable stress change at critical sections on the structure. The ultrasound interferometry method should indicate if the concrete experiences tension because of the diurnal thermal loading. If an acceptable stress range can be established for a structure at a specific location, this stress range can be assessed periodically during enhanced inspections for deviations or excursions into the tension region. The general concept is illustrated in Figure 166.

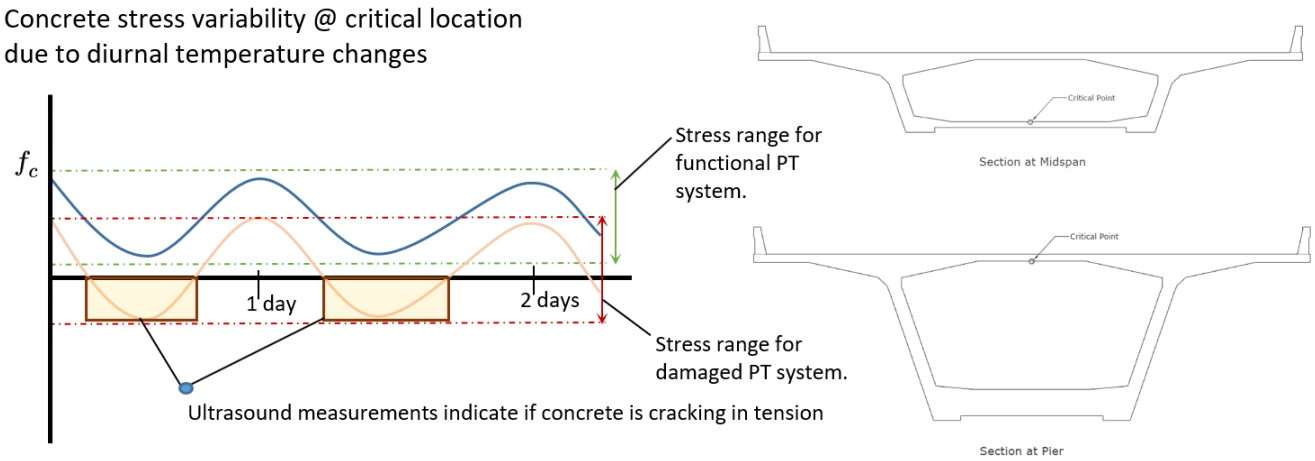

Figure 166. Diurnal temperature effects and stress variability for functional and damaged PT systems

A preliminary finite element analysis conducted for this study indicates that a modest temperature gradient of 35 °F over the top flange of a Type 3 AASHTO (Figure 167) girder is sufficient to generate measurable stresses in the beam. This includes a compressive stress range of ~800 psi in the top flange and a tensile stress range of 250 psi in the web. The magnitudes of thermally-induced stresses is well documented for segmental bridges and should provide ample excitation for the ultrasound interferometry to detect cracking.

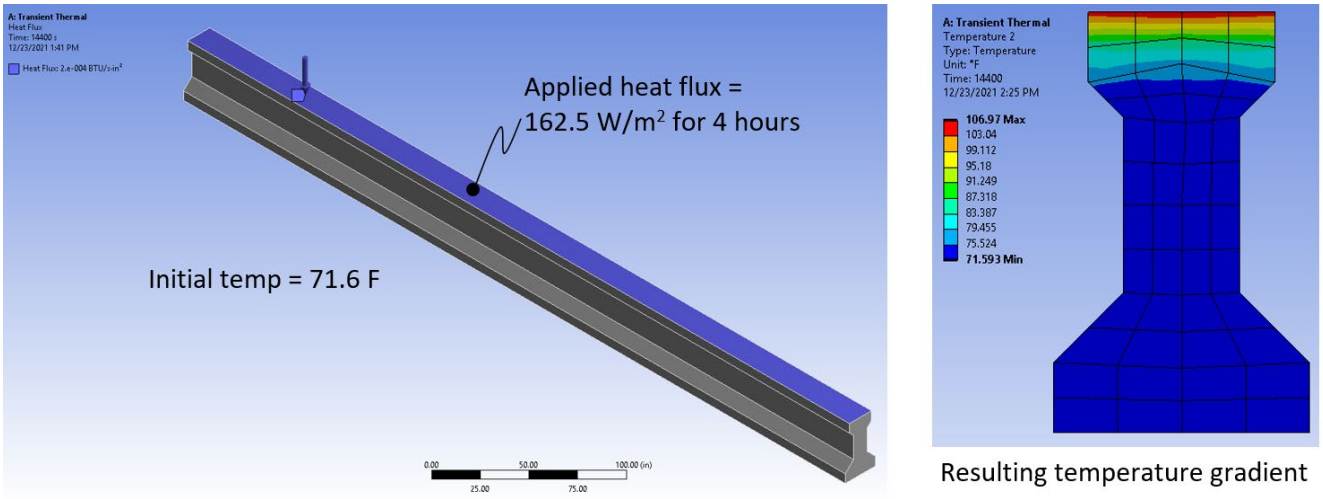

Figure 167. Finite element model for thermal gradient in Type 3 AASHTO Girder.

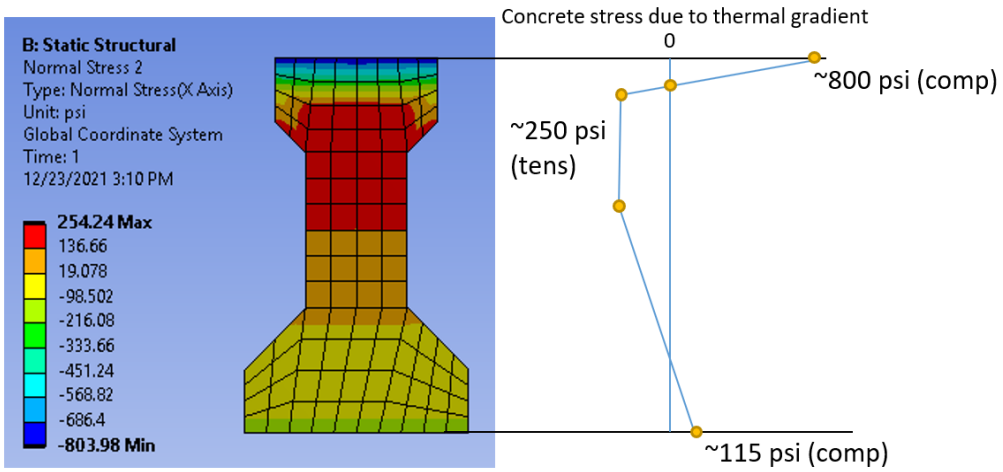

Figure 168. Thermal stresses due to temperature gradient

To capture the stress effects of thermal loading, one ultrasound transducer would need to be bonded on each side of a joint in a segmental bridge. The ultrasound pulse could then be generated periodically over a 24- to 72-hour period to capture the range of thermal stresses. The resulting velocity shift could then be plotted as a function of time (instead of stress) to produce a graph similar to those obtained in the current study. Stress effects due to vehicle loading may also influence the results, but, if the segment joint is not actively experiencing cracking, the shape characteristics for the suite of curves developed for different start times and window intervals should remain consistent.

A final issue that requires consideration is whether or not ultrasonic energy generated by something other than the transducer might alter the captured signal. This may limit the efficacy of the interferometry if errant or stray signals are incident at the receiver.

The following is a summary of recommended next steps for future research:

1. Time-varying finite element analysis of typical post-tensioned structures subjected to diurnal temperature changes.
2. Investigate the impacts of diurnal temperature effects on the three large-scale specimens used in the current study. These specimens can be exposed to thermal loading in the storage yard of the FDOT structures lab.
3. Trial deployment on an in-service post-tensioned bridge to evaluate the efficacy of the post-tensioning system. This work would serve as a proof of concept for in-service structures.

7 References

1. FDOT (2016). *FDOT Structures design guidelines.* Retrieved December 8, 2020 from, https://fdotwww.blob.core.windows.net/sitefinity/ docs/default-source/structures/structuresmanual/2016jan_structures_manual1096382794.zip.

2. FDOT (2014). *FDOT SDG Bulletin 14-06 – Revisions to policy for post-tensioning tendons*. Retrieved 8 December 2020 from https://fdotwww.blob.core.windows.net/sitefinity/docs/default-source/structures/bulletins/2014/sdb14-06.pdf.

3. FDOT (2021). *FDOT Structures Design Guidelines*. Retrieved December 8, 2020 from, https://fdotwww.blob.core.windows.net/sitefinity/docs/default-source/structures/structuresmanual/currentrelease/2021/vol1sdg.pdf.

4. Hamilton, H. R., Rice, J. A., Brenkus, N. R., Abdullah, A. B. M., Bhatia, R., & Skelton, D. (2017). Replaceable unbonded tendons for post-tensioned bridges. Retrieved December 10, 2020 from https://rosap.ntl.bts.gov/view/dot/34819.

5. Little, B., Staehle, R., & Davis, R. (2001). Fungal influenced corrosion of post-tensioned cables. *International biodeterioration & biodegradation*, *47*(2), 71-77.

6. Castaneda, C. (2017). *Flexible Filler Corrosion Protection of Unbonded Post-Tension Tendons* [Doctoral dissertation, Florida Atlantic University]. College of Engineering & Computer Science. Retrieved December 10, 2020 from, http://fau.digital.flvc.org/islandora/object/fau%3A38005/datastream/OBJ/view/Flexible_Filler_Corrosion_Protection_of_Unbonded_Post-Tension_Tendons.pdf.

7. Post-Tensioning Institute – Technical Advisory Board (2015). Selection of Filler Material for Multistrand PT Tendons. *PTI Technical Notes, Issue 19*. Retrieved December 10, 2020 from, https://www.post-tensioning.org/Portals/13/Files/Pdfs/Education/Technical%20Note_19.pdf.

8. Roustan, W., & Erblat, A. (2020, June 18). State of emergency declared over 'severe corrosion' on Roosevelt Bridge in Stuart. Retrieved December 15, 2020, from, https://www.sun-sentinel.com/news/florida/fl-ne-stuart-bridge-cracks-20200617-ax4hfrknqjbf7fdynchi3we3ze-story.html.

9. Detman, G., & Rodriguez, A. (2020, June 17). Roosevelt Bridge closed due to cracks, not in danger of 'imminent collapse'. Retrieved December 15, 2020, from, https://cbs12.com/news/local/southbound-lanes-of-roosevelt-bridge-in-stuart-closed-for-repairs

10. Freij, H., Dukeman, D., Sagüés, A. A., & Alexander, C. (2019). Development of tendon imaging sensor. Retrieved December 17, 2020, from https://fdotwww.blob.core.windows.net/sitefinity/docs/default-source/research/reports/fdot-bdv25-977-24-rpt.pdf.

11. Dukeman, D., Freij, H., Sagüés, A. A., & Alexander, C. (2019). Field demonstration of tendon imaging methods. Retrieved December 17, 2020, from

https://fdotwww.blob.core.windows.net/sitefinity/docs/default-source/research/reports/fdot-bdv25-977-52-rpt.pdf.

12. FDOT (2016). *Grouting of bridge post-tensioning tendons.* Training Manual. Retrieved December 17, 2020, from https://fdotwww.blob.core.windows.net/sitefinity/docs/default-source/construction/construction/training/selfstudy/tutorial/final-grouting-training-manual-7-30-02.pdf.
13. Ray, J. D., Haskins, R. W., & Evans, J. A. (2019). *Guided wave Testing of trunnion rods at West Point Lock and Dam, West Point, Georgia* (No. ERDC/CHL CHETN-IX-49). ERDC Vicksburg United States. Retrieved December 21, 2020, from https://apps.dtic.mil/dtic/tr/fulltext/u2/1076218.pdf.
14. FDOT (2018). *FDOT FY2021-22 Standard Plans.* Index 462-002. Retrieved December 21, 2020, from https://fdotwww.blob.core.windows.net/sitefinity/docs/default-source/design/standardplans/2022/idx/462-002.pdf.
15. Hurlebaus, S., Hueste, M., Karthik, M., & Terzioglu, T. (2016). Condition assessment of bridge post-tensioning and stay cable systems using NDE methods. *Transportation Research Board of the National Academies.* Retrieved December 22, 2020, from http://onlinepubs.trb.org/onlinepubs/nchrp/docs/NCHRP14-28_FR.pdf.
16. Azizinamini, A. (2017). Non-destructive testing (NDT) of a segmental concrete bridge scheduled for demolition, with a focus on condition assessment and corrosion detection of internal tendons. Retrieved December 23, 2020, from https://rosap.ntl.bts.gov/view/dot/32365.
17. NDT Technologies, Inc. (2020). Retrieved December 23, 2020, from https://www.ndttech.com/.
18. NDT Technologies, Inc. (2020). Retrieved December 23, 2020, from https://www.ndttech.com/products/gallery/.
19. Azizinamini, A. (2012). *Improved inspection techniques for steel prestressing /Post-tensioning strand* No. BDK80 977-13)FDOT.
20. Azizinamini, A. (2012). *FDOT protocol for condition assessment of steel strands in post-tensioned segmental concrete bridges* No. BDK80 977-13)FDOT.
21. Azizinamini, A. (2017). *Non-destructive testing (ndt) of a segmental concrete bridge scheduled for demolition, with a focus on condition assessment and corrosion detection of internal tendons* No. BDV29-977-05)FDOT.
22. Ebeling, R. M., Strom, R. W., Hite Jr, J. E., Haskins, R. W., & Evans, J. A. (2013). *Assessing corrosion damage and corrosion progression in multistrand anchor systems in use at Corps projects*. Army Engineer Waterways Experimentation Station Vicksburg, MS, Information Technology Lab. Retrieved December 24, 2020, from https://apps.dtic.mil/sti/pdfs/ADA582963.pdf.

23. Ebeling, R. M., Strom, R. W., Hite Jr, J. E., Haskins, R. W., & Evans, J. A. (2013). *Assessing corrosion damage and corrosion progression in multistrand anchor systems in use at Corps projects*. Army engineer waterways experiment station Vicksburg, MS information technology lab.

24. Haskins, R. W., Evans, J. A., & Ebeling, R. M. (2016). Development of a new nondestructive inspection strategy for corroded multistrand anchor cables. Retrieved December 26, 2020, from https://erdc-library.erdc.dren.mil/jspui/bitstream/11681/20275/1/ERDC-CHL%20CHETN-IX-42.pdf.

25. Ebeling, R. M., White, B. C., Evans, J. A., Haskins, R. W., & Miller, E. L. (2016). *Corrosion Induced Loss of Capacity of Post Tensioned Seven Wire Strand Cable Used in Multistrand Anchor Systems Installed at Corps Projects*. Army engineer waterways experiment station Vicksburg, MS, United States. Retrieved December 26, 2020, from https://apps.dtic.mil/sti/pdfs/AD1031854.pdf.

26. Alexander, C. L., Chen, Y. M., & Orazem, M. E. (2017). Impedance-based detection of corrosion in post-tensioned cables: phase 2 from concept to application. Retrieved December 27, 2020, from https://trid.trb.org/view/1477466.

27. Hoshi, Y., Koike, T., Tokieda, H., Shitanda, I., Itagaki, M., & Kato, Y. (2019). Non-contact measurement to detect steel rebar corrosion in reinforced concrete by electrochemical impedance spectroscopy. *Journal of The Electrochemical Society*, *166*(11), C3316. Retrieved December 27, 2020, from https://iopscience.iop.org/article/10.1149/2.0371911jes/pdf.

28. Chase, S. B., & Balakumaran, S. S. (2020). Magnetic flux leakage device for evaluation of prestressed concrete box bridges (No. VTRC 20-R14). *Virginia Transportation Research Council*. Retrieved December 27, 2020, from http://www.virginiadot.org/vtrc/main/online_reports/pdf/20-r14.pdf.

29. Fernandes, B., Nims, D., & Devabhaktuni, V. (2014). Comprehensive MMF–MFL inspection for corrosion detection and estimation in embedded prestressing strands. *Journal of Civil Structural Health Monitoring*, 4, 43-55.

30. Xu, F., Wang, X., & Wu, H. (2012). Inspection method of cable-stayed bridge using magnetic flux leakage detection: principle, sensor design, and signal processing. *Journal of mechanical science and technology*, 26, 661-669.

31. Mullins, L., & Pearson, H. M. (1949). The x-ray examination of concrete. *Civil Engineering and Public Works Review*, London, England, 44(515), 256-258.

32. Whiffin, A.C. (1954), "Locating Steel Reinforcing Bars in Concrete Slab," *The Engineer, London, UK*, 887-888.

33. Standard, B. (1986). Testing concrete, *Recommendations for Radiography of Concrete*. BS 1881.

34. Bray, D. E., & Stanley, R. K. (1989). *Nondestructive Evaluation.* McGraw Hill. New York.

35. Mitchell, T. M. (2003). *Radioactive/nuclear methods. In Handbook on nondestructive testing of concrete* (pp. 258-279). CRC Press.

36. Bligh, R. P., JAMES, R., Bray, D. E., & Nakirekanti, S. (1993). NDE techniques for detecting grout defects in cable stays. Final report (No. FHWA/TX-93-1268-1F).

37. Frigerio, T., Mariscotti, M. A. J., Ruffolo, M., & Thieberger, P. (2004). Development and application of computed tomography in the inspection of reinforced concrete. *Insight-Non-Destructive Testing and Condition Monitoring*, 46(12), 742-745.

38. Mariscotti, M. A. J., & Husni, R. (2006). *Reinforced Concrete Tomography and Its Application to Bridge assessment. In NDE Conference on Civil Engineering*, St. Louis, MO, ASNT, Edited by Imad Al-Qadi and Glenn Washer. (Vol. 349).

39. Pimentel, M., Figueiras, J., Mariscotti, M., Thieberger, P., Ruffolo, L. M., & Frigerio, T. (2010). Gamma-ray inspection of post tensioning cables in a concrete bridge. *Structural Faults & Repair* 2010.

40. Mariscotti, M. A., Jalinoos, F., Frigerior, T., Ruffolo, M., & Thieberger, P. (2009). Gamma-Ray imaging for void and corrosion assessment. *Concrete international,* 31(11), 48-53.

41. Azizinamini, A., & Gull, J. (2012). Improved inspection techniques for steel prestressing/post-tensioning strand: Volume I. Retrieved December 13, 2020 from https://rosap.ntl.bts.gov/view/dot/25056/dot_25056_DS1.pdf.

42. Sagüés, A. A. (2017). U.S. Patent No. 9,651,357. Washington, DC: U.S. Patent and Trademark Office.

43. Durability of Post-tensioning Tendons: Technical Report: Proceedings of a Workshop Held at Ghent University on 15-16 November 2001. Vol. 15. fib Fédération internationale du béton, 2001.

44. Harder, J., & Webster, N. (2001). Durability of post-tensioning tendons: Canadian experience. *BULLETIN-FIB*, *15*, 51-74.

45. Fallis, G., Ball, J. C., & Moad, A. (2007). Innovative corrosion evaluation system for unbonded post-tensioned cables. *Concrete Repair Bulletin*, 7-8.

46. Naso, T. R. (2017). A stitch in time saves nine: A post tensioning repair case study. *Journal of Post Tensioning Institute*, *13*(2), 53-60.

47. Bonger, A. D., Hosoda, A., Salem, H., & Kaba, K. (2019). Numerical simulation of rupture protrusion of vertically tightened PC steel bars using Applied Element Method. *Internet Journal of Society for Social Management Systems*, *12*(1), 110.

48. Shear, A. E., Donnelly, J. P., & Lewis, M. E. (2011). Tendon Failure Investigation and Drying in a Two-Way Unbonded Post-Tensioned Roof Slab. In *Structures Congress 2011*, 1759-1770.

49. Lee, S. K. (2022). *Corrosion-Induced Durability Issues and Maintenance Strategies for Post-Tensioned Concrete Bridges* (No. FHWA-HRT-22-090). United States. Federal Highway Administration. Office of Infrastructure Research and Development.

50. Planès, T., & Larose, E. (2013). A review of ultrasonic Coda Wave Interferometry in concrete. *Cement and Concrete Research*, *53*, 248-255.

51. Aki, K. (1969). Analysis of the seismic coda of local earthquakes as scattered waves. *Journal of Geophysical Research*, *74*(2), 615-631.

52. Anugonda, P., Wiehn, J. S., & Turner, J. A. (2001). Diffusion of ultrasound in concrete. *Ultrasonics*, *39*(6), 429-435.

53. Song, H., & Popovics, J. S. (2019). Extracting non-propagating oscillatory fields in concrete to detect distributed cracking. *The Journal of the Acoustical Society of America*, *146*(4), 2655-2670.

54. Ahn, E., Shin, M., Popovics, J. S., & Weaver, R. L. (2019). Effectiveness of diffuse ultrasound for evaluation of micro-cracking damage in concrete. *Cement and Concrete Research*, *124*, 105862.

55. Zhong, B., Zhu, J., & Morcous, G. (2020). Development of an NDT Tool for in-Situ Assessment of Prestress Loss. Retrieved December 28, 2020 from, https://digitalcommons.unl.edu/cgi/viewcontent.cgi?article=1244&context=ndor.

56. Demırcı, A., Görgülü, K., & Durutürk, Y. S. (2004). Thermal conductivity of rocks and its variation with uniaxial and triaxial stress. *International Journal of Rock Mechanics and Mining Sciences*, *41*(7), 1133-1138.

57. Jin, L., Zhang, R., & Du, X. (2017). Computational homogenization for thermal conduction in heterogeneous concrete after mechanical stress. *Construction and Building Materials*, *141*, 222-234.

58. OR Technology (2016). Retrieved December 28, 2020, from https://www.or-technology.com/en/products/vet/amadeo-p-systems.html#Add-ons.

59. MinXray, Inc. (2019). Retrieved December 28, 2020, from https://www.minxray.com/wp-content/uploads/2019/05/MINC20518_X-Ranger-Sell-Sheet_FINAL-web1.pdf.

60. Consolazio, G. & Hamilton, H.R. (2017). Flexural Capacity of Concrete Elements with Unbonded and Bonded Prestressing. https://fdotwww.blob.core.windows.net/sitefinity/docs/default-source/structures/structuresresearchcenter/final-reports/2022/bdv31-977-93-final-report-w-all-appendices.pdf. Accessed October 28, 2023.

61. Ahn, E., Shin, M., Popovics, J. S., & Weaver, R. L. (2019). Effectiveness of diffuse ultrasound for evaluation of micro-cracking damage in concrete. *Cement and Concrete Research*, *124*, 105862.

62. Gondim, R. M. L., & Haach, V. G. (2021). Monitoring of ultrasonic velocity in concrete specimens during compressive loading-unloading cycles. *Construction and Building Materials*, 302, 124218.

63. FDOT (2022). Approved Post-Tensioning System Vendor Drawings For Use with January 2016 through January 2022 Specifications. Retrieved August, 25, 2023, from https://fdotwww.blob.core.windows.net/sitefinity/docs/default-source/structures/cadd/standards/approvedptdrawings/eci-6-12-internal-flexible-filler.pdf.

64. Sikadur (2023). Retrieved August 25, 2023, from https://usa.sika.com/en/construction/repair-protection/multi-purpose-epoxies/adhesives/sikadur-31-sba-normalset.html on August 25, 2023.

Appendix A - Design Drawings for Large-Scale Test Specimens

Sheet Index	
Sheet ID	Title
1	Index
2	General Notes
3	Specimem A - General Dimensions
4	Specimem A - General Zone and Shear Reinforcement
5	Specimem A - Local Zone and Anchorage
6	Specimem B - General Dimensions
7	Specimem B - General Zone and Shear Reinforcement
8	Specimem B - Local Zone and Anchorage
9	Specimen B - Diagram for Bursting Calculations
10	Specimem C - General Dimensions
11	Specimem C - Reinforcement
12	Specimem C - Match Cast Details
13	Rebar Details (#3 & #4)
14	Rebar Details (#5 & #7)
15	Test Setup
16	Instrumentation Plan - Specimen A
17	Instrumentation Plan - Specimen B
18	Instrumentation Plan - Specimen C
19	Stressing Plan
20	Load Testing Plan
21	Filler Injection Plan
22	Yard Layout Plan

EMBRY-RIDDLE Aeronautical University

EMBRY-RIDDLE AERONAUTICAL UNIVERSITY
DEPARTMENT OF CIVIL ENGINEERING
1 AEROSPACE BLVD
DAYTONA BEACH, FL 32114

FDOT

SHEET TITLE: Sheet Index

6/6/23

PROJECT NAME: INSPECTION OF FLEXIBLE FILLERS

SHEET NO.
1 of 22

General Notes:

Materials

Concrete shall be FDOT class IV
f'c (28 day) = 5500 psi

The same concrete mix shall be used for all beams.

Mild reinforcement shall be ASTM A615 grade 60 (fy 60 ksi)

Prestressing strand shall be ASTM A416 270 ksi Lo-Lax

Fabricator shall provide data sheets from concrete, strand, and rebar suppliers.

Fabricator shall provide material samples to ERAU/FDOT as follows:

(8) 6" dia x 12" cylinders from each concrete batch: (4) cylinders cure with girder, (4) lab cure

(8) 36" pieces of prestressing strands free from sand, dust, etc. Samples taken directly off of reel.

Schedule

Contact Jeff Brown at ERAU at least (1) week prior to casting: 386-226-7458 or browj112@erau.edu

Allow 24 hours minimum between placement of reinforcing and placement of concrete to allow of placement of research instrumentation.

Other

Unless otherwise noted, fabrication of girders shall follow typical procedures and practices for FDOT bridge girders.

Cover beams with heavy tarp during curing.

Inspections will be provided by on-site FDOT personnel and by ERAU.

No patch-work or finishing is required.

Construction shall be in accordance with FDOT Standard Specifications, January 2022

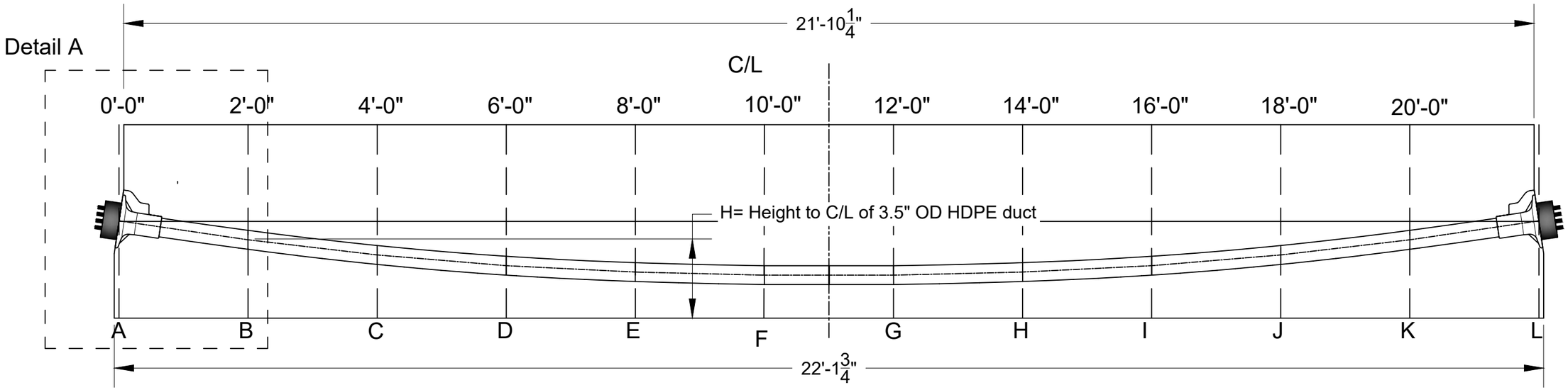

Section	A	B	C	D	E	F	G	H	I	J	K	L
H	1'-6"	1'-2 3/8"	0'-11 5/8"	0'-9 5/8"	0'-8 3/8"	0'-8"	0'-8"	0'-8 3/8"	0'-9 5/8"	0'-11 5/8"	1'-2 3/8"	1'-6"

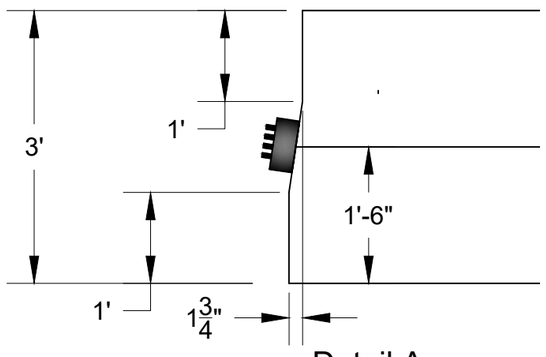

Detail A

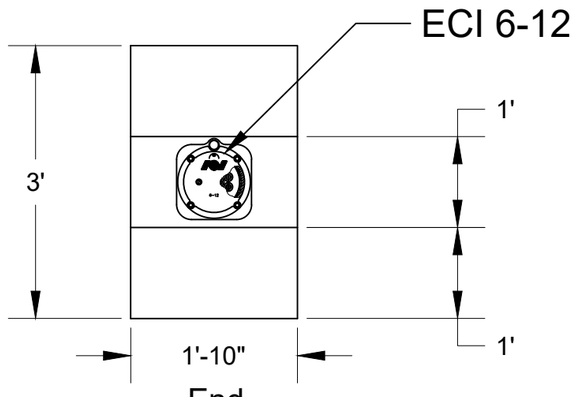

End

EMBRY-RIDDLE Aeronautical University™

EMBRY-RIDDLE AERONAUTICAL UNIVERSITY
DEPARTMENT OF CIVIL ENGINEERING
1 AEROSPACE BLVD
DAYTONA BEACH, FL 32114

FDOT

SHEET TITLE: Specimen A (General Dimensions)

6/6/23

PROJECT NAME: INSPECTION OF FLEXIBLE FILLERS

SHEET NO.
3 of 22

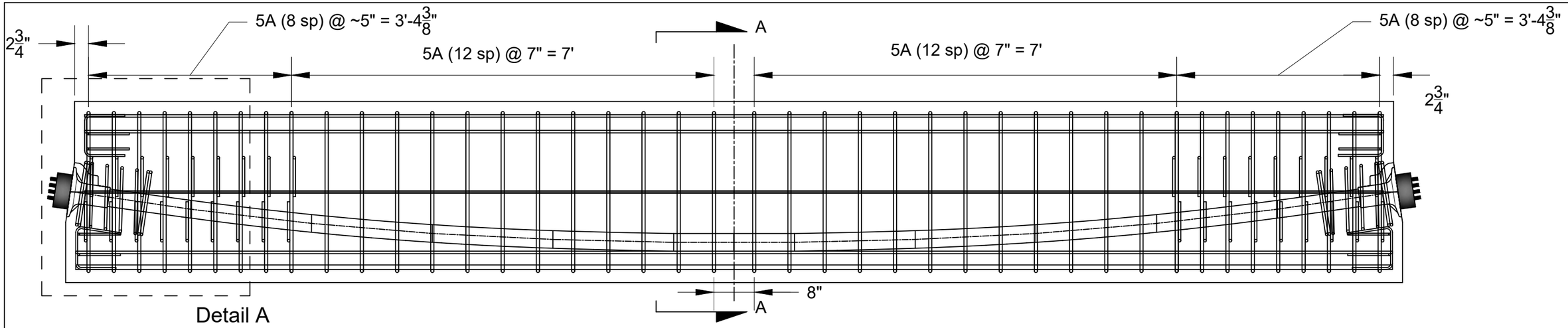

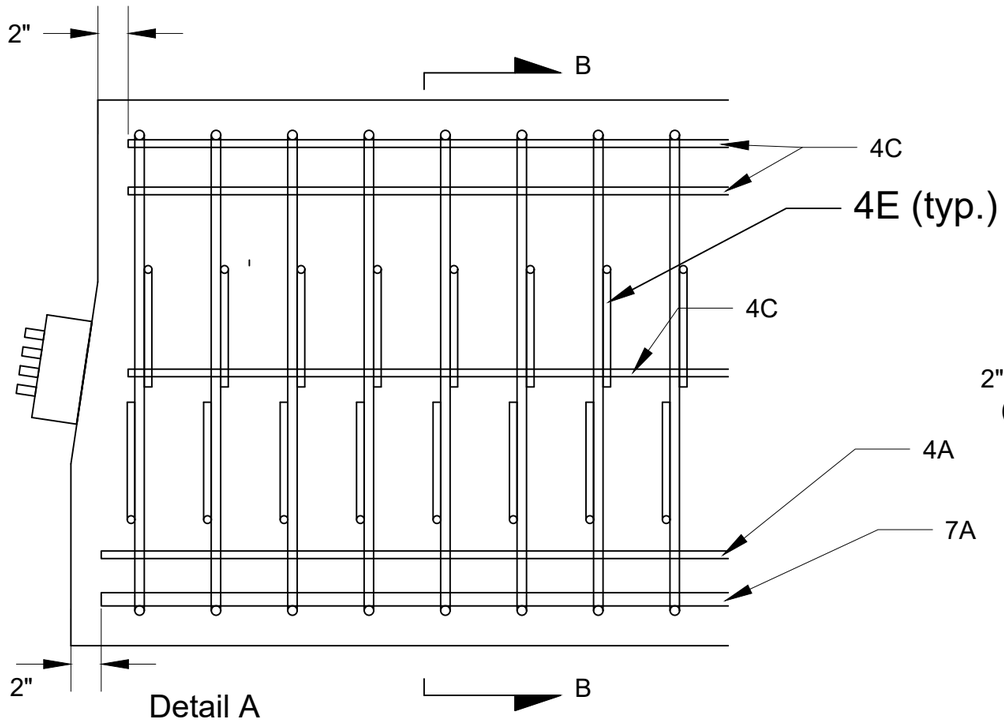

Detail A
(Anchorage, local zone and spalling reinforcement not shown)

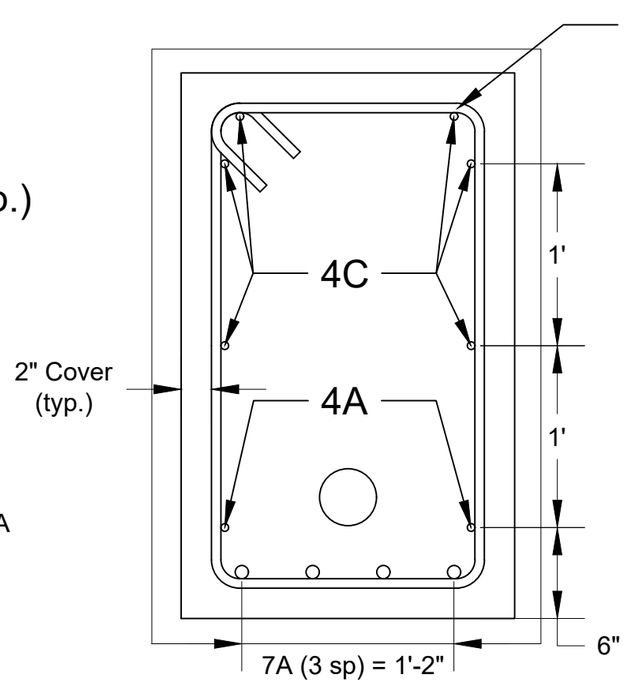

Section A-A

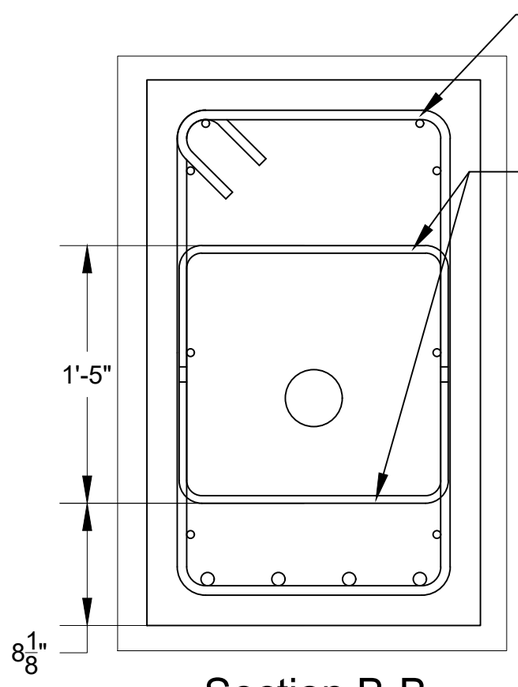

Section B-B

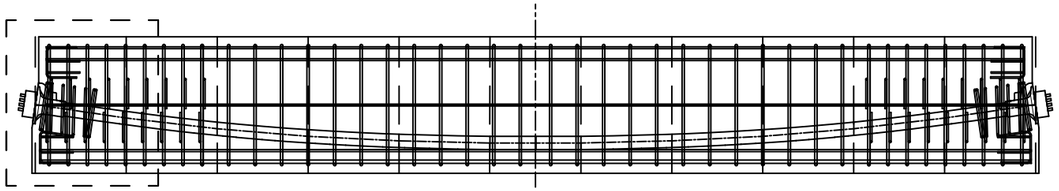

Detail A

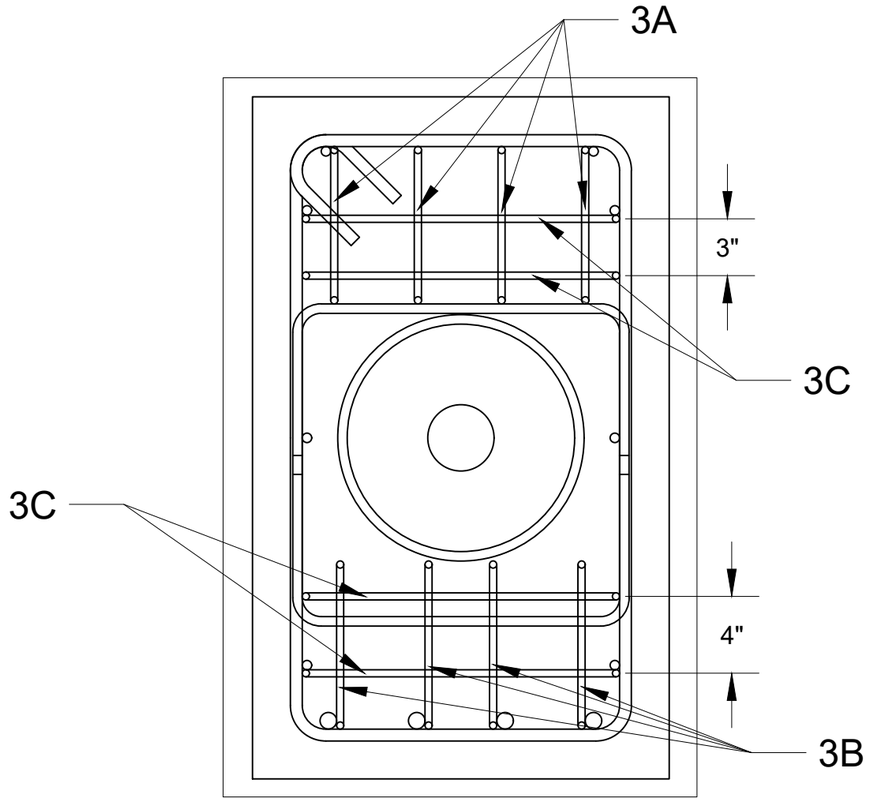

Section A-A

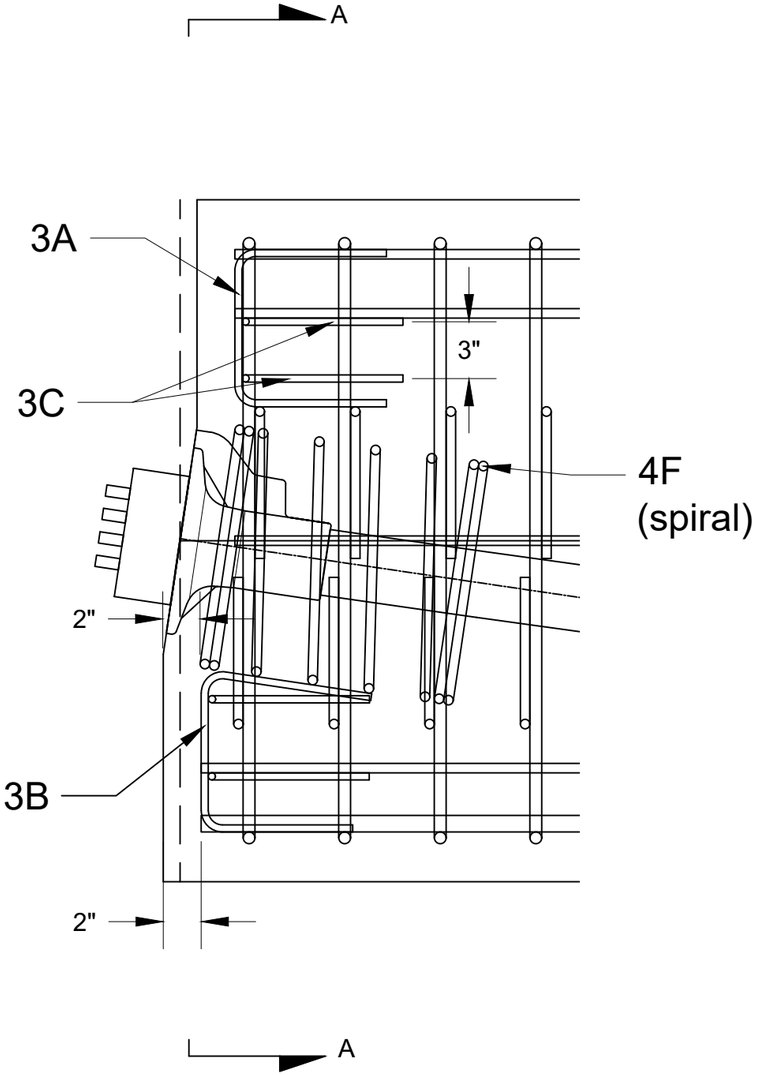

Detail A

EMBRY-RIDDLE Aeronautical University	EMBRY-RIDDLE AERONAUTICAL UNIVERSITY DEPARTMENT OF CIVIL ENGINEERING 1 AEROSPACE BLVD DAYTONA BEACH, FL 32114	FDOT	SHEET TITLE: Specimen A (Local Zone and Anchorage)	6/6/23
			PROJECT NAME: INSPECTION OF FLEXIBLE FILLERS	SHEET NO. 5 of 22

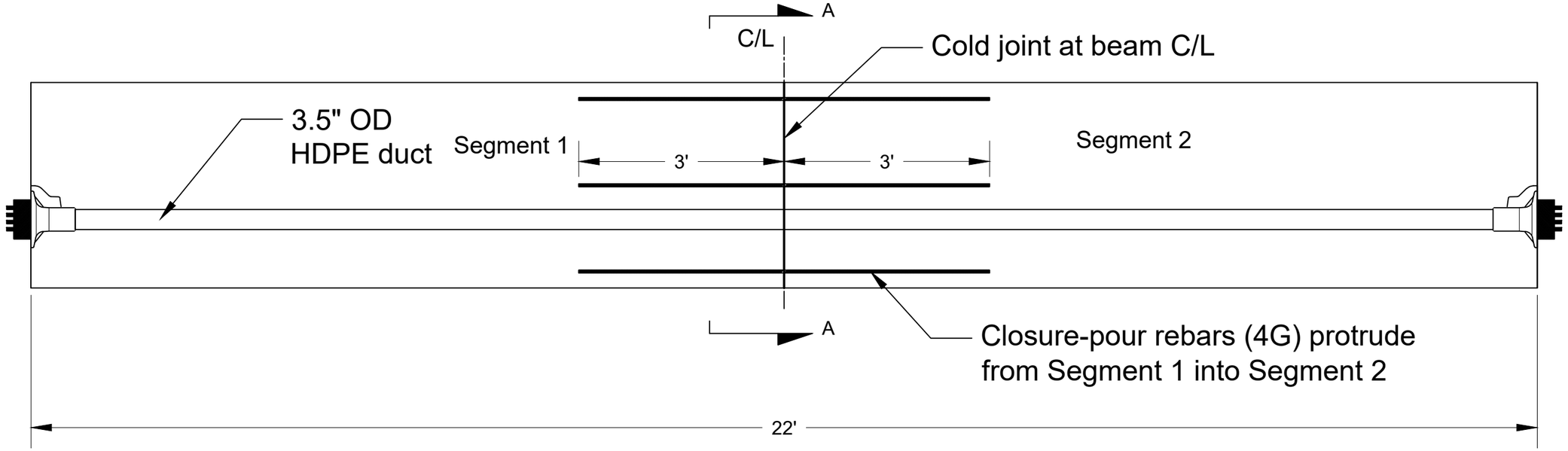

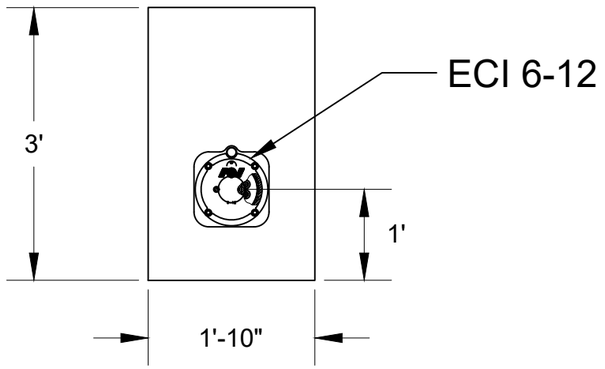

End

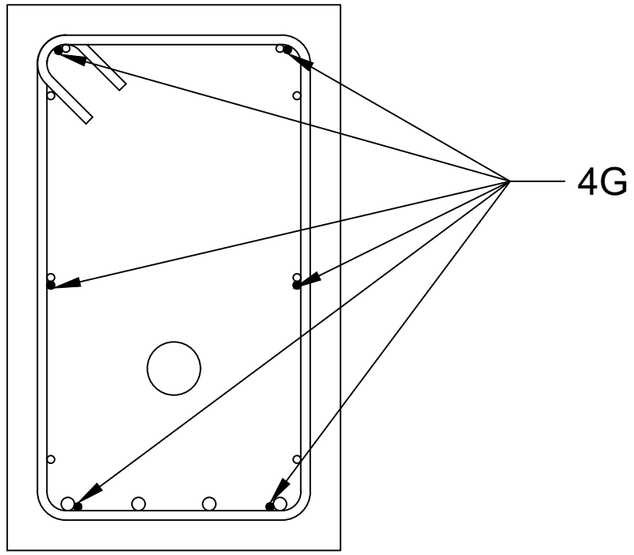

Section A-A

EMBRY-RIDDLE Aeronautical University™

EMBRY-RIDDLE AERONAUTICAL UNIVERSITY
DEPARTMENT OF CIVIL ENGINEERING
1 AEROSPACE BLVD
DAYTONA BEACH, FL 32114

FDOT

SHEET TITLE: Specimen B (General Dimensions)

6/6/23

PROJECT NAME: INSPECTION OF FLEXIBLE FILLERS

SHEET NO.
6 of 22

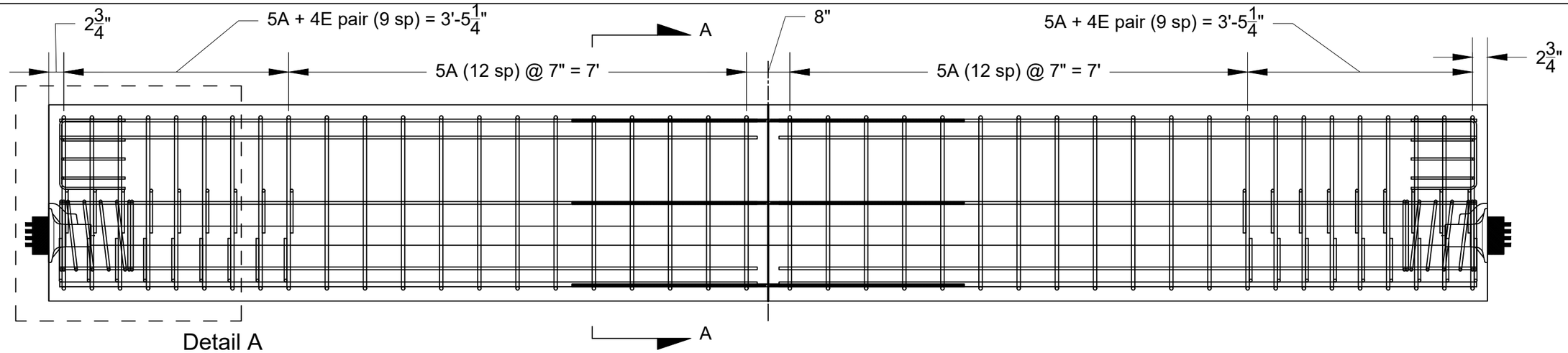

Detail A

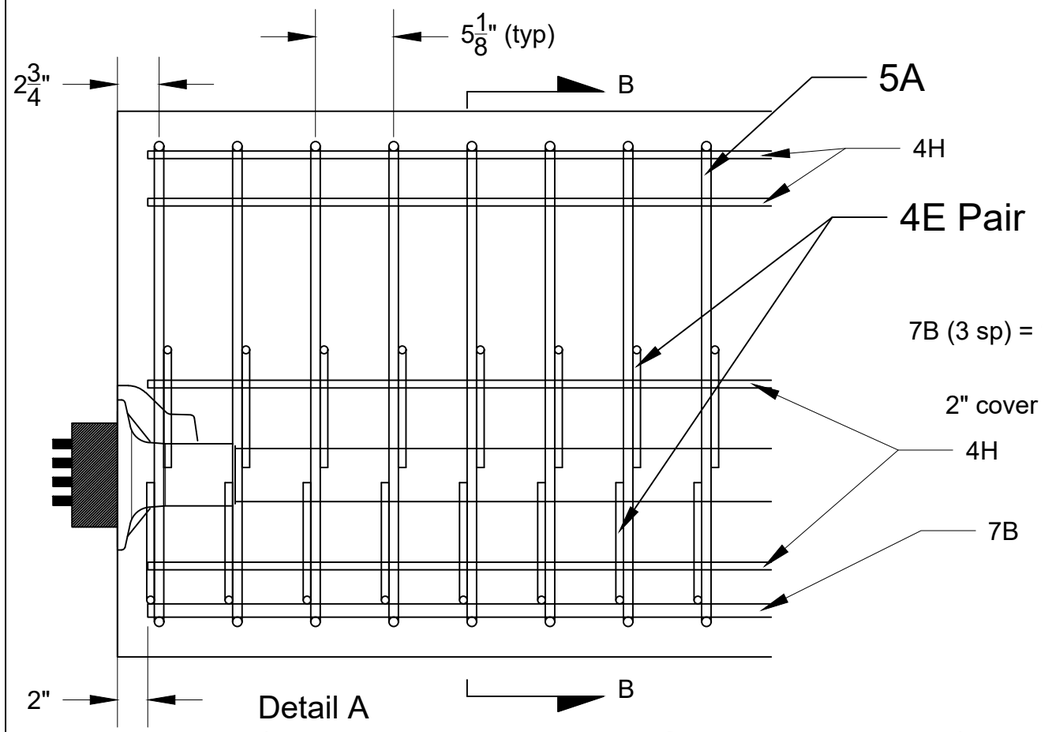

Detail A
(Local zone and spalling reinforcement not shown)

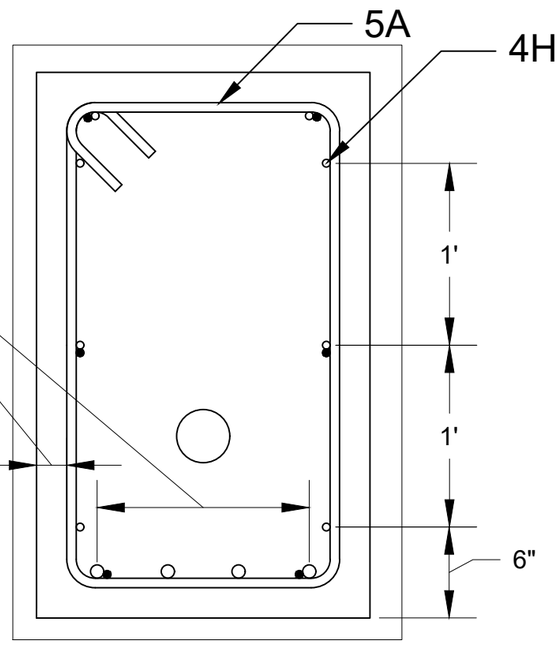

Section A-A

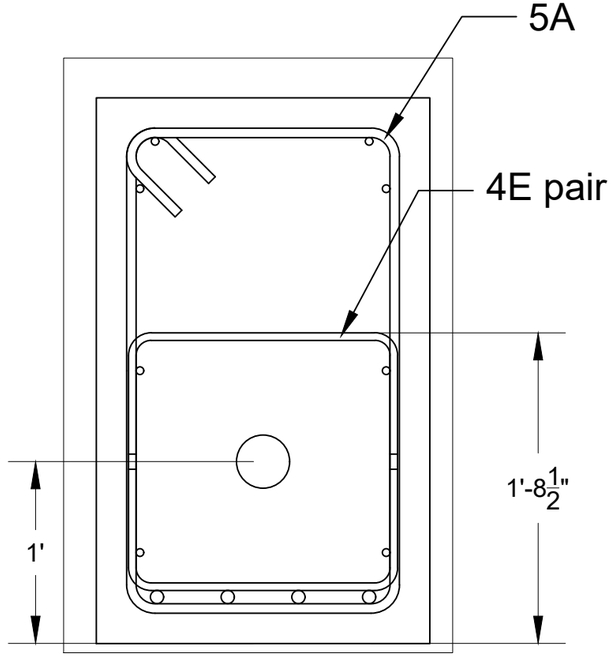

Section B-B

EMBRY-RIDDLE Aeronautical University	EMBRY-RIDDLE AERONAUTICAL UNIVERSITY DEPARTMENT OF CIVIL ENGINEERING 1 AEROSPACE BLVD DAYTONA BEACH, FL 32114	FDOT	SHEET TITLE: Specimen B (General Zone and Shear Reinforcement) 6/6/23 PROJECT NAME: INSPECTION OF FLEXIBLE FILLERS SHEET NO. 7 of 22

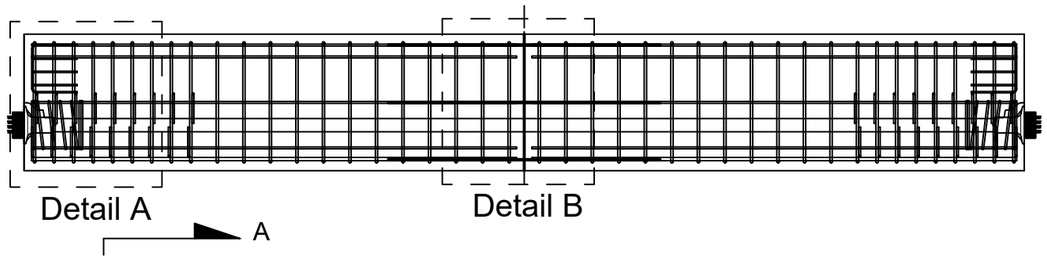

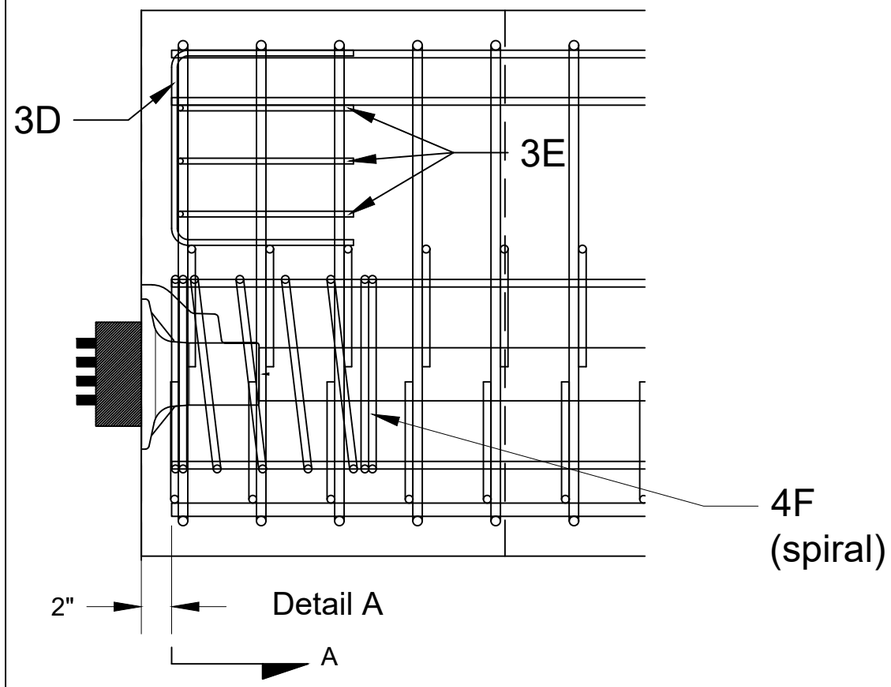

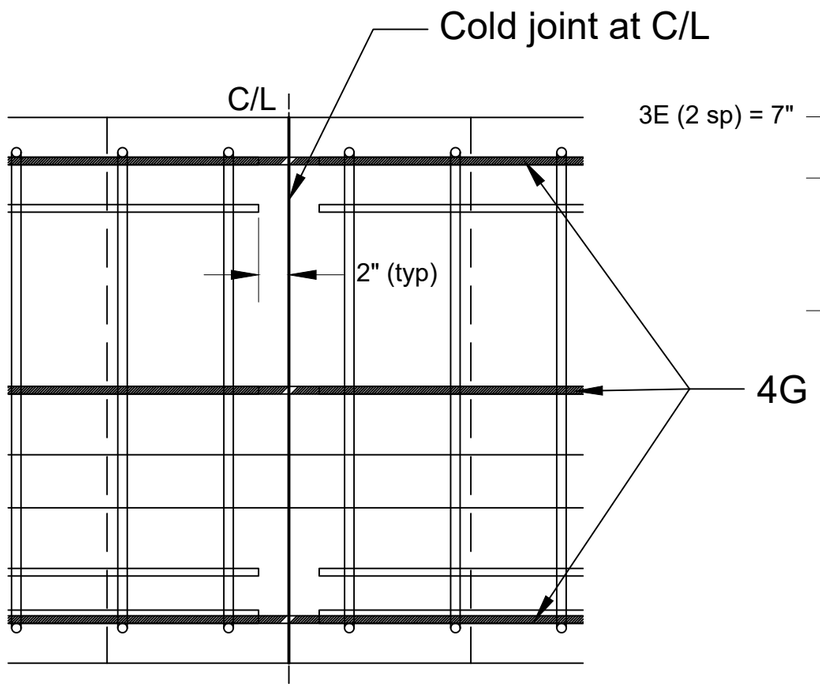

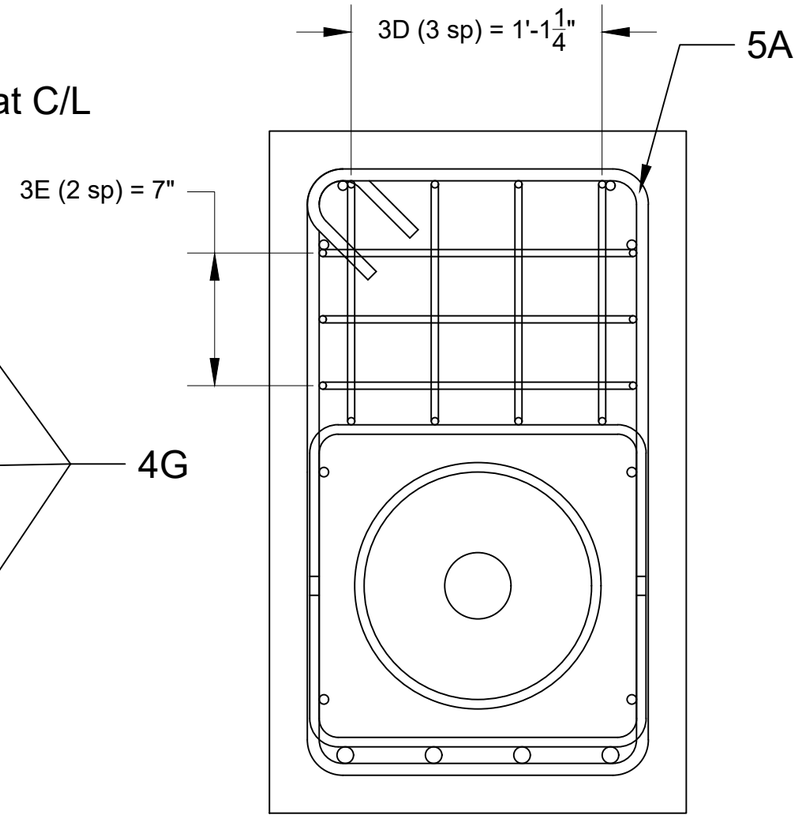

Section A-A

EMBRY-RIDDLE Aeronautical University	EMBRY-RIDDLE AERONAUTICAL UNIVERSITY DEPARTMENT OF CIVIL ENGINEERING 1 AEROSPACE BLVD DAYTONA BEACH, FL 32114	FDOT	SHEET TITLE: Specimen B (Local Zone, Anchorage and Cold Joint)	6/6/23
			PROJECT NAME: INSPECTION OF FLEXIBLE FILLERS	SHEET NO. 8 of 22

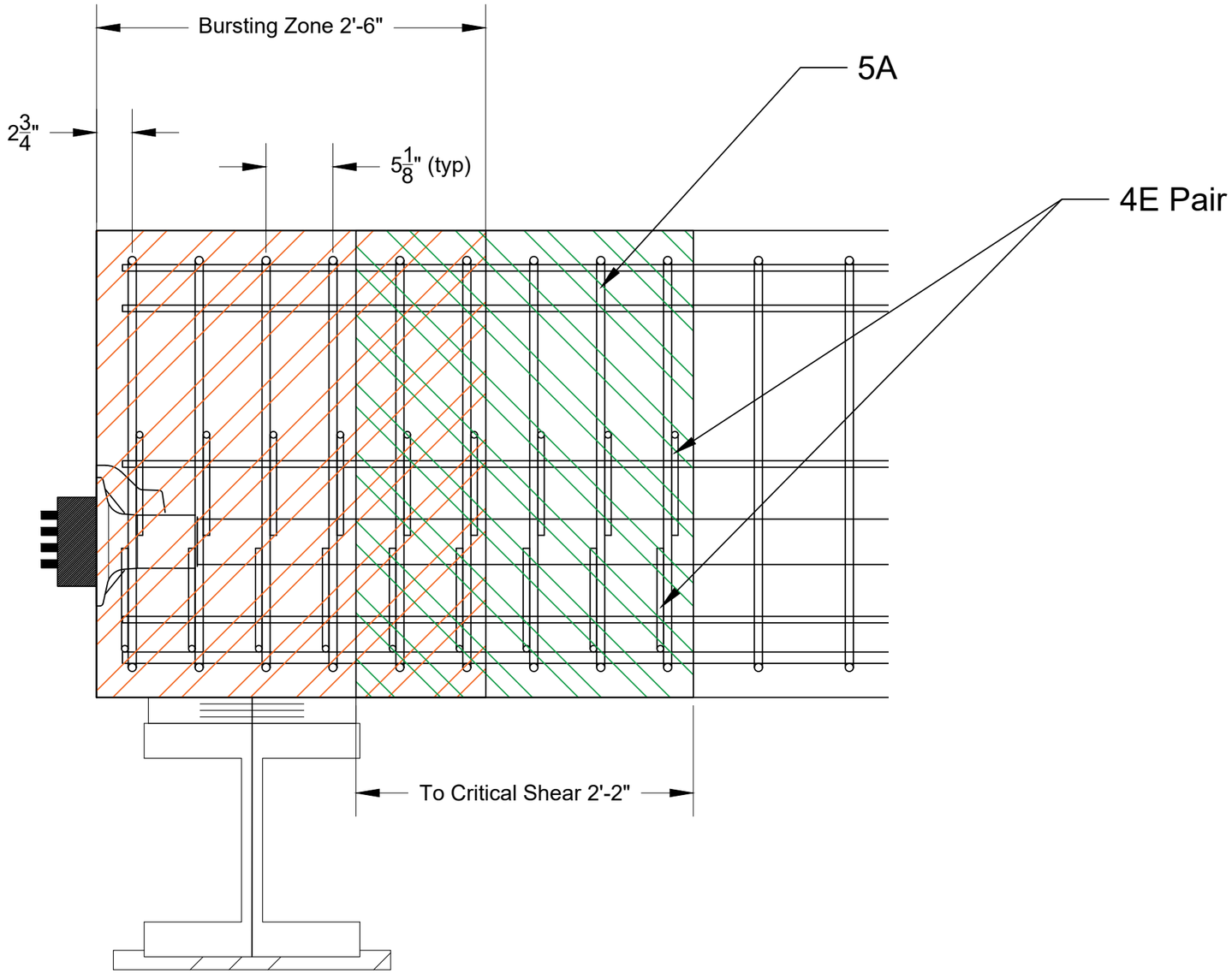

EMBRY-RIDDLE Aeronautical University

EMBRY-RIDDLE AERONAUTICAL UNIVERSITY
DEPARTMENT OF CIVIL ENGINEERING
1 AEROSPACE BLVD
DAYTONA BEACH, FL 32114

FDOT

SHEET TITLE: Specimen B (General Zone and Shear Reinforcement) 6/6/23

PROJECT NAME: INSPECTION OF FLEXIBLE FILLERS

SHEET NO. 9 of 22

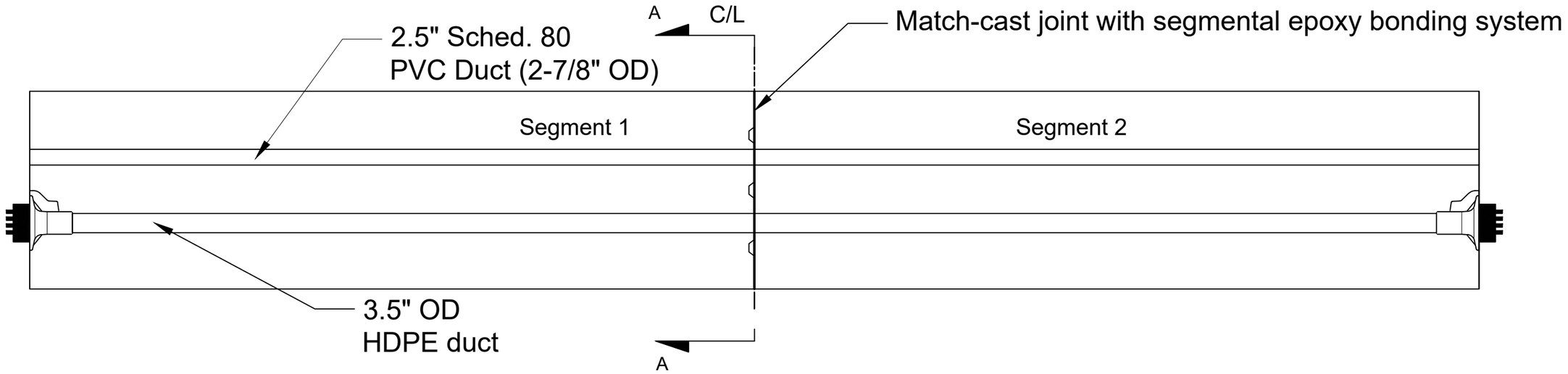

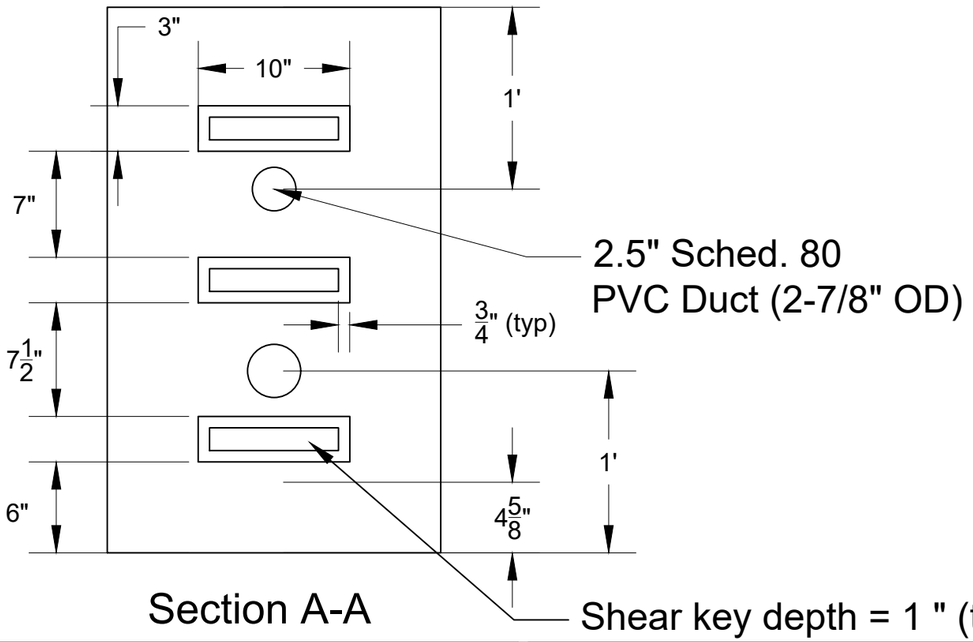

Section A-A

Note: All external geometry, internal reinforcing steel and anchorage layout is the same as Specimen B

EXCEPT:

1. Bars 4G are not included

2. Vertical spacing of Bars 3E. See sheet 11 of 22

EMBRY-RIDDLE Aeronautical University	EMBRY-RIDDLE AERONAUTICAL UNIVERSITY DEPARTMENT OF CIVIL ENGINEERING 1 AEROSPACE BLVD DAYTONA BEACH, FL 32114	FDOT	SHEET TITLE: Specimen C (General Dimensions)	6/6/23
			PROJECT NAME: INSPECTION OF FLEXIBLE FILLERS	SHEET NO. 10 of 22

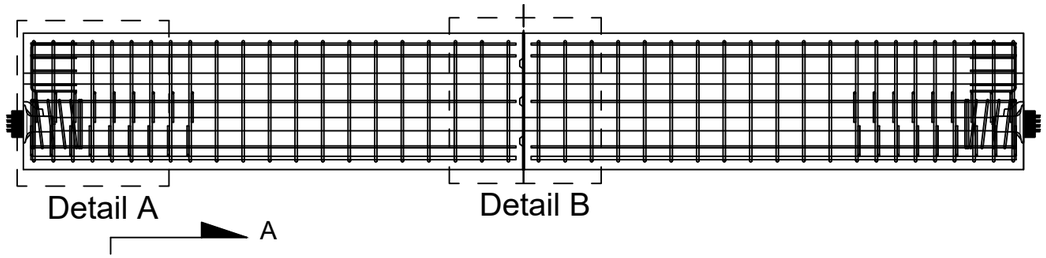

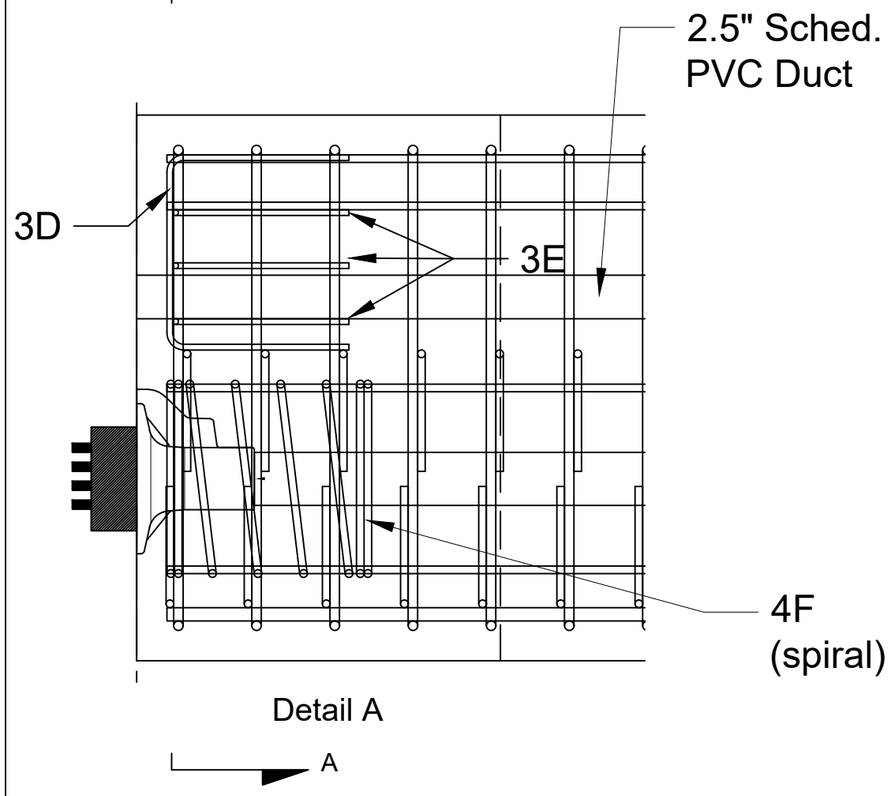

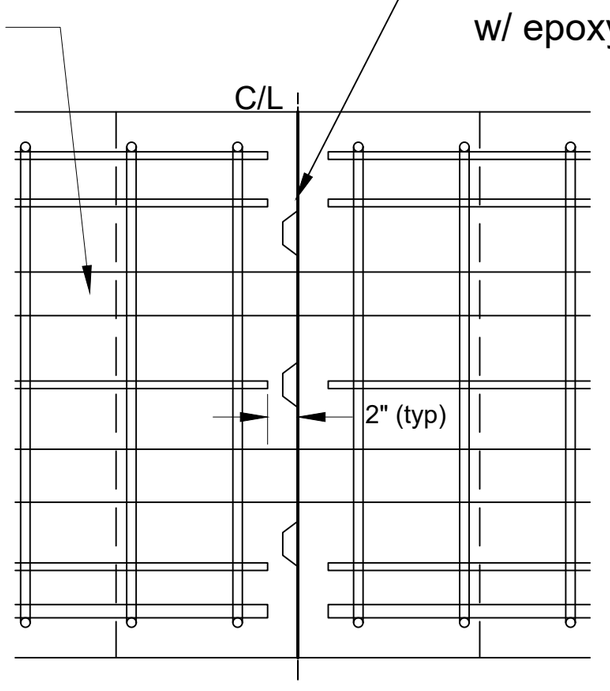

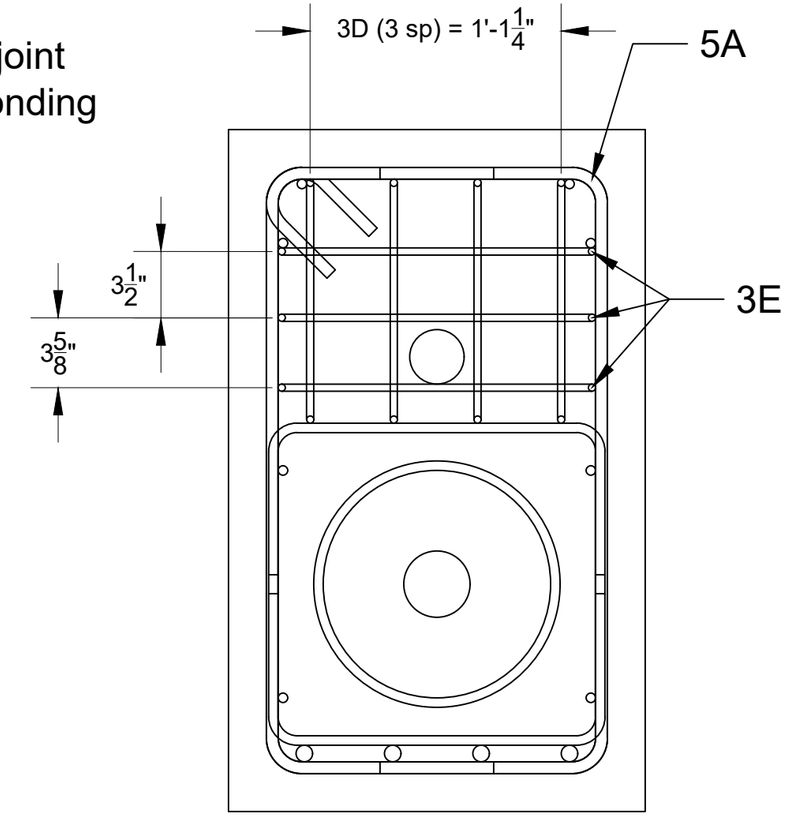

Section A-A

EMBRY-RIDDLE Aeronautical University	EMBRY-RIDDLE AERONAUTICAL UNIVERSITY DEPARTMENT OF CIVIL ENGINEERING 1 AEROSPACE BLVD DAYTONA BEACH, FL 32114	FDOT	SHEET TITLE: Specimen C (Local Zone, Anchorage and Cold Joint)	6/6/23
			PROJECT NAME: INSPECTION OF FLEXIBLE FILLERS	SHEET NO. 11 of 22

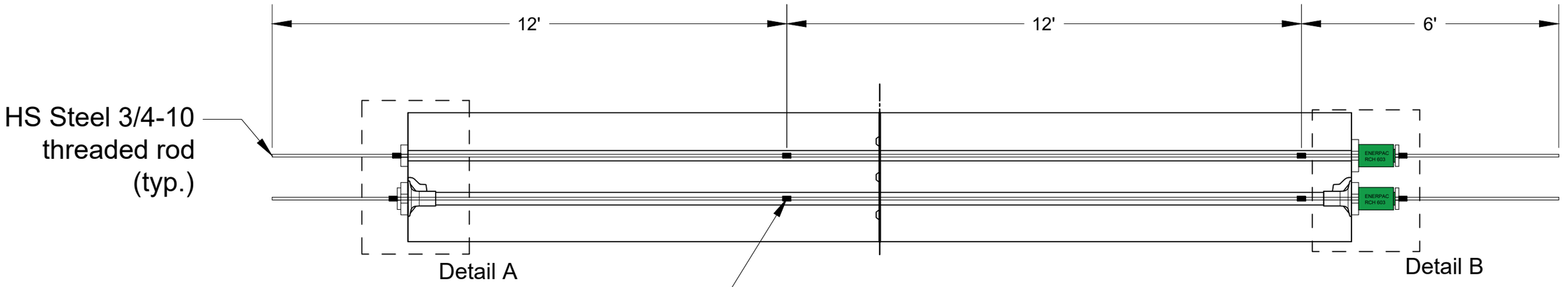

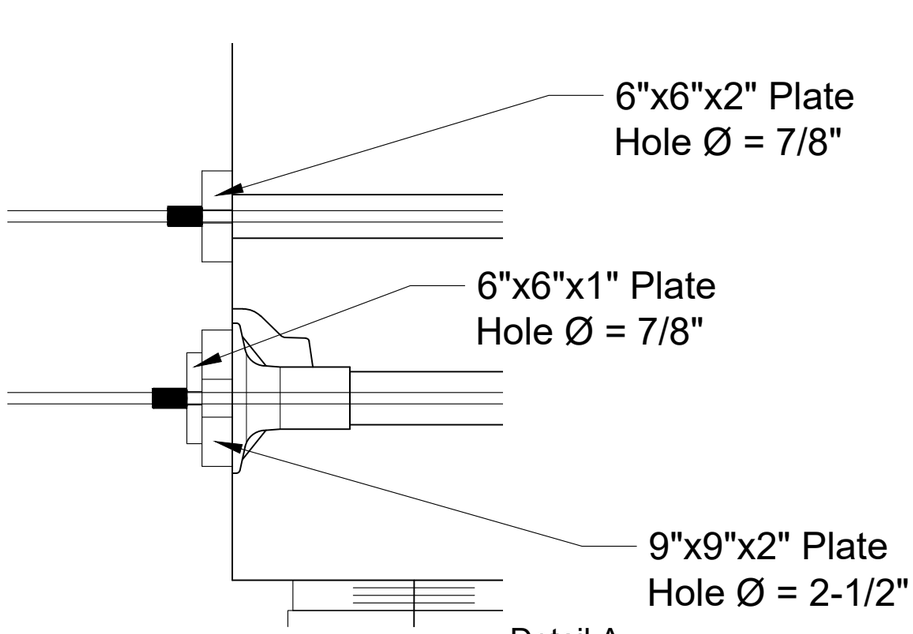

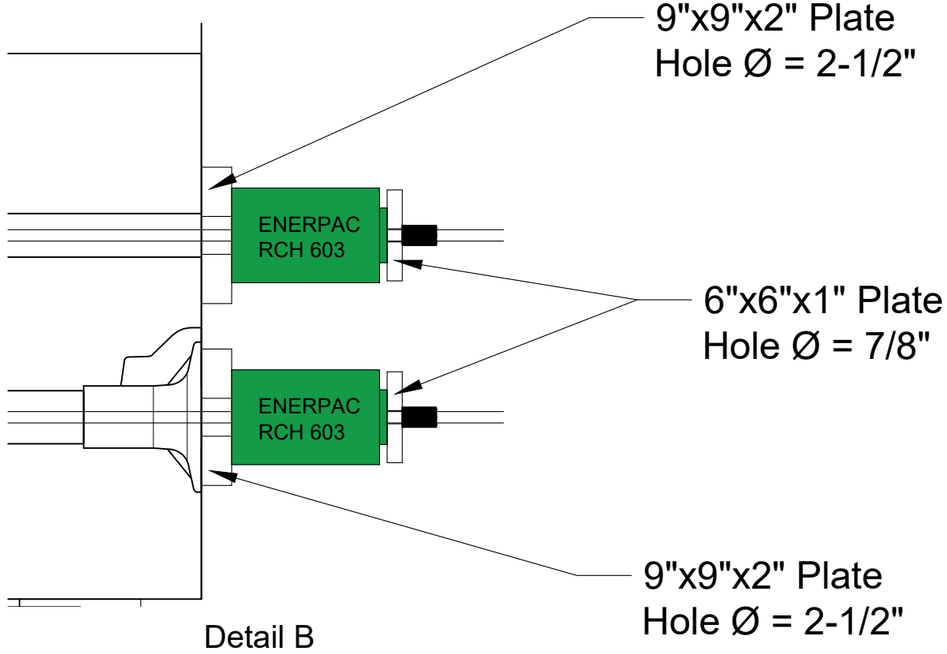

Notes:
See Section 452-8.5 of FDOT Standard Specifications for Road and Bridge Construction for details on segment joining.
Target force is 16 kips on each jack.
Total Force = 32 kips
Stress bottom jack to 2 kips and ensure proper seating.
Stress top jack to 8 kips.
Stress bottom jack to 16 kips.
Stress top jack to 16 kips.

EMBRY-RIDDLE Aeronautical University
EMBRY-RIDDLE AERONAUTICAL UNIVERSITY
DEPARTMENT OF CIVIL ENGINEERING
1 AEROSPACE BLVD
DAYTONA BEACH, FL 32114

FDOT

SHEET TITLE: Specimen C Match Casting

6/6/23

PROJECT NAME: INSPECTION OF FLEXIBLE FILLERS

SHEET NO.
12 of 22

REBAR List					
Bar ID	Spec. A	Spec. B	Spec. C	Total	Cut Length
3A	8			8	2'-0 1/4"
3B	8			8	2'-1 1/2"
3C	8			8	2'-9 3/4"
3D		8	8	16	3'-0 7/8"
3E		6	6	12	3'-4"
4A	2			2	21'-9 3/4"
4C	6			4	21'-6 1/4"
4E	36	36	36	108	2'-9 3/4"
4F	2	2	2	6	
4G		6		6	6'-0"
4H		16	16	32	10'-8"

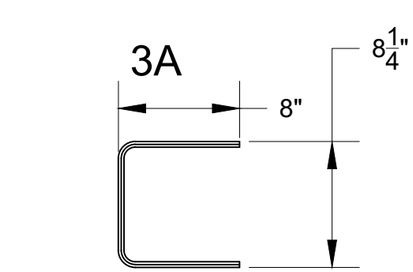

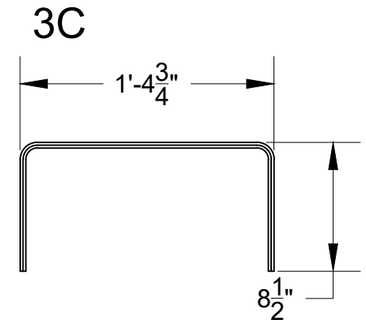

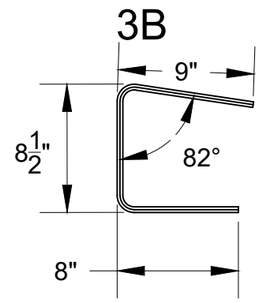

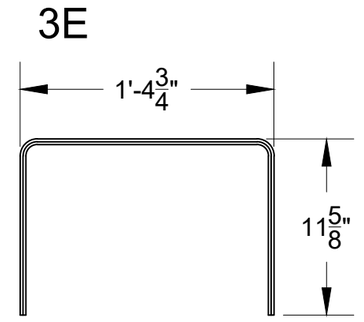

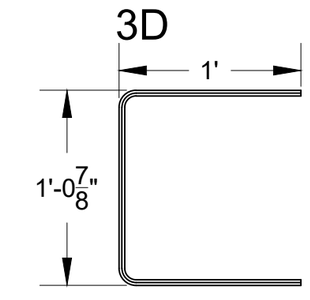

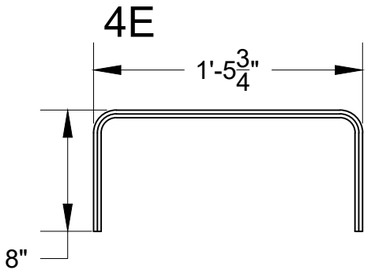

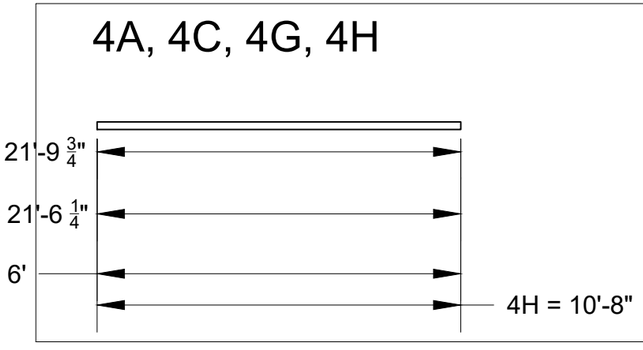

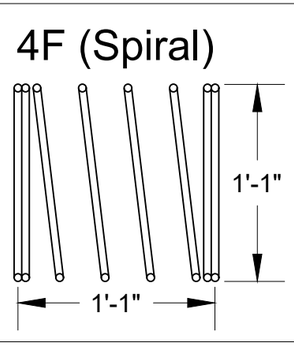

EMBRY-RIDDLE Aeronautical University™

EMBRY-RIDDLE AERONAUTICAL UNIVERSITY
DEPARTMENT OF CIVIL ENGINEERING
1 AEROSPACE BLVD
DAYTONA BEACH, FL 32114

FDOT

SHEET TITLE: BEAM REINFORCEMENT SUMMARY (#3 & #4 bars)

6/6/23

PROJECT NAME: INSPECTION OF FLEXIBLE FILLERS

SHEET NO.
13 of 22

REBAR List					
Bar ID	Spec. A	Spec. B	Spec. C	Total	Cut Length
5A	36	36	36	108	9'-2 1/4"
7A	4			4	21'-9 3/4"
7B		8	8	16	10'-8"

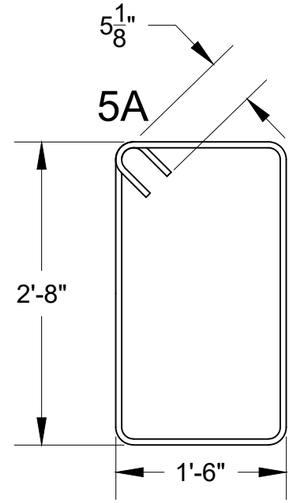

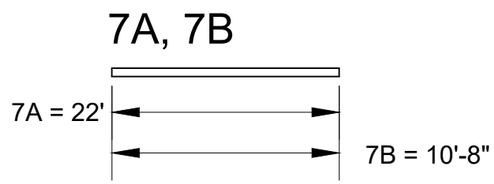

Rebar Sizes		
Bar ID	Bar Size	Min. Inside Bend Dia.
3A/B/C/D/E	#3	All bends per FDOT Standard Plan Index 415-001
4A/C/E/F/G/H	#4	
5A	#5	
7A/B	#7	

EMBRY-RIDDLE Aeronautical University
EMBRY-RIDDLE AERONAUTICAL UNIVERSITY
DEPARTMENT OF CIVIL ENGINEERING
1 AEROSPACE BLVD
DAYTONA BEACH, FL 32114

FDOT

SHEET TITLE: BEAM REINFORCEMENT SUMMARY (#5 & #7 bars)

6/6/23

PROJECT NAME: INSPECTION OF FLEXIBLE FILLERS

SHEET NO. 14 of 22

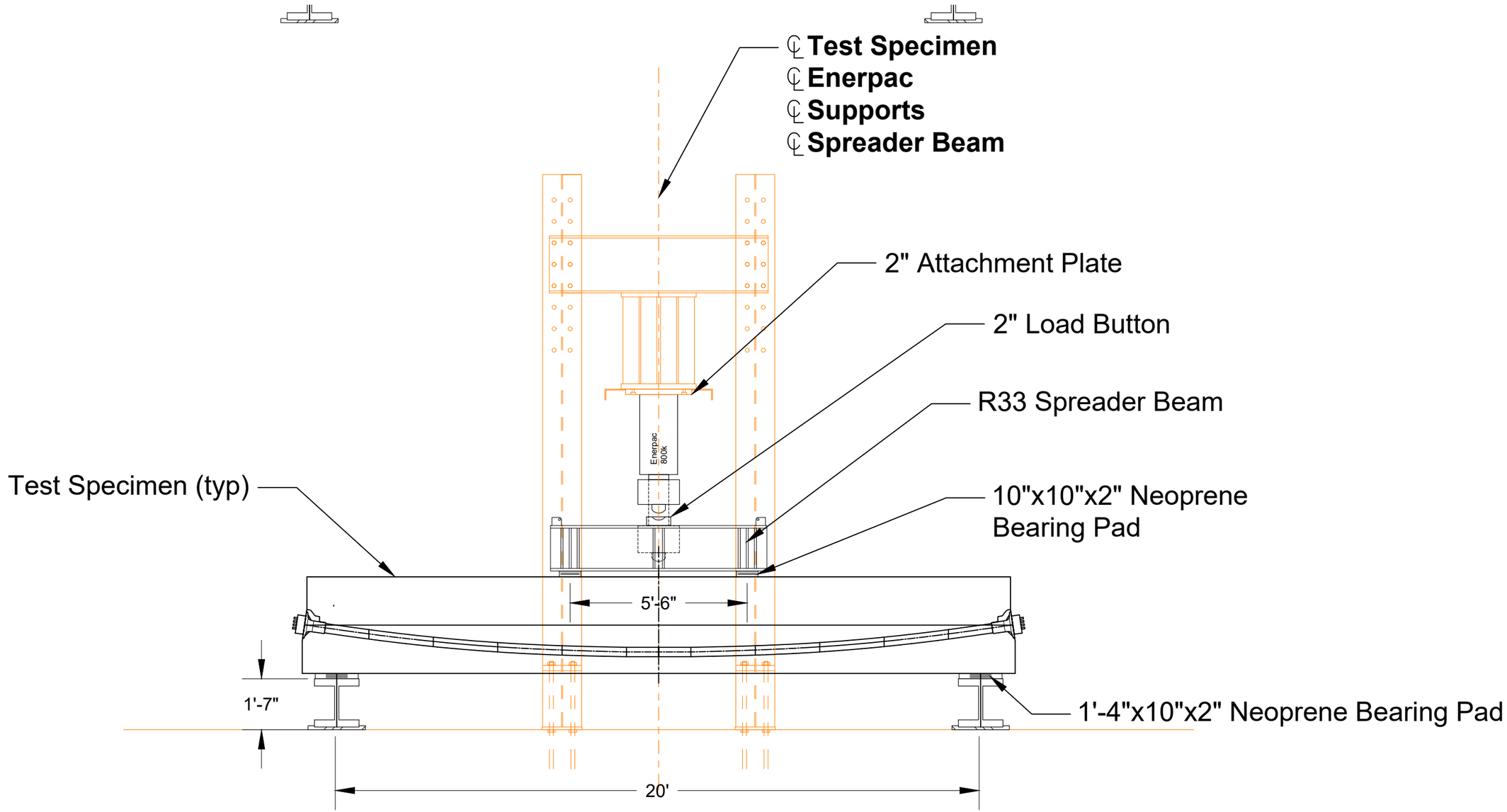

EMBRY-RIDDLE Aeronautical University	EMBRY-RIDDLE AERONAUTICAL UNIVERSITY DEPARTMENT OF CIVIL ENGINEERING 1 AEROSPACE BLVD DAYTONA BEACH, FL 32114	FDOT	SHEET TITLE: Load Frame and Testing Plan	6/6/23
			PROJECT NAME: INSPECTION OF FLEXIBLE FILLERS	SHEET NO. 15 of 22

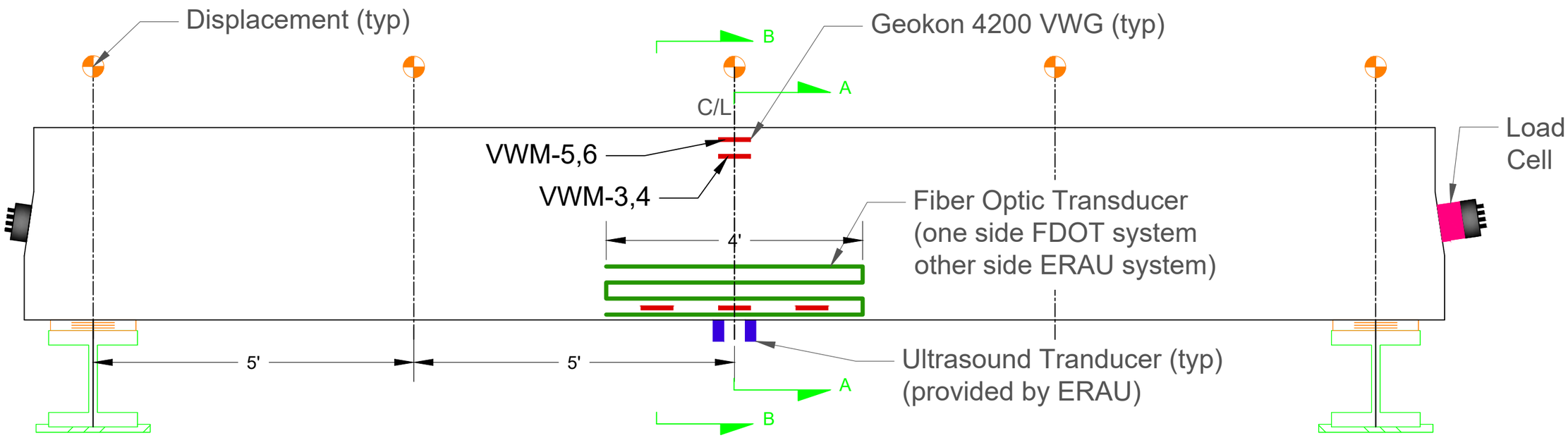

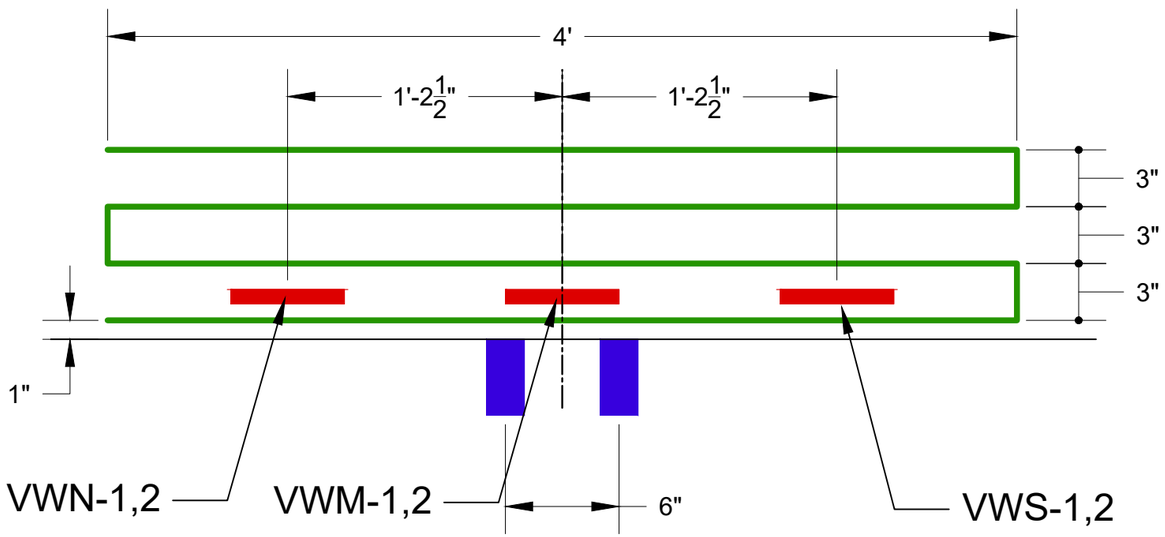

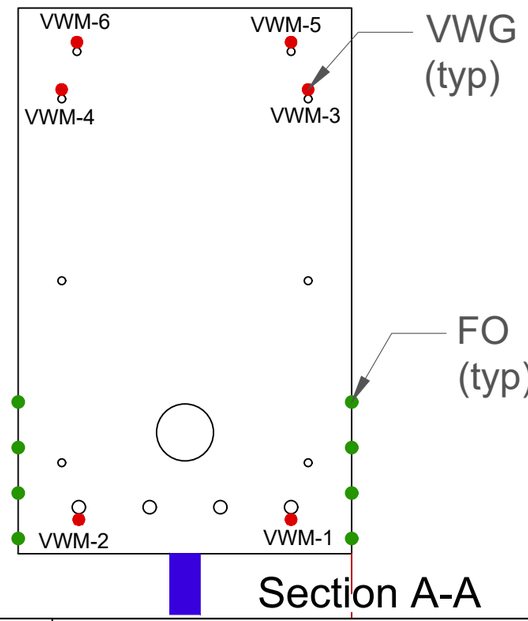

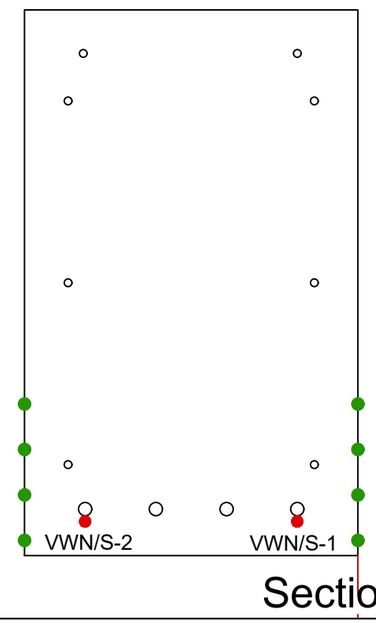

EMBRY-RIDDLE Aeronautical University™

EMBRY-RIDDLE AERONAUTICAL UNIVERSITY
DEPARTMENT OF CIVIL ENGINEERING
1 AEROSPACE BLVD
DAYTONA BEACH, FL 32114

FDOT

SHEET TITLE: Instrumentation Plan - Specimen A

6/6/23

PROJECT NAME: INSPECTION OF FLEXIBLE FILLERS

SHEET NO.
16 of 22

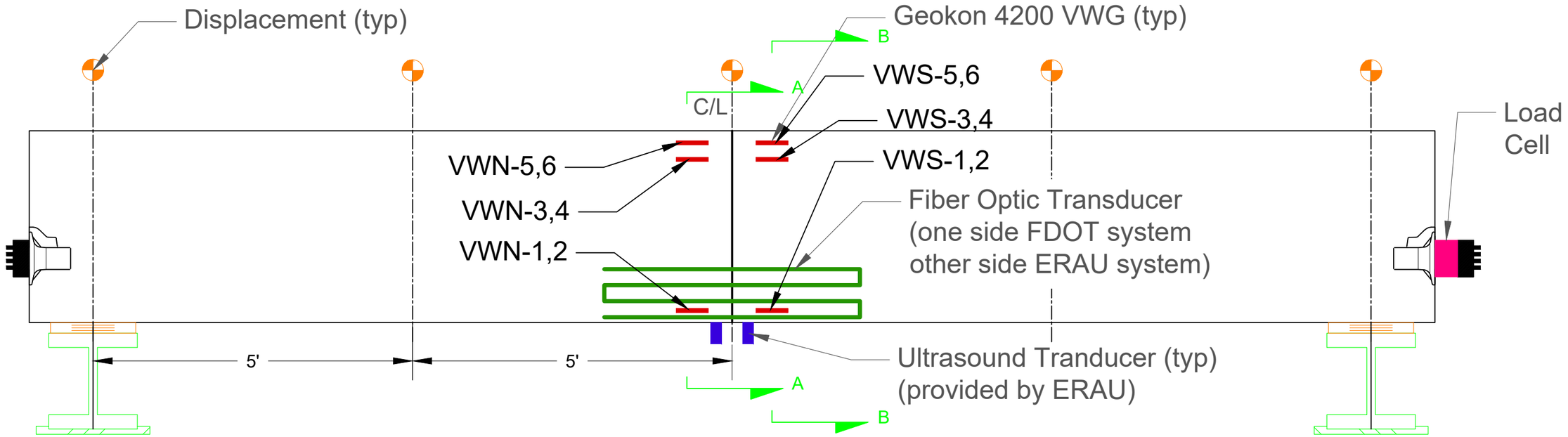

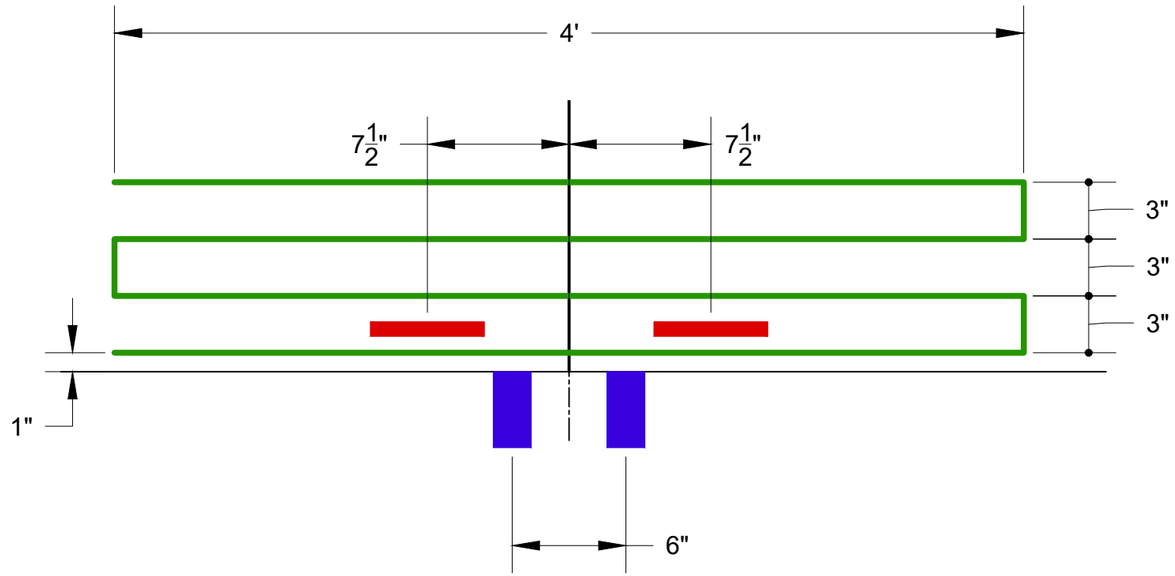

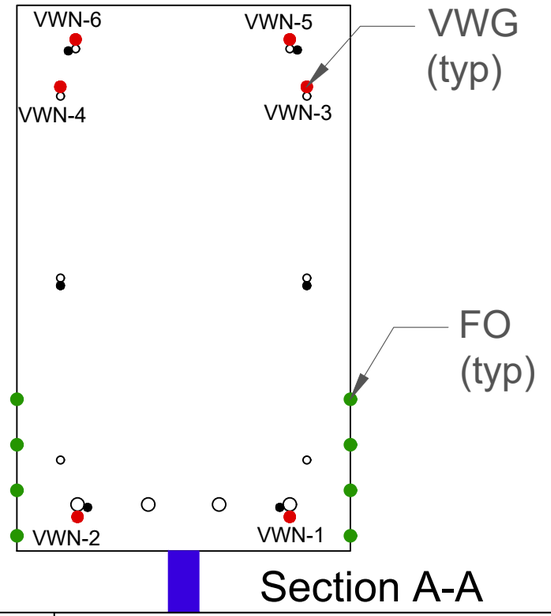

Section A-A

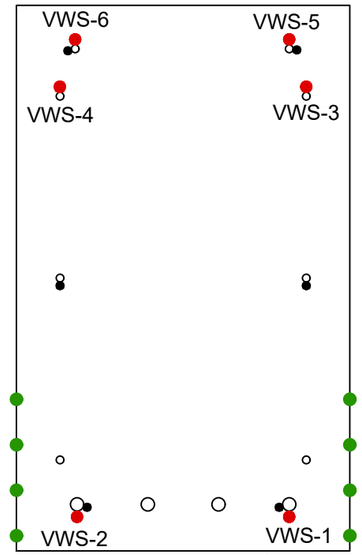

Section B-B

EMBRY-RIDDLE Aeronautical University™

EMBRY-RIDDLE AERONAUTICAL UNIVERSITY
DEPARTMENT OF CIVIL ENGINEERING
1 AEROSPACE BLVD
DAYTONA BEACH, FL 32114

FDOT

SHEET TITLE: Instrumentation Plan - Specimen B

6/6/23

PROJECT NAME: INSPECTION OF FLEXIBLE FILLERS

SHEET NO.
17 of 22

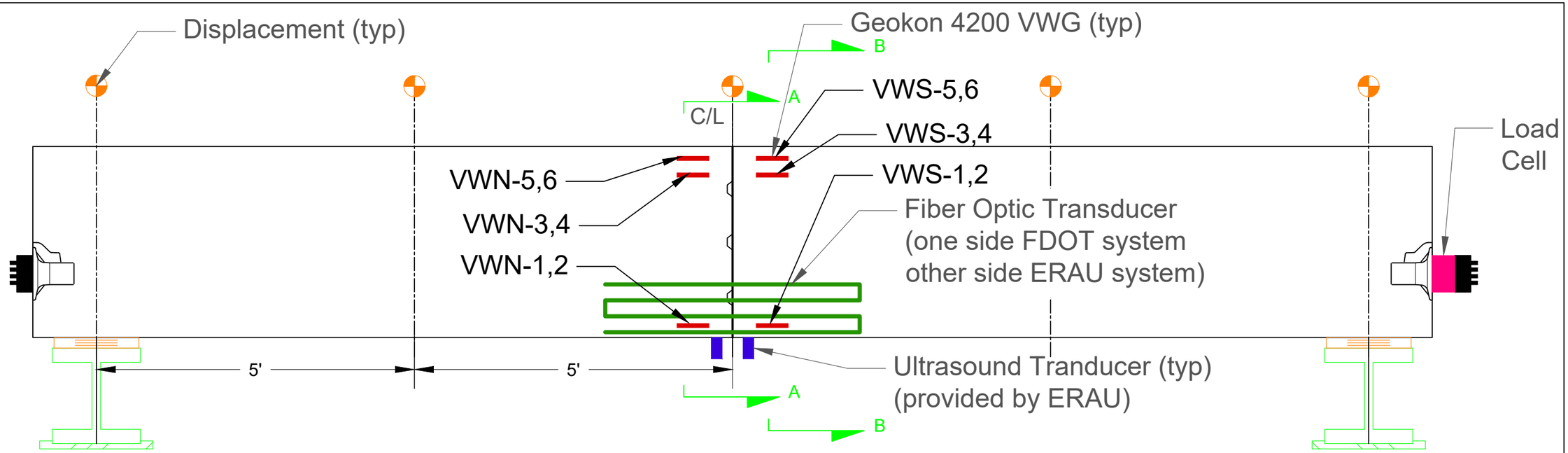

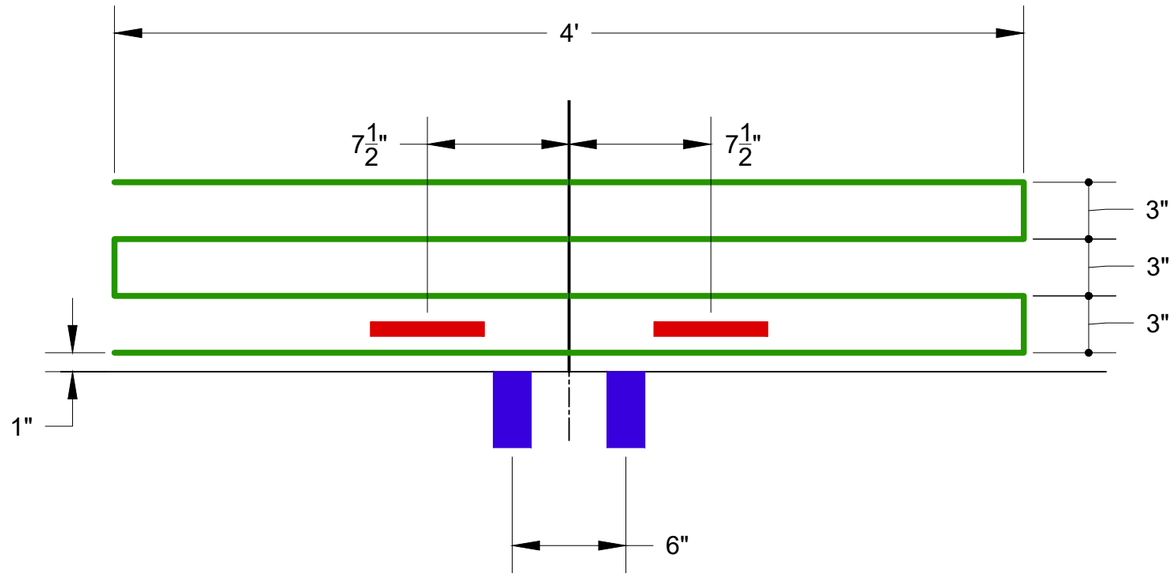

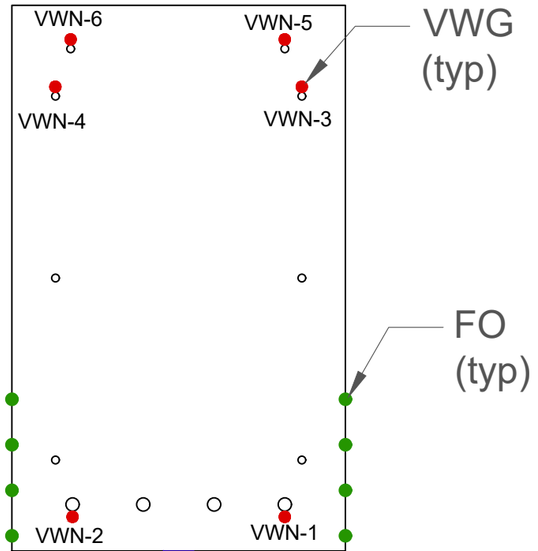

Section A-A

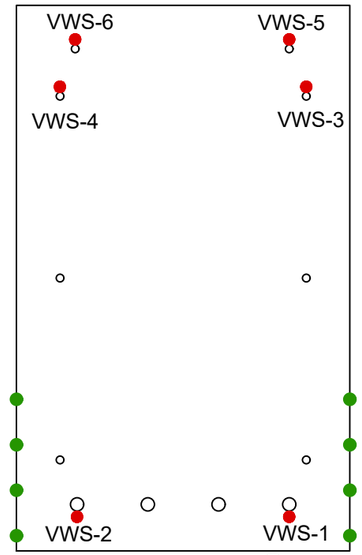

Section B-B

EMBRY-RIDDLE Aeronautical University™

EMBRY-RIDDLE AERONAUTICAL UNIVERSITY
DEPARTMENT OF CIVIL ENGINEERING
1 AEROSPACE BLVD
DAYTONA BEACH, FL 32114

FDOT

SHEET TITLE: Instrumentation Plan - Specimen B

6/6/23

PROJECT NAME: INSPECTION OF FLEXIBLE FILLERS

SHEET NO.
18 of 22

Notes:

1. Specimens will be post-tensioned after the concrete reaches the specified compressive strength
2. Hardware required is provided in Table 1
3. Strand layout is provided in Figure 1
4. Target PT force corresponds to 35% of fpu

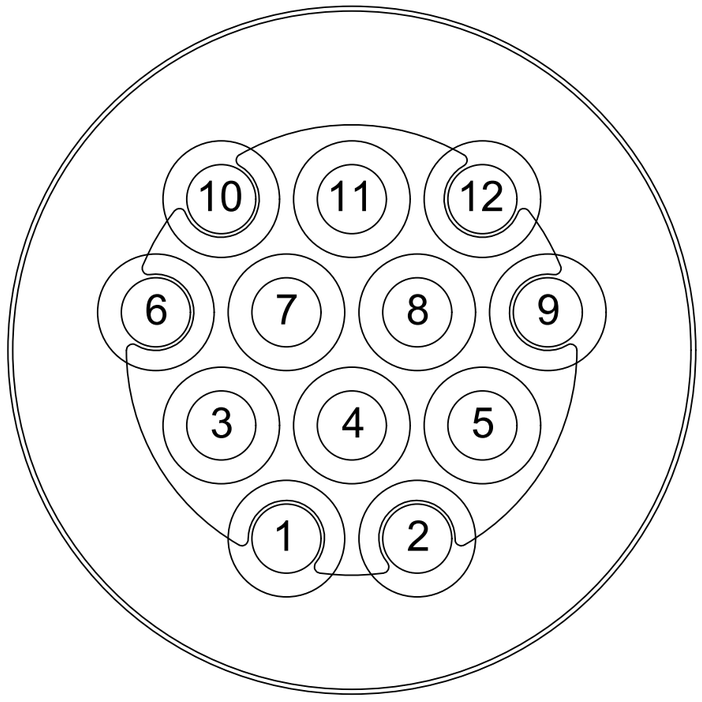

Figure 1

Table 1: Hardware Required	
Live End	Dead End
(1) Multi-strand jack	(1) Alignment washer set
(1) Jack stressing plate	(1) Load cell
(1) Wedge plate & anchor head	(1) Wedge plate & anchor head
(12) Wedges	(12) Wedges

Table 2: Tendon Details				
Specimen	# of Tendons	# of Strands	Strand Length	Tendon Force
A	1	12	35'-0"	246 kip
B	1	12	35'-0"	246 kip
C	1	12	35'-0"	246 kip

Data Collection During Stressing:

1. Pause jacking force at 25-kip increments for data collection
2. Collect data from following sensors at 25 kip increments:
   - 2.1. Ultrasound
   - 2.2. VWG
   - 2.3. Fiber Optics (FDOT and ERAU)

EMBRY-RIDDLE Aeronautical University

EMBRY-RIDDLE AERONAUTICAL UNIVERSITY
DEPARTMENT OF CIVIL ENGINEERING
1 AEROSPACE BLVD
DAYTONA BEACH, FL 32114

FDOT

SHEET TITLE: Stressing Plan

6/6/23

PROJECT NAME: INSPECTION OF FLEXIBLE FILLERS

SHEET NO. 19 of 22

Testing Plan Notes:

1. The objective of the testing is to induce "barely visible cracking" in each specimen.
2. The target load for cracking is 84 kips in 4-pt bending
3. Three distinct load values related to serviceability will be identified: Pc_fo, Pc_ut, and Pc_bv
4. Pc_fo is the applied load where crack initiation is detectable in the fiber optic data
5. Pc_ut is the applied load where crack initiation is detectable in the ultrasound data
6. Pc_bv is the applied load where crack initiation is detected from visual inspection
7. Target loading rate is ~10 kip/minute

Table 1: Target loads for UT scans

Jacking	4-pt 1 (Increase)	4-pt 1 (Decrease)	4-pt 2 (Increase)	4-pt 2 (Decrease)	4-pt 3 (Increase)	4-pt 3 (Decrease)
Load (kip)	Load (kip)	Load (kip)	Load (kip)	Load (kip)	Load (kip)	Load (kip)
0	0	100	0	105% Pc_ut	0	105% Pc_fo
25	10	90	40	Pc_ut	40	Pc_fo
50	20	80	80% Pc_ut	95% Pc_ut	80% Pc_fo	95% Pc_fo
75	30	60	85% Pc_ut	90% Pc_ut	85% Pc_fo	90% Pc_fo
100	40	40	90% Pc_ut	85% Pc_ut	90% Pc_fo	85% Pc_fo
125	50	20	95% Pc_ut	80% Pc_ut	95% Pc_fo	80% Pc_fo
150	60	0	Pc_ut	40	Pc_fo	40
175	70		105% Pc_ut	0	105% Pc_fo	0
200	80		110% Pc_ut		110% Pc_fo	
225	90					
246	100					
	110 (Note 1,2)					

Note 1: Loading will continue until barely visible cracking is observed.

Note 2: Pc_fo, Pc_ut, and Pc_bv will be determined during 4-pt 1 loading. 4-pt 2 loading will attempt to increase resolution at -20%/+10% of Pc_ut. 4-pt 3 loading will increase resolution at -20%/+10% of Pc_fo

EMBRY-RIDDLE Aeronautical University™
EMBRY-RIDDLE AERONAUTICAL UNIVERSITY
DEPARTMENT OF CIVIL ENGINEERING
1 AEROSPACE BLVD
DAYTONA BEACH, FL 32114

FDOT

SHEET TITLE: Stressing Plan

6/6/23

PROJECT NAME: INSPECTION OF FLEXIBLE FILLERS

SHEET NO. 20 of 22

Vacuum assist Injection of Civetea Wax into Internal Specimen

Targets
Temp = between 212 deg F and 240 deg F
Tendon volume = 15 gal
Tendon volume + waste = 17 gal
Velocity = 40 70 ft/min
Flow = 15 gpm
Max pressure (at inlet) = 75 psi
Max pressure (at pump) = 145 psi

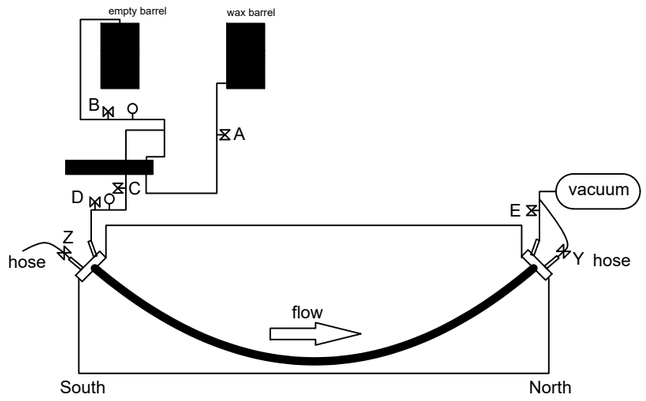

Figure 1—Schematic of set up for vacuum injection

1.1 Pre injection:

1. Air test: Increase tendon pressure with pump to 50 psi. Accept the test if pressure drop is less than 25 psi in 1 minute.
2. Vacuum test: Vacuum pump to 90% vacuum and stop the pump. Wait one minute. If the loss of vacuum after 1 minute exceeds 10%, repair leaks and repeat test, as necessary.
3. Heat filler to between 212 deg F and 240 deg F. Occasionally stir the filler material to ensure uniform temperature.
4. Ensure that all hoses are clear and preheated.
5. Position video cameras and LED lights at each of the windows to record injection.
6. Position personnel at both ends with buckets and wet towels. Personnel should be visible to the pump operator.

1.2 Injection:

1. Position drums adjacent to pump.
2. Place return line in empty barrel.
3. Connect discharge line to the pump. Leave the outlet end of the discharge line open.
4. Preheat the pump to 250° F.
5. Start data acquisition system and begin video recording.
6. Begin pulling a vacuum. Target vacuum: 28 in. Hg.
7. Before connecting the discharge line to the inlet valve, start the pump and discharge 2 gallons into a clean container. Make sure hose is discharging WAX, NO AIR.
8. Connect discharge line to inlet valve.
9. Open in line valves. Make sure cap valves are CLOSED.
10. Open discharge line valves and throttle pump to 10 on dial. Inject filler continuously at approximately 15 gpm.
11. When filler is noted in the discharge line, close outlet valve before filler enters vacuum pump.
12. Close inlet valve and stop pump. Lock in pressure = 30 45 psi.
13. Disconnect discharge line and reverse pump to pull filler from injection hose and deliver back into drum. Disconnect hoses and clean.

IR Readings	Temperature (F)
Start temp, barrel:	
Concrete surf temp:	
End temp, barrel:	

*From IWC project by Dr. Hamilton & Dr.Consolazio

Table 3: Filler Requirements

Specimen	# Strands per tendon	Length of duct	Volume of duct	Volume of strands	Filler vol. per duct	Filler vol. total
A	12	22'-1 1/8"	1950 in^3	690 in^3	5.5 gal	5.5 gal
B/C	12	22'-0"	1942in^3	688 in^3	5.5 gal	11 gal

EMBRY-RIDDLE Aeronautical University™
EMBRY-RIDDLE AERONAUTICAL UNIVERSITY
DEPARTMENT OF CIVIL ENGINEERING
1 AEROSPACE BLVD
DAYTONA BEACH, FL 32114

FDOT

SHEET TITLE: Filler Injection Plan

6/6/23

PROJECT NAME: INSPECTION OF FLEXIBLE FILLERS

SHEET NO.
21 of 22

EMBRY-RIDDLE Aeronautical University™	EMBRY-RIDDLE AERONAUTICAL UNIVERSITY DEPARTMENT OF CIVIL ENGINEERING 1 AEROSPACE BLVD DAYTONA BEACH, FL 32114	FDOT	SHEET TITLE: Yard Layout	6/6/23
			PROJECT NAME: INSPECTION OF FLEXIBLE FILLERS	SHEET NO. 22 of 22

Appendix B - Design Calculations for Large-Scale Test Specimens

Design Calculations for Large-Scale Testing
Inspection of Flexible Fillers

Specimens B&C (Straight Tendon)
Specimen A (Draped Tendon)

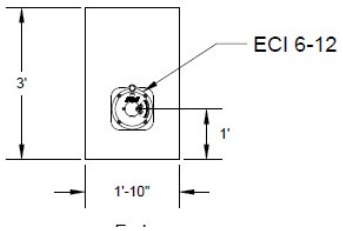

Cross-Section Geometry — Spec. B/C

$b := 22\ in \qquad h := 36\ in$

$d_{cover} := 2\ in$

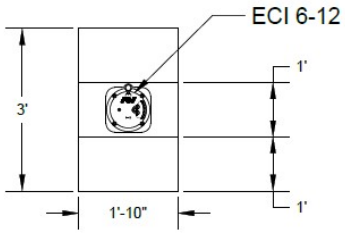

Spec. A

Rebar Sizes

Long. Steel - #7 bars (bottom layer -- ml)
#4 bars for temperature (tl)

$d_{ml\_bar} := \frac{7}{8}\ in \qquad A_{ml\_bar} := \frac{\pi \cdot d_{ml\_bar}^{\ 2}}{4}$

$N_{ml\_bar} := 4 \qquad A_{s\_ml} := N_{ml\_bar} \cdot A_{ml\_bar} = 2.41\ in^2$

$d_{tl\_bar} := 0.5\ in \qquad A_{tl\_bar} := \frac{\pi \cdot d_{tl\_bar}^{\ 2}}{4}$

Area and Moment of Inertia

$N_{tl\_bar} := 6 \qquad A_{s\_tl} := N_{tl\_bar} \cdot A_{tl\_bar}$

$I_g := \frac{b \cdot h^3}{12} = \left(8.55 \cdot 10^4\right)\ in^4$

Stirrups - #5 bars

$A_g := b \cdot h = 792\ in^2$

$d_{stirr} := 0.625\ in \qquad A_{stirr} := \frac{\pi \cdot d_{stirr}^{\ 2}}{4}$

Reinforcement Ratio Calculations

$400\ mm = 15.75\ in$
$650\ mm = 25.59\ in$

$$\rho := \frac{N_{ml\_bar} \cdot A_{ml\_bar} + N_{tl\_bar} \cdot A_{tl\_bar}}{A_g} = 4.52 \cdot 10^{-3}$$

$$d := h - d_{cover} - d_{stirr} - \frac{d_{ml\_bar}}{2} = 32.9\ in$$

Temperature and Shrinkage

$$A_s \geq \frac{1.30bh}{2(b+h)f_y}$$

except that:

$$0.11 \leq A_s \leq 0.60$$

where:

A_s = area of reinforcement in each direction and each face (in.^{2}/ft)
b = least width of component section (in.)
h = least thickness of component section (in.)
f_y = specified minimum yield strength of reinforcement ≤75.0 ksi

$$A_{s\_ts} := \frac{1.3 \cdot 22 \cdot 36}{2 \cdot (22+36) \cdot 60} = 0.148 \qquad \text{(required)}$$

Temperature Steel Provided

Side Face

$$\frac{3 \cdot A_{tl\_bar}}{3} = 0.2\ in^2$$

Top Face

$$\frac{2 \cdot A_{tl\_bar}}{\frac{22}{12}} = 0.21\ in^2$$

Non-Commercial Use Only

Material Properties

Concrete compressive strength and unit weight:

$f'_c := 5500\ psi$ $\gamma_c := 145\ \frac{lbf}{ft^3}$

Concrete modulus of elasticity

$E_c := 1820 \cdot \sqrt{\frac{f'_c}{1000\ psi}} \cdot ksi = \left(4.27 \cdot 10^3\right)\ ksi$

Concrete modulus of rupture

$f_r := 0.24 \cdot \sqrt{\frac{f'_c}{1000\ psi}} \cdot ksi = 0.56\ ksi$

Steel tensile strength and modulus of elasticity

Mild steel: Post-tensioning steel:

$f_y := 60\ ksi$ $f_{pu} := 270\ ksi$ $f_{py} := 0.9 \cdot f_{pu}$

$E_s := 29000\ ksi$

Structure Properties

$L := 20\ ft$ $L_P := 5.5\ ft$ Spacing between load points for 4-pt bending

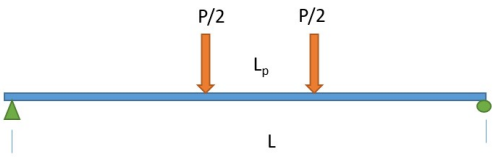

Dead Load

$w_{DC} := b \cdot h \cdot \gamma_c = 797.5\ \frac{lbf}{ft}$

$M_{DC} := \frac{w_{DC} \cdot L^2}{8} = 39.88\ kip \cdot ft$ Dead Load moment at midspan due to self-weight

Structural Analysis for beam without post-tensioning

Cracking moment calculations

$M_{cr} := \frac{f_r \cdot I_g}{\frac{h}{2}} = 222.89\ kip \cdot ft$

Flexural capacity

$a := \frac{A_{s\_ml} \cdot f_y}{0.85 \cdot f'_c \cdot b} = 1.4\ in$

Non-Commercial Use Only

$$M_n := A_{s\_ml} \cdot f_y \cdot \left(d - \frac{a}{2}\right) = 387.68 \ \textit{kip} \cdot \textit{ft}$$

Cracking Load for 4-pt bending

$$M_{cr} = \frac{P_{cr}}{2} \cdot \frac{\left(L - L_p\right)}{2} + M_{DC}$$

$$P_{cr} := \frac{\left(M_{cr} - M_{DC}\right) \cdot 4}{L - L_P} = 50.49 \ \textit{kip}$$

Ultimate load for 4-pt bending

$$P_u := \frac{\left(M_n - M_{DC}\right) \cdot 4}{L - L_P} = 95.95 \ \textit{kip}$$

Shear Capacity (Non-Prestressed Section)

Determine effective shear depth. This is distance that V_s must be provided using shear stirrups

$$d_e = \frac{A_{ps} f_{ps} d_p + A_s f_y d_s}{A_{ps} f_{ps} + A_s f_y}$$

$A_{ps} := 0 \ \textit{in}^2$ $f_{ps} := 270 \ \textit{ksi}$ $d_p := 6 \ \textit{in}$

$A_s := A_{s\_ml} = 2.41 \ \textit{in}^2$ $f_s := 60 \ \textit{ksi}$ $d_s := d = 32.94 \ \textit{in}$

$$d_e := \frac{A_{ps} \cdot f_{ps} \cdot d_p + A_s \cdot f_s \cdot d_s}{A_{ps} \cdot f_{ps} + A_s \cdot f_s} = 32.94 \ \textit{in}$$

$d_v := \max\left(0.9 \ d_e, 0.72 \cdot h\right) = 29.64 \ \textit{in}$ $0.9 \ d_e = 29.64 \ \textit{in}$ $0.72 \cdot h = 25.92 \ \textit{in}$

$$V_u := \frac{P_u}{2} + \left(w_{DC} \cdot \frac{L}{2} - w_{DC} \cdot \left(8 \ \textit{in} + d_v\right)\right) = 53.45 \ \textit{kip}$$

8" is from C/L to edge of bearing pad

Non-Commercial Use Only

$$V_c = 0.0316\beta\lambda\sqrt{f'_c}\ b_v d_v$$

$$\beta = \frac{4.8}{(1+750\varepsilon_s)}$$

$$\varepsilon_s = \frac{\left(\frac{|M_u|}{d_v} + 0.5N_u + |V_u - V_p| - A_{ps}f_{po}\right)}{E_s A_s + E_p A_{ps}}$$

$M_u := V_u \cdot d_v = 132.03\ \textit{kip} \cdot \textit{ft}$

$A_{ps} = 0\ \textit{in}^2 \qquad N_u := 0\ \textit{kip} \qquad V_p := 0\ \textit{kip}$

$E_p := 28500\ \textit{ksi}$

$$\varepsilon_s := \frac{\frac{M_u}{d_v} + 0.5 \cdot N_u + (V_u - V_p)}{E_s \cdot A_s} = 1.53 \cdot 10^{-3}$$

$$\beta := \frac{4.8}{1 + 750 \cdot \varepsilon_s} = 2.23$$

$$V_c := .0316 \cdot \beta \cdot \sqrt{\frac{f'_c}{1000\ \textit{psi}}} \cdot \textit{ksi} \cdot (b) \cdot (.72 \cdot h) = 94.38\ \textit{kip}$$

5.7.2.3—Regions Requiring Transverse Reinforcement

Except for slabs, footings, and culverts, transverse reinforcement shall be provided where:

- $V_u > 0.5\phi(V_c + V_p)$

or

- Where consideration of torsion is required by Eq. 5.7.2.1-3.

where:

V_u = factored shear force (kip)

V_c = nominal shear resistance of the concrete (kip)

V_p = component of prestressing force in the direction of the shear force

Φ = resistance factor specified in Article 5.5.4.2

$$V_u := \frac{P_u}{2} + \left(\frac{w_{DC} \cdot L}{2} - w_{DC} \cdot (8\ \textit{in} + d_v)\right) = 53.45\ \textit{kip}$$

$\phi := 0.9$

$0.5 \cdot \phi \cdot V_c = 42.47\ \textit{kip}$

Minimum shear reinforcement is required for non-prestressed section

Non-Commercial Use Only

Post Tensioning

Design beam so full PT force for 12-strand tendon can be applied

$d_{strand} := 0.6\ in$ $A_{strand} := 0.217\ in^2$ Distance to tendon from bottom

$N_{strands} := 12$ $f_{pu} := 270\ ksi$ $H := 12\ in = 12\ in$

% of ultimate stress at jacking

$p_{ult} := 0.8$

Prestress Force

$P_s := N_{strands} \cdot A_{strand} \cdot f_{pu} \cdot p_{ult} = 562.46\ kip$

$e_p := -\left(\frac{h}{2} - H\right) = -6\ in$

$M_{ps} := P_s \cdot e_p = -281.23\ kip \cdot ft$

Concrete Stress Calculations after Jacking

$\left(M_{DC} - M_{ps}\right) = 321.11\ kip \cdot ft$

Midspan

Bottom

$$\sigma_{c\_Bm} := -\frac{P_s}{A_g} + \frac{-\left(M_{DC} + M_{ps}\right) \cdot -\left(\frac{h}{2}\right)}{I_g} = -1.32 \cdot 10^3\ psi$$ (compression)

Top

$$\sigma_{c\_Tm} := -\frac{P_s}{A_g} + \frac{-\left(M_{DC} + M_{ps}\right) \cdot \left(\frac{h}{2}\right)}{I_g} = -100.69\ psi$$ (compression)

End

Bottom

$$\sigma_{c\_Be} := -\frac{P_s}{A_g} + \frac{-M_{ps} \cdot -\left(\frac{h}{2}\right)}{I_g} = -1.42 \cdot 10^3\ psi$$ (compression)

Max allowable is

$-0.65 \cdot f'_c = -3.58\ ksi$

Non-Commercial Use Only

Top

$$\sigma_{c\_Te} := -\frac{P_s}{A_g} + \frac{-M_{ps} \cdot \left(\frac{h}{2}\right)}{I_g} = 0 \ psi$$

Cracking Moment

- $M_{cr} = \gamma_3 \left[\left(\gamma_1 f_r + \gamma_2 f_{cpe} \right) S_c - M_{dnc} \left(\frac{S_c}{S_{nc}} - 1 \right) \right]$

(5.6.3.3-1)

where:

M_{cr} = cracking moment (kip-in.)

f_r = modulus of rupture of concrete specified in Article 5.4.2.6

f_{cpe} = compressive stress in concrete due to effective prestress forces only (after allowance for all prestress losses) at extreme fiber of section where tensile stress is caused by externally applied loads (ksi)

M_{dnc} = total unfactored dead load moment acting on the monolithic or noncomposite section (kip-in.)

S_c = section modulus for the extreme fiber of the composite section where tensile stress is caused by externally applied loads (in.^{3})

S_{nc} = section modulus for the extreme fiber of the monolithic or noncomposite section where tensile stress is caused by externally applied loads (in.^{3})

Appropriate values for M_{dnc} and S_{nc} shall be used for any intermediate composite sections. Where the beams are designed for the monolithic or noncomposite section to resist all loads, S_{nc} shall be substituted for S_c in the above equation for the calculation of M_{cr}.

The following factors shall be used to account for variability in the flexural cracking strength of concrete, variability of prestress, and the ratio of nominal yield stress of reinforcement to ultimate:

γ_1 = flexural cracking variability factor

= 1.2 for precast segmental structures

= 1.6 for all other concrete structures

γ_2 = prestress variability factor

= 1.1 for bonded tendons

= 1.0 for unbonded tendons

γ_3 = ratio of specified minimum yield strength to ultimate tensile strength of the nonprestressed reinforcement

= 0.67 for AASHTO M 31 (ASTM A615), Grade 60 reinforcement

= 0.75 for AASHTO M 31 (ASTM A615), Grade 75 reinforcement

= 0.76 for AASHTO M 31 (ASTM A615), Grade 80 reinforcement

= 0.75 for A706, Grade 60 reinforcement

= 0.80 for A706, Grade 80 reinforcement

= 0.67 for AASHTO M 334 (ASTM A1035), Grade 100 reinforcement

= For prestressing steel, γ_3 shall be taken as 1.0.

The provisions of Article 5.10.6 shall apply.

$f_r = 0.56 \ ksi$

$f_{cpe} := -\sigma_{c\_Be} = 1.42 \ ksi$

(does not include M_{DC})

$S_c := \frac{I_g}{\frac{h}{2}} = \left(4.75 \cdot 10^3\right) \ in^3$

$\gamma_1 := 1.2$ Assume segmental

$\gamma_2 := 1.0$

$\gamma_3 := 0.67$

$M_{cr} := \gamma_3 \cdot \left(\gamma_1 \cdot f_r + \gamma_2 \cdot f_{cpe}\right) \cdot S_c$

$M_{cr} = 556.05 \ kip \cdot ft$

Cracking force for 4-pt bending

$$P_{cr} := \frac{\left(M_{cr} - M_{DC}\right) \cdot 4}{L - L_P} = 142.39 \ kip$$

Ultimate flexural capacity

$$M_n = A_{ps} f_{ps} \left(d_p - \frac{a}{2} \right) + A_s f_s \left(d_s - \frac{a}{2} \right) - A'_s f'_s \left(d'_s - \frac{a}{2} \right) + \alpha_1 f'_c \left(b - b_w \right) h_f \left(\frac{a}{2} - \frac{h_f}{2} \right)$$

(5.6.3.2.2-1)

where:

A_{ps} = area of prestressing steel (in.^{2})

f_{ps} = average stress in prestressing steel at nominal bending resistance specified in Eq. 5.6.3.1.1-1 (ksi)

$A_{ps} := N_{strands} \cdot A_{strand} = 2.6 \ in^2$

$d_p := 24 \ in$

$A_s := A_{s\_ml} = 2.41 \ in^2$

Non-Commercial Use Only

d_p = distance from extreme compression fiber to the centroid of prestressing tendons (in.)

A_s = area of nonprestressed tension reinforcement (in.^{2})

f_s = stress in the nonprestressed tension reinforcement at nominal flexural resistance (ksi), as specified in Article 5.6.2.1

d_s = distance from extreme compression fiber to the centroid of nonprestressed tensile reinforcement (in.)

A'_s = area of compression reinforcement (in.^{2})

f'_s = stress in the nonprestressed compression reinforcement at nominal flexural resistance (ksi), as specified in Article 5.6.2.1

d'_s = distance from extreme compression fiber to the centroid of compression reinforcement (in.)

f'_c = design concrete compressive strength (ksi)

$$d_s := d = 32.94\ \textit{in}$$

Determine stress in prestressing steel at nominal capacity

$$f_{ps} = f_{pe} + 900\left(\frac{d_p - c}{\ell_e}\right) \le f_{py}$$

in which:

$$\ell_e = \left(\frac{2\,\ell_i}{2 + N_s}\right)$$

for T-section behavior:

$$c = \frac{A_{ps} f_{ps} + A_s f_s - A'_s f'_s - \alpha_1 f'_c (b - b_w) h_f}{\alpha_1 f'_c \beta_1 b_w}$$

for rectangular section behavior:

$$c = \frac{A_{ps} f_{ps} + A_s f_s - A'_s f'_s}{\alpha_1 f'_c \beta_1 b}$$

$$f_{pe} := f_{pu} \cdot p_{ult} = 216\ \textit{ksi} \qquad b = 22\ \textit{in}$$

$$d_p = 24\ \textit{in} \qquad f_s := f_y = 60\ \textit{ksi}$$

$$l_e := 20\ \textit{ft}$$

$$f'_c = 5.5\ \textit{ksi}$$

$\beta_1 := 0.65$ for 8.5 ksi concrete

$$\alpha_1 := 0.85$$

where:

c = distance from extreme compression fiber to the neutral axis assuming the tendon prestressing steel has yielded, given by Eqs. 5.6.3.1.2-3 and 5.6.3.1.2-4 for T-section behavior and rectangular section behavior, respectively (in.)

ℓ_e = effective tendon length (in.)

ℓ_i = length of tendon between anchorages (in.)

N_s = number of plastic hinges at supports in an assumed failure mechanism crossed by the tendon between anchorages or discretely bonded points assumed as:

- For simple spans 0
- End spans of continuous units 1
- Interior spans of continuous units 2

f_{py} = yield strength of prestressing steel (ksi)

f_{pe} = effective stress in prestressing steel after losses (ksi)

Guess Values

$$c := 12\ \textit{in}$$
$$f_{ps} := f_{pe} + 15\ \textit{ksi}$$

Constraints

$$f_{ps} = f_{pe} + 900\ ksi \cdot \left(\frac{d_p - c}{l_e}\right)$$
$$c = \frac{A_{ps} \cdot f_{ps} + A_s \cdot f_s}{\alpha_1 \cdot f'_c \cdot \beta_1 \cdot b}$$

Solver

$$\begin{bmatrix} f_{ps} \\ c \end{bmatrix} := \textbf{find}\left(f_{ps}, c\right) = \begin{bmatrix} 259.94 \\ 12.28 \end{bmatrix} \begin{bmatrix} \textit{ksi} \\ \textit{in} \end{bmatrix}$$

Non-Commercial Use Only

Prestressing steel has yielded

$$f_{ps} := f_{py} \qquad c := \frac{A_{ps} \cdot f_{ps} + A_s \cdot f_s}{\alpha_1 \cdot f'_c \cdot \beta_1 \cdot b} = 11.62\ in \qquad a := \beta_1 \cdot c = 7.56\ in$$

$$M_n := A_{ps} \cdot f_{ps} \cdot \left(d_p - \frac{a}{2}\right) + A_s \cdot f_s \cdot \left(d_s - \frac{a}{2}\right)$$

$$M_n = 1417\ kip \cdot ft$$

Force at ultimate moment capacity for 4-Pt bending

$$P_u := \frac{(M_n - M_{DC}) \cdot 4}{L - L_P} = 379.9\ kip$$

Develop complete V&M diagrams for ultimate load

$$V_{DC}(x) := w_{DC} \cdot \frac{L}{2} - w_{DC} \cdot x$$

$$V_L(x) := \begin{cases} \text{return } \dfrac{P_u}{2} & \text{if } x \le \dfrac{(L - L_P)}{2} \\ \text{return } 0 & \text{else if } \dfrac{(L - L_P)}{2} < x \le \dfrac{(L + L_P)}{2} \\ \text{return } \dfrac{-P_u}{2} & \text{else if } x > \dfrac{(L + L_P)}{2} \end{cases}$$

$$\frac{(L - L_P)}{2} = 7.25\ ft$$

Apply Strength 1 load factors for shear design assuming that P_u is a live load

$$V_u(x) := 1.25 \cdot V_{DC}(x) + 1.75 \cdot V_L(x)$$

Moment diagrams obtained by integrating shear:

$$M_{DC}(x) := \int_0^x V_{DC}(x)\, dx$$

$$M_L(x) := \int_0^x V_L(x)\, dx$$

Will not apply load factors for moment

$$M_u(x) := M_{DC}(x) + M_L(x)$$

Non-Commercial Use Only

Need to design shear stirrups to resist factored shear force, V_U

Determine effective shear depth. This is distance that V_s must be provided using shear stirrups

$$d_e = \frac{A_{ps} f_{ps} d_p + A_s f_y d_s}{A_{ps} f_{ps} + A_s f_y} \qquad d_e := \frac{A_{ps} \cdot f_{ps} \cdot d_p + A_s \cdot f_s \cdot d_s}{A_{ps} \cdot f_{ps} + A_s \cdot f_s} = 25.66\ \textit{in}$$

$$d_v := \max\left(0.9\ d_e, 0.72 \cdot h\right) = 25.92\ \textit{in} \qquad 0.9\ d_e = 23.09\ \textit{in} \qquad 0.72 \cdot h = 25.92\ \textit{in}$$

$V_U := V_u\left(d_v + 8\ \textit{in}\right) = 339.57\ \textit{kip}$ (Factored Shear at Critical Section)

$M_U := M_u\left(d_v\right) = 425.66\ \textit{kip} \cdot \textit{ft}$ (Moment at critical section for shear)

$$\beta = \frac{4.8}{(1 + 750\varepsilon_s)}$$

$$\varepsilon_s = \frac{\left(\frac{|M_u|}{d_v} + 0.5N_u + |V_u - V_p| - A_{ps} f_{po}\right)}{E_s A_s + E_p A_{ps}}$$

$A_{ps} = 2.6\ \textit{in}^2$ $N_u := 0\ \textit{kip}$ $V_p := 0\ \textit{kip}$

$E_p := 28500\ \textit{ksi}$ $f_{po} := 0.7 \cdot f_{pu} = 189\ \textit{ksi}$

$$\varepsilon_s := \frac{\frac{M_U}{d_v} + 0.5 \cdot N_u + \left(V_U - V_p\right) - A_{ps} \cdot f_{po}}{E_s \cdot A_s + E_p \cdot A_{ps}} = 3.09 \cdot 10^{-4}$$

$\beta := \frac{4.8}{1 + 750 \cdot \varepsilon_s} = 3.9$ $\theta = 29 + 3500\varepsilon_s$ $\theta := \left(29 + 3500 \cdot \varepsilon_s\right) \cdot \textit{deg} = 30.08\ \textit{deg}$

$\alpha := 90\ \textit{deg}$ (α is the angle of the stirrups)

$V_c := .0316 \cdot \beta \cdot \sqrt{\frac{f'_c}{1000\ \textit{psi}}} \cdot \textit{ksi} \cdot (b) \cdot (.72 \cdot h) = 164.69\ \textit{kip}$ (This seems more reasonable)

$V_c = 164.69\ \textit{kip}$

Non-Commercial Use Only

Determine required shear strength for steel

$$V_s := \frac{V_U}{0.9} - V_c = 212.61 \ kip$$

$$V_s = \frac{A_v f_y d_v (\cot\theta + \cot\alpha)\sin\alpha}{s}$$

Determine required spacing for region outside of bursting zone

$d_{b4} := 0.5 \ in$ $\quad d_{b5} := \frac{5}{8} \cdot in$ *diameters of #4 and #5 bars

$A_{b4} := \frac{\pi \cdot d_{b4}^2}{4}$ $\quad A_{b5} := \frac{\pi \cdot d_{b5}^2}{4}$

Investigate different spacing options for 2-leg and 4-leg stirrups

Try 2-leg, #4 bar

$$s_{2l\_b4} := \frac{2 \cdot A_{b4} \cdot f_y \cdot d_v \cdot (\cot(\theta) + \cot(\alpha))\ \sin(\alpha)}{V_s} = 4.96 \ in$$

Try 2-leg, #5 bar

$$s_{2l\_b5} := \frac{2 \cdot A_{b5} \cdot f_y \cdot d_v \cdot (\cot(\theta) + \cot(\alpha))\ \sin(\alpha)}{V_s} = 7.7 \ in$$

Try 4-leg, #4 bar

$$s_{2l\_b4} := \frac{4 \cdot A_{b4} \cdot f_y \cdot d_v \cdot (\cot(\theta) + \cot(\alpha))\ \sin(\alpha)}{V_s} = 9.92 \ in$$

Try 4-leg, #5 bar

$$s_{2l\_b5} := \frac{4 \cdot A_{b5} \cdot f_y \cdot d_v \cdot (\cot(\theta) + \cot(\alpha))\ \sin(\alpha)}{V_s} = 15.5 \ in$$

Max spacing = $\frac{d_v}{2} = 12.96 \ in$

Use #5 2-leg stirrups @7 inches

Non-Commercial Use Only

Anchorage design for fully-stressed tendon, Spec. B and C -- No Draping

5.8.4.5.3—Bursting Forces

The bursting forces in anchorage zones, T_{burst}, may be taken as:

$$T_{burst} = 0.25 \sum P_u \left(1 - \frac{a}{h}\right) + 0.5 \left|\Sigma \left(P_u \sin \alpha\right)\right| \qquad (5.8.4.5.3\text{-}1)$$

The location of the bursting force, d_{burst}, may be taken as:

$$d_{burst} = 0.5\,(h - 2e) + 5e \sin \alpha \qquad (5.8.4.5.3\text{-}2)$$

where:

T_{burst} = tensile force in the anchorage zone acting ahead of the anchorage device and transverse to the tendon axis (kip)

P_u = factored tendon force (kip)

d_{burst} = distance from anchorage device to the centroid of the bursting force, T_{burst} (in.)

a = lateral dimension of the anchorage device or group of devices in the direction considered (in.)

e = eccentricity of the anchorage device or group of devices with respect to the centroid of the cross-section; always taken as positive (in.)

h = lateral dimension of the cross-section in the direction considered (in.)

α = angle of inclination of a tendon force with respect to the centerline of the member; positive for concentric tendons or if the anchor force points toward the centroid of the section; negative if the anchor force points away from the centroid of the section (degrees)

The location and distribution of bursting reinforcement shall satisfy the requirements of Article 5.9.5.6.5b.

$P_u := 1.2\ P_s = 674.96\ \textit{kip}$ Factored PT Force (note re-definition)

$a := 9.75\ \textit{in}$ width of anchorage plate

$h_z := 22\ \textit{in}$ for width dimension

$h_y := 36\ \textit{in}$ for height dimension

$e_y := 6\ \textit{in}$ $\quad e_z := 0$

$\alpha = 0$ for Spec. B and C.

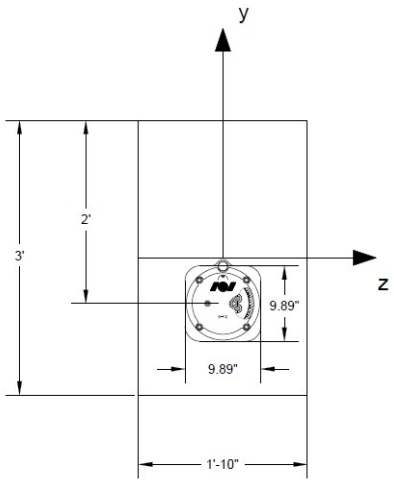

Factored bursting forces:

$$T_{By\_u} := 0.25 \cdot P_u \cdot \left(1 - \frac{a}{h_y}\right) = 123.04\ \textit{kip}$$

$$T_{Bz\_u} := 0.25 \cdot P_u \cdot \left(1 - \frac{a}{h_z}\right) = 93.96\ \textit{kip}$$

Distance from end to centroid of bursting forces:

$$d_{By} := 0.5 \cdot \left(h_y - 2 \cdot e_y\right) = 12\ \textit{in}$$

$$d_{Bz} := 0.5 \cdot \left(h_z\right) = 11\ \textit{in}$$

Limits of Bursting Zone

y-direction

$2.5 \cdot d_{By} = 30\ \textit{in}$ $\quad 1.5 \cdot h_y = 54\ \textit{in}$

use $h_{burst\_y} := 2.5 \cdot d_{By} = 30\ \textit{in}$

z-direction

$2.5 \cdot d_{Bz} = 27.5\ \textit{in}$ $\quad 1.5 \cdot h_z = 33\ \textit{in}$

use $h_{burst\_z} := 2.5 \cdot d_{Bz} = 27.5\ \textit{in}$

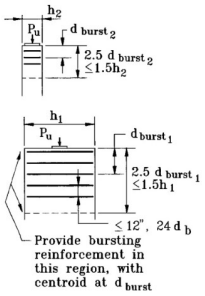

Steel required for bursting $\quad A_{stirr} = 0.31\ \textit{in}^2$

$$A_{s\_By} := \frac{T_{By\_u}}{0.85 \cdot f_y} = 2.41\ \textit{in}^2$$

8-#5 or 12-#4

$$A_{s\_Bz} := \frac{T_{Bz\_u}}{0.85 \cdot f_y} = 1.84\ \textit{in}^2$$

9-#4 or 6-#5

Non-Commercial Use Only

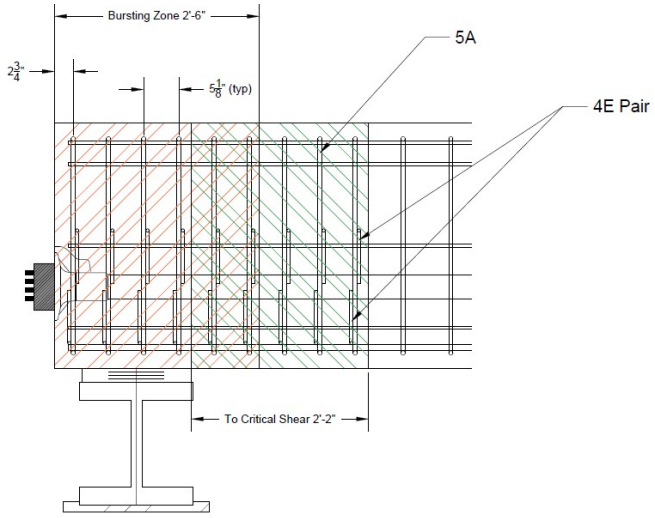

AASHTO Guidance is limited on regions where bursting and shear effects occur simultaneously.

Total required steel in y-direction for bursting zone is 8-#5 bars. Total steel provided in bursting zone is 12-#5 bars. Same spacing for #5 bars is extended through Critical Shear Zone.

Total required steel in z-direction for bursting zone is 10-#4 bars. Total steel provided in bursting zone is 12-#4 bars. Same spacing for #4E pair bars is extended through Critical Shear Zone.

Steel required for spalling

$$A_{s\_spall} := \frac{0.02 \cdot P_u}{0.85 \cdot f_y} = 0.26\ \textit{in}^2$$

3-#3 or 2-#4

Note: $P_u = 674.96\ \textit{kip}$ is jacking force

Concrete compressive stresses in anchorage region:

5.8.4.5.2—Compressive Stresses

The concrete compressive stress ahead of the anchorage devices, f_{ca}, calculated using Eq. 5.8.4.5.2-1, shall not exceed the limit specified in Article 5.9.5.6.5a:

$$f_{ca} = \frac{0.6 P_u \kappa}{A_b\left(1 + \ell_c\left(\frac{1}{b_{eff}} - \frac{1}{t}\right)\right)} \qquad (5.8.4.5.2\text{-}1)$$

in which:

if $a_{eff} \le s < 2a_{eff}$, then:

$$\kappa = 1 + \left(2 - \frac{s}{a_{eff}}\right)\left(0.3 + \frac{n}{15}\right) \qquad (5.8.4.5.2\text{-}2)$$

if $s \ge 2a_{eff}$, then:

$$\kappa = 1 \qquad (5.8.4.5.2\text{-}3)$$

where:

- κ = correction factor for closely spaced anchorages
- a_{eff} = lateral dimension of the effective bearing area of the anchorage measured parallel to the larger dimension of the cross-section (in.)
- b_{eff} = lateral dimension of the effective bearing area measured parallel to the smaller dimension of the cross-section (in.)
- P_u = factored tendon force (kip)
- t = member thickness (in.)
- s = center-to-center spacing of anchorages (in.)
- n = number of anchorages in a row
- ℓ_c = longitudinal extent of confining reinforcement of the local zone but not more than the larger of 1.15 a_{eff} or 1.15 b_{eff} (in.)
- A_b = effective bearing area (in.^{2})

The effective bearing area, A_b, in Eq. 5.8.4.5.2-1 shall be taken as the larger of the anchor bearing plate area, A_{plate}, or the bearing area of the confined concrete in the local zone, A_{conf}, with the following limitations:

$\kappa := 1$

$A_b := 9.9\ \textit{in} \cdot 9.9\ \textit{in} = 98.01\ \textit{in}^2$

$l_c := 13\ \textit{in}$

$b_{eff} := 9.9\ \textit{in}$

$t := 22\ \textit{in}$

$$f_{ca} := \frac{0.6 \cdot P_u \cdot \kappa}{\left(A_b \cdot \left(1 + l_c \cdot \left(\frac{1}{b_{eff}} - \frac{1}{t}\right)\right)\right)}$$

$f_{ca} = 2.4\ \textit{ksi}$

Maximum compressive stress cannot exceed

$0.6 \cdot f'_c \cdot \phi = 2.97\ \textit{ksi}$

Non-Commercial Use Only

Development length for bars in simulated closure pour

The modified tension development length, ℓ_d, in in. shall be taken as:

$$\ell_d = \ell_{db} \times \left(\frac{\lambda_{rl} \times \lambda_{cf} \times \lambda_{rc} \times \lambda_{er}}{\lambda} \right)$$

in which:

$$\ell_{db} = 2.4 d_b \frac{f_y}{\sqrt{f'_c}}$$

where:

ℓ_{db} = basic development length (in.)
λ_{rl} = reinforcement location factor
λ_{cf} = coating factor
λ = concrete density modification factor as specified in Article 5.4.2.8
λ_{rc} = reinforcement confinement factor
λ_{er} = excess reinforcement factor
f_y = specified minimum yield strength of reinforcement (ksi)
d_b = nominal diameter of reinforcing bar or wire (in.)
f'_c = compressive strength of concrete for use in design (ksi)

$$l_{db} := 2.4 \cdot d_{b4} \cdot \frac{\frac{f_y}{ksi}}{\sqrt{\frac{f'_c}{ksi}}} = 30.7\ in$$

$$\frac{246}{562} = 0.44$$

Structural Analysis for Load Testing to Induce "Barely Visible Cracking". Tendon will be stressed to 50% of maximum to simulate PT loss.

Actual Jacking Force

$p_{ult} := 0.35$ Stress to 35% of Ultimate

$N_{strands} = 12$ $A_{strand} = 0.22\ in^2$ $f_{pu} = 270\ ksi$

$$P_{jack} := N_{strands} \cdot A_{strand} \cdot f_{pu} \cdot p_{ult}$$

$$P_{jack} = 246.08\ kip$$

Cracking Moment

Moment generated by jacking force:

$M_{ps} := P_{jack} \cdot e_p = -123.04\ kip \cdot ft$

$f_r = 0.56\ ksi$

Stress in tension zone generated by jacking

$$\sigma_{c\_Be} := -\frac{P_{jack}}{A_g} + \frac{-M_{ps} \cdot -\left(\frac{h}{2}\right)}{I_g} = -621.41\ psi$$

Non-Commercial Use Only

$$S_c := \frac{I_g}{\frac{h}{2}} = \left(4.75 \cdot 10^3\right)\ in^3$$

$\gamma_1 := 1.2$ Assume segmental
$\gamma_2 := 1.0$
$\gamma_3 := 0.67$

Stress at midspan (without DC)
$f_{cpe} := -\sigma_{c\_Be}$

Cracking Moment
$M_{cr} := \gamma_3 \cdot \left(\gamma_1 \cdot f_r + \gamma_2 \cdot f_{cpe}\right) \cdot S_c$

$M_{cr} = 344.07\ kip \cdot ft$

Cracking force for 4-pt bending

$$P_{cr} := \frac{\left(M_{cr} - M_{DC}\left(10\ ft\right)\right) \cdot 4}{L - L_P} = 83.92\ kip$$

Non-Commercial Use Only